Engineering Carbon Nanostructures: Development of Novel Aerogel-Nanotube Composites and Optimization Techniques for Nanotube Growth

by

Stephen Alan Steiner III

B.S., Chemistry Course, University of Wisconsin–Madison (2004)

Submitted to the Department of Materials Science and Engineering in partial fulfillment of the requirements for the degree of

Master of Science in Materials Science and Engineering

at the

MASSACHUSETTS INSTITUTE OF TECHNOLOGY

June 2006

Author .....

Department of Materials Science and Engineering

May 31, 2006

Certified by .....

Mildred S. Dresselhaus

Institute Professor

Thesis Supervisor

Certified by .....

Jing Kong

Assistant Professor, Department of Electrical Engineering and Computer Science

Thesis Supervisor

Certified by .....

Francesco Stellacci

Finmeccanica Assistant Professor, Department of Materials Science and Engineering

Thesis Supervisor

Accepted by .....

Samuel M. Allen

POSCO Professor of Physical Metallurgy

Chair, Department Committee on Graduate Studies

Engineering Carbon Nanostructures: Development of Novel Aerogel-Nanotube Composites and Optimization Techniques for Nanotube Growth

by

Stephen Alan Steiner III

Submitted to the Department of Materials Science and Engineering
on May 31, 2006, in partial fulfillment of the
requirements for the degree of
Master of Science in Materials Science and Engineering

Abstract

Carbon aerogels offer several unique advantages which make them ideal for evaluating a metal's ability to catalyze nanotube growth, including *in situ* carbothermic reduction of oxidized nanoparticles to their catalytic metallic phase as they form and production of a bulk quantity of nanoparticles which can be easily characterized. In this work, metal-doped carbon aerogels of seven transition metals were synthesized, characterized, and evaluated for their ability to catalyze growth of carbon nanotubes by thermal chemical vapor deposition (CVD). It was found that carbon aerogels doped with Fe, Rh, Re, Au, and Nb all catalyzed the formation of nanotubes in moderate to high yields, resulting in a direct growth of nanotubes on the exterior surfaces of aerogel monoliths. Ta was found to grow nanotubes only after thorough reduction of its oxides. Growth with W was inconclusive. CVD growth of nanotubes throughout the interior porosity of metal-doped carbon aerogels was also achieved by templating a network of interconnected macropores into the monoliths.

Surface-based nanoparticles composed of rhenium, gold, and varying combinations of gold and rhenium were investigated for their ability to catalyze carbon nanotube growth. Nanoparticles of these metals were nucleated onto silicon wafers from solutions of anhydrous $ReCl_5$ and $AuCl_3$. After deposition, the nanoparticles were reduced under hydrogen for 10 min and then oxidized in air for 4 min. The samples were then processed by CVD employing hydrogen and ethanol-saturated Ar for 10 min. Nanoparticles deposited from metal chloride solutions with a 1:1 molar ratio of gold to rhenium or higher were found to result in high yields of single-walled nanotubes, where nanoparticles deposited from solutions with less than a 1:4 gold-to-rhenium ratio resulted in no nanotube growth.

Lastly, a new low-pressure CVD system specialized for nanotube growth was developed. The objectives of the system are to provide a flexible architecture for developing new nanotube growth techniques and to lower the minimum temperature required for nanotube growth. The system features a separate sample heating plate for thermally activating nanoparticles and hot filament for carbon feedstock cracking. The system also features the ability to easily install or remove modules for electric field- and plasma-assisted growths.

Thesis Supervisor: Mildred S. Dresselhaus
Title: Institute Professor
Department of Electrical Engineering and Computer Science, Department of Physics

Thesis Supervisor: Jing Kong
Title: Assistant Professor
Department of Electrical Engineering and Computer Science

Thesis Supervisor: Francesco Stellacci
Title: Finmeccanica Assistant Professor
Department of Materials Science and Engineering

Acknowledgements

Before anyone else, I would like to express my profound gratitude to the Department of Materials and Science and Engineering for giving me what has been a life-changing opportunity to study at MIT. I especially thank Professors Francesco Stellacci and Yet-Ming Chiang for their advocacy and for believing in me, for without them I would not be in graduate study today. Thank you for everything you have given me, and for everything yet to come.

I express an equally profound gratitude to Professors Jing Kong and Millie Dresselhaus, two people of outstanding vision and character whom I stand in awe of. Their persistent encouragement, discipline, and willingness to give unorthodox ideas full hearing has been fundamentally beneficial to me as a scientist, an engineer, and an individual. I am truly grateful for everything you have given me, and I only hope that I will somehow be able to give something back to you over the course of our journey which lies ahead.

Of course, none of this work would have been possible without the financial support of Lawrence Livermore National Laboratory and our collaboration with Drs. Ted Baumann and Joe Satcher. Ted has been a mentor to me like no other throughout the course of this work. I could not have possibly asked for anyone more expert and more creative in aerogels to work with. His ingenuity, insight, and mastery of chemistry and materials science inspire me, and I hope that one day I will be able to achieve his level of enlightenment in nanoscience.

Beyond the scope of this project, I extend my deepest gratitude to all of the aerogel scientists at Lawrence Livermore for their continued mentorship and correspondence over the past seven years, which has enabled me to contribute to the field of aerogel science starting at a young age. You are superheroes to me. Most of all, I acknowledge Dr. Tom Tillotson, without whom I would have never been able to make aerogels or build a supercritical dryer to begin with. And Tom, I haven't forgotten that I still owe you a cup of coffee (at the very least).

I would also like to thank my co-investigator Aurea Zare for our partnership in researching carbon nanotube growth on gold-rhenium catalysts (and other capers). Her constant encouragement, perseverance, and friendship have benefited me greatly. You are a remarkable and gifted individual, Aurea, and I am confident you will excel greatly in the future.

I would like to thank my UROP (and friend) Rong Hu for her hard work, willingness to learn, jovial spirit, and for bailing me out numerous times when work

loads exceeded processing capacity. I would also like to thank her for showing me another side of life at MIT, and for making me feel at home here. I wish you well, Rong.

I would like to deeply thank Kaveh Milaninia for his tremendous assistance in developing the AMANO system and for his guidance throughout my time here at MIT. His expertise and competence in materials science is unmatched, and I know he will end up making an outstanding, jaded professor some day.

I would like to thank Alfonso Reina Cecco, Hyungbin Son, Ben Wunsch, Eduardo Bàrros, and Hootan Farhat for their assistance in collecting data for this work, for productive and entertaining conversations, and for being outstanding colleagues.

I would like to thank Libby Shaw for her assistance, mentorship, and commitment to excellence in performing the extensive XPS analyses required for this work.

I would like to thank Dr. Scott Speakman for his mentorship in XRD, and for what will undoubtedly be interesting X-ray experiments in the future.

I would like to thank Professor Lorna Gibson for pointing me to Millie's group to begin with and for taking the time to listen to me when I first arrived at MIT.

I would like to acknowledge Aerogel Technologies, LLC for the use of their innovative supercritical dryers, supporting materials, and FLAPL™ process automation software technology throughout the course of this work, with a special thanks to Vice President of Engineering Mark Schneider.

I am also certainly obligated to acknowledge my sensais Mrs. Jeanne Schuett, Mr. Jon Gilmore, Mr. Ron LeMay, Professor Bob West, and Professor Petey Young for showing me what I am capable of, teaching me in the ways of creativity, and for giving me the chance to be what I am (whatever that may be).

Most of all, I would to thank my parents Steve and Lorna, my sister Sam, my grandmother Edith, and my closest friends Tim Cavanaugh and Joey Adashek, for things too great and too numerous to express with human language.

Table of Contents

List of Figures

List of Tables

Chapter 1

Introduction, Overview, Background, and Objectives

1.1 Introduction

The need for high-surface-area electrically conductive materials has steadily increased over the past few years as the demand for advanced energy storage and energy generation technologies has escalated. The performance and energy density of supercapacitors, fuel cells, and long-lived rechargeable batteries has improved tremendously as a result of the development of electrodes based on nanostructured materials [1-4]. It is now more evident than ever that within nanotechnology lies the potential to revolutionize the world's current concept of how energy can be stored and used.

Carbon aerogels and carbon nanotubes are two examples of electrically conductive nanostructured materials with remarkable potential for use in high-surface-area electrodes [5-9]. The fundamentals of aerogel preparation are now well understood, and future research with these materials will primarily take the form of applications development. The fundamental mechanisms of nanotube growth, however, are not yet fully understood, and thus progress in this area will require further fundamental investigations to propel applications development.

At its essence, progress in nanotechnology is made one of two ways. The first way is through identification of a technique (either accidentally or intentionally) that

enables production of nanoscale features and refinement of that technique until a reliable technology is distilled. The second way, and often the more lucrative of the two, is through the development of a new process by exploiting bugs encountered in a different system—as bugs encountered in nanoscale processes are almost always more sophisticated and more fundamental than anything intentionally engendered at the nanoscale. Significant progress in both aerogels and nanotubes has been made both ways over the past 15 years.

Being able to identify value in unexpected results is as beneficial as being able to steer the development of a system to a particular outcome. This thesis relays the story of how unexpected developments encountered in the synthesis and characterization of Fe-doped carbon aerogels led to the discovery of several valuable insights into fundamentals of carbon nanotube growth.

1.2 Overview of This Work

This work begins by describing the synthesis and characterization of Fe-doped carbon aerogels (Chapter 2), the last in the series of metal-doped carbon aerogels planned for study by our group due to waning interest in the research community [8, 10-15]. It was initially expected that graphitic nanoribbons resulting from catalytic solid-state transformation of carbon by metal nanoparticles during pyrolysis of these materials would be observed [11, 13]. However in characterizing this system, no such structures were found. The origins and consequences of this finding led to a novel development which has revealed new potential for these materials—metal-doped carbon aerogels can catalyze the growth of carbon nanotubes by thermal chemical vapor deposition (CVD).

Growth of carbon nanotubes on aerogels was first demonstrated by Hunt et al in 1994 through chemical vapor intrusion of silica aerogel materials [16-18]. Since then, numerous groups have developed metal oxide aerogel-based catalysts for the growth of single-wall and multiwall carbon nanotubes, either employing the incorporation of Group VIIIB or Group VIB salts into alumina, silica, or magnesium oxide-based aerogels [19-35], or by preparing mixed-matrix aerogels of Group VIIIB or Group VIB metal oxides and alumina, silica, or magnesium oxide [36-38]. The

advantages here are production of a bulk quantity of nanoparticles for scalable mass production of nanotubes, a material which is both a textural promoter (which helps prevent agglomeration of catalyst nanoparticles and thus facilitates growth of single-wall carbon nanotubes [39]) and a catalyst, and high growth yields characteristic of supported catalysts. Additionally, nanocomposites of carbon aerogels and activated carbon fibers have been prepared [5]. Neither catalysis of carbon nanotube growth by carbon aerogel-based materials nor growth of carbon nanotubes on a carbon aerogel-based material have been previously demonstrated. Experiments previously performed in our group involving the catalytic decomposition of carbon monoxide over cobalt-infused carbon aerogels resulted in the formation of various graphitic nanostructures including so-called "nanofilaments", but no definitive growth of carbon nanotubes was observed [13].

Following discussion of the synthesis and characterization of Fe-doped carbon aerogels, Chapter 2 continues by detailing the synthesis and characterization of carbon aerogel-carbon nanotube composites derived from Fe-doped carbon aerogels. It is shown that the addition of carbon nanotubes to a carbon aerogel monolith significantly improves monolith's electrical conductivity with only a slight loss of specific surface area (due to obstruction of the aerogel's microporosity).

Chapter 3 then explores the development of various techniques towards controlling nanotube growth in these composites and maximizing the surface area contribution from the added nanotubes, as well as several novel discoveries made in the development of those techniques.

Lessons learned in correlating the compositional profile of nanoparticles in an Fe-doped carbon aerogel sample with the propensity for that sample to catalyze nanotube growth began to suggest that it is primarily metallic nanoparticles which catalyze growth, and that oxidized and carburized species do not actually serve a direct catalytic role. Rather, these species represent precursors to catalytic nanoparticles or poisoned forms of catalyst nanoparticles. In conjunction with results from other work conducted in our group [40] and reports in the literature [41-43], a model of chemical state-sensitive nanotube catalyst activity was developed and is presented at the end of Chapter 3.

Subsequent to the work done on Fe-doped carbon aerogels, it was concluded that characterization of metal-doped carbon aerogels pyrolyzed under different conditions can actually serve as a useful method for evaluating how nanoparticles of a given metal will behave when bombarded with excess amounts of carbon and oxygen at elevated temperatures--a system analogous in many ways to chemical vapor deposition-based growth of carbon nanotubes. Additionally, metal-doped carbon aerogels can then be used to grow nanotubes directly. Thanks to the presence of the bulk quantities of nanoparticles attainable through pyrolysis of a metal-doped carbon aerogel, characterization of nanoparticle phase assignments and surface chemistries can then be performed, enabling direct correlation of a sample's nanoparticle compositional profile with its propensity to catalyze nanotube growth.

Based on this conclusion, metal-doped carbon aerogels systems of six additional metals—Rh, Re, Au, Nb, Ta, and W—were investigated in the context of characterizing the ability of these metals to catalyze nanotube growth. In doing so, it was hoped that it may be possible to ascertain whether or not oxidized or carburized species of elements other than Fe exhibit behavior that suggests oxides are carbides are not directly responsible for catalyzing nanotube growth. The results of this work are presented in Chapter 4, along with predictions of the characteristics of an "ideal" nanotube catalyst for deterministic growth.

Concurrent with the development of the model for catalyst activity presented in Chapter 3 and the predictions of the characteristics of the ideal nanotube catalyst made in Chapter 4, work in developing surface-based nanoparticle catalysts which would be free from hypothesized carbide-poisoning mechanisms was conducted. Two "carbide-proof" elements—Au and Re—were investigated, Au as an example of an element whose oxides are very unstable, and Re as an example of an element which forms a number of stable oxides. Results of this work are presented in Chapter 5.

Lastly, efforts were undertaken to address aspects of nanotube growth by thermal chemical vapor deposition which cannot be addressed at the nanoparticle level but must be addressed at the CVD level. Chapter 6 describes the culmination

of these efforts—the development of a new chemical vapor deposition system concept designed for optimizing growth of carbon nanotubes.

Lessons learned and conclusions from these studies are then presented in Chapter 7.

The remainder of this chapter presents background information about aerogels and carbon nanotubes which may be valuable in understanding the origins and motivations behind the work presented in this thesis.

1.3 Background

1.3.1 Introduction to Aerogel[1]

Overview

Aerogels are a class of nanostructured, mesoporous solids which exhibit an array of extreme materials properties. By definition, an aerogel is a mesoporous solid exhibiting a porosity of no less than 50%. However, in practice most aerogels exhibit porosities ranging from 90 to 99% and possess a significant percentage of microporosity as well. The term aerogel does not refer to a particular substance, but rather to a geometry which a substance can take on. This said, aerogels can be composed of a wide variety of substances, including silica; virtually any transition metal, lanthanide, or actinide oxide; several main group metal oxides; organic and biological polymers; compound semiconductors; metals; and carbon. Composites of aerogels and nanoparticles of various materials are also routinely prepared. In general, the aerogel of a substance takes on most of the materials properties of the bulk form of that substance, with improvements in some materials properties and losses in others due to length-scale effects which arise from the aerogel's nanostructure.

Aerogels boast of a number of impressive materials properties, including the lowest densities of all known materials (ranging from 0.1 to 0.0011 g cm^{-3}), the lowest mean free paths for diffusion of any material[2], and the highest specific

[1] Adapted from "What is Aerogel?", © 2001-2006 Stephen Steiner. Used with permission.

[2] Arguably, microporous materials such as zeolites have an even smaller mean pore diameter than aerogels. The porosity in such materials is so small, however, that most gases are incapable of diffusing through them at all.

surface areas of all monolithic (non-powder) materials (ranging from 250 to 2500 m^2 g^{-1}). Together, these three properties facilitate a number of other extreme materials properties, including the slowest speed of sound through any material and, depending on the composition of the aerogel, thermal conductivities among the lowest of all known materials.

Structure and Preparation

Aerogel is the solid nanostructured framework of a gel isolated from its liquid component, prepared in such a way that the morphology and pore structure of the gel's solid component is preserved. A gel is a colloidal system in which a porous network of interconnected solid particles spans the volume of a liquid medium. This solid particle matrix gives the gel its rigidity, whereas the liquid (being the majority of the gel's volume) determines its density. The pores in a gel typically range anywhere from 5 to 250 nm in diameter in a Guassian-type distribution.

If the liquid in a gel is removed through evaporation, capillary forces exerted by the evaporation liquid cause the pore network of the gel to collapse in on itself, affording a dense, low-porosity material called xerogel (which typically exhibits <10% of the porosity of the original gel). Hydrogen-bonding interactions between struts of the gel's collapsed framework can then result in adhesion, rendering the collapse of the pore network irreversible. Pacifying the surface of the gel with a hydrophobic capping agent prior to evaporative drying can enable partial reversal of this pore collapse to yield a material with ~70% porosity, referred to as ambigel.

Aerogels, on the other hand, are most commonly produced by supercritically extracting the liquid from a gel. Supercritical drying is a process in which the liquid in a gel is slowly heated and pressurized past its critical point thereby transforming the liquid into a supercritical fluid. As a substance approaches its critical point, the surface tension of its liquid phase gradually decreases until reaching zero at the critical point. The supercritical fluid, which exhibits no surface tension, behaves like a gas in that it expands to fill the volume of its container and can thus be removed from the pores of the gel through gentle isothermal depressurization.

So-called subcritical methods for producing aerogels (such as reversal of evaporation-induced pore network collapse) typically result in materials with low mesoporosity and comparatively low overall porosity. As a result, the preferred terms for materials produced through these methods are "ambigel", "aerogel-like", or "porous nanoarchitecture". Similarly, the supercritical drying of gels with low mesoporosity character and are primarily macroporous instead results in materials which are also best differentiated by referring to them as "aerogel-like".

Gel precursors used in the preparation of aerogels are typically produced through a sol-gel polymerization process. A typical sol-gel process entails a solution-phase chemical reaction which results in the formation of nanosized particles comprised of three-dimensional polymer networks (i.e., a sol). Continued polymerization in the solution results in the eventual collision of these nanoparticles into a single, continuous polymer network spanning macroscopic length scales (i.e., a gel). The chemistry employed in the preparation of gels for aerogel production varies greatly (depending on the desired aerogel composition) and is arguably the most challenging aspect of engineering an aerogel. Sol-gel chemistry is notoriously pH-sensitive, in that the success of gelation and the pore morphology which results can vary greatly simply because of the pH of the solution. This frequently means the difference between formation of a mesoporous gel and a macroporous gel.

1.3.2 Carbon Aerogels

In the late 1980's, Rick Pekala at Lawrence Livermore National Laboratory extended the techniques for preparing inorganic aerogels to organic polymers of resorcinol-formaldehyde and melamine-formaldehyde [44, 45]. It was found that by pyrolyzing such aerogels under an inert atmosphere, intrinsically mesoporous aerogels of carbon could be produced [44, 45]. With surface areas upwards of 1000 $m^2\ g^{-1}$ and appreciable electrical conductivity (up to 60 $S\ cm^{-1}$), the potential of these materials for use as high-surface-area electrodes became immediately apparent [46]. The specific capacitance of electrodes made from carbon aerogels has since been demonstrated to be ~86 $F\ g^{-1}$ [6]. As an example of the tremendous potential of these materials, the advent of commercialized carbon aerogel for use in capacitor

electrodes resulted in an increase in a maximum capacitance of ~1 F available for component capacitors in the early 1990s to greater than 65 F by the end of the decade.

Unfortunately, carbon aerogels exhibit a fundamental trade-off pertaining to specific surface area (proportional to bulk density) and electrical conductivity [7, 46]. Increasing the surface area of an aerogel typically requires decreasing the material's bulk density. However, doing so decreases the electrical conductivity of the material by an even great amount (as σ for carbon aerogels scales as $\rho^{1.5}$ to $\rho^{2.4}$). As a result, the maximum specific surface area of carbon aerogels practical for use in electrodes was greatly limited and thus the utility of carbon aerogels for such applications was also.

1.3.3 Metal-Doped Carbon Aerogels

In response to this problem, Livermore developed a technique for improving the electrical conductivity of carbon aerogels by introducing metals into the polymer backbone (referred to as "doping") [10]. In this technique, the aerogel precursor is a phenolic resin-based gel prepared by polymerizing the potassium salt of 2,4-dihydroxybenzoic acid (instead of 1,3-dihydroxybenzene) with formaldehyde. This results in a gel with carboxylate groups attached to every monomer unit of its polymeric backbone, each with a potassium ion ionically bound. These potassium carboxylate groups can then serve as ion exchange sites for binding metal ions to the gel's backbone. Doping is accomplished simply by soaking the gel in a solution containing ions of the desired metal dopant and allowing for the ions to diffuse into the gel.

Pyrolysis of the metal-doped phenolic aerogels derived from such gels affords mesoporous carbon aerogels laden with metal nanoparticles [10, 11, 13-15]. The size and compositional profiles of these nanoparticles were found to be a function of the temperature and duration of the pyrolytic process used to prepared the carbon aerogel, in accordance with the thermodynamic and kinetic relations which govern the coarsening of such particles.

Carbon aerogels doped with copper, nickel, and cobalt have been thoroughly characterized by our group over the past several years [8, 10-15]. Synthesis of aerogel-like macroporous carbons doped with iron, cobalt, nickel, chromium, molybdenum, and tungsten has also been reported and characterized [47].

Pyrolysis of Co- and Ni-doped carbon aerogels at elevated temperatures was found to result in the formation of graphitic nanoribbons in the vicinity of the metal-containing nanoparticles in the aerogel [11]. This pyrolysis-induced catalysis of the surrounding nanocrystalline carbon framework into graphitic ribbons was thus expected to similarly occur for Fe-doped carbon aerogels as well. However, upon characterization of these materials, no such graphitization was observed. The details of this are discussed in Chapter 2.

1.3.4 Growth of Carbon Nanotubes on Aerogel Monoliths

The absence of graphitic shells or nanoribbons coating over the iron nanoparticles in the carbon aerogel enabled thorough characterization of the nanoparticle surface chemistries of Fe-doped carbon aerogels by X-ray photoelectron spectroscopy (XPS). Given the apparent large population of surface-accessible iron nanoparticles in these materials, it was hypothesized that it may be possible to use a chemical vapor deposition technique to induce growth of carbon nanotubes these nanoparticles. Indeed, CVD on Fe-doped carbon aerogels was found to catalyze growth of carbon nanotubes, resulting in growth of nanotubes directly on the aerogel monolith. Such carbon aerogel-carbon nanotube composites are the first of their kind reported. Successful nanotube growth was limited to a "sweet spot' of processing conditions, however. The origin of this was later attributed to the presence of nanoparticles in the aerogel of a specific compositional profile which was found to be a function of pyrolysis time and temperature. The synthesis and characterization of these composites is also described in Chapter 2.

As mentioned earlier, growth of carbon nanotubes on inorganic carbon aerogels has been reported by a number of groups. Also as mentioned, growth of various carbon nanostructures over metal-doped carbon aerogels has been demonstrated

previously as well. Growth of carbon nanotubes on carbon aerogels, however, is new to this work.

1.3.5 Introduction to Carbon Nanotubes

Carbon nanotubes are an allotrope of carbon comprised of cylindrical rolls of graphite with diameters ranging from 0.4 nm to ~50 nm in diameter [48-51]. Carbon nanotubes composed of several concentric cylinders are referred to as "multiwall", whereas nanotubes consisting of only one cylinder are referred to as "single-wall". Needless to say, carbon nanotubes are currently the focus of a great deal of attention in the research community because of their remarkable mechanical and electronic properties.

Carbon nanotubes can be synthesized through a number of techniques, including electric arc discharge between two graphite electrodes, spray pyrolysis of a metal-containing compound in a hydrocarbon atmosphere, laser ablation of a material into nanoparticles in the presence of carbon-containing gases, and chemical vapor deposition (CVD) of carbon-containing gases over metal-containing nanoparticles. Of these three methods, CVD is by far the most versatile in terms of ability to control nanotube diameter, length, and doping. Plasmas and electric fields can also be implemented in CVD for improving certain aspects of the process [52]. CVD growth of multiwall carbon nanotubes was first demonstrated in the 1970's [51] and the techniques for CVD growth of multiwall and single-wall carbon nanotubes have been refined by numerous groups over the past decade [36, 52-65],. In practice, however, the reproducibility CVD growth of carbon nanotubes is often somewhat tenuous. This work focuses exclusively on the synthesis of carbon nanotubes by thermal CVD (as opposed to plasma- or electric field-assisted growth)[3].

In a typical CVD process, metal-containing nanoparticles are deposited on a surface (such as a silicon wafer). The wafer is then placed under a flow of carbon-containing feedstock gas(es) (such as methane, ethylene, acetylene, methanol, and/or ethanol), hydrogen, and (optionally) an inert diluting gas (such as Ar) at

[3] It should be noted here that the mechanisms of nanotube synthesis arc discharge and laser ablation are fundamentally different from those of heterogeneous catalysis-based nanotube growth by thermal CVD and therefore are difficult to compare.

elevated temperatures (600-1000°C). During this process, the feedstock gases are decomposed ("cracked") into carbon, in part by thermolysis and in part through catalytic dehydrogenation by the nanoparticles. What happens next has yet to be fully understood, but the following is a reasonable approximation based on available data. Carbon then diffuses into a nanoparticle until a certain concentration of carbon in the nanoparticle is reached. Additional diffusion of carbon into the nanoparticle causes carbon to precipitate out of the nanoparticle in a crystalline form. Carbon's preferred crystalline form under standard conditions is graphite—planes of hexagonally arranged sp^2-hybridized carbon atoms, but due to dimensional restraints imposed by the nanoparticle, the precipitating carbon defaults into a cylindrical shape. Provided additional diffusion of carbon into the nanoparticle, additional carbon can be added on to this cylindrical structure and cause the structure to extrude out from the nanoparticle, resulting in a carbon nanotube. Chemical vapor deposition can also be conducted using a "floating precursor', in which catalyst nanoparticles are formed in the vapor stream during CVD by thermolytic decomposition of an organometallic compound [66, 67]. The length of nanotubes produced through this type of process, however, is limited by the length of the CVD furnace's hot zone.

In general, the diameter of a nanotube correlates with the diameter of the nanoparticle from which it grew [56, 68]. With larger diameter nanoparticles (>1.8 nm), concentric nanotubes can grow from a single nanoparticle, resulting in a multiwall carbon nanotube. With very large particles (>100 nm in diameter), the dimensional restrains inherent to nanosized particles begin to alleviate and rolled-up, spiraling sheets of graphite can form. These types of structures are called carbon fibers. It has been proposed that growth of nanotubes over small diameter nanoparticles (1-5 nm) is primarily attributable to a mechanism involving diffusion of carbon over the nanoparticle surface, with diffusion of carbon into the bulk of the nanoparticle becoming increasingly prevalent with increasing nanoparticle diameter [68]. Single-wall and double-wall carbon nanotubes are thus believed to grow primarily through a surface-diffusion mechanism, multi-wall nanotubes through a

combination of surface- and bulk-diffusion mechanisms, and carbon fibers primarily through a bulk-diffusion mechanism.

Growth of long nanotubes is of great interest for applications such as electrical interconnects for integrated circuits and the development of fibers for high strength-to-weight ratio composites [43, 69]. Although production of long (multi-centimeter) nanotubes has been reported [60, 64, 65, 70], in practice it is difficult to achieve such results.

1.3.6 Termination Mechanisms in Nanotube Growth

Five basic termination mechanisms for nanotube growth are proposed based on reports from the literature and empirical observations.

- *Feedstock exhaustion* [71, 72], in which the rate at which carbon going into the nanoparticle falls below a critical value and further precipitation of crystalline carbon cannot continue. This can be caused from a lack of cracked feedstock gas or simply from a lack of feedstock gas. If the rate of feedstock replenishment is just below the rate required for continuous extrusion of a nanotube, a "start-stop" mechanism may occur resulting in "bamboo-like" internal structuring of the nanotube [72]. Feedstock exhaustion is the mechanism which terminates an otherwise active nanotube growth when CVD feedstock gas flow is turned off.
- *Surface build-up* [60, 73, 74], in which a build-up of amorphous carbon, graphitic layers, or other material forms on the surface of a nanoparticle, obscuring the catalyst surface. This results in both impeding further diffusion of carbon into the nanoparticle and disabling catalytic cracking of feedstock gas. Surface build-up can also occur if carbon precipitated from the nanoparticle encapsulates the nanoparticle with a fullerenic shell.
- *Mechanical jamming*, in which a nanotube is physically impinged and arresting further extrusion of the nanotube and possibly resulting in the precipitation of carbon over the rest of the nanoparticle. This can in turn result in surface build-up on the nanoparticle, thereby preventing growth from being reinitiated even if the jam is alleviated. Mechanical jamming can occur from

entanglement with other nanotubes, van der Waals attraction between the nanotube and a surface [70], or from restricted growth space.

- *Kinetic particle coarsening* [27, 33, 39, 56, 57, 68, 75], in which catalyst nanoparticles agglomerate into particles too large to facilitate nanotube growth.
- *Catalyst poisoning* [41, 42, 60, 65], in which a chemical change occurs in the nanoparticle disabling the nanoparticle's ability to catalyze nanotube growth and/or to crack feedstock gas. Of the five termination mechanisms proposed here, catalyst poisoning is the least understood and the least well characterized.

1.3.7 Preventing Termination of Nanotube Growth

The following is a discussion of how each termination mechanism can be averted.

1.3.7.1 Feedstock Exhaustion

Unexpected feedstock exhaustion can be averted simply by ensuring an adequate supply of feedstock gas for as long as growth is desired and by ensuring the process is carried out at a temperature high enough for adequate thermolytic and catalytic cracking of the feedstock gas to occur. This is primarily a CVD-affiliated termination mechanism.

1.3.7.2 Surface Build-Up

Surface build-up is avoidable by careful engineering of a CVD process. In practice, however, this can be somewhat tricky to mitigate. The most common cause of surface build-up is due to excessive feedstock cracking. This can certainly occur if the process is run too hot or if a high flow rate of an easily cracked gas (such as acetylene) is used. In addition to temperature adjustment, excessive feedstock cracking can be controlled by adjusting the amount of hydrogen present in the stream [60, 73]. Modeling feedstock gas cracking with the equation,

$$C_xH_y \rightarrow xC + \frac{y}{2}H_2 \qquad (1\text{-}1)$$

by the law of mass action, the expression for the concentrations of each species at equilibrium is given by,

$$\frac{[C]^x[H_2]^{y/2}}{[C_xH_y]} = k_{eq} \qquad (1\text{-}2)$$

where k_{eq} is the equilibrium rate constant. Le Châtlier's principle states that if the concentration of hydrogen is increased, the equilibrium will shift to the left in favor of the feedstock gas, thereby reducing the amount of carbon present as well. A carefully equilibrated CVD process can still lead to surface build-up, in which case trace amounts of an "etching agent" such as oxygen, water vapor, or ammonia can be employed to combat deposition of excess carbon [40, 43, 60, 64, 65, 70, 75] . Of course, present in too high a concentration, these agents will result in etching of nanotubes as well. As a result, effective implementation of etching agents can be tricky. In general, surface build-up is a CVD-addressable issue.

1.3.7.3 Mechanical Jamming

Mechanical jamming can be avoided through a number of techniques. Adequate spacing of catalyst nanoparticles can help prevent entangling of extruding nanotubes. Entangling generally only occurs for systems which exhibit a base-growth mechanism. For complex substrate topographies, further consideration must be made in placing the nanoparticles at locations such that extruding nanotubes do not encounter any obstacles before reaching their desired length. Contact of a nanotube with the substrate surface is a more ubiquitous problem. The summation of Van der Waals forces exerted by the surface along the length of a nanotube can easily overwhelm the extrusion power of a nanoparticle and cause a jam. One method which can be employed to avoid this is the use of a high total

CVD flow rate to cause the nanotubes to "float" in the vapor stream (like kite string held in the wind) as they grow [70]. Overall, mechanical jamming is a topographical problem, however can be addressed through adjustment of CVD process parameters to a certain degree.

1.3.7.4 Particle Coarsening

Use of a textural support such as aerogels or zeolites [27, 33, 75] can prevent particle coarsening by impeding surface-based diffusion. Particle coarsening can also be prevented by simply spacing nanoparticles sufficiently far apart.

1.3.7.5 Catalyst Poisoning

Of the four termination mechanisms proposed here, chemical poisoning is the least understood and the least well characterized. It is the belief of the author that so-called "sweet spots" frequently encountered by researchers in the preparation of nanotube catalysts arise from process-induced variations in the chemical composition of catalyst nanoparticles. Some such variations, in turn, result in poisoned (catalytically inactive) species. For example, it has been observed that variations in oxidative and reductive pretreatments used to prepare nanoparticle catalysts have a significant effect on the length and quality of nanotubes which result from use of that catalyst in thermal CVD [8, 10-15, 47]. It is also known that CVD can induce chemical changes in catalyst nanoparticles. It is believed that in many nanotube catalyst preparation techniques, the resulting nanoparticle chemical compositions peculiar to that technique may only result in nanotube growth when a certain set of CVD conditions is also implemented, i.e., a chemical change induced by the CVD process is required to render the nanoparticles into a catalytic state (hence a "sweet spot" in processing conditions). In short, there is a need for identifying the properties characteristic of effective nanotube catalysts (such as oxidation states, ability to catalyze dehydrogenation reactions, reactivity with carbon, etc.) and characterizing the chemical poisoning mechanisms which such catalysts are susceptible to. These needs must be met in order to develop robust, reproducible, controllable nanotube growth techniques for transition to industry.

1.4 Objectives

The objectives of this work are twofold. The first objective of this work focuses on the development of new carbon aerogel-based materials with potential for use in applications such as high-surface-area electrodes, physisorption storage of hydrogen, and heterogeneous catalysis. The second objective of this work focuses on understanding the nature of catalyst poisoning in heterogeneous catalysis-based growth of carbon nanotubes by thermal chemical vapor deposition. This is done by demonstrating growth of carbon nanotubes on transition metals with significantly different phase diagrams with carbon and oxygen (the two most ubiquitous elements during CVD which are likely to cause catalyst poisoning). By identifying the characteristics required for a nanoparticle to be catalytic towards nanotube growth, more robust nanotube growth techniques can potentially be developed. Elucidation of nanoparticle catalyst poisoning mechanisms will also aid in the discovery of techniques for the producing indefinitely long carbon nanotubes which could be used in the production of advanced composite materials for applications such as the space elevator.

Chapter 2

Synthesis and Characterization of Iron-Doped Carbon Aerogels: Novel Catalysts for Direct Growth of Carbon Nanotubes on Carbon Aerogel

2.1 Introduction

The synthesis and characterization of carbon aerogels doped with various transition metals (such as copper, nickel, and cobalt) has been previously reported by our group and others [11, 47]. In these systems, pyrolysis of the metal-doped polymeric precursor invokes the dopant metal to undergo particle coarsening, resulting in the formation of metallic nanoparticles dispersed throughout the aerogel. Provided thermal activation, these nanoparticles have been found to be able to in turn induce a restructuring of the surrounding nanocrystalline carbon framework into graphitic nanoribbons and other graphitic nanostructures. With sufficient temperature and time, significant graphitization of the aerogel can occur [18, 49, 53]. The doping of carbon aerogels with metal also enhances the electrical conductivity of the material, desirable for high-surface-area electrode applications.

The effects nickel and cobalt are known to have on the carbon structure of an aerogel during pyrolysis raised the question of how iron would behave in this environment. Iron-based catalysts are known to catalyze growth of graphitic nanostructures (such as carbon nanotubes) [76], however at the same time, iron-carbon systems are also unusually rich in phases—more so than cobalt or nickel [13]. This suggested iron-doped carbon aerogels may have an added complexity over cobalt or nickel.

Interestingly, initial characterizations of iron-doped carbon aerogels revealed that the expected pyrolysis-induced graphitization of the aerogel's carbon structure did not seem to occur for pyrolysis temperatures up to 1050°C and pyrolysis times up to 12 h. Rather, it appeared that many of the iron-containing nanoparticles in the aerogel had reacted with the surrounding carbon framework to form iron carbide nanoparticles instead of catalytically restructuring the surrounding nanocrystalline and amorphous carbon into graphitic nanostructures. Surprisingly, it was then discovered that where this system failed to produce graphitic structures during pyrolysis, it proved to be capable of catalyzing growth of carbon nanotubes by thermal chemical vapor deposition. The graphitic nanoribbons and nanoshells characteristic of Co- and Ni-doped carbon aerogels could also be invoked by chemical vapor deposition. Previous attempts at "solid-state" transformation of carbon in Co-infused carbon aerogels into carbon nanotubes and growth of carbon nanotubes by decomposition of carbon monoxide over Co-infused carbon aerogels have been made, resulting in the formation of carbon thin films, nanofilaments, and nanoshells, but apparently not carbon nanotubes [77, 78].

In this section, the synthesis and characterization of iron-doped carbon aerogels is presented along with a technique for preparing novel monolithic carbon aerogel-carbon nanotube composites, enabled by the unique chemistry of the Fe-doped carbon aerogel system.

2.2 Experimental

2.2.1 Materials and Methods

Preparation of Precursor Gel

A solution of potassium 2,4-dihydroxybenzoate was prepared by adding K_2CO_3 (1.29 g, 9.4 mmol) to a solution of 2,4-dihydroxybenzoic acid (2.9 g, 18.8 mmol) in deionized water (100 mL). Formaldehyde (2.98 g 37% w/v in water, 37 mmol) was then added along with an additional amount of K_2CO_3 (26 mg, 0.188 mmol) to serve as a polymerization catalyst. The solution was then stirred for 24 h, after which the solution was transferred into plastic or glass vials, sealed, and thermoset in an oven at 80°C for 72 h. The resulting K^+-loaded gels were obtained as dark red, transparent monoliths. The gels were then removed from their plastic vials, optionally sliced into discs with a razor blade, and soaked in a solution of 0.1 M aqueous $Fe(NO_3)_3$, $FeCl_3$, $FeSO_4$, or $(NH_4)_2Fe(SO_4)_2$ for 3 d, with fresh solution exchanged in every 24 h. Unless otherwise noted, all samples referred to heretofore were prepared with $Fe(NO_3)_3$. A set of acid-neutralized gels prepared by ion exchange with 0.1 M HCl instead of iron salt were also prepared to serve as controls. Ion-exchanged gels were then soaked in deionized water for 3 d with fresh water exchanged in every 24 h to remove excess unbound ions from the pores of the gels. A third solvent exchange into acetone was then performed in a similar manner over the course of 3 d to make the gel liquor compatible for exchange and subsequent supercritical extraction with carbon dioxide.

Supercritical Drying

Gels were placed in a supercritical extractor and soaked under liquid carbon dioxide (5.2 MPa and 15°C) for 2 d, flushing the extractor with fresh liquid carbon dioxide every 6 h. Once the gels were sufficiently diffused through with liquid carbon dioxide, the vessel was heated past the critical point of carbon dioxide (31.1°C and 7.38 MPa) at a rate of 1°C to a temperature of 50°C and pressure of 9.65 MPa. The vessel was allowed to remain at these conditions for 1-2 h followed by isothermal depressurization below the critical point of carbon dioxide over the course of ~1 h. At this point the vessel was allowed to cool and depressurize to

ambient conditions over the course of about 1 h. The newly formed Fe-doped phenolic aerogels were then removed from the vessel.

Pyrolysis

Fe-doped phenolic aerogels were carbonized by pyrolyzing at 600°C, 800°C, and 1050°C under an N_2 or Ar atmosphere for 1-10.5 hrs. Pyrolyzed samples are denoted by a part number with the format "Dxxxx", where "D" is the dopant (Fe for Fe-doped and H for the acid-neutralized controls) and "xxxx" is the pyrolysis temperature in degrees Celsius.

Chemical Vapor Deposition

Fe-doped carbon aerogels pyrolyzed at temperatures ranging from 600°C to 1050°C were processed by chemical vapor deposition (CVD) to synthesize carbon nanotubes on the aerogel monoliths. In a typical process, an aerogel was placed in a small ceramic crucible or segment of quartz tubing and inserted into the middle of a 2.5-cm diameter quartz process tube. Ar was then flowed through the tube at a rate of 200 sccm for 20-40 minutes to remove as much air from the mesoporosity of the aerogel as possible. The tube was then placed into a clamshell furnace preheated to a temperature ranging from 800-950°C. Upon opening, the furnace temperature would drop 50-100°C. A target temperature of 600°C, 700°C, or 800°C was then set on the furnace temperature controller and attained within 2-3 m. H_2, CH_4 and/or C_2H_4 were flowed over the aerogel for 10-20 minutes at this temperature. The tube was then taken out of the furnace and placed under a flow of 500 sccm Ar until the tube cooled to ambient temperature. Samples having undergone CVD are denoted with a part number with the format "Fexxxx-yyyy", where "xxxx" is the temperature at which the aerogel was pyrolyzed and "yyyy" is the temperature at which CVD was performed.

2.2.2 Characterization

Surface area determination and analysis of pore statistics were performed by Brunauer-Emmett-Teller (BET) and Barrett-Joyner-Halenda (BJH) methods using an

ASAP 2020 Surface Area Analyzer (Micromeritics Instrument Corporation). Samples of approximately 100 mg were heated to 150°C under vacuum (10^{-5} torr) for 15 h to remove adsorbed species. Nitrogen adsorption data for surface area determination were then taken at six relative pressures between 0.05 and 0.30 at 77 K, with the entire isotherm comprised of fifty-four points. Bulk densities of the aerogels were determined through dimensional analysis and weighing of monolithic samples. High-resolution transmission electron microscopy (HRTEM) of Fe-doped carbon aerogels and derived nanotube composites was performed on a JEOL JEM-200CX operating at 200 keV. X-ray diffraction (XRD) spectra were obtained using a Rigaku 300 X-ray diffractometer operating with the following measurement parameters: high voltage = 60 kV; current = 300 mA; divergence slit = 1°; scatter slit = 1°; receiving slit = 0.3°; scan mode = continuous; scan type = standard; axis = $2\theta/\theta$; scan = 5° to 85°C; scan speed = 10° min^{-1}; sampling interval = 0.05°. X-ray photoelectron spectroscopy (XPS) spectra were obtained on an AXIS HIS 165 and ULTRA Spectrometer (Kratos Analytical Limited, England) using Al K radiation (energy = 1486.6 eV) in a vacuum of 5×10^{-9} torr. Samples were prepared by grinding into a fine powder, adhering to adhesive copper tape, and mounting the copper tape on a sample holder using double-sided adhesive tape. X-ray slots of 750 by 350 μm, an X-ray power of 150 W (15 kV and 10 mA), and a pass energy of 80 eV were used for all measurements. High-resolution scanning electron microscopy (HRSEM) was performed with a JEOL 6320 microscope operating at 5 kV. Raman spectra were obtained using a custom-built micro-Raman spectrometer at excitation wavelengths of 785 nm, 676 nm, 752 nm, and 514 nm. Electrical conductivity of monoliths was determined at 22°C by placing two flat, gold-plated probes (each with a contact area of 1.03×10^{-2} cm^2) on opposite sides of a monolithic aerogel disc of known thickness, pushing the probes into the disc, and measuring the electrical resistance between them with a multimeter. As the effective contact area between the aerogel and probes was found to be a function of the pressure exerted on the probes, the value measured just before fracture of the monolith was used to calculate the conductivity.

2.3 Results and Discussion

2.3.1 X-Ray Diffraction (XRD)

Figure 2-1 shows the XRD spectra for undoped (acid-neutralized) and Fe-doped carbon aerogels prepared with $Fe(NO_3)_3$ and pyrolyzed at temperatures ranging from 600-1050°C for 10.5 h. The spectrum for Fe-doped samples pyrolyzed at 600°C is very similar to the spectrum for undoped samples, with only minor peaks attributable to Fe(110) and Fe(200) at 44.5 and 65.0 two-theta, respectively. These two peaks become much more pronounced with increasing pyrolysis temperature, implying that the mean Fe crystallite diameter increases with increasing pyrolysis temperature (consistent with a particle coarsening mechanism). At pyrolysis temperatures above 600°C, an array of additional peaks emerges from the baseline as well, attributable to Fe_3C (cohenite- or cementite-phase iron carbide). Figure 2-2 shows peak-fitting for cohenite in these samples. With this association in mind, the small peak at ~38° two-theta in the spectrum for the sample pyrolyzed at 600°C spectrum (Figure 2-1) is likely attributable to Fe_3C as well, indicating that this species begins to form at low temperatures. A broad peak centered at ~21° two-theta is also present in each spectrum, corresponding to the presence of carbon crystallites. Table 2-1 lists crystallite sizes for carbon as a function of pyrolysis temperature, derived using the Scherrer equation,

$$d = \frac{0.89\lambda}{\beta \cos(\theta)} \tag{2-1}$$

where λ is the X-ray wavelength used ($\lambda_{Cu}(K_\alpha)$ = 0.15418 nm), β is the full-width-at-half-maximum (FWHM) of the diffraction peak, and 2θ is the diffraction angle of the peak. The large FWHM value for the carbon band located at ~21° two-theta of each sample suggests the aerogel's carbon framework possesses low crystallinity. The calculated mean carbon crystallite size was found to be between 0.9-1.0 nm regardless of pyrolysis temperature or iron salt used. Thus, it appears that the aerogel's carbon framework does not graphitize appreciably over the range of

pyrolysis temperatures investigated, with or without the presence of iron, however is still nanocrystalline in structure. Raman spectroscopy further substantiates this claim in that the D-band to G-band ratio, a general measure of the ratio of defective carbon structures to ordered carbon structures, does not change meaningfully with pyrolysis temperature (see Section 2.4). Using a value of 0.142 nm for the lattice parameter of graphite, it is estimated that an average carbon crystallite in these materials contains approximately 40-50 carbon atoms.

Using the Scherrer equation (2-1), the average crystallite size for iron and iron carbide nanoparticles in Fe-doped carbon aerogels was also calculated (Table 2-1).

	Mean Carbon Crystallite Size (nm)	Mean Iron Crystallite Size (nm)*	Mean Iron Carbide Crystallite Size (nm)**
$Fe(NO_3)_3$, 600°C	0.9 (0.1)	60.8 (7.5)	ND
$Fe(NO_3)_3$, 800°C	1.0 (0.1)	30.7 (18.4)	35.1 (4.5)
$Fe(NO_3)_3$, 1050°C	0.9 (0.1)	25.8 (17.6)	21.1 (1.7)
$(NH_4)_2Fe(SO_4)_2$, 1050°C	1.0 (0.1)	10.7 (1.8)	15.0 (0.5)
$FeSO_4$, 1050°C	1.0 (0.1)	20.9 (2.0)	16.9 (0.5)
$FeCl_3$, 1050°C	1.0 (0.1)	49.4 (14.1)	58.9 (2.3)
Undoped, 1050°C	1.0 (0.1)	ND	ND

ND=Not Detected

* Mean iron crystallite size as determined from the integrated area of the Fe(110) peak

** Mean iron carbide crystallite size as determined from the integrated area of the Fe_3C(211) peak for cohenite-containing sample and from the integrated area of the $Fe_{15.1}C$(200) peak for austentite-containing samples

Table 2-1 Average crystallite sizes of carbon, iron, and iron carbide nanoparticles as determined by XRD for Fe-doped carbon aerogels and acid-neutralized control.

Figure 2-3 shows the XRD spectra for Fe-doped carbon aerogels prepared with $Fe(NO_3)_3$, $(NH_4)_2Fe(SO_4)_2$, $FeSO_4$, and $FeCl_3$, all pyrolyzed at 1050°C for 10.5 h. Surprisingly, the spectra for these materials turn out to be markedly different. The array of peaks attributable to cohenite-phase iron carbide seems to only be present in samples prepared with $Fe(NO_3)_3$. Peak-fitting of samples prepared with other iron salts (Figure 2-4) suggests the presence of an iron carbide with the stoichiometry $Fe_{15.1}C$ (austenite-phase). Presumably, this "salt effect" arises from

one of the two following scenarios. One possibility is that different counteranions affect the efficacy of the ion-exchange process, meaning different iron salts to incorporate into the gel skeleton with varying degrees of effectiveness. This would result in salt-dependent iron loading variations which would, in turn, influence the stoichiometry of iron carbide which would be formed during pyrolysis. This is substantiated by the observation that the mean crystallite size for iron is different for different loading salts (Table 2-1).

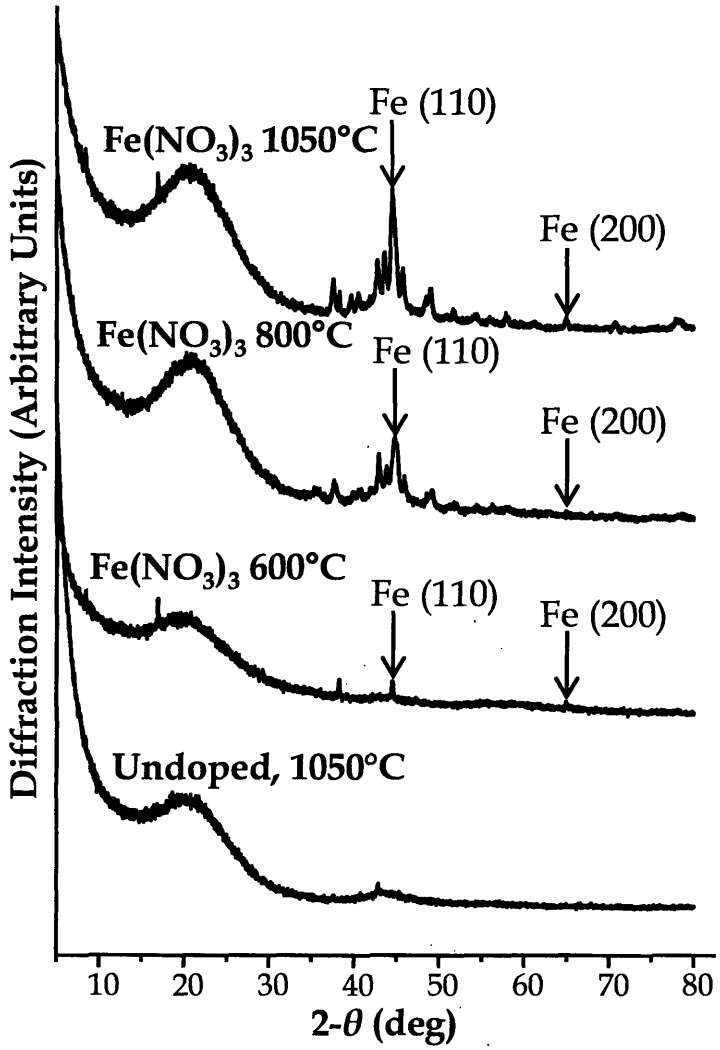

Figure 2-1 XRD spectra for undoped and Fe-doped carbon aerogel samples doped with iron(III) nitrate as a function of pyrolysis temperature. Crystallites of carbon *(broad peak centered at ~21°)*, iron *(labeled peaks)*, and iron carbide *(remaining unlabelled peaks)* are observed. The increase in peak intensity with increasing pyrolysis temperature for iron and iron carbide is a result of increased particle coarsening.

A second possibility is that counteranions that were assumed to be washed away over the course of multiple solvent exchanges and supercritical extraction somehow persist into pyrolysis, where they influence the thermodynamic landscape of particle coarsening in the aerogel before being ultimately volatilized. XPS experiments did not detect any increased concentration of sulfur, nitrogen, or chlorine in pyrolyzed Fe-doped samples over undoped samples that would be indicative of such leftover counteranions, however.

In addition to apparent compositional differences, the relative ratio of iron to iron carbide and the mean diameter of metal-containing nanoparticles also vary with the loading salt used to dope the aerogel. Table 2-2 lists the ratio of the integrated area under the Fe(110) peak to the $Fe_{15.1}C(200)$ peak for austenite-phase-containing materials and compared to the $Fe_3C(211)$ peak for cohenite-phase-containing materials. It is believed that maximizing metallic iron content is desirable for nanotube growth.

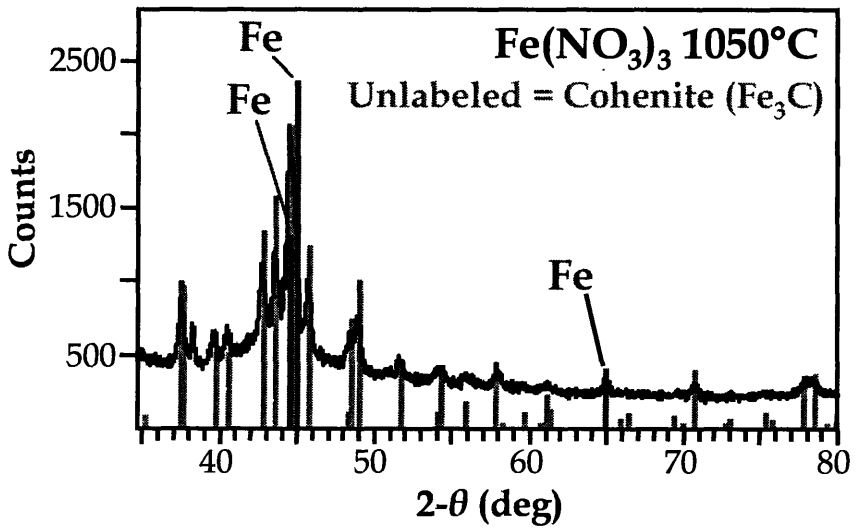

Figure 2-2 Peak fitting of iron *(labeled Fe)* and iron carbide *(unlabelled for clarity)* for Fe-doped carbon aerogels prepared with iron nitrate. The phase of iron carbide which results after pyrolysis, in this case Fe_3C, appears to be dependent on loading salt used to dope the aerogel.

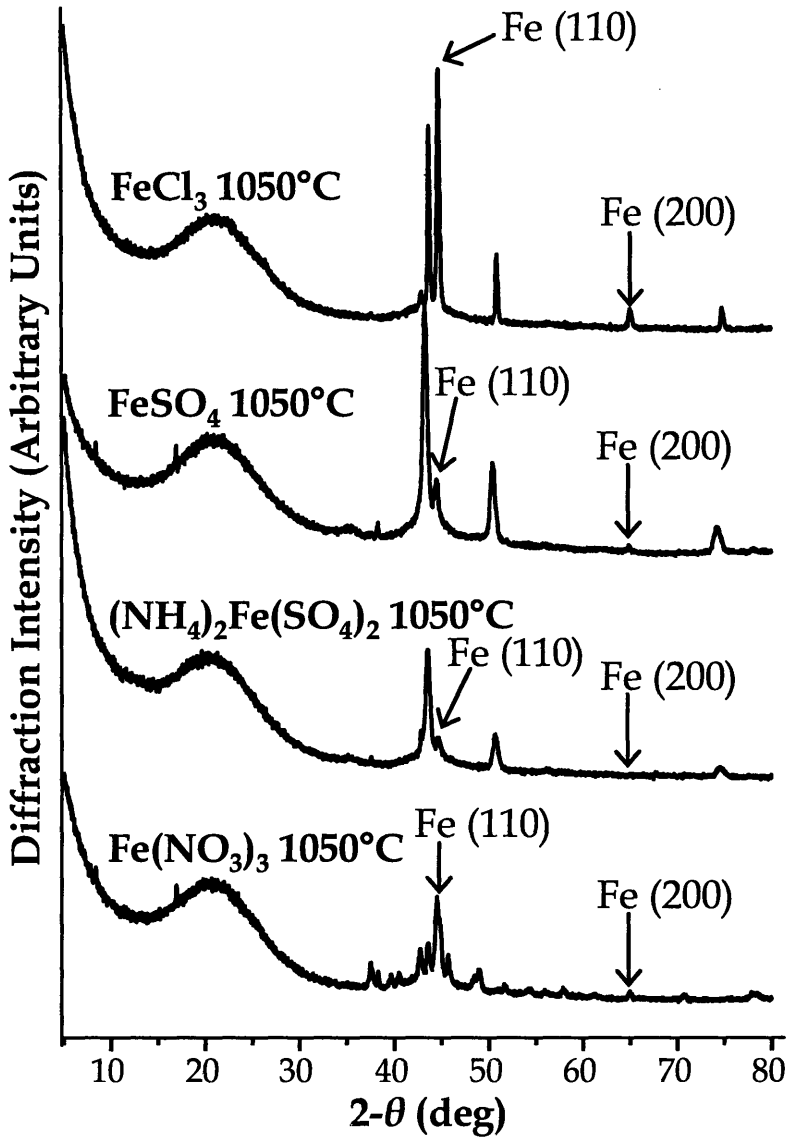

Figure 2-3 XRD spectra for Fe-doped carbon aerogels prepared with different iron salts. Crystallites of carbon *(broad peak centered at ~21°)*, iron *(labeled)*, and iron carbide *(remaining unlabelled peaks)* are observed in each sample, however the phase of iron carbide present is apparently dependent on the loading salt used to dope the gel. Iron(III) nitrate results in iron carbide with a stoichiometry of Fe_3C *(cohenite or cementite)* whereas other salts result in the formation of $Fe_{15.1}C$ *(austenite)*. The ratio of iron and iron carbide signal intensity is also dependent on the loading salt used.

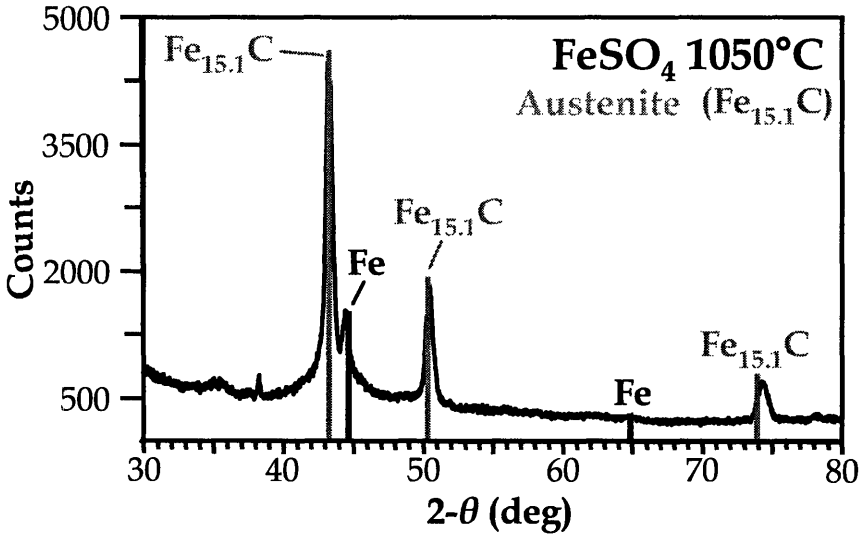

Figure 2-4 Peak fitting of iron carbide peaks for Fe-doped carbon aerogels prepared with iron(II) sulfate, showing the presence of iron carbide in the austenite phase instead of cohenite. Iron(II) ammonium sulfate and iron(III) chloride produce similar spectra.

Sample	Ratio of Fe:Fe_xC Signals*
$Fe(NO_3)_3$, 1050°C	1.26
$(NH_4)_2Fe(SO_4)_2$, 1050°C	0.62
$FeSO_4$, 1050°C	0.85
$FeCl_3$, 1050°C	0.42

* Based on ratio of Fe(110) to Fe_3C(211) integrated peak areas for cohenite-containing sample and Fe(110) to $Fe_{15.1}C$(200) for austenite-containing samples.

Table 2-2 Ratio of integrated areas for iron and iron carbide signals for various loading salts. Iron(III) nitrate appears to be preferable for favoring a higher metallic iron content.

2.3.2 X-Ray Photoelectron Spectroscopy (XPS)

Figure 2-5 shows the Fe 2p region of XPS spectra for Fe-doped carbon aerogels prepared with iron(III) nitrate as a function of pyrolysis temperature. As XPS is only sensitive to the first few atomic layers of a sample, these signals provide compositional information about the surface of nanoparticles distributed throughout the aerogel. No signals corresponding to Fe are observed in undoped carbon aerogels. Unpyrolyzed Fe-doped polymer aerogels exhibit signals

attributable to FeOOH and Fe^{2+} (presumably iron bound to carboxylate or phenol moieties in the aerogel) [77, 78]. Both signals are observed for samples pyrolyzed at 600°C for 10.5 h as well, however with a relatively significant reduction in the FeOOH signal intensity. Correlating this diagnosis with the XRD spectrum of these samples, it appears that the iron is still primarily atomically dispersed throughout the partially-carbonized backbone of the aerogel. At a pyrolysis temperature of 800°C, signals attributable to Fe_2O_3 and Fe_3C emerge [41, 77]. As described, these samples exhibit the presence of Fe and Fe_3C crystallites in their XRD spectrum implying the presence of Fe crystallites with oxidized and/or carburized surfaces as well as Fe_3C crystallites with carburized surfaces. At a pyrolysis temperature of 1050°C, the signal corresponding to Fe_2O_3 shifts to a lower binding energy accompanied by a reduction in signal intensity, implying carbothermic reduction to of Fe_2O_3 to FeO [77, 79]. Signals attributable to Fe_3C predominate, implying the majority of iron-containing nanoparticle surfaces are carburized in these samples. Table 2-3 lists the calculated percentages of C and Fe in various Fe-doped carbon aerogels as determined by peak-fitting of XPS spectra. Assuming the surface composition of carbon and iron-containing nanoparticles in the aerogel is representative of the bulk composition of the aerogel, the ion-exchange technique appears to result in Fe-loading of 0.2-2% depending on the loading salt used to dope the aerogel. The apparent level of doping diminishes with increasing pyrolysis temperature. This is likely due to a reduction in the surface-to-volume ratio for iron nanoparticles in the aerogel from particle coarsening.

XPS spectra for samples pyrolyzed at 800°C for times ranging from 1-10.5 h were acquired to watch the evolution of surface-accessible iron particles with time (Figure 2-6). The intensity of the spin-orbit split pair of peaks attributed to Fe_3C increases with time, showing the thermodynamics of the system tends towards carburization with time. XPS also proved to be able to detect the presence of iron in samples at shorter pyrolysis times and lower pyrolysis temperatures than XRD.

Loading Salt	Pyrolysis Temp (°C)	Percent C	Percent Fe	Percent O
$Fe(NO_3)_3$	600	97.98	2.11	-
$Fe(NO_3)_3$	800	98.95	1.05	-
$Fe(NO_3)_3$	1050	99.25	0.75	-
$(NH_4)_2Fe(SO_4)_2$	1050	99.37	0.63	-
$FeSO_4$	1050	98.67	1.33	-
$FeCl_3$	1050	99.82	0.18	-
HCl (Undoped)	1050	94.83	0.00	3.41

Table 2-3 Percent concentrations by mass of carbon and iron for Fe-doped and undoped carbon aerogel samples as determined by XPS. $FeSO_4$ seems to result in the highest level of doping.

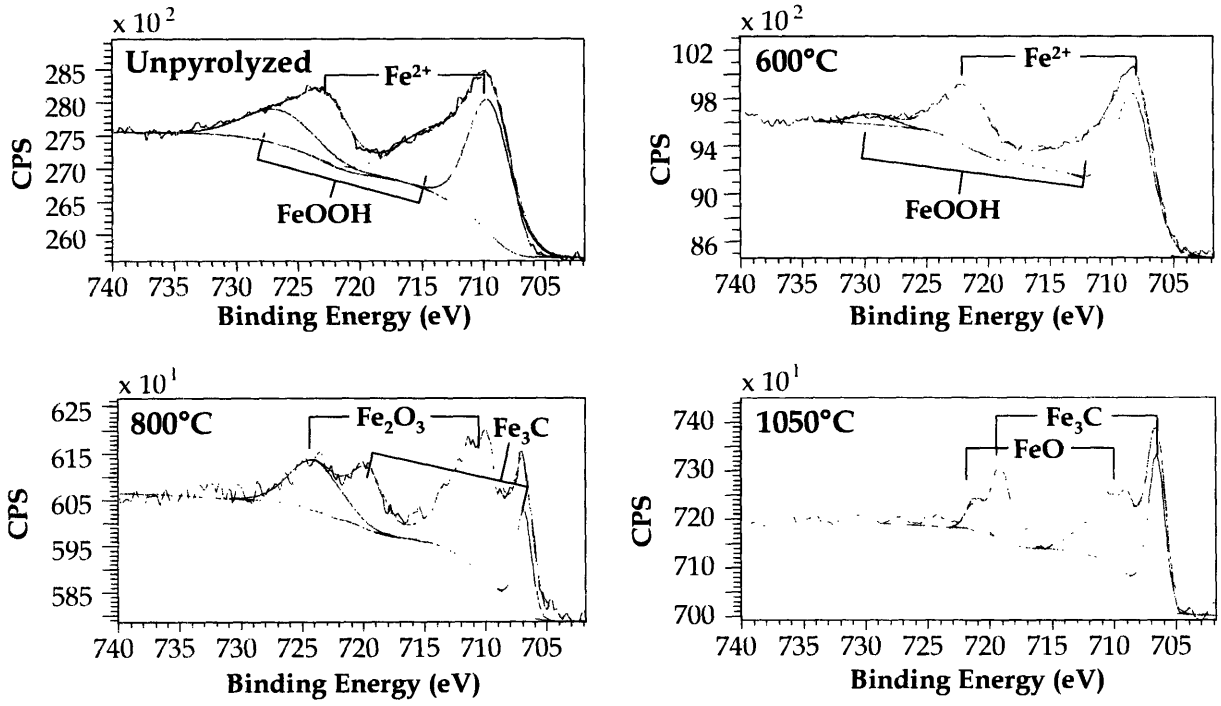

Figure 2-5 XPS spectra for Fe-doped carbon aerogels as a function of pyrolysis temperature (satellite peaks omitted for clarity). Before pyrolysis, iron oxyhydroxide precipitates (Fe^{3+}) and iron bound to the polymer backbone (Fe^{2+}) are observed. After pyrolysis at 600°C for 10.5 h, most of the iron in the aerogel is still in these surface forms. At 800°C, signals attributable primarily to Fe_2O_3 and as well as Fe_3C emerge. Reduction of Fe_2O_3 to the lower oxidation state oxide FeO and an overtaking by Fe_3C are then observed at 1050°C.

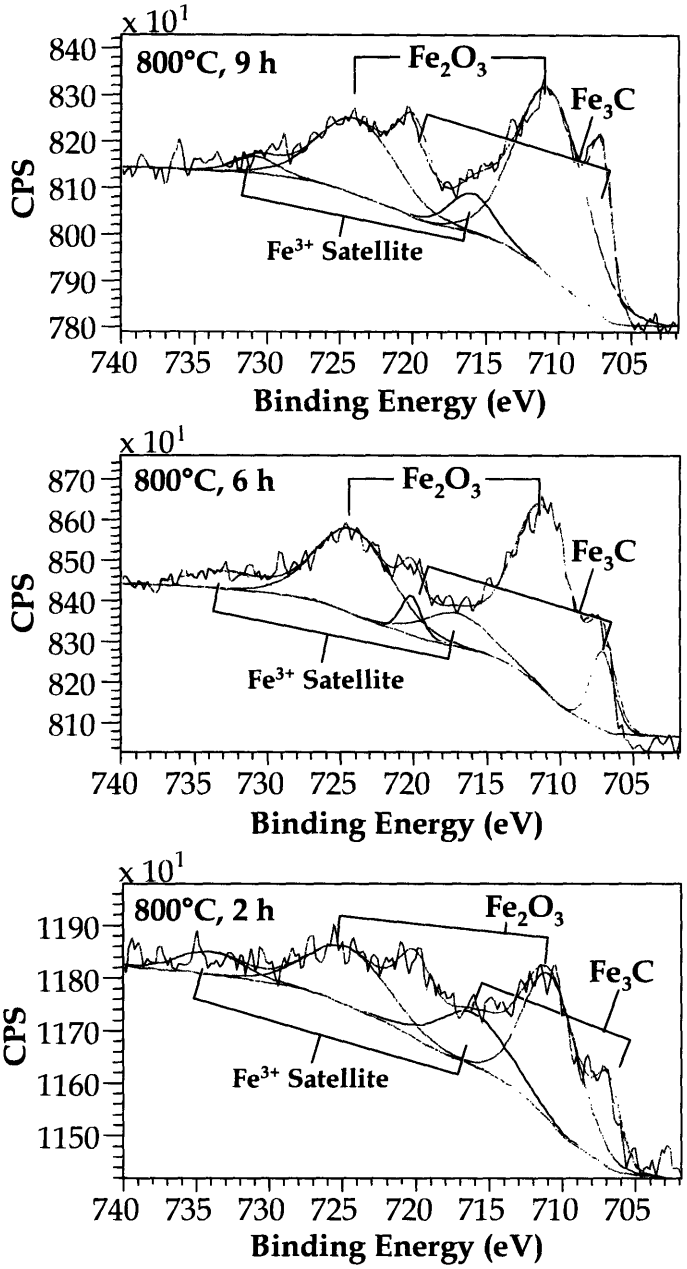

Figure 2-6 XPS spectra as a function of pyrolysis time for Fe-doped carbon aerogels pyrolyzed at 800°C. The system tends towards the surface carburization of iron-containing nanoparticles with time.

Correlating the information collected from XPS with the information collected from XRD, an overall picture of the evolution of iron-containing nanoparticles in Fe-doped carbon aerogels as a function of pyrolysis time and temperature can be deduced. First, it appears that the pyrolysis temperature governs the mean

diameter and composition of the nanoparticles which evolve. Pyrolysis time seems to primarily affect the surface chemistry of the nanoparticles. Samples pyrolyzed at 600°C exhibited low signal intensity in their XRD spectra, suggesting only a small population of small-diameter iron crystallites are present. XPS analysis of these samples, on the other hand, detects the highest signal intensity for iron at this temperature. As mentioned, it appears that after pyrolysis at 600°C, most of the iron is still atomically dispersed throughout the aerogel, with only a few crystallites of iron emerging. Additionally, it appears that some of the iron is still in the form of iron oxyhydroxide, the iron species prevalent pre-pyrolysis. At 800°C, XRD shows the emergence of iron and iron carbide crystallites. XPS indicates the surfaces of the iron nanoparticles to be oxidized with a coating of Fe_2O_3 or carburized. Finally at 1050°C, carburized nanoparticle surfaces dominate. Thus, it appears that a transition from oxidized nanoparticle surfaces to carburized nanoparticle surfaces occurs with increasing pyrolysis time. Although metallic iron crystallites are present in samples pyrolyzed at 800°C and 1050°C, XPS only detects their composition to a depth of a few monolayers. As a result, only oxidized and carburized iron is observed in XPS. Overall, the fate of iron in the presence of the overwhelming excess of carbon and oxygen from the aerogel is apparently to carburize.

2.3.3 Raman Spectroscopy

Raman spectra as a function of pyrolysis temperature for Fe-doped carbon aerogels prepared with iron(III) nitrate and undoped samples are shown in Figure 2-7. Previous Raman studies of carbon aerogels report the ubiquitous G-band (located at ~1580 cm^{-1}) and the disordered-induced D-band (located at ~1360 cm^{-1}) modes [80]. Raman spectra for Fe-doped carbon aerogels similarly exhibit these two modes, however their locations appear to change with pyrolysis temperature and Raman excitation wavelength (Table 2-4). The broad linewidths of these bands imply a low overall crystallinity, consistent with findings from XRD. In samples doped with iron(III) nitrate, a strong fluorescence effect is observed in the spectra of Fe-doped carbon aerogels (Figure 2-7). This effect is identifiable by a continuously

escalating signal starting at ~1500 cm^{-1} which becomes more pronounced with increased pyrolysis temperature and increased laser excitation energy. As this signal is absent in undoped carbon aerogels and in samples prepared iron salts other than $Fe(NO_3)_3$, it is most likely caused by cohenite-phase iron carbide nanoparticles. Furthermore, based on the observation made from XRD that iron carbide nanoparticles emerge with increasing pyrolysis temperature in this system, it can similarly be concluded that this fluorescence is probably caused by iron carbide. A broad, shouldered G' band enabled by double-resonant processes is observed in spectra taken with an excitation wavelength of 752 nm (shift ~2970 cm^{-1}, FWHM ~640 cm^{-1}), apparently absent in spectra taken at 785 nm and obscured by fluorescence effects at 676 nm and 514 nm. The relative shift between the D-band and G-band peak centers appears to increase with increasing pyrolysis temperature. The D-band center shifts significantly with laser excitation energy (increasing ~60 cm^{-1} between 515 nm and 785 nm excitation wavelengths), which can only be attributed to differences in electron-defects interactions occurring through a double-resonance mechanism. No meaningful shift in G-band center with laser energy is observed (other than due to fluorescence effects), which is expected since the G-band arises from first-order processes.

Table 2-5 lists the ratio of the D-band to G-band integrated areas (I_D/I_G) after background subtraction as a function of pyrolysis temperature. The D-band to G-band ratio only shows a meaningful trend at 515 and 676 nm, however this is probably due to enhanced signal contribution in the G-band region because of the fluorescence effect mentioned earlier. A change in the D-band to G-band ratio would be expected with a change in laser excitation energy since the D-band arises from second-order processes and scales with laser excitation energy differently than the G-band, which, as mentioned, arises from a first-order process.

Knight's formula allows calculation of approximate crystallite size using the relation

$$L_a = C_\lambda (I_D / I_G)^{-1} \qquad (4\text{-}1)$$

where L_a is the average crystallite size, I_D/I_G is the ratio of the integrated area of the D-band to that of the G-band, and C_λ is a fitting parameter which adjusts for the laser wavelength used to generate the spectrum. Values for this fitting parameter were determined using the relation $C_\lambda \approx C_0 + \lambda C_1$, where C_0 is estimated to be -12.6 nm and C_1 is estimated to be 0.033, C_λ was estimated to be 9.708 [81]. Crystallite sizes calculated by Knight's formula as a function of pyrolysis temperature are listed in Table 2-5. The values here imply a slightly larger carbon crystallite size (~2.5 nm) over the value calculated from XRD (~1.0 nm), however are still reasonably close. Again, no change in carbon crystallite size as a function of pyrolysis temperature is observed, providing further evidence that the carbon structure of the aerogel is not significantly graphitized or otherwise ordered by the presence of Fe during pyrolysis over the temperature range investigated.

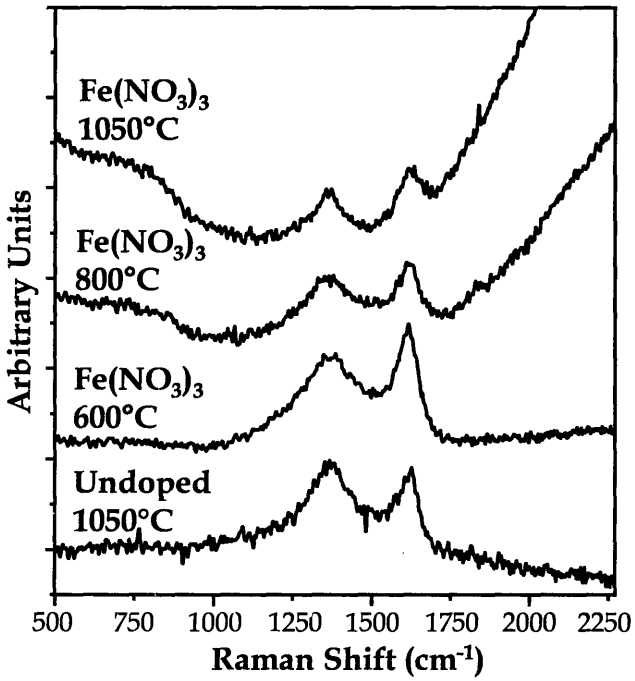

Figure 2-7 Raman spectra (excitation wavelength of 514 nm) as a function of pyrolysis temperature for undoped and Fe-doped carbon aerogels prepared with $Fe(NO_3)_3$. A D-band, G-band, and G'-band (not shown) are observed in all samples. Samples prepared with iron(III) nitrate exhibit a runaway fluorescence effect at higher pyrolysis temperatures, attributed to cohenite-phase iron carbide nanoparticles.

The dependence of the D-band/G-band shift on the pyrolytic evolution of the aerogel and the D-band dependence on excitation wavelength suggest that Raman spectroscopy could be a useful non-destructive *in situ* process monitoring technique in the commercial manufacture of metal-doped carbon aerogels. Correlating Raman spectra of a given sample with reference XRD and XPS spectra would provide reference points for adjusting process parameters during manufacture for efficient adjustment of desired materials properties.

		Excitation Wavelength			
	Pyrolysis Temperature	515 nm	676 nm	752 nm	785 nm
D -Band (cm^{-1})	600°C	1366.3	1338.7	1323.4	1303.5
	800°C	1354.8	1334.0	1311.2	1298.8
	1050°C	1355.1	1310.9	1309.1	1300.4
G-Band (cm^{-1})	600°C	1609.4*	1581.3*	1575.1	1571.5
	800°C	1613.0*	1586.5*	1574.8	1574.5
	1050°C	1616.0*	1570.9*	1584.1	1579.1
Shift (cm^{-1})	600°C	243.1	242.7	251.7	268.0
	800°C	258.3	252.5	263.5	275.7
	1050°C	260.9	260.1	274.9	278.6

*Approximate G-band location after background subtraction of fluorescence effect; the actual G-band peak location is probably lower in energy.

Table 2-4 D-band and G-band peak positions for Fe-doped carbon aerogels as a function of pyrolysis temperature and Raman excitation wavelength.

Pyrolysis Temperature	Excitation Wavelength				Mean L_a (nm)
	515 nm*	676 nm*	752 nm	785 nm	
600°C	2.31	2.59	3.48	8.47	2.68
800°C	1.91	2.82	3.83	9.87	2.57
1050°C	1.48	3.57	3.48	8.69	2.68
Undoped, 1050°C	2.42	3.06	3.76	-	2.74

* Pronounced fluorescence effect in G-band region complicates peak fitting

Table 2-5 Ratio of D-band to G-band integrated areas (I_D/I_G) and approximate crystallite size L_a for Fe-doped carbon aerogels prepared with iron(III) nitrate as a function of pyrolysis temperature and excitation wavelength.

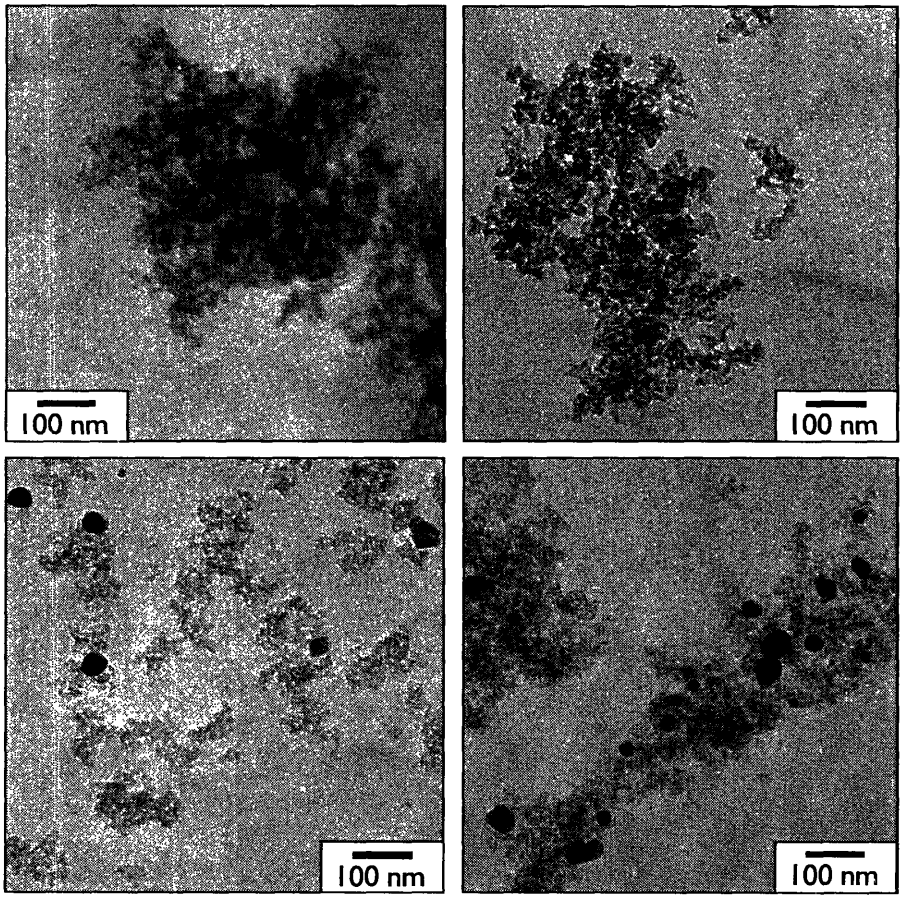

Figure 2-8 TEM micrographs of undoped carbon aerogel pyrolyzed for 10.5 h at 1050°C (top left) and Fe-doped aerogels pyrolyzed for 10.5 h at 600°C (top right), 800°C (bottom left), 1050°C (bottom right).

2.3.4 Transmission Electron Microscopy (TEM)

TEM micrographs for Fe-doped and undoped carbon aerogels are shown in Figure 2-8. Dark crystallites of iron-containing nanoparticles can be seen among a framework of nanocrystalline carbon particles. H1050 and Fe600 appear virtually identical, implying iron has only partially begun to agglomerate after 10.5 h at 600°C. Iron-containing nanoparticles distributed throughout the nanocrystalline carbon framework are seen as dark spots in Fe800 and Fe1050, with a higher population of large (~30 nm) particles observed in Fe1050.

2.3.5 Effects of CVD on Fe-Doped Carbon Aerogels

Several CVD process variables were investigated for determining the optimal conditions for growing carbon nanotubes on Fe-doped carbon aerogels. It seems that there exists a "sweet spot" of pyrolysis and CVD parameters which results in high-yield growth of nanotubes on the aerogel monolith, outside of which yield and/or nanotube quality are sacrificed. Table 2-6 summarizes the efficacy of various pyrolysis and CVD temperatures for 10-minute growths performed with 1000 sccm CH_4, 20 sccm C_2H_4, and 500 sccm H_2. Aerogels pyrolyzed at 800°C undergoing CVD at 700°C (Fe800-700) were found to grow the highest yield of nanotubes, with measured nanotube diameters (as determined from SEM and TEM) indicative of multiwall nanotubes. This was later substantiated by the observation of layered nanotube walls under TEM. No nanotube growth was observed for CVD temperatures of 600°C or for samples pyrolyzed at 600°C. Growth at CVD temperatures of 700°C on samples pyrolyzed at 1050°C (Fe1050-700) resulted in a reduced yield of nanotubes compared with Fe800-700 samples, with larger diameters and a larger overall degree of defectiveness. The larger mean diameter of nanotubes observed in Fe1050 samples may because of the presence of larger diameter nanoparticles, which would be consistent with the increased rate of particle coarsening expected for higher pyrolysis temperatures. Growth at CVD temperatures of 800°C on samples pyrolyzed at 1050°C (Fe1050-800) resulted in low yields of nanotubes (<3 tubes/μm^2), however much smaller diameter nanotubes and quite possibly single-walled nanotubes. Varying the ratio of CVD gases was also

found to affect the quality of nanotubes grown. Decreasing the total flow by reducing the concentration of methane resulted in longer, larger diameter nanotubes. SEM micrographs for Fe800-700 samples grown with 30 sccm CH_4, 20 sccm C_2H_4, and 500 sccm H_2 for 20 min are shown in Figure 2-9. SEM imaging of Fe800-700 samples shows an average nanotube length of ~4 μm. The nanotubes in these and other samples appear to grow through a tip-growth mechanism (based on the observation of small bulges at the tips of the nanotubes when viewed by SEM). This apparent tip-growth mechanism effectively removes many of the nanoparticles formed during pyrolysis from the aerogel. SEM imaging of cross-sections of Fe800-700 samples did not reveal nanotubes beyond a depth of ~1 μm into the interior porosity of the aerogel. Exposing a new surface on an already-grown monolith and performing CVD a second time resulted in the growth of carbon nanotubes across the new surface, as well as an apparent increase in diameter of already-existing nanotubes. This increase in diameter is likely due to the deposition of additional external graphitic walls or possibly amorphous carbon onto the nanotubes. The layer of nanotubes grown on the monolith was found to be easily removed and only very delicately attached to the surface of the monolith. Contact with a sharp object (such as the tip of a pair of pointed tweezers or a conductivity probe) resulted in a nanotube-less crater on the aerogel where contact was made. Gentle contact with blunt objects and surfaces was found not to disturb the nanotube layer.

The shallow penetration depth of nanotube growth observed is most likely due to the short mean free path of diffusion intrinsic to mesoporous materials such as aerogels. To circumvent this, an attempt was made to grow carbon nanotubes within the interior confined porosity of the bulk monolith by diffusively pre-loading small samples of Fe800 (chunks roughly 6 mm in diameter) with CVD gases prior to heating. This was accomplished by placing the aerogels in a quartz tube under a flow of 30 sccm methane, 20 sccm ethylene, and 500 sccm hydrogen for 40 min. The quartz tube was then placed in the tube furnace and held at 700°C for 10 min, still under the same flow of gases. HRTEM and HRSEM images of cores taken from several millimeters into the bulk interior of these samples did not show growth of

nanotubes beyond a depth of about 1 μm from the monolith surface (see Chapter 3). These images did show the formation of other graphitic nanostructures, however.

Figure 2-10 shows TEM images of Fe800-700 samples. TEM reveals nanotubes grown on the aerogel to be multiwalled and defective. Other tubular graphitic nanostructures, nanoribbons, and nanoshells not observed prior to CVD are also present. TEM further verifies a tip-growth mechanism, as dark iron-containing nanoparticles can be seen in the tips of the nanotubes, and reveals the nanotubes are actually anchored to the nanocrystalline carbon framework of the aerogel. TEM of cores taken from cross-sections of Fe800-700 samples also failed to definitively detect nanotubes beyond a depth of ~1 μm of exposed monolith surface.

	Fe600	**Fe800**	**Fe1050**
CVD at 600°C	No nanotubes	No nanotubes	No nanotubes
CVD at 700°C	No nanotubes	High yield, medium-diameter multiwall nanotubes	Moderate yield, large diameter defective multiwall nanotubes
CVD at 800°C	No nanotubes	No nanotubes	Low yields of small diameter nanotubes (<3 tubes/μm^2)

Table 2-6 Summary of the effects of pyrolysis temperature and CVD temperature on the success of nanotube growth.

Given the results of the compositional characterizations of pre-CVD Fe-doped carbon aerogels, the presence of a "sweet spot" of pyrolysis and CVD conditions which resulted in the highest yield and highest quality of nanotubes seems to indicate that only nanoparticles with a particular compositional profile and within a particular size range are catalytic towards growing nanotubes, and only at certain CVD temperatures. This is an interesting result in terms of better understanding heterogeneous catalysis of nanotubes with iron in general—the mixture of iron compounds and the amount carbon content present in the nanoparticles seem to play a critical role as to whether the nanoparticles will be catalytic or not, as well as the CVD temperature which will result in optimal nanotube growth. In carbon aerogels, the compositional profile of nanoparticles produced by particle coarsening

is statistical, not deterministic, and so some nanotubes are able to grow on samples prepared outside of the "sweet spot" of optimal pyrolysis and CVD conditions. It is the experience of the author that this is the case with many other statistically-sensitive nanoparticle preparation methods, such as the production of iron nanoparticles through annealing of ferritin, the nature of which is discussed in detail in Chapter 3.

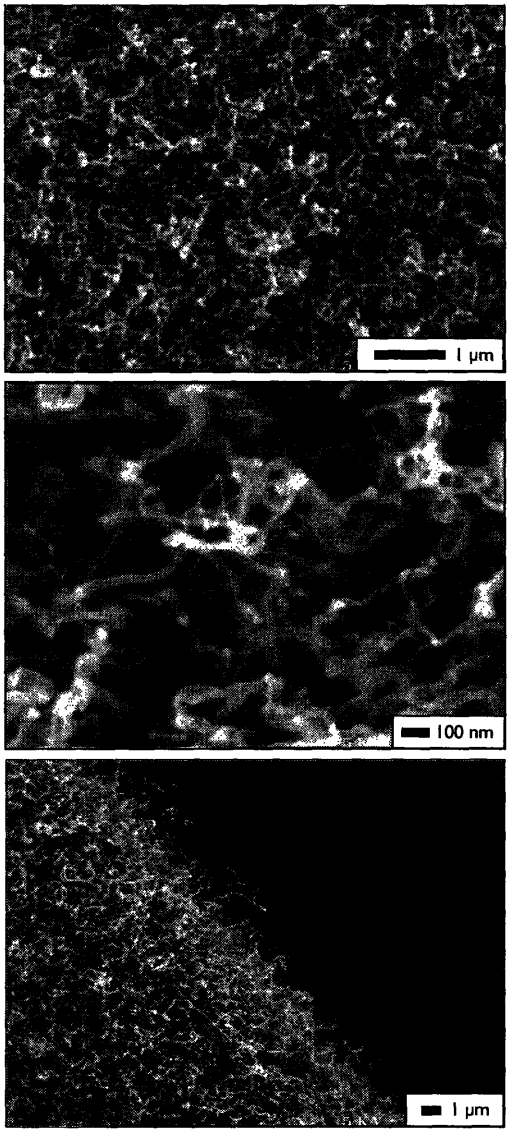

Figure 2-9 SEM micrographs of Fe-doped carbon aerogel after chemical vapor deposition exhibiting high yield growth of multiwall carbon nanotubes. The nanotubes appear to grow through a tip-growth mechanism, emerging from no more than 1 µm of depth into the porosity of the aerogel.

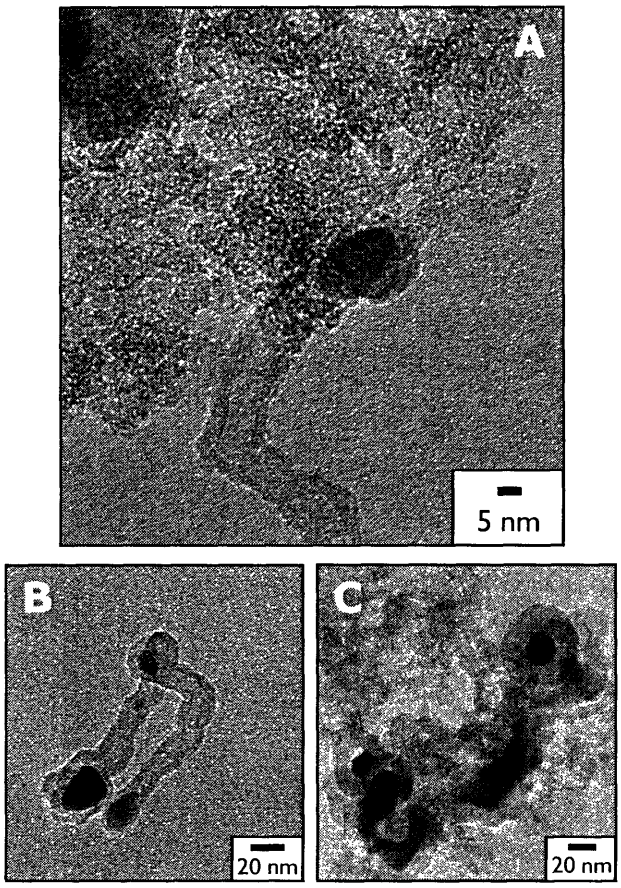

Figure 2-10 TEM micrographs of Fe-doped carbon aerogel sample after chemical vapor deposition: *(a)* multiwall nanotube attached to the amorphous carbon framework of the aerogel; *(b)* wayward nanotube detached from the aerogel monolith, with embedded nanoparticle catalyst (dark spot on the left) and "anchor scab" from where it was attached to the aerogel (gray spot on the right); *(c)* other graphitic nanostructures including nanoribbons and nanoshells.

2.3.6 Surface Area and Electrical Conductivity

BET nitrogen surface area measurements and electrical conductivity measurements for Fe800 samples before and after CVD are shown in Table 2-7. Electrical conductivity through the thickness of monolith discs of Fe800 aerogels was found to be ~170 S cm^{-1}. Subsequent growth of nanotubes at 700°C on Fe800 aerogels was found to increase this value to ~290 S/cm. These values compare with a typical value of 50-100 S cm^{-1} for undoped carbon aerogels [6, 7, 44, 46].

CVD growth of nanotubes was found to result in an increase in mass, but also in a decrease in BET surface area of ~200 m^2/g. This is believed to be due to nanotubes, other graphitic nanostructures, and amorphous carbon deposits obstructing access to micropores in the monolith (pores <2 nm in diameter) thereby limiting diffusion of gas. This hypothesis is substantiated by the measured external surface areas (calculated from BET theory [82]) and micropore surface areas (calculated from BJH theory [83]) before and after CVD, which indicate that CVD does not affect the accessible external surface area (non-micropore surface area) but does reduce the accessible micropore area. Powderizing monolithic carbon aerogel-carbon nanotube composite monoliths and performing CVD a second time resulted in an increase in both BET surface area and accessible micropore area over the carbon aerogel-carbon nanotube composite monolith, implying interior nanoparticles that were inaccessible during the first growth were exposed when the monolith was powderized.

Electrical conductivity of undoped carbon aerogels is improved with increasing aerogel density, however only at significant expense of surface area. Growth of carbon nanotubes offers a technique for improving the electrical conductivity without significantly compromising surface area.

	Before CVD	After CVD	Change	CVD on Powder
BET Surface Area ($m^2 g^{-1}$)	789	590	-25.2%	693
External Surface Area ($m^2 g^{-1}$)	433	430	-0.7%	429
Micropore Area ($m^2 g^{-1}$)	355	160	-54.9%	264
Electrical Conductivity ($S cm^{-1}$)	172	291	+69.2%	--
Mass (mg)	106.5	135.5	+27.2%	--

Table 2-7 BET surface area and electrical conductivity measurements for Fe800-700 samples.

2.4 Conclusions

Fe-doped carbon aerogels were found to contain a mixture of iron and iron carbide nanoparticles as a result of pyrolysis, with very little graphitization of the aerogel's nanocrystalline carbon framework to temperatures up to 1050°C.

Performing CVD on Fe-doped carbon aerogels prepared under certain conditions was found to result in the formation of carbon nanotubes and other graphitic nanostructures, affording novel monolithic carbon aerogel-carbon nanotube composites. The improvements in electrical conductivity from both carbon aerogels with iron and subsequent growth of carbon nanotubes on the aerogel monolith suggest new techniques for improving the conductivity of high-surface-area, intrinsically mesoporous carbon aerogel materials without increasing bulk density or substantially sacrificing surface area. Only a small loss in surface area resulting from CVD was observed due to obstruction of aerogel microporosity, however it may be possible that the surface area lost due to obstruction of microporosity can be recovered and even exceeded by decreasing the diameter of the nanotubes grown, increasing the length or nanotubes grown, and by increasing the coverage of nanotubes over the aerogel.

Coupled with the ability to cast aerogels of this type into arbitrary forms, the improvements in electrical conductivity demonstrated by the addition of carbon nanotubes to the aerogel monolith give carbon aerogel-carbon nanotube composites a unique and appealing potential for use as high-surface-area monolithic electrodes for application in supercapacitors, desalination systems, fuel cells, and possibly physisorption-based hydrogen storage.

Lastly, information pertaining to nanoparticles which are catalytic towards carbon nanotube growth and nanoparticles which are apparently not catalytic towards carbon nanotube growth was obtained. This was made possible largely by the presence of a bulk quantity of nanoparticles in the aerogel which enabled phase identifications of crystallites through XRD and facile analysis of surface chemistry through XPS. Capitalizing on the discovery of this feature for Fe-doped carbon aerogels, analyses of six other metal-doped carbon aerogel systems in the context of characterizing the propensity of other metals for catalyzing carbon nanotube growth are presented in Chapter 4.

Chapter 3

Development of Techniques For Optimizing Growth of Carbon Nanotubes on Fe-Doped Carbon Aerogel Monoliths

3.1 Introduction

The ability to both enhance the electrical conductivity and specific surface area of carbon aerogels is highly desirable for applications requiring high-surface-area electrodes, such as supercapacitors, fuel cells, and rechargeable batteries. Previously, improving the electrical conductivity of a carbon aerogel required increasing the density of the aerogel, thereby reducing the material's specific surface area [6, 7, 44, 46]. Similarly, maximizing the surface area of a carbon aerogel, required producing a material with a higher porosity, meaning a lower bulk density and thus a lower electrical conductivity. Simultaneous improvement of these two parameters seemed not possible, as they are apparently inversely related. Introduction of metals such as copper, cobalt, nickel, and iron into a carbon aerogel (through ion-exchange doping, post-pyrolysis diffusive doping, or by simply adding metal salts into a resorcinol-formaldehyde sol) has proved to be one way to improve

the conductivity for a given density [8, 10-13, 47, 80], but ultimately is also limited in the ability to maximize both surface area and electrical conductivity for the same reasons undoped carbon aerogels are.

As demonstrated in the previous chapter, growth of carbon nanotubes on the surface of an Fe-doped carbon aerogel monolith was found to be an alternative method for improving the conductivity of a carbon aerogel without requiring an increase in aerogel density (and thus a significant decrease in specific surface area). Unfortunately, CVD growth of nanotubes was found to result in a decrease of the specific surface area of carbon aerogel monoliths for a different reason. Based on t-plot surface area analysis of nitrogen desorption isotherms collected for untreated and CVD-treated Fe-doped carbon aerogels [82, 83], the surface area was found to decrease after growth, likely due to the presence of nanotubes and other graphitic nanostructures partially obstructing access to the aerogel's porosity. CVD on powderized samples resulted in materials with a higher surface area than CVD-treated monoliths, still exhibiting a decreased percentage of accessible microporosity (pores <2 nm in diameter), but at the same time a higher external surface area contribution from the larger population of nanotubes.

So, can a monolithic carbon aerogel-carbon nanotube composite be engineered to capitalize on the electrical conductivity benefits of growing carbon nanotubes and other graphitic nanostructures directly on the monolith without compromising, possibly even enhancing, the specific surface area? As mentioned, the surface area cost from the addition of nanotubes to the aerogel is in the form of microporosity obstruction resulting from CVD. However, it may be possible to compensate for this loss of surface area, even exceed it, by increasing the amount of surface area contributed by the addition of nanotubes. Some potential ways of doing this would be to increase the number of nanotubes added to the monolith, increase the length of the nanotubes grown, and decrease the average nanotube diameter.

In this chapter, a survey of three proof-of-concept techniques designed to work towards optimizing nanotube growth on Fe-doped carbon aerogels are explored, with the objective of maximizing the specific surface area these composites. Recommendations for producing idealized carbon aerogel-carbon nanotube

composites are then made based on lessons learned from development of these techniques. Propositions for tangential research trajectories based on novel discoveries made during the development of these techniques are also presented. Lastly, a model describing chemical state-sensitive catalytic activity and how it relates to pyrolysis of metal-doped carbon aerogels is presented.

3.2 Growth of Nanotubes Within the Confined Porosity of an Aerogel

As mentioned, in characterizing the ability of Fe-doped carbon aerogels to catalyze nanotube growth, nanotubes were only observed to grow on the exterior edges of aerogel monoliths. The ability to access catalytic nanoparticles in the interior of a bulk monolith would be desirable for creating a long-range nanocomposite material, as well as for maximizing specific surface area.

Growth of graphitic nanostructures within the confined porosity of inorganic aerogels has been demonstrated by Hunt, Liu, and number of others [13, 16-18, 36, 62]. Growth of graphitic nanostructures and even so-called "nanofilaments" has also been previously demonstrated on carbon aerogels infused with cobalt through a post-pyrolysis diffusion doping technique [13]. In this method, cobalt is introduced into a carbon aerogel by soaking a pyrolyzed, undoped carbon aerogel in an aqueous solution of a cobalt salt, followed by sub-critical drying and annealing. Thermal decomposition of carbon monoxide over such aerogels was found to result in the formation of nanofilaments, however it was not conclusively demonstrated whether or not such nanofilaments where actually carbon nanotubes and whether or not they can grow within the confined porosity of the aerogel.

To the best of the author's knowledge, definitive growth of carbon nanotubes within the interior of an aerogel monolith has not been previously demonstrated. Here, the question of whether or not it is possible to achieve growth on nanoparticles within the confined interior porosity of a carbon aerogel is evaluated.

3.2.1 Infusion CVD

The limited penetration of carbon nanotube growth on the surface of Fe-doped carbon aerogels investigated in Chapter is partially due to the extremely short mean free path of diffusion inherent to mesoporous materials, which limits the penetration depth of deposition techniques which rely on mass-transport-based delivery of reactants. The limited penetration observed is also partially due to the fact that the average pore diameter for the Fe-doped carbon aerogels investigated is only approximately 6 nm (as determined in Chapter 2 by Harkins and Jura t-Plot analysis [82, 83] of nitrogen adsorption/desorption isotherms for Fe-doped carbon aerogels, see Table 3-1)—on the order of the diameter of a single wall nanotube itself. This extreme limitation in volume offers little room for nanotubes to grow (let alone fit). Coupled with the ultraslow rates of gas diffusion through the mesoporous network of the aerogel, it can be concluded that CVD gases in this scenario would also be consumed much faster than they could be replenished, severely limiting the potential for growth of graphitic nanostructures.

	Fe800 (Monolith)	Fe800-700 (Powder)
External BET Surface Area	433.8 $m^2 g^{-1}$	429.4 $m^2 g^{-1}$
Micropore BET Surface Area	353.3 $m^2 g^{-1}$	264.0 $m^2 g^{-1}$
Total Surface Area	789.1 $m^2 g^{-1}$	693.3 $m^2 g^{-1}$
Mean Pore Diameter from BET	6.5 nm	7.5 nm

Table 3-1 Surface area and mean pore diameter for Fe-doped carbon aerogels before and after CVD growth of nanotubes.

3.2.1.1 Experimental

Samples were prepared according to the methods described in Section 2.2. The same sample part numbering system described in Section 2.2 is used in this chapter as well.

To compensate for the slow rate of mass transport through the aerogel, an "infusion CVD" growth technique was developed. In this technique, an aerogel monolith is placed inside a quartz process tube under a flow of 30 sccm methane, 20 sccm ethylene, and 500 sccm hydrogen at room temperature for 60 minutes. This is done to allow time for the gases necessary for CVD growth of nanotubes to diffuse

into the interior porosity of the monolith. After 60 minutes, CVD was initiated by placing the process tube in an electric tube furnace preheated to 900°C. After opening and closing the furnace to place the process tube inside, the temperature of the furnace would drop by approximately 150-200°C. The tube was then held at 700°C for 20 minutes after which the tube was removed from the furnace, the CVD gases were turned off, and the argon turned on to a rate of 200 sccm until the process tube was cool.

3.2.1.2 Characterization

SEM imaging of the exterior surface of the monolith (see Figure 3-1) verified successful growth of nanotubes, comparable in diameter, length, and yield to those grown by the standard non-infusion CVD technique used in Chapter 2. The monolith was then sliced in half with a razor blade to image the interior by SEM (see Figure 3-2). No nanotubes were observed within the interior of the monolith by SEM; however the length scale of the mesoporosity of Fe-doped carbon aerogels (Table 3-1) suggests that if nanotubes or other graphitic nanostructures had grown in the monolith interior, they would probably only be visible by TEM. TEM imaging of cores taken from the interior of the monolith, however, showed only the formation of graphitic shells around the nanoparticles and no extrusion of tubular graphitic nanostructures.

3.2.1.3 Conclusions

Ultimately, the low mean free path of diffusion and limited volume within the mesoporosity of the aerogel seem to preclude nanotube growth in the confined porosity of an aerogel by CVD through obvious approaches.

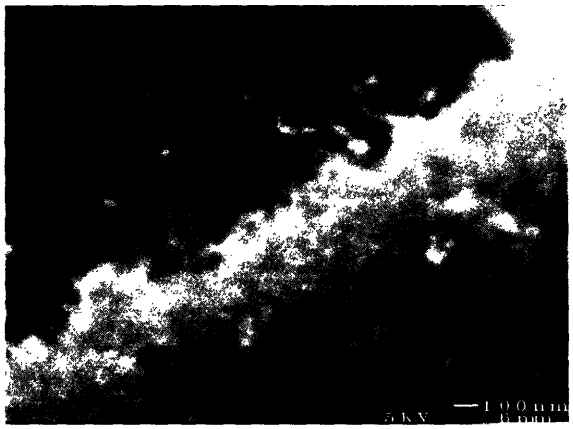

Figure 3-1 Verification of nanotube growth on the exterior surface of an Fe800-700 aerogel sample after infusion CVD.

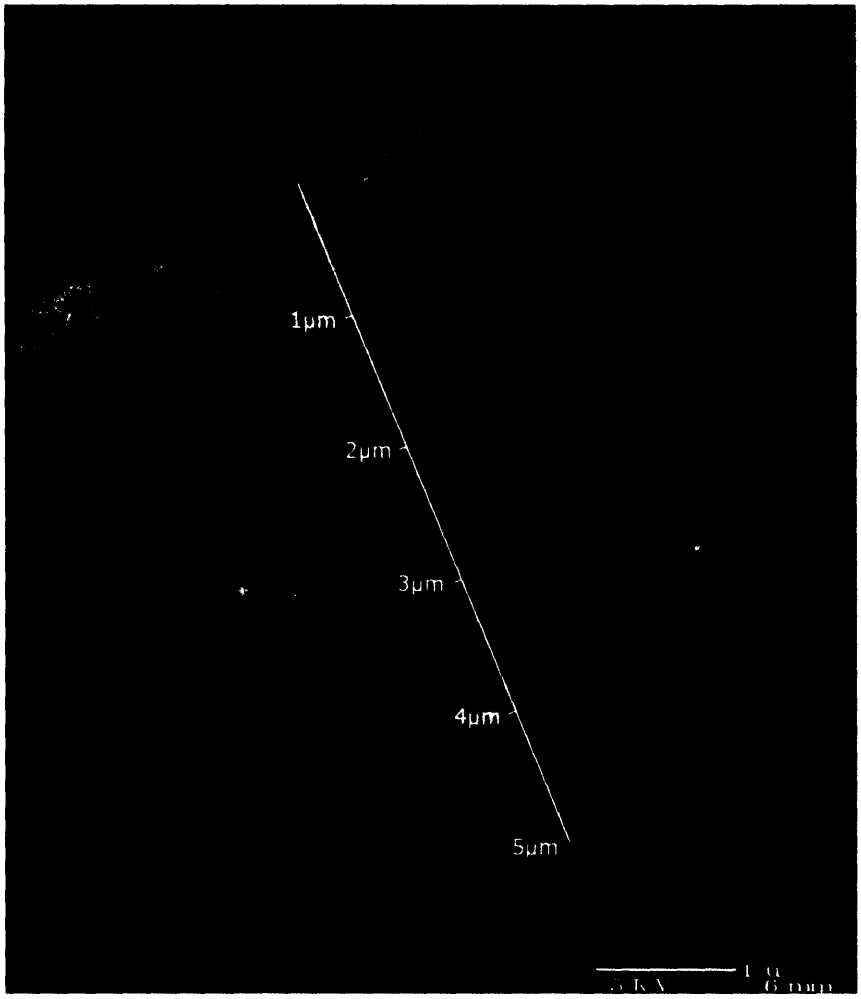

Figure 3-2 SEM survey of a cross-section of Fe800-700 showing no discernable growth of nanotubes beyond a depth of ~1 μm from the exterior surface of the monolith.

3.2.2 Introduction of a Macroporous Gas Diffusion Network

As the primary problems associated with growing nanotubes within the interior porosity seemed to arise from the material's small mean pore diameter, it was hypothesized that increasing the mean pore diameter might enable improved diffusion of CVD gases throughout the interior of the monolith and also might allow more room for nanotubes to grow. Increasing the intrinsic mean pore diameter of the aerogel is typically done through a density adjustment during the preparation of the precursor gel. This, however, results in a reduction in specific surface area of the material and consequently a reduction in electrical conductivity as well.

Livermore has previously demonstrated a technique for templating a regular ordered array of macropores into carbon aerogel films [12]. In this technique, an array of close-packed polystyrene microspheres is prepared by vacuum filtration of suspended microsphere solution over filter paper. Resorcinol-formaldehyde sol is poured over the template and is thermoset to form a gel. The microsphere template is then dissolved with toluene, leaving behind a thin layer of gel possessing an ordered array of macropores beyond the percolation limit. The gel is subsequently supercritically dried and pyrolyzed to afford a carbon aerogel with a bimodal pore structure—macroporosity arising from the templating and mesoporosity intrinsic to the aerogel framework. This technique does not facilitate preparation of large monoliths well, as forming an ordered template through filtration of suspended microsphere solution becomes increasingly difficult with increasing thickness, and requires the use of large volumes of expensive microsphere suspensions.

With these considerations in mind, a new templating technique using polydisperse polymethyl methacrylate (PMMA) microspheres was developed to enable production of bulk carbon aerogel monoliths possessing a bimodal porosity. PMMA microspheres are readily available in dry form, inexpensive, and can be easily dissolved by acetone and a number of other solvents facilitating easy removal of the template. Aerogels produced through this technique possess a distribution of macropores beyond the percolation limit analogous to the distribution of diameters of PMMA microspheres used in the template and a distribution of mesopores similar to untemplated carbon aerogels. Aerogels exhibiting a bimodal distribution

of pore sizes are referred to as "stratoporous" aerogels in this work to differentiate between such materials and purely mesoporous aerogels.

This new macropore templating technique was then combined with the ion exchange technique to produce Fe-doped stratoporous carbon aerogels possessing networks of macropores beyond the percolation limit. Standard CVD and infusion CVD growths of nanotubes on 1-cm diameter monolithic discs of this material were then attempted and evaluated.

3.2.2.1 Materials and Methods

Preparation of Precursory Sol

K_2CO_3 (1.29 g) and dihydroxybenzoic acid (2.90 g) were added to 100 g of deionized water with stirring. After the acid was completely neutralized and solubilized (~45 min), formaldehyde (2.98 g, 37% w/w in water) and additional K_2CO_3 (26 mg) were added. The solution was then stirred at room temperature for ~24 h to afford a slightly pink sol.

Preparation of Templated Gel

Dry poly(methyl methacrylate) (PMMA) granules (Aldrich, MW=350,000) were added to a 1.8-mL plastic vial partially filled with sol. The vial was then shaken vigorously until complete wetting of the PMMA granules was achieved. After settling of the granules, additional portions of sol and PMMA were subsequently added until the vial was completely packed with granules and the meniscus of the sol was level with the top of the compacted granules. The vial was then sealed with an o-ring cap and placed in oven at 80°C to thermoset. After 72 h, a reddish-orange gel was obtained. The gel was then removed from the oven, sliced into ~1 cm discs, and dropped into a vial of acetone to remove the PMMA microparticle template. To ensure complete removal of the template, the gels were allowed to soak in acetone for 3 d with fresh acetone exchanged in every 24 h.

Doping of Gels With Iron

After template removal, the acetone in the gels was replaced with deionized water by soaking over the course of 3 d with fresh water exchanged in every 24 h. The gels were then soaked in aqueous solutions of $Fe(NO_3)_3$ with a concentration of 0.1, 0.01, or 0.001 M for 3 d. Again, fresh solution was exchanged in every 24 h to ensure complete diffusion. The gels were then exchanged into deionized water again over the course of 3 d to remove any unbound ions from the pores of the gel, followed by exchange into pure acetone over the course of another 3 d.

Preparation of Fe-Doped Stratoporous Carbon Aerogels

After doping and subsequent solvent exchange into acetone, the gels were placed in a high-pressure vessel and soaked under liquid carbon dioxide under its own vapor pressure. The vessel was flushed with fresh CO_2 every 6 h for 2 d to exchange the acetone in the gels for liquid CO_2. The CO_2 in the gels was then supercritically extracted affording Fe-doped polymer aerogels possessing a bimodal macroporous/mesoporous pore structure (heretofore referred to as "stratoporous"). The aerogels were then pyrolyzed in a 1" quartz tube placed in an electric clamshell tube furnace at 800°C under a flow of 200 sccm Ar for 10.5 h. This processing resulted in a low-density stratoporous carbon aerogel with porosity that was appreciable to the naked eye.

Growth of Nanotubes by Standard CVD

An aerogel sample was placed in a quartz process tube under a flow of 200 sccm Ar for 20 min to remove air from within its pores. The process tube was then placed in an electric tube furnace preheated to 900°C. After opening and closing the furnace to place the process tube inside, the temperature of the furnace would drop by ~150-200°C at which point the temperature was set to 700°C. After 1.5-2 min the temperature would equilibrate to 700°C at which point a flow of 30 sccm CH_4, 20 sccm C_2H_4, and 500 sccm H_2 was introduced and the Ar was turned off. After 20 minutes at these conditions, the tube was removed from the furnace, the CVD gases

were turned off, and the argon turned on to a rate of 200 sccm until the tube had cooled.

Growth of Nanotubes by Infusion CVD

An aerogel sample was placed in a quartz process tube under a flow of 30 sccm methane, 20 sccm ethylene, and 500 sccm hydrogen at room temperature for a length of time (typically 60 min) to allow the CVD gases to diffuse into the interior porosity of the monolith. Following this, the process tube was placed in an electric tube furnace preheated to 900°C and the process proceeded identically to the standard CVD process. Stratoporous carbon aerogel-carbon nanotube composites produced by infusion CVD are denoted by a part number with the format "ST-Fexxxx-Icc-yyy", where "xxxx" is the temperature the aerogel was pyrolyzed at (for 10.5 h), "cc" is the length of time that CVD gases were allowed to diffuse into the aerogel prior to growth in minutes, and "yyy" is the temperature at CVD was carried out.

Characterization

The density of stratoporous Fe-doped aerogels was obtained through weighing and dimensional analysis of monolithic discs. Evaluation of the nanotube growth was performed by surveying various cross-sections of monoliths with scanning electron microscopy performed with a JEOL 6320 microscope operating at 5 kV. Evaluation of nanotube diameter and quality was performed by transmission electron microscopy with a JEOL JEM-200CX microscopy operating at 200 keV.

3.2.2.2 Results and Discussion

Figure 3-3 shows SEM images of pre-pyrolysis stratoporous Fe-doped phenolic aerogels. A network of macroporous cells ranging from 25 to 150 μm in diameter arising from the template is observed. In the center of the cells are connective punctures, regions where two PMMA microspheres were in contact in the template, indicating that the pore network is beyond the percolation limit. The solid walls of the material are in and of themselves mesoporous since the formulation used to

prepare the gel is the same as that used to prepare untemplated mesoporous Fe-doped carbon aerogels. Survey of the monolith indicates complete removal of the PMMA microsphere template. Both the unpyrolyzed and pyrolyzed aerogels are extremely low in density (26.7 mg cm^{-3} pre-pyrolysis, 4.2 mg cm^{-3} after), highly responsive to static electricity, relatively easy to crush, and many times more delicate than their untemplated counterparts.

Figure 3-4 shows SEM images of the exterior and interior cross-sections of Fe-doped carbon aerogels after a standard CVD growth. High yields of multiwall carbon nanotubes approximately 0.5-1 μm in length are observed on the exterior of the monolith. The interior of the monolith (beyond 0.2 cm from the edge), however, exhibited no growth of nanotubes. Appreciable yield of nanotubes are visible on cross-sectional areas to a depth of approximately 1 mm from the edge of the monolith, but is significantly reduced in comparison with the edge.

Figure 3-5 shows SEM images from Fe-doped carbon aerogels after infusion CVD growth (denoted ST-Fe800-I60-700). Again, high yields of multiwall carbon nanotubes are observed on the exterior. Unlike the standard, non-infusion CVD growth, however, high yields of nanotubes are also observed throughout the entire interior porosity of the monolith as well. In fact, SEM surveys of monolith cross-sections at various interior depths found no regions which did not grow nanotubes. As seen in Figure 3-5, the nanotubes grown on the exterior edges of the monolith were comparable in length, diameter, and yield to those grown on untemplated Fe-doped carbon aerogels (approximately 1 μm in length), however those found on interior structures were found to be much shorter (<0.5 μm in length). This is likely due to feedstock exhaustion during growth as the CVD gases diffused into the macroporosity of the monolith before growth are consumed faster than they can be diffusively replenished.

Figure 3-6 shows TEM survey images of ST-Fe800-I60-700, verifying the presence of carbon nanotubes within the confined porosity of the aerogel. Like their untemplated counterparts, the stratoporous Fe-doped carbon aerogels catalyze growth of defective multiwall nanotubes. It appears that a number of large-diameter, defective multiwall nanotubes and possibly non-nanotube carbon

nanofilaments are also present, distinguishable from nanotubes based on the lack of obvious layered walls and an electron-transparent center.

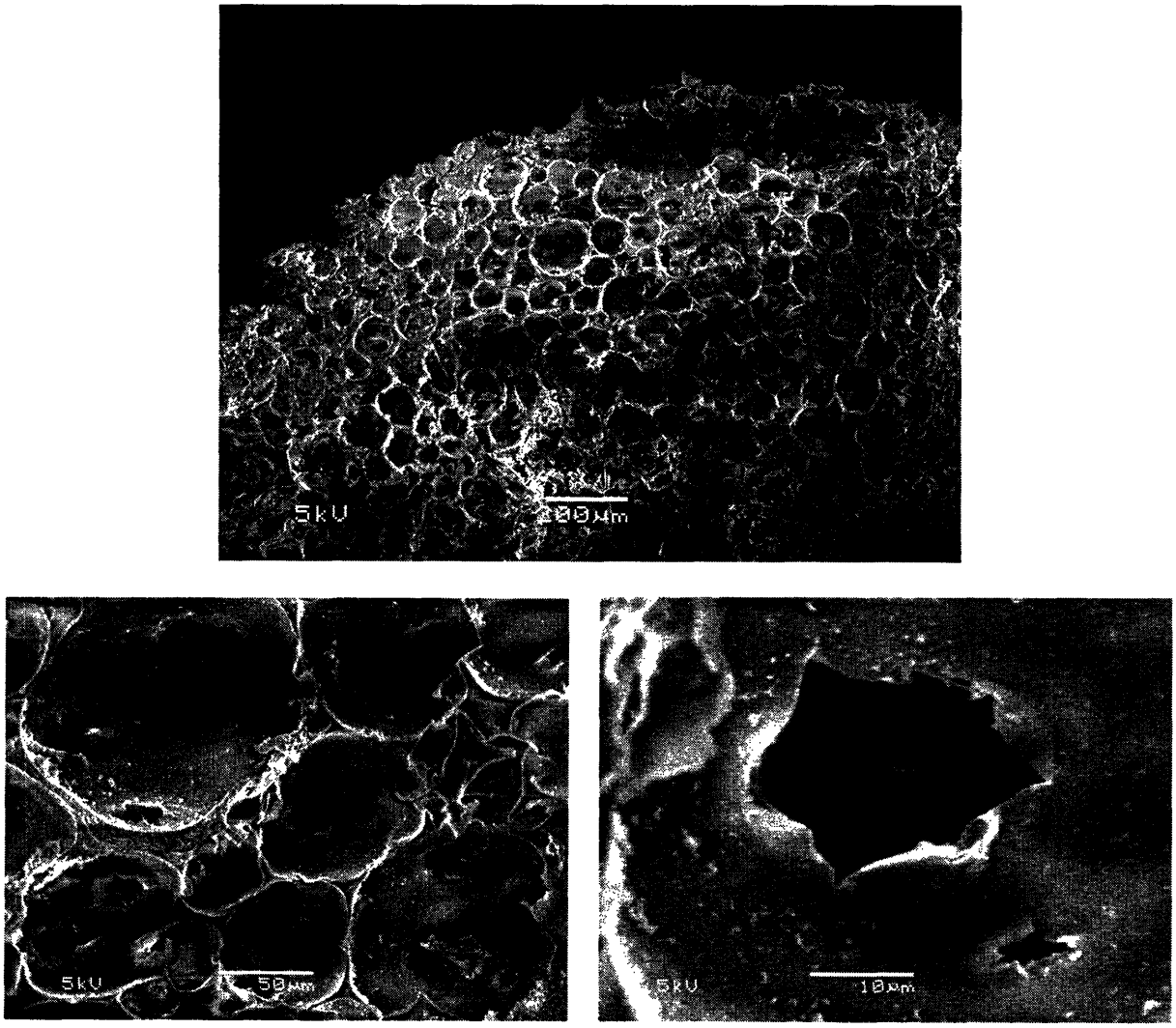

Figure 3-3 Stratoporous Fe-doped phenolic aerogels exhibiting a bimodal porosity; *(top)* overview of macroporosity resulting from microsphere templating; *(bottom left)* cross-section of a monolith interior showing this porosity to be beyond the percolation limit; *(bottom right)* connection channel uniting macroporous cells into a single network. The walls of the material are composed of intrinsically mesoporous aerogel.

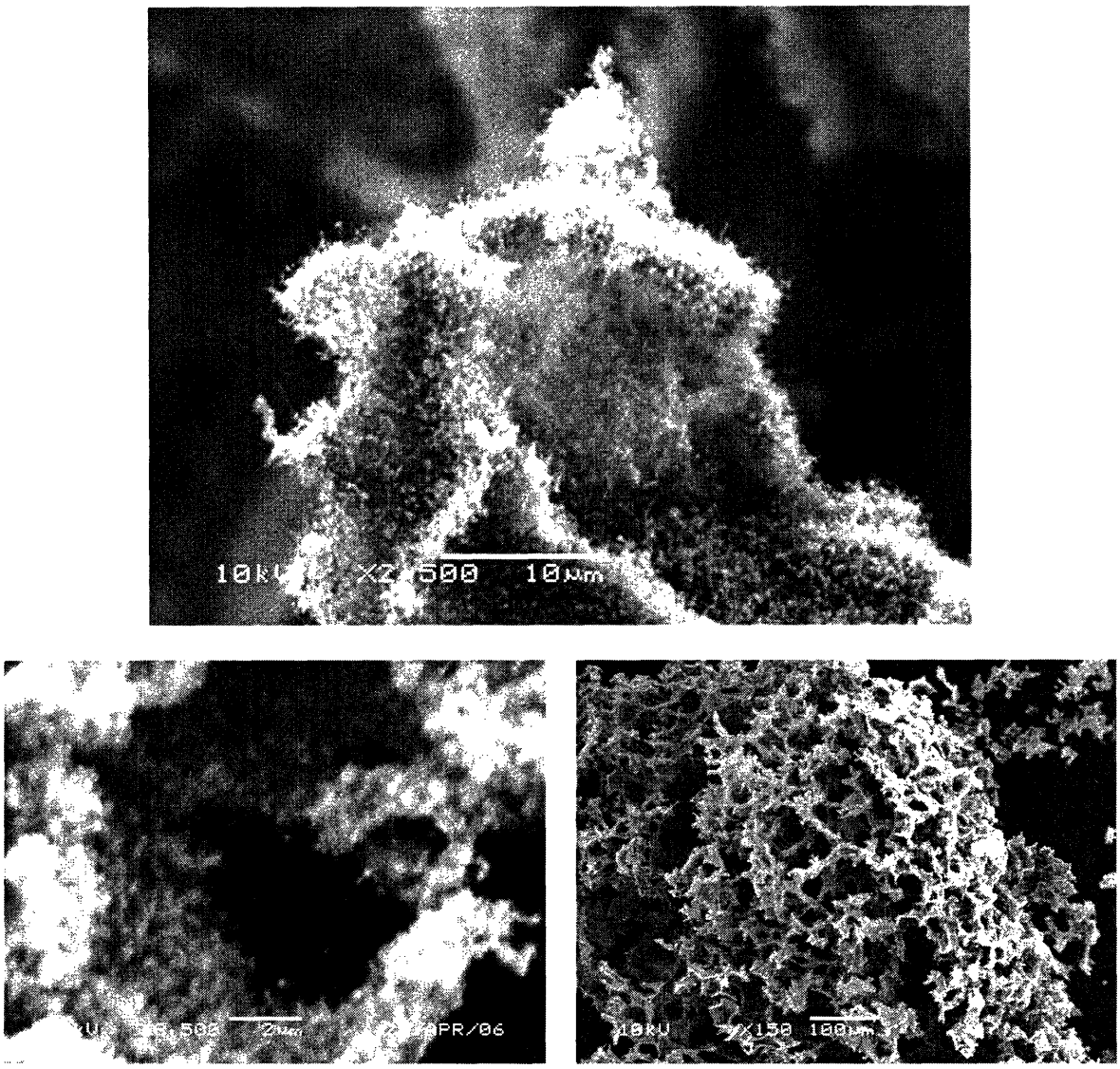

Figure 3-4 Results of standard CVD growth on Fe-doped stratoporous carbon aerogels. High yields of carbon nanotubes are observed on exterior features of the monolith (top), however beyond a depth of 0.2 mm into the monolith, the nanotube yield diminishes greatly (bottom left). At the very center of the monolith, no growth of any kind is observed (bottom right).

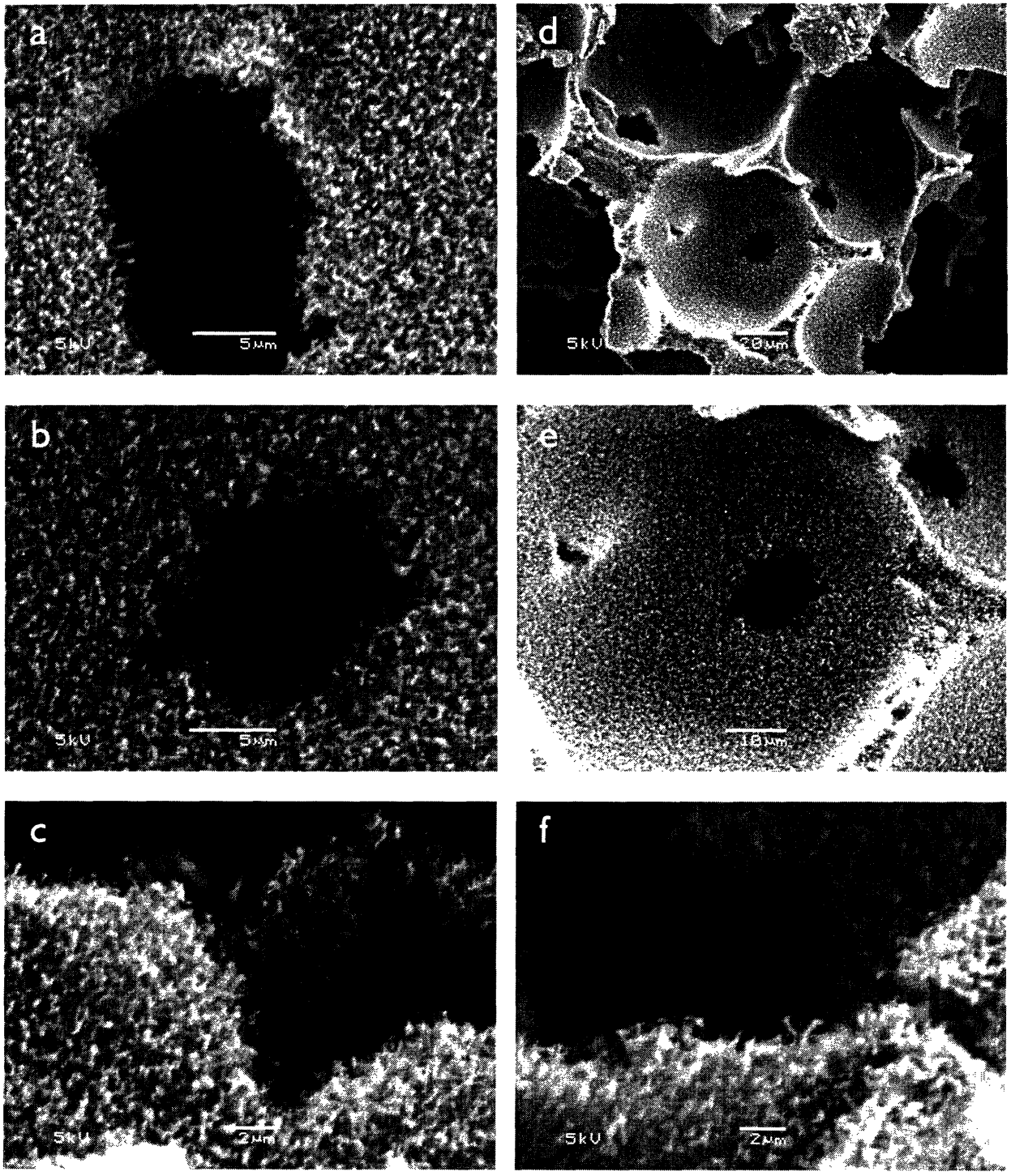

Figure 3-5 Results of infusion CVD growth on Fe-doped stratoporous carbon aerogels. *(a)* Nanotube growth on the top of the monolith; *(b)* nanotube growth 0.5 cm into the center of a monolith cross-section; *(c)* nanotube growth on the underside of the monolith in contact with the quartz process tube during growth; *(d)* texturing of macroporous cells due to nanotube growth; *(e)* detail of *d*; *(e)* interior nanotubes of varying diameters.

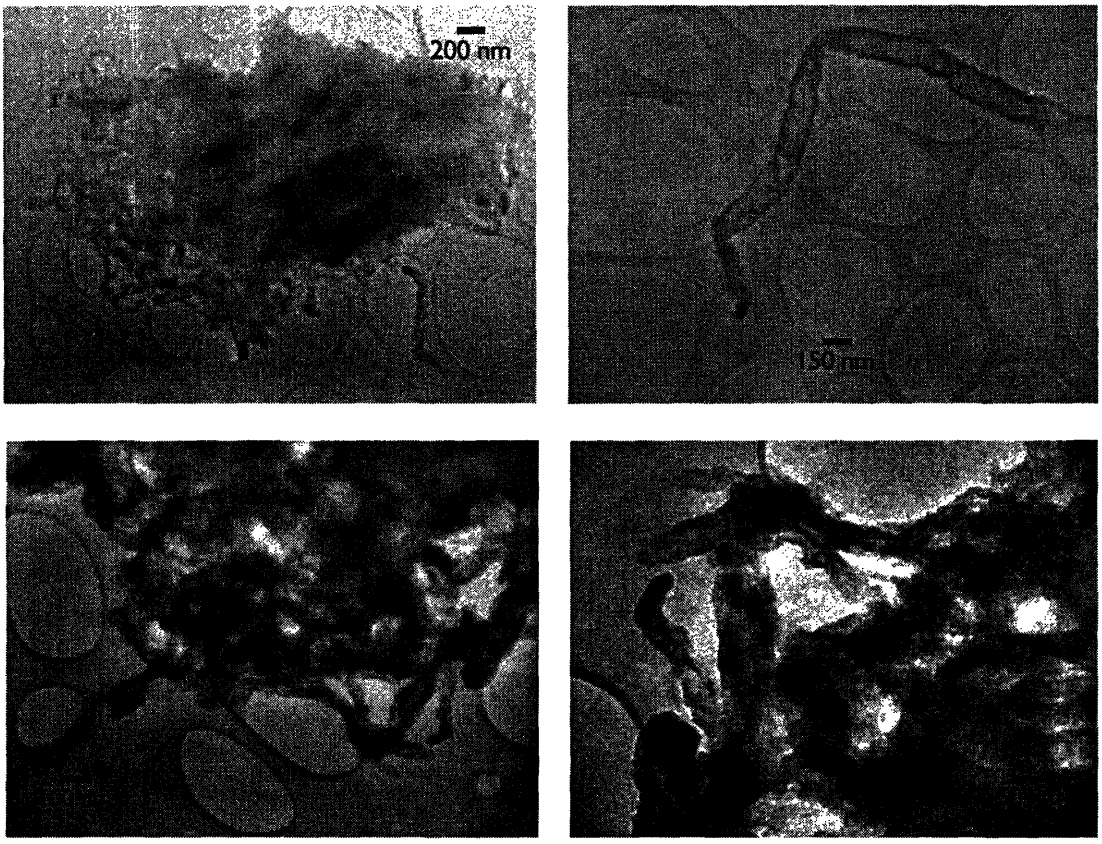

Figure 3-6 TEM surveys of interior cores from Fe-doped stratoporous carbon aerogels processed by infusion CVD. Clusters of defective, multiwall nanotubes and carbon fibers stemming out from masses of carbon aerogel are observed.

Conclusions

When used in combination with infusion CVD growth, macropore templating is an effective way of accessing a higher percentage of an Fe-doped carbon aerogel's catalytic nanoparticles for carbon nanotube growth without having to powderize the material. The larger particles in the aerogel were found to generate very large diameter, defective multiwall carbon nanotubes and carbon fibers. Although in this investigation nanotubes within the interior porosity were fairly short (about 2 μm due to exhaustion of CVD feedstock), this could conceivably be overcome. Performing a step-wise growth process in which low-temperature gas infusion and CVD are repeated several times in succession, in effect resupplying the interior porosity of the monolith with feedstock gas each cycle, could allow nanotube growth to continue. Reinitiation of nanotube growth has been successfully

demonstrated on untemplated Fe-doped carbon aerogels and would likely succeed with stratoporous monoliths as well.

In addition to facilitating CVD within the confined porosity of the monolith, stratoporous Fe-doped carbon aerogels show potential for use as precursors for other materials and for use as high-surface-area electrodes. The improved mean free path of diffusion facilitated by the macroporous network would also enhance mass transport of ions in an electrolytic capacitor, for example. It could also enable atomic layer deposition (ALD) or CVD of metal throughout the porosity of a bulk carbon aerogel monolith for producing bulk monolithic nanoporous metal substrates. Bulk nanoporous metals would be of tremendous value as electrodes, heterogeneous catalysts in catalytic converters, and rapid release hydride-based hydrogen storage substrates.

Although it is possible to achieve coverage of nanotubes through the entire interior using these techniques, the most notable disadvantage to stratoporous aerogels produced in this investigation is their delicacy and tendency to crush easily. Cross-linking of the polymer gel precursor could potentially mitigate this problem.

3.3 Doping of Carbon Aerogels With Prefabricated Monodisperse Nanoparticles

Every Fe-doped carbon aerogel-carbon nanotube composite investigated thus far has only exhibited growth of multiwall carbon nanotubes ranging in quality. One method of increasing the specific surface area of carbon aerogel-carbon nanotube composites would be to induce growth of single-wall carbon nanotubes instead. Doing so would also produce a material more appealing for physical analysis and better suited for *in situ* process monitoring by Raman spectroscopy.

The critical parameter which must be controlled in order to generate single-wall carbon nanotubes instead of multiwall carbon nanotubes is diameter the of the nanoparticles in the aerogel [56, 68]. The non-deterministic nature of coarsening-based nanoparticle production via pyrolysis of metal-doped carbon aerogels

complicates control over nanoparticle diameters by merely adjusting process parameters. As a result, a different technique for controlling the diameter of nanoparticles in the aerogel may be required.

One possibility would be to prefabricate monodisperse iron-containing nanoparticles and to form a gel around them (Figure 3-7). Production of monodisperse nanoparticles is routinely done through the inverse micelle technique. Liu *et al.* demonstrated a procedure for synthesizing monodisperse, small-diameter (5 nm) water-soluble Fe_3O_4 nanoparticles [84] which could be potentially integrated into a standard resorcinol-formaldehyde polymerization reaction easily [44, 45]. *In situ* carbothermic reduction of such particles by the surrounding carbon aerogel structure could then result in monodisperse metallic iron nanoparticles throughout the carbon aerogel.

Metallic iron monodisperse nanoparticles have also been made [85, 86], but must be synthesized in a high-boiling-point solvent such as dioctyl ether and thus require hydrophobic surfactants to solubilize. As a result, such nanoparticles are not soluble in water or polar organics which are required for phenolic resin polymerizations to proceed.

In this study, a technique for producing monodisperse nanoparticle-carbon aerogel composites is demonstrated, providing an alternative technique to ion exchange for doping carbon aerogels with metals. These composites are then evaluated for their ability to grow carbon nanotubes and, more specifically, single-wall carbon nanotubes.

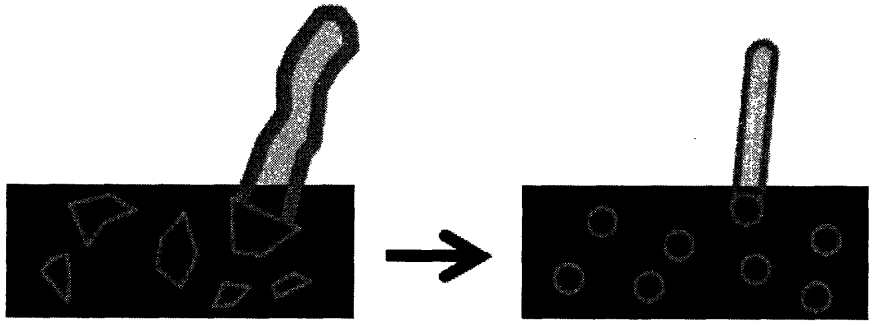

Figure 3-7 Schematic representation of experiment goals.

3.3.1 Materials and Methods

Synthesis of Monodisperse Fe_3O_4 Nanoparticles [84]

Magnetic Fe_3O_4 nanoparticles were prepared by slow addition of aqueous $FeCl_2$ (2 g dissolved in 5.0 mL 2 M HCl) to an aqueous solution of $FeCl_3$ (3.2 g $FeCl_3$ in 20.0 mL 2 M HCl) at room temperature. The solution was then stirred vigorously for 30 min followed by dropwise addition of 30.0 mL NH_4OH (28% in water). The resulting precipitate was centrifuged and the supernatant decanted to afford Fe_3O_4 nanoparticles. The particles were then mixed with an aqueous solution of tetramethylammonium hydroxide (20.0 mL, 25% w/w) which served as a surfactant to stabilize the particles in water by repulsive double-layer interactions. Nanoparticles produced through this method were determined to be ~6-10 nm in diameter by imaging with TEM.

Preparation of Composite Nanoparticle-Phenolic Gel Precursor

A saturated nanoparticle suspension was prepared by vigorously shaking a vial of nanoparticle-saturated supernatant over excess precipitated nanoparticles and drawing off the liquid component which resulted. Resorcinol (0.207 g, 1.88 mmol), formaldehyde (0.298 g of 37% w/w aqueous solution, 3.68 mmol), and K_2CO_3 (2.6 mg, 0.0188 mmol) were then added to 10.0 g of this suspension with stirring. Within a few minutes of mixing, the solution became a dark yellow-green color which transitioned to cola-brown. The solution was allowed to stir for 24 h after which it was sealed in 1.8-mL plastic cryovials and placed in a drying oven at 80°C for 3 d to thermoset. After 3 d, the gels were then removed from their cryovials, sliced into discs, and placed under acetone. Solvent exchange into acetone was then performed over the course of 3 d to make the gel liquor compatible for exchange and subsequent supercritical extraction with carbon dioxide.

Supercritical Drying

Gels were placed in a supercritical extractor and soaked under liquid carbon dioxide (5.2 MPa and 15°C) for 2 d, with the extractor flushed through with fresh liquid carbon dioxide every 6 h. Once the gels were sufficiently diffused through

with liquid carbon dioxide, the vessel was heated past the critical point of carbon dioxide (31.1°C and 7.38 MPa) at a rate of 1°C per min to a temperature of 50°C and pressure of 9.65 MPa. The vessel was allowed to remain at these conditions for 1-2 h followed by isothermal depressurization below the critical point of carbon dioxide over the course of ~1 h. At this point the vessel was allowed to cool and depressurize to ambient conditions over the course of ~1 h. The newly formed nanoparticle-doped phenolic aerogels were then removed from the vessel.

Pyrolysis and Chemical Vapor Deposition

Nanoparticle-doped aerogels were placed in a 1-cm diameter by 2.5-cm segment of quartz tubing and inserted into the middle of a 2.5-cm diameter by 30.0 cm quartz process tube. Ar was then flowed through the tube at a rate of 200 sccm for 20-40 minutes to remove as much air from the mesoporosity of the aerogel as possible. The tube was then placed into a clamshell furnace preheated to a temperature of 900°C. Upon opening, the furnace temperature would drop by 50-100°C. A target temperature of 800°C was then set on the furnace temperature controller and attained within 2-3 m. The aerogel was maintained at this temperature for a period of time ranging from 10-30 minutes during which carbonization of the polymer framework occurred. At this point the monolith was optionally taken out of the furnace, allowed to cool, and removed from the quartz tube for CVD at a later time. Alternatively, the sample was left in the furnace and CVD growth of carbon nanotubes was immediately initiated. Prior to CVD, the furnace temperature set point was adjusted to 700°C, at which point the furnace was opened to allow rapid cooling to that temperature. CVD was then performed by flowing a mixture of 500 sccm H_2, 30 sccm CH_4 and 20 sccm C_2H_4 over the aerogel at 700°C for 10-25 minutes. Upon completion of the CVD process, the tube was taken out of the furnace and placed under a flow of 500 sccm Ar until cool. Samples are denoted by a part number with the format "FeNPxxxx/aa-yyyy/bb", where "xxxx" is the temperature at which the aerogel was pyrolyzed, "/aa" is the length of the pyrolysis in minutes, "yyyy" is the temperature at which CVD was performed, and "/bb" is the length of the CVD in min.

Characterization

High-resolution scanning electron microscopy was performed with a JEOL 6320 operating at 5 kV. High-resolution transmission electron microscopy of metal-doped carbon aerogels and derived nanotube composites was performed on a JEOL JEM-200CX operating at 200 keV. XPS spectra were obtained on an AXIS HIS 165 and ULTRA Spectrometer (Kratos Analytical Limited, England) using Al K radiation (energy = 1486.6 eV) in a vacuum of 5 x 10^{-9} torr. Samples were prepared by grinding into a fine powder, adhering to adhesive copper tape, and mounting the copper tape on a sample holder using double-sided adhesive carbon tape. X-ray slots of 750 by 350 μm, an X-ray power of 150 W (15 kV and 10 mA), and a pass energy of 20-80 eV (dependent on the metal being analyzed) were used. Density was calculated by dimensional analysis of monolithic aerogel discs.

3.3.2 Results

Fe_3O_4 nanoparticle-doped carbon aerogels were measured to be significantly denser (0.78 g cm^{-3}) than undoped carbon aerogels prepared with the same concentration of resorcinol and formaldehyde (~0.30 g cm^{-3}). Additionally, a substantial densification over the unpyrolyzed monoliths (0.43 g cm^{-3}) is observed. Figure 3-8 shows TEM images from unpyrolyzed nanoparticle-doped phenolic aerogels. The mesoporosity inherent to true carbon aerogels is absent in these materials. Instead, clusters approximately 50-150 nm in diameter are joined together to form macroporous voids. This type of morphology for carbon aerogels is known to occur when the pH of the phenolic resin polymerization is very alkaline. In this system, tetramethylammonium hydroxide (TMAH) used to stabilize the Fe_3O_4 nanoparticles apparently raises the pH of the reaction solution and drives the polymerization towards a densified, macroporous morphology instead of a low-density, intrinsically mesoporous structure. Although such a morphology exhibits a lower specific surface area (~300-400 m^2 g^{-1} instead of 700-800 m^2 g^{-1}) [7], it is not without its advantages. The densified structure is many times stronger than a mesoporous nanoarchitecture and thus would be expected to have better electrical conductivity [46]. Within the scope of this study, the macroporous composites are

suitable for proof-on-concept growth of nanotubes on carbon aerogels, but for optimizing carbon aerogel-carbon nanotube composite surface area, a mesoporous nanoarchitecture is desirable. It is unclear whether the nanoparticle double-layer itself is responsible for raising the reaction pH during polymerization of the gel precursor or whether it is due to the presence of excess TMAH in solution with the nanoparticles. In the former case, a mesoporous material could be produced by offsetting the increase in pH resulting from the nanoparticles during polymerization or using dilute solutions of nanoparticles. In the latter case, a mesoporous material could be produced by removing excess TMAH. A third option would be to utilize a different ligand for solubilizing the nanoparticles, which may be more difficult.

Varying pyrolysis and CVD growth times were attempted for the nanoparticle-doped samples. Table 3-2 lists a few representative preparation conditions surveyed. It was quickly determined that pyrolysis times comparable to those used for the ion-exchanged materials (6-10.5 h) were much too long for successful growth using these composites. CVD growth on composites pyrolyzed for 10.5 h showed virtually no growth of carbon nanotubes, with the exception of a few large-diameter fibers. The reasons for this are believed to be two-fold. First, pyrolysis-induced particle coarsening is not necessary (nor desirable) optimally-sized nanoparticles are already present in the aerogel before pyrolyzing. Secondly, the iron in the ion-exchanged materials starts in the 3+ state (effectively Fe_2O_3) which requires carbothermic reduction to the metallic state before catalytic growth of nanotubes can be observed. Iron in Fe_3O_4 is in a mixed valence state of 3+ and 2+, also requiring carbothermic reduction to the metallic state in order to be rendered catalytically active. For the carbothermic reduction of Fe_2O_3, Fe_3O_4, and FeO to metallic iron, the change in free energy is calculated to be [79]:

$$2Fe_2O_3 + 3C \rightarrow 4Fe + 3CO_2 \quad \Delta_f G_{800°C} = 312.9\ \text{kJ/mol Fe} \tag{3-1}$$

$$Fe_3O_4 + 2C \rightarrow 3Fe + 2CO_2 \quad \Delta_f G_{800°C} = 290.1\ \text{kJ/mol Fe} \tag{3-2}$$

$$2FeO + C \rightarrow 2Fe + CO_2 \quad \Delta_f G_{800°C} = 219.5\ \text{kJ/mol Fe} \tag{3-3}$$

$$3Fe + C \rightarrow Fe_3C \quad \Delta_f G_{800°C} = -485.7\ \text{kJ/mol Fe} \tag{3-4}$$

which shows Fe_3O_4 is more easily reduced to metallic iron than Fe_2O_3. Thus, to avoid carburization of nanoparticles in these composites, a shorter pyrolysis is required.

Sample Part Number	Pyrolysis Time (800°C)	Length of CVD Process (700°C)	Nanotube Growth?
FeNP-800/630-700/10	10.5 h	10 min	Low yields, highly defective, large diameter NT
FeNP-800/30-700/10	30 min	10 min	High yields, short defective NT, some carbon fibers
FeNP-800/10-700/25	10 min	25 min	Low yields, multi-micron high quality NT

Table 3-2 Summary of process parameters and CVD results for select Fe_3O_4 nanoparticle-doped carbon aerogel samples.

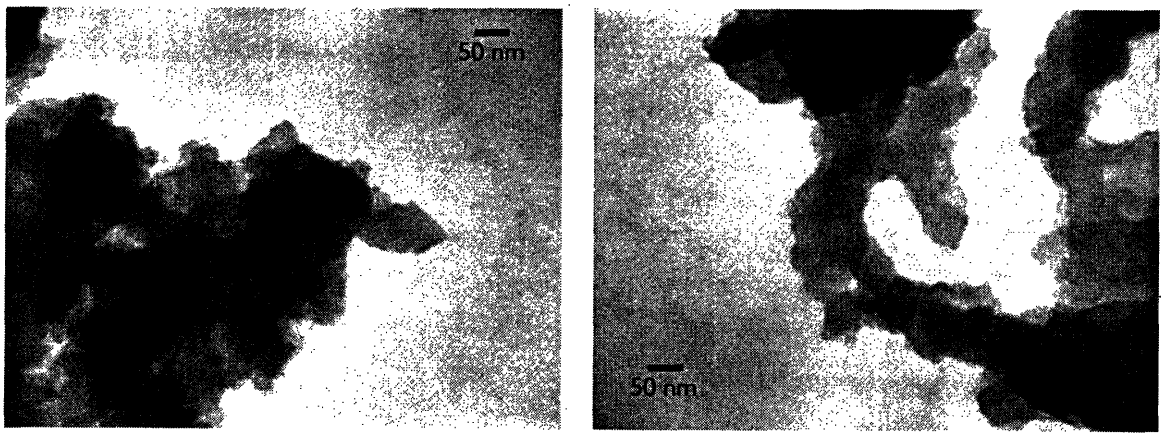

Figure 3-8 TEM images of Fe_3O_4 nanoparticle-doped phenolic aerogels revealing densified, macroporous networks of particles instead of a mesoporous nanoarchitecture.

It was ascertained that pyrolysis times on the order of 30-60 min were sufficient to prepare a sample for nanotube growth. Figure 3-9 shows SEM images from 10-minute CVD growth on samples pyrolyzed for 30 min. A modest population of short nanotubes is observed across the surface of the sample, with occasional large-diameter fibers. These fibers are believed to originate from areas containing large clusters of nanoparticles, resulting from either particle coarsening during pyrolysis or magnetic clustering of the nanoparticles while in solution. The presence of carbon nanotubes is verified under TEM (Figure 3-10), however the nanotubes observed are multiwalled as opposed to single-walled and are fairly defective.

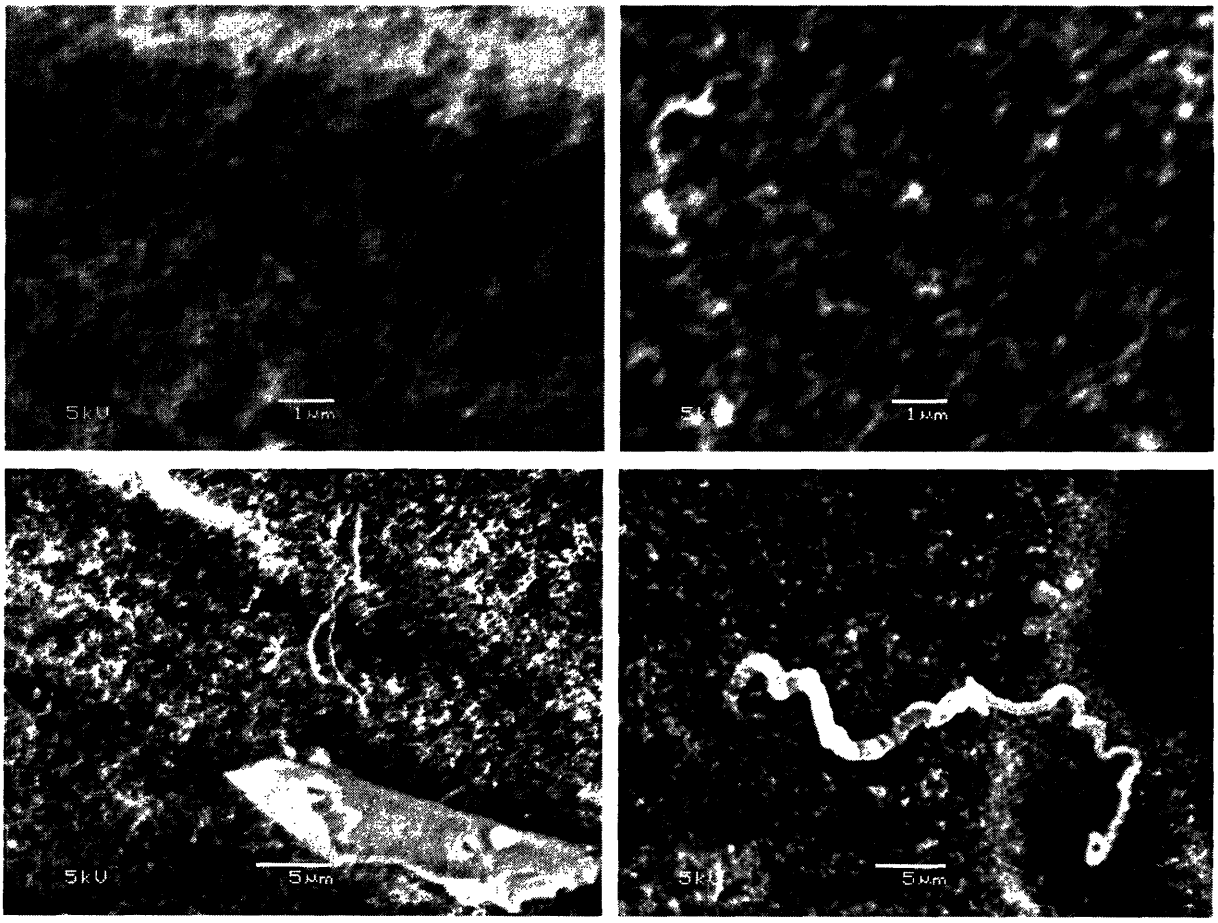

Figure 3-9 SEM images of Fe800/30-700/10. Nanotubes ~1 µm long are observed over most of the sample, with occasional 0.5-1 µm diameter fibers observed. The fibers are believed to originate from clusters of nanoparticles embedded in the aerogel.

To determine if even shorter pyrolysis times would be advantageous, samples pyrolyzed for only 10 min immediately followed by CVD (without cooling down) were investigated. Very long (20-50 μm), curly nanotubes are observed, however present only in extremely low yield. Figure 3-11 shows SEM images from samples pyrolyzed for 10 min after a 25-minute CVD growth. TEM imaging (Figure 3-12) verified the observed structures were in fact nanotubes, however diffraction from the edges of the tubes again revealed them to be multiwalled. A number of remarkable, unexpected nanostructures are observed in these samples, including "nanoropes" comprised of two uniformly intertwined multiwall carbon nanotubes extending for over 25 μm (Figure 3-12) and a graphitic "nanobox" with sides ~300 nm by 300 nm (Figure 3-13). Agglomerations of nanoparticles (Figure 3-13) are still observed in these samples despite only being at elevated temperatures for 35 min. It is thus concluded that particle agglomeration observed in this system is not attributable to kinetic particle coarsening, but rather to solution-phase magnetic clustering of the nanoparticles. Nanocrystallites are observed across the surface as well, possibly composed of iron oxide or iron oxyhydroxide.

3.3.3 Discussion

Although the target objective of developing a methodology for growing single-wall carbon nanotubes on a carbon aerogel was not attained in these experiments, a number of other important discoveries were made. The nanorope structures observed in FeNP800/10-700/25 samples are appealing nanostructures for mechanical applications involving carbon nanotubes. Based on observations of nanoparticles in the heads of the nanoropes observed under TEM, is believed that these ropes result when exactly two catalytically-active nanoparticles are joined together at a single connection point but are still differentiable as two nanoparticles. During CVD, the nanotubes extruded from these nanoparticles are brought together by van der Waals interactions and remain intertwined as growth continues. The observed clustering of the nanoparticles due to magnetization in solution which was detrimental for forming small-diameter nanotubes may be an advantageous feature

in the preparation of such dimeric particle clusters for intentional nanorope production.

The varying degrees of success for nanotube growth observed for different processing parameters provide additional evidence in pin-pointing the nature of the experimental conditions necessary to render iron-based catalysts catalytically active towards nanotube growth. For example, the observation of successful growth of long carbon nanotubes on FeNP800/10-700/25 but only in extremely low yields contrasted against the high yields of short nanotubes observed for FeNP800/30-700/x samples provides useful indirect evidence of the role of carbothermic reduction in rendering nanoparticles catalytic.

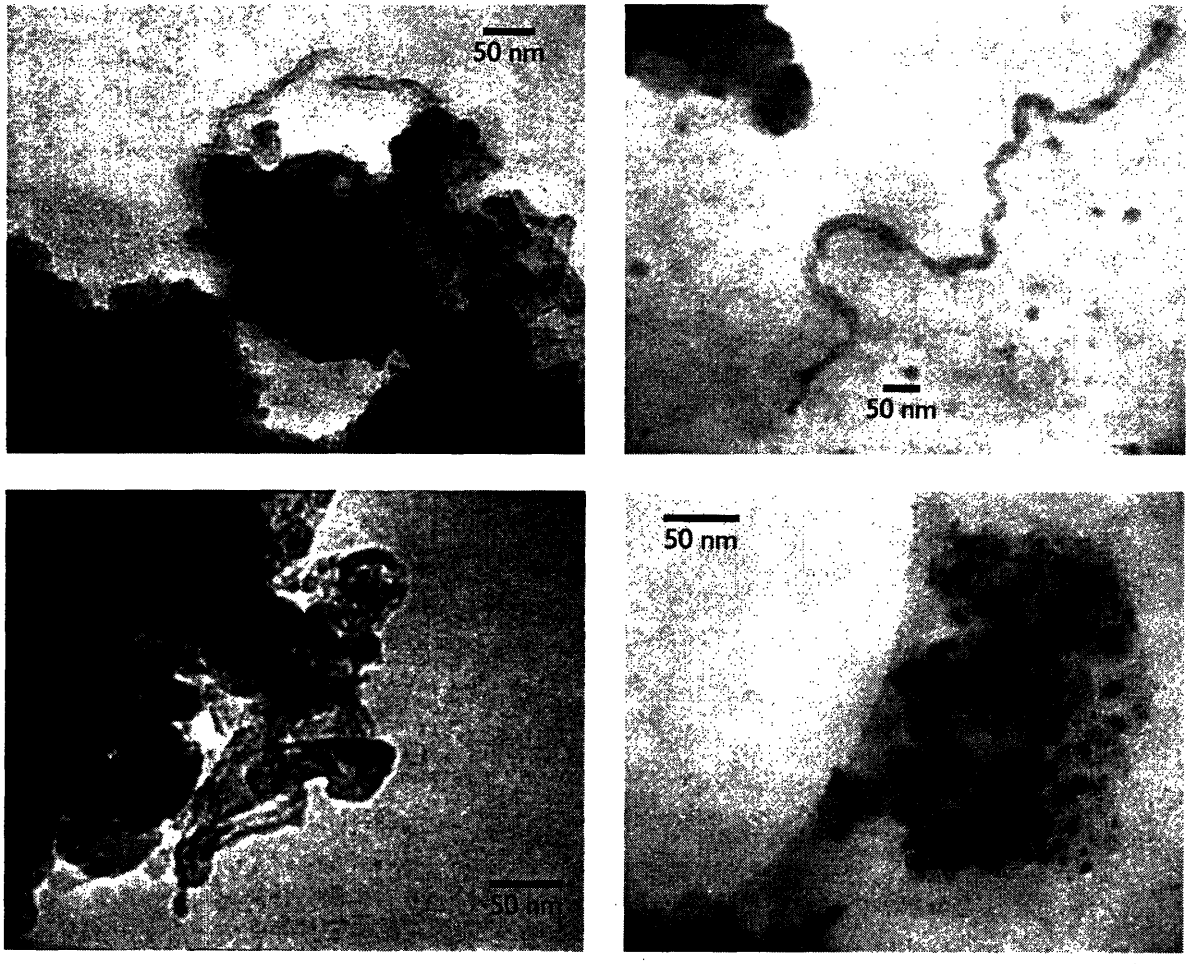

Figure 3-10 TEM images of FeNP-800/30-700/10; *(top and bottom left)* defective, multiwall nanotubes extending out from carbonized aerogel; *(top right)* wayward multiwall nanotube ~1 μm long; *(bottom right)* undesired agglomerations of nanoparticles embedded in the aerogel.

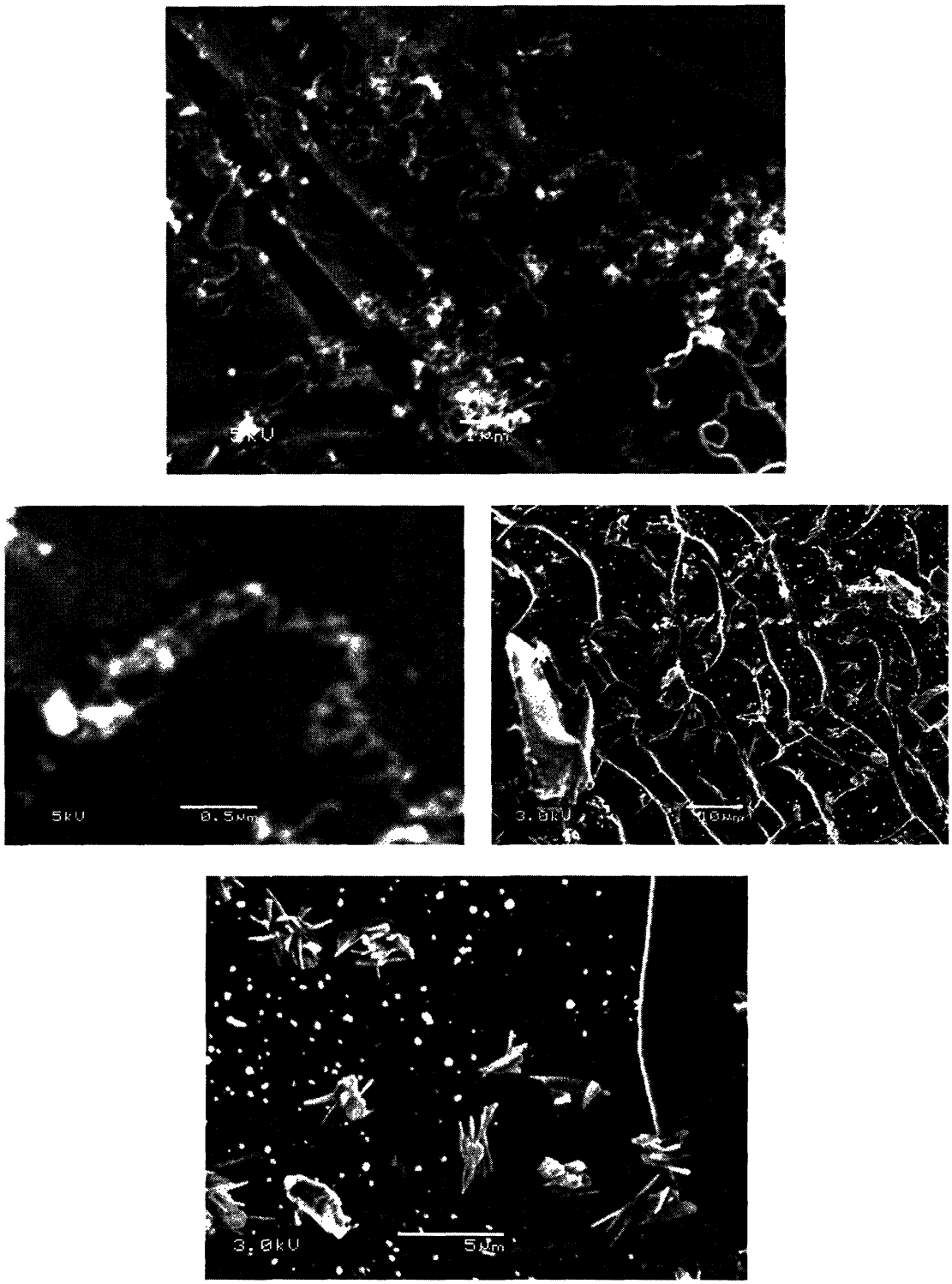

Figure 3-11 SEM images of FeNP800/10-700/25. Long nanotubes are observed at various locations on the aerogel *(top, middle left)*. However most of the surface is barren *(middle right)*. Crystalline microstructures, assumedly comprised of iron oxide or iron oxyhydroxide, are also seen *(bottom)*.

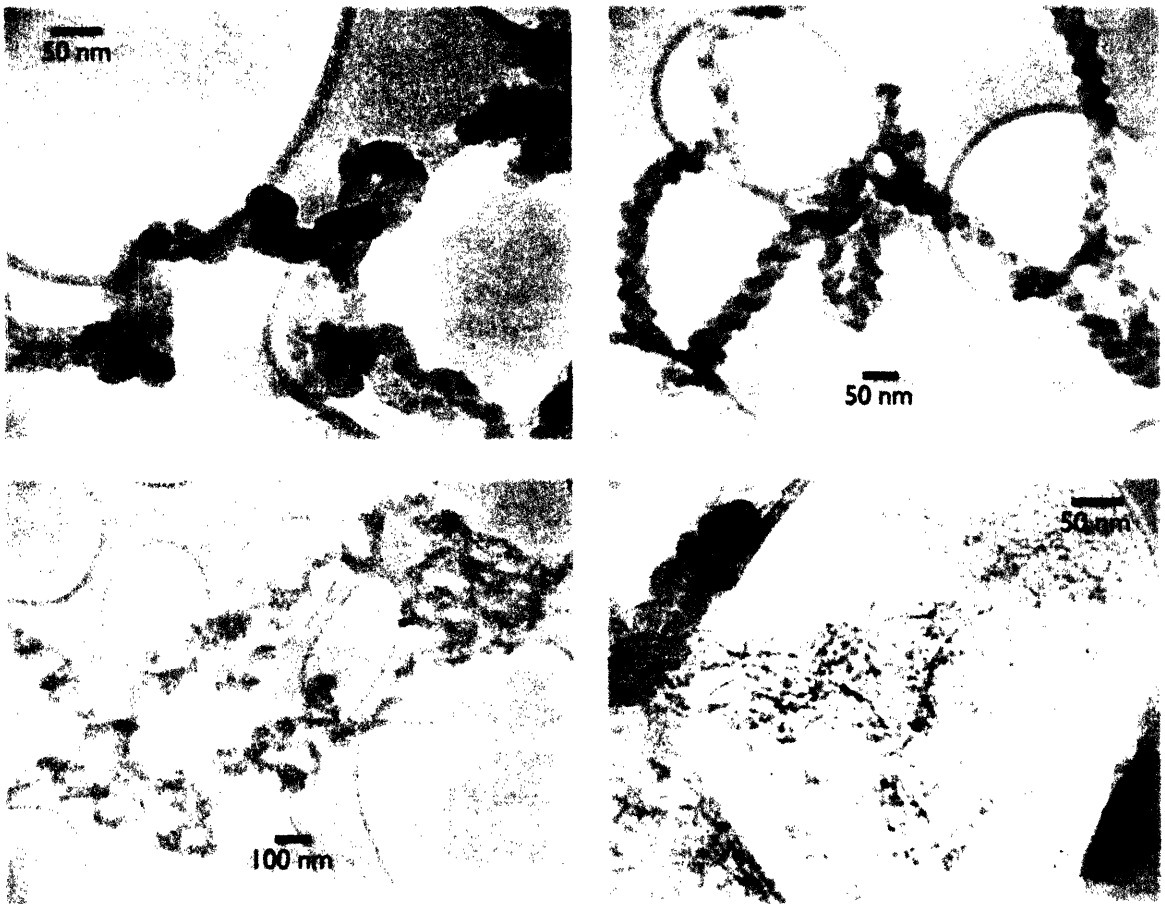

Figure 3-12 TEM images of FeNP800/10-700/25. The long, curly nanotubes observed under SEM are verified here to be multiwall carbon nanotubes ~25 nm in diameter *(top left)*. A number of remarkable "nanoropes", composed of two uniformly intertwined multiwall carbon nanotubes, are found as well *(top right, bottom left)*. Webs of smaller fibers, possibly single-wall carbon nanotubes, were found near the head of one of the nanoropes *(lower right)*.

The pairing of long nanotube length at the expense of yield (and conversely, large yields of nanotubes at the expense of length) has been observed in research involving ferritin-based nanoparticle catalysts performed in our group [40]. This research involves the growth of long (millimeter-length scale) nanotubes employing ferritin-derived nanoparticles (see Figure 3-14). In a typical procedure, a silicon wafer is soaked in a solution of ferritin, dried, and oxidized at 900°C for a period of time to remove the organic component of the ferritin and anneal the remaining iron into nanoparticles. If this oxidative process is omitted, CVD results in very high yields of short nanotubes. If this oxidative process is performed for 5 minutes, CVD

results in growth of millimeter-long nanotubes, however in very low yield. If this oxidative process is followed by a reductive hydrogen treatment (400 sccm H_2 and 600 sccm Ar at 700°C for 10 min), CVD again results in very high yields of short nanotubes. Other groups which use a reductive pre-treatment have reported enhanced yields in doing so as well [43, 75].

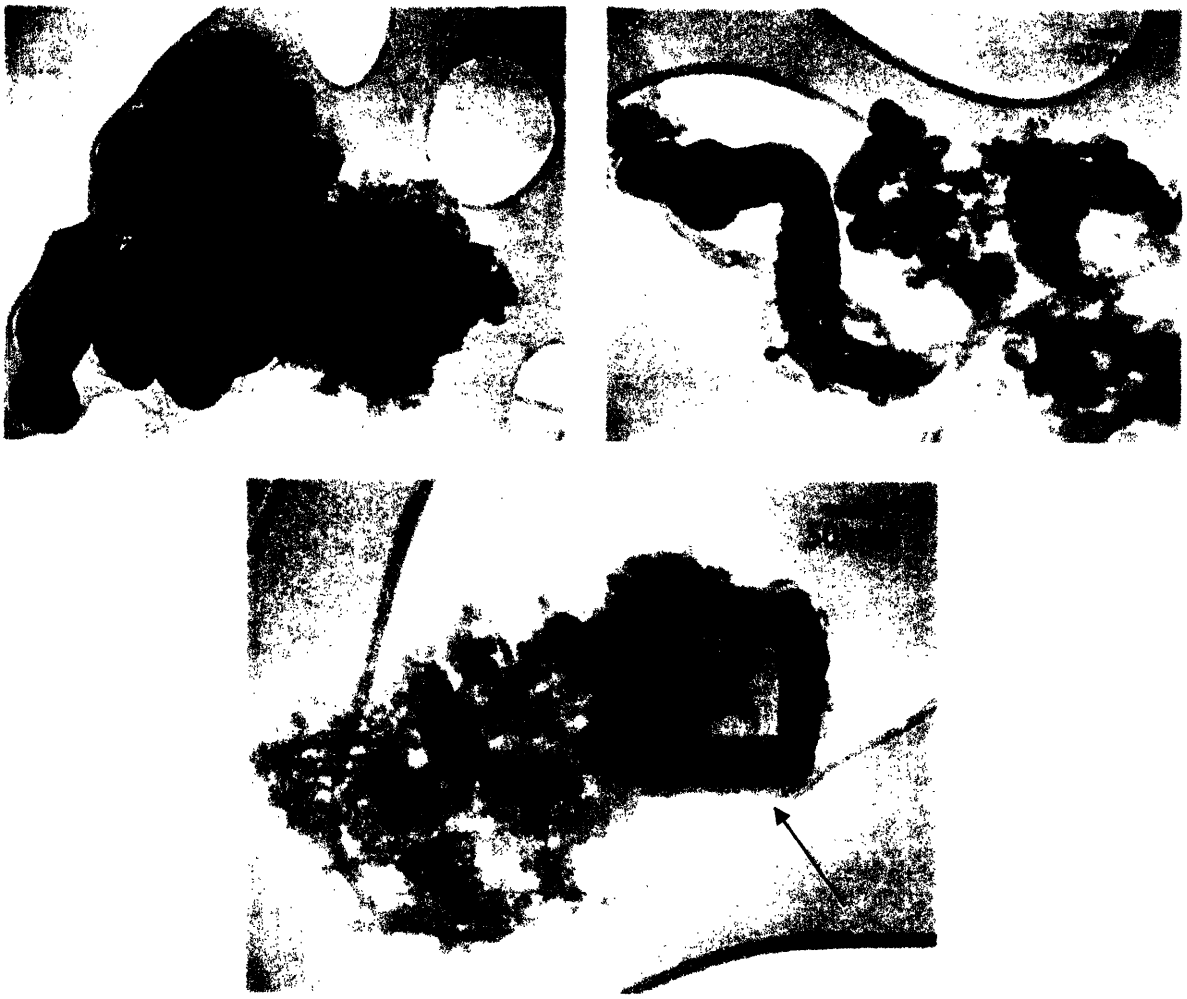

Figure 3-13 Additional TEM images of FeNP800/10-700/25. Agglomerated clusters of Fe_3O_4 nanoparticles of varying size, likely due to solution-phase magnetic clustering, are found throughout the sample *(top left)*. As a result, nanotubes of varying diameters result *(top right)*. A number of other carbon nanostructures including graphitic shells *(also seen in top right)* and a graphitic "nanobox" *(bottom)* are also observed.

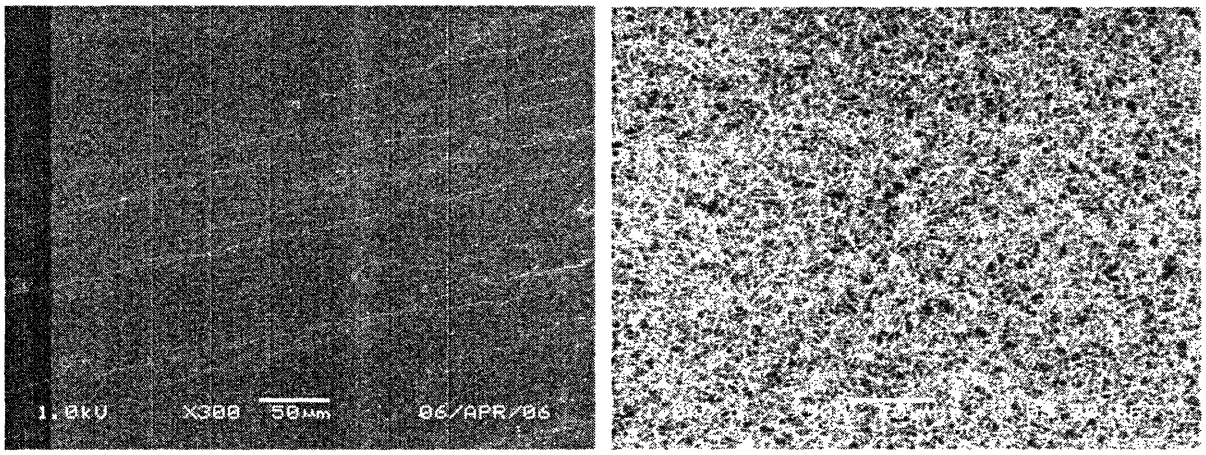

Figure 3-14 Oxidation of ferritin-derived nanoparticle catalysts prior to CVD enables long nanotube growth at the expense of yield *(left)*; following oxidation, a reductive process prior to CVD activates virtually every nanoparticle on the surface but at the expense of length *(right)*. *(Results courtesy of Alfonso Reina, MIT. Used with permission.)*

The following is a proposed model which unites these results with those observed for CVD growth of nanotubes on Fe_3O_4 nanoparticle-doped carbon aerogels and Fe-doped carbon aerogels.

In the Fe_3O_4 nanoparticle-carbon aerogel composite system, pyrolysis of the composite represents carbothermic reduction. After a short pyrolysis, some of the nanoparticles are perfectly reduced to metallic iron without excess carbon and will thus experience long catalytic lifetimes. Most of the nanoparticles, however, have only been partially reduced and are not yet catalytically active. Increasing the duration of the pyrolysis results in the reduction of a greater number of nanoparticles to the metallic state, but also enables more time for diffusion of carbon into the nanoparticles. As a result, these particles are sensitive to carbon formation upon diffusion of additional carbon during CVD and thus experience a shorter catalyst lifetime. The product of this scenario is a few, long nanotubes from CVD on samples pyrolyzed for short lengths of time, and high populations of short nanotubes from CVD on samples pyrolyzed for longer lengths of time. As the length of the pyrolysis treatment tends towards infinity, complete carburization of nanoparticles in the aerogel results, in which case all of the nanoparticles are rendered catalytically inactive. This corroborates with the observed extremely low nanotube yield after CVD on nanoparticle-aerogel composites pyrolyzed for 10.5 h.

The in Fe-doped carbon aerogels investigated in Chapter 2, an increase in carburization was associated with a reduction in nanotube yield. It has been suggested that in CVD growth of nanotubes [41] and in heterogeneous catalysis systems similar to CVD growth of nanotubes [42] that carbides are associated with inactive catalyst particles. In the case of carbon nanotube growth, there are two reasons why carbides are probably not active catalyst species. First, carbides are also not known to be particularly catalytic towards dehydrogenation reactions [87, 88]. Secondly, diffusion of carbon through the ceramic metal carbide lattice is just too slow at CVD growth temperatures to facilitate the mechanisms required for diffusion, nucleation, and precipitation of carbon in nanotube growth [88]. Under the right circumstances, however, metal carbide nanoparticles may be capable of decomposing into a mixture of metal carbide and carbon-saturated metal which could then allow for precipitation of a crystalline carbon nanotube [41, 89], or potentially be oxidized back to a catalytic metallic state by oxidizing agents.

A similar argument can be made for iron oxides in that the diffusion of carbon through the covalently-bonded metal oxide lattice is impractically slow to enable a nanotube growth mechanism without at least partial reduction of the nanoparticle to introduce defect sites which can enhance diffusion of carbon into the nanoparticle. Evidence of this may be demonstrated by the Fe-doped carbon aerogels investigated in Chapter 2, in which aerogels with high oxide/oxyhydroxide content did not successfully catalyze nanotube growth at any CVD growth temperature. It should be noted that metal oxides may also serve in the role of dehydrogenation catalysts [90], but again the presence of defects are important even in this capacity to facilitate charge transfer from the catalyst to incoming substrate molecules. Again, oxides can be intentionally reduced with hydrogen, hydrocarbons, or carbon either before or during CVD to produce catalytic nanoparticles. Oxygen present in partially-oxidized nanoparticles also will help fight carburization, if this is indeed an undesirable mechanism. The combination of the ability to dehydrogenate feedstock gases and to fight carburization makes partial oxidation of catalyst nanoparticles desirable even, but again full oxidation will likely render the nanoparticle uncatalytic.

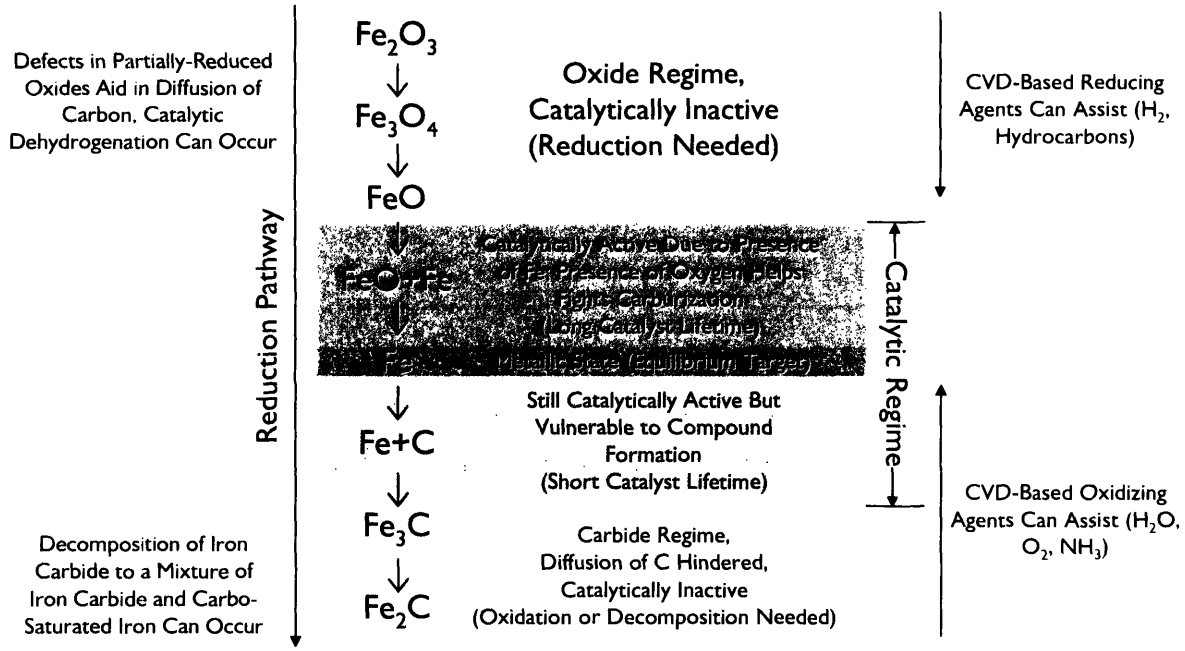

Figure 3-15 Proposed model of chemical state-sensitive nanotube catalyst activity, used to correlate the effects of various catalyst and CVD processing conditions with nanotube growth results. This general concept of this model may extend to other metals as well.

In a deterministic heterogeneous nanotube catalysis system, however, transparent processes such as nanoparticle-enhanced feedstock cracking (dehydrogenation) and *in situ* reduction of nanoparticles to a catalytic state would be well characterized, intelligently controlled, and non-statistical in nature. The rich chemistry of iron, cobalt, and nickel facilitates the tendency for a range of chemical states to emerge among catalyst nanoparticles, each of which may contribute to the overall CVD growth of nanotubes in a different way (such as by facilitating feedstock cracking, diffusion of carbon into the nanoparticle, nucleation of graphite, combating catalyst poisoning, etc.). The emergence of these various compositions and the nature of their respective contributions are likely statistical in nature and are certainly not well characterized. Thus, it is proposed that the "ideal" nanotube catalyst would be a material whose sole function is the diffusion, nucleation, and precipitation of crystalline carbon and which would not be susceptible to chemical changes during growth or require a pretreatment for activation that could result in a statistical spread of chemical states among catalyst nanoparticles.

In summary, it is hypothesized that pure iron oxides and iron carbides are not catalytic, although both species play important roles in iron-based heterogeneous catalysis of nanotube growth. The actual catalyst responsible for the nucleation and self-assembly of the carbon nanotube is proposed to be metallic iron. This model should apply to other transition metals as well, particularly cobalt, nickel, and tungsten. Although various chemical states of iron probably play different roles in the overall CVD growth of carbon nanotubes and make iron an excellent catalyst for CVD growth all around, in a purely deterministically-controlled system, iron would not be an ideal catalyst.

The proposed model also fully accounts for the results of carbon nanotube growth on the Fe-doped carbon aerogels discussed in Chapter 2 (in particular the "sweet spot" of processing parameters observed for that system) and is consistent for the results of Iijima [64, 65] and Dai [60] in their demonstrations of long nanotube growth through water- and oxygen-assisted CVD, respectively.

3.3.4 Conclusions

A novel technique for producing nanoparticle-containing carbon aerogel composites was demonstrated and shown to be capable of producing materials which are catalytic towards carbon nanotube growth. This technique is potentially capable of producing nanoparticle-carbon aerogel composites containing nanoparticles of any composition (including nanoparticles with complex stoichiometries), giving it a unique advantage over ion-exchange-based doping of carbon aerogels. Novel nanorope structures arising from the nanoparticle clustering in the aerogel are observed. The length and yield of nanotubes grown using these composites were found to be inversely related and highly sensitive to the length of pyrolysis used to carbonize the aerogel. Results from varying process parameters in this system substantiated results observed for growth of carbon nanotubes on Fe-doped carbon aerogels (Chapter 2) and other reports [43, 70, 75] pertaining to the role of reduction in the preparation of Fe-based nanotube catalysts. A new model for the catalytic activity of iron-based carbon nanotube catalysts is presented.

3.4 Particle Tailoring in Fe-doped Carbon Aerogels

Despite the non-deterministic nature of nanoparticle formation in metal-doped carbon aerogels, it was hypothesized that more thorough exploration of the process parameter space in Fe-doped carbon aerogel production may elucidate conditions where single-wall carbon nanotube growth is favored. In this section, the results of CVD growth on Fe-doped carbon aerogels prepared with 0.001 M $Fe(NO_3)_3$ as opposed to the standard 0.1 M $Fe(NO_3)_3$ used in Chapter 2 are evaluated to determine if reducing the amount of iron present in the aerogel could translate into smaller nanoparticle diameters and thus smaller nanotube diameters.

3.4.1 Effects of Reducing the Doping Level of Fe

3.4.1.1 Experimental

Preparation of Fe-doped Carbon Aerogels

Fe-doped carbon aerogels were prepared as described in Chapter 2 with 0.001 M $Fe(NO_3)_3$ in place of 0.1 M $Fe(NO_3)_3$. Solvent exchange, supercritical drying, and pyrolysis, were all carried out as written. Fe-doped carbon aerogels with varying dopant concentrations are denoted by the part number "FemmmmMxxxx", where "mmmm" is the concentration of the dopant in mol L^{-1} and "xxxx" is the temperature at which the aerogel was pyrolyzed (for 10.5 h). Chemical vapor deposition on Fe0.001M800 monoliths was performed as described in Chapter 2 at a temperature of 700°C under a flow of 20 sccm ethylene, 30 sccm methane, and 500 sccm for 20 minutes. Samples processed by CVD are denoted with an additional part number suffix "-yyyy", where "yyyy" is the temperature at which CVD was carried out, producing the part number "Fe0.001M800-700" for the CVD-processed Fe-doped carbon aerogels discussed in this section.

Characterization

Characterization of the effects of CVD on Fe-doped carbon aerogel monoliths was accomplished through SEM imaging as described in Chapter 2.

3.4.1.2 Results and Discussion

It was initially uncertain whether soaking the precursory K^+-doped phenolic gels in diluted $Fe(NO_3)_3$ would result in a lower level of doping or not since the exact mechanism of the ion exchange technique was unknown. Although it was originally by our group that the mechanism involved a one-time, static incorporation of an iron ion on the gel backbone, it was hypothesized by the author that the role of the potassium carboxylate groups was actually to *limit* attachment of iron ions to the polymer backbone and less to serve binding sites. The justification for this is as follows.

The first attempts at controlling the dopant level in Fe-doped carbon aerogels were made by attempting to control the number of carboxylate groups in the gel. This was done by replacing the 1,3-dihydroxybenzoic acid used in the preparation of the K+-doped phenolic gels with a mixture of resorcinol (which has the same structure as 1,3-dihydroxybenzoic acid minus the carboxylate group) and 1,3-dihydroxybenzoic acid in the ratio desired for tuning the doping level. For example, a target doping level of 1/1000th that typical used would require 1 mmol 1,3-dihydroxybenzoic acid to 999 mmol resorcinol. The amount of K_2CO_3 used to neutralize the acid was then scaled accordingly to prepare the potassium salt of 1,3-dihydroxybenzoic acid.

It was found that when either 100% resorcinol-formaldehyde-derived ("RF") gels or hybrid resorcinol/potassium 1,3-dihydroxybenzoate-formaldehyde-derived ("R/DF") gels were soaked in solutions of 0.1 M $Fe(NO_3)_3$, a millimeter-thick black skin resulted around the perimeter of the gel monolith (indicating that doping had occurred), beyond which no diffusion of iron into the interior of the monolith was observed. Spectrophotometric analysis of the $Fe(NO_3)_3$ solution used to dope the gels after three days of soaking revealed the gels had absorbed 11 times more iron than would be expected if the solution had merely equilibrated its concentration by volume. For 100% dihydroxybenzoate-formaldehyde ("DF") gels, however, soaking of gel monoliths in 0.1 M $Fe(NO_3)_3$ resulted in approximately uniform diffusion of iron throughout the interior of the monolith. In the RF and R/DF gels, phenol groups on the surface of the gel backbone apparently act as strong ligating sites for

incoming Fe^{3+} ions. As a result, an ionic barrier forms and prevents further diffusion of ions into the gel. In the case of the DF gels, potassium carboxylate groups along the surface of the gel backbone serve as weak ligating sites which iron ions can attach to and detach from with an equilibrium rate constant close to unity. The summed effect of the carboxylate groups across the gel surface produces a dynamic "ionic skin" which acts as a diffusion-enhancing mechanism to draw ions throughout the interior porosity of the gel. Once supercritically dried, ions bound to the polymer backbone remain bound. In a mechanism where the carboxylate groups serve as static binding sites for incoming ions, an ionic barrier would be expected to form. As this was experimentally determined not to be the case, it was concluded that DF gels could be doped with an arbitrary concentration of metal ions simply by adjusting the concentration of aqueous metal salt solution used.

Soaking of DF gels in $Fe(NO_3)_3$ of decreasing molarity indeed resulted in gel monoliths of decreasing opacity indicating uniform diffusion of metal ions throughout the gel. Allowing gels to soak in dilute concentrations of $Fe(NO_3)_3$ over the course of several weeks was not found to result in an increase in loading of iron into the gel.

Thus, Fe-doped carbon aerogels derived from gels doped with 0.001 M $Fe(NO_3)_3$ were prepared as described in Section 3.4.1.1. Figure 3-16 shows SEM images after CVD on Fe0.001M800 monoliths for 20 minutes. The results of this growth were in stark opposition to what was originally expected. High yields of short, large diameter carbon fibers—thicker than the structures observed for samples doped with 0.1 M $Fe(NO_3)_3$—are observed over the entire surface of the monolith. Occasional long (~5 μm) multiwall nanotubes, longer carbon fibers (~5 μm), and bundles of curly, small-diameter nanotubes (the intentioned structures) are found as well.

XRD from this sample showed virtually no crystallinity present, with a broad peak centered around 40° two-theta corresponding to a crystallite size of ~2 nm. Taking into consideration all available data, the mean diameter of the fibers observed does not match the size distribution of nanoparticles in the material as best as can be detected by XRD. It is thus assumed that the graphitic fibers are formed

by the collective catalytic activity of many ultrasmall nanoparticles (<1 nm in diameter) in close proximity to one another which together catalyze growth of larger graphitic sheets.

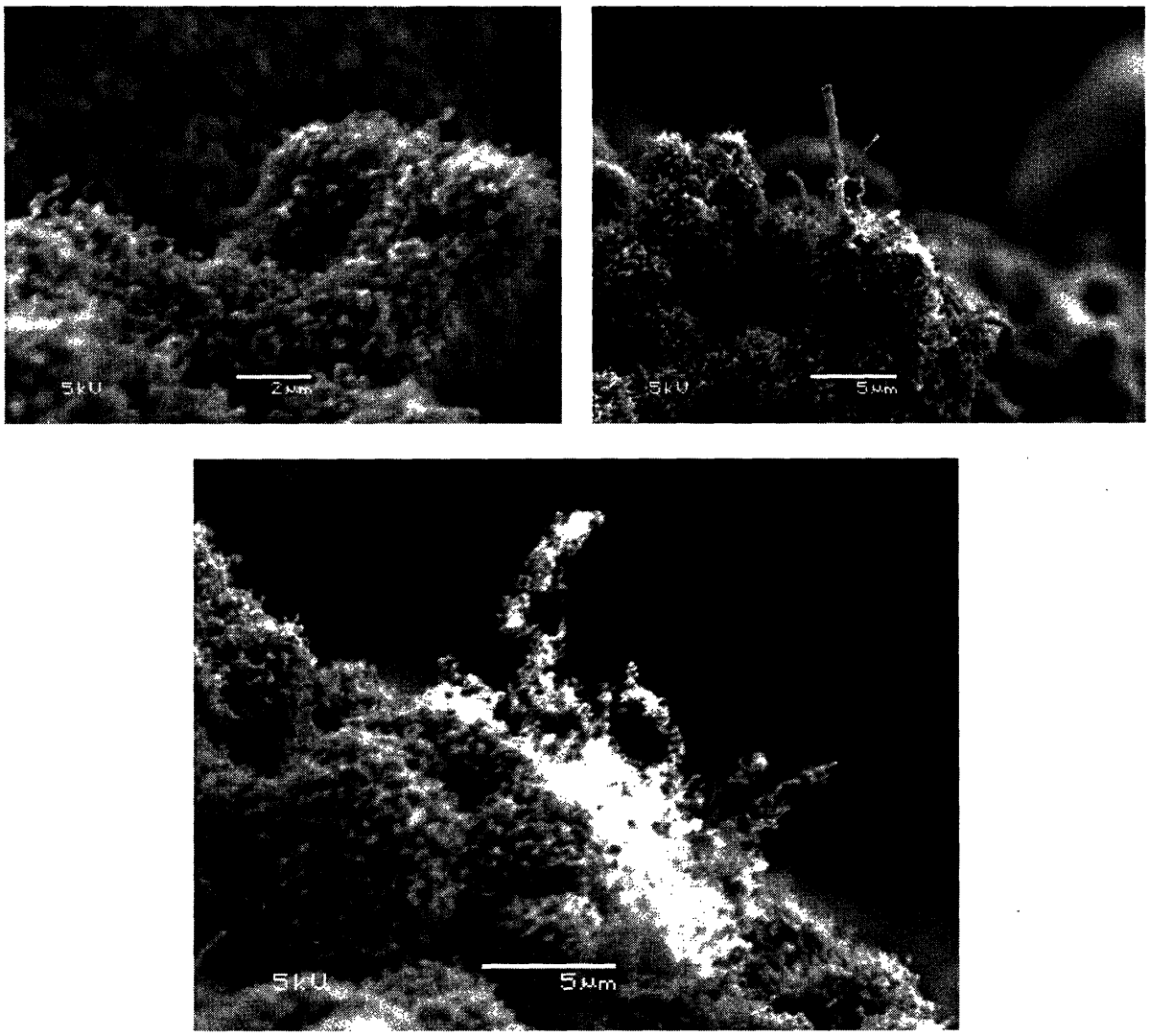

Figure 3-16 Short, thick graphitic fibers are found covering virtually the entire surface of Fe0.001M800-700 monoliths *(top left)*, with occasional long carbon fibers *(top right)* and bundles of small-diameter nanotubes *(bottom)*, which were the intentioned structures.

3.4.1.3 Conclusions

Reducing the doping level of Fe in the aerogel had the unexpected effect of producing short, large-diameter graphitic fibers, presumably due to the collective catalytic effect of many ultrasmall nanoparticles clustered closely together in the

monolith. Although bundles of small-diameter nanotubes were found on the sample as hypothesized, they were a minority product. With additional particle coarsening or slightly increasing the doping level, slightly larger nanoparticles suitable for catalyzing nanotube growth by themselves may result, in turn enabling growth of high populations of small-diameter nanotubes.

3.5 Conclusions

Although a deterministic technique for growing high yields of single-wall carbon nanotubes on an iron-doped carbon aerogel has still not been established, the techniques presented in this chapter suggest venues increasing the coverage nanotubes over the aerogel monolith and new synthetic routes for producing novel nanostructured carbons.

The successful demonstration of implementing a macroporous templating technique for enhancing gas diffusion into carbon aerogel monoliths for chemical vapor deposition growth of carbon nanotubes inspires a number of other interesting possible materials which could be prepared through chemical vapor deposition or atomic layer deposition on these materials, such as nanoporous metal composites.

A new method for introducing metal nanoparticles in carbon aerogels was demonstrated and may offer a starting point for deterministic synthesis of carbon nanoropes through a self-assembly process. Such a process may be useful for generating nanotube structures for high strength-to-weight ratio composites. Furthermore, the nanoparticle-aerogel composites' response to chemical vapor deposition shed further light on the tenuous catalytic state of iron which was observed in Chapter 2 and by many in the nanotube synthesis community. From this, a new model proposing a chemical-composition-sensitive catalytic activity for Fe was developed. This model may extend to other metals as well, as will be explored in Chapter 4.

Further exploration of the process-parameter space in Fe-doped carbon aerogel production revealed a counterintuitive technique for growing carbon fibers in place of carbon nanotubes through chemical vapor deposition by reducing the dopant concentration.

In summary, the rich chemistry of the iron system was found to enable engineering of a multitude of graphitic nanostructures, and carbon aerogels further proved to be a useful testing ground for exploring this chemistry.

Chapter 4

Metal-Doped Carbon Aerogels as Systems for Evaluating a Metal's Propensity to Catalyze Carbon Nanotube Growth

4.1 Background

The discovery that nanoparticles in Fe-doped carbon aerogels could catalyze carbon nanotube growth provided several insights into the composition and oxidation state required for a nanoparticle to catalyze nanotube growth. It was determined that samples with high populations of carburized nanoparticles (or at least nanoparticles possessing carburized surfaces) and samples containing high populations of surface-oxidized nanoparticles were not effective in growing carbon nanotubes in comparison to samples with high populations of purely metallic nanoparticles, leading to the conclusion that only metallic iron is catalytically active.

Lessons learned from this system suggested that, in many ways, metal-doped carbon aerogels may serve as an ideal environment for studying the propensity of

other metals for catalyzing* carbon nanotube growth, and that such systems could aid in determining whether oxidized and carburized species other metals exhibit catalytic behavior or not. The Fe-doped system was found to be relatively robust in its ability to reliably grow carbon nanotubes under a variety of different CVD conditions and over a range of approximately 100°C. This reduced the amount of experimentation required to ascertain the process parameters required for successful nanotube growth. Furthermore, the ease of characterizing nanoparticle composition profiles in the Fe system by using XRD and XPS in conjunction with the ability to correlate this information with successful and unsuccessful growths proved to be valuable in deducing which species in the aerogel were catalytic. Finally, the overwhelming abundance of amorphous and nanocrystalline carbon present during the coarsening of nanoparticles in the aerogel was found to effectively act as a coking agent that reduces oxidized species to the catalytic metallic state. As mentioned in Chapter 2, iron in the unpyrolyzed phenolic aerogel is likely in the form of iron oxyhydroxide oligomers, which in conjunction with the oxygen from carboxylate moieties present throughout the aerogel backbone, gives rise to oxidized iron nanoparticles during the initial stages of pyrolysis. When pyrolyzed at the right temperature and for the right amount of time, the reductive environment of the carbon aerogel generates high yields of catalytically active particles throughout the aerogel (the "sweet spot"). When pyrolyzed at higher temperatures and/or for longer times, this environment further reduces the iron in the nanoparticles to iron carbides. This is in many ways analogous to the fate of Fe nanoparticles on a silicon substrate being bombarded by a constant stream of carbon feedstock gas during CVD-based growth of carbon nanotubes.

With these ideas in mind, it was hypothesized that other metals could be evaluated for the ability to catalyze carbon nanotube growth through systematic investigation of their metal-doped carbon aerogel systems. The motivations for doing this were threefold, as follows.

---

* References made in regard to a species being catalytic or uncatalytic strictly refer to the ability to catalyze carbon nanotube growth by thermal CVD.

First, identifying new catalysts for nanotube growth is currently a main objective of our research group in its pursuit of chirality-controlled growth of carbon nanotubes. It has been demonstrated using ^{13}C NMR that growth of single-wall carbon nanotubes employing common catalysts (such as cobalt, cobalt-molybdenum, iron, and iron-molybdenum) produce metallic and semiconducting nanotubes in a ratio of 1:2, whereas rhodium-palladium alloys result in a metallic-to-semiconducting ratio of 1:1 [91]. This implies that it may be possible to control the ratio of nanotube chiralities grown through CVD by selecting the proper metal(s) for catalysis. An exhaustive search of the literature found that only Fe, Co, Ni, Ru, Rh, Pd, Pt, Mn, Cr, Mo, W, Cu, Au, and select bimetallics of these elements have been demonstrated to catalyze nanotube growth through thermal CVD [61, 63, 67, 92-98]. These elements represent only the Group VIB elements, eight of the Group VIII elements, and two of two of the Group IB elements. Demonstrating the ability of additional metals to catalyze growth is thus useful in elucidating how changing catalyst composition can be used to control chirality.

Secondly, identifying metals which are catalytic towards nanotube growth yet exhibit markedly different chemistry, different tendencies for oxide and carbide formation, and different melting points, and prefer to crystallize into different crystal structures will aid in such things as elucidating poisoning mechanisms, designing "voodoo-free" nanoparticle preparations, and defining the properties characteristic of the ideal nanotube catalyst.

Lastly, production of new metal-doped carbon aerogel systems is valuable for development of conductive high-surface-area materials, understanding nanostructured carbon materials, and potentially for discovering useful precursors for preparing nanoporous metals.

In this chapter, six new metal-doped carbon aerogel systems—Rh, W, Ta, Nb, Au, and Re—are explored in the context of evaluating whether or not these metals and related species are capable of catalyzing carbon nanotube growth. With the exception of Au, these are the first examples of these systems. Rhenium, gold, and rhodium were selected as three examples of "carbophobic" metals, that is, metals which have no known stable carbide or only exhibit carbide formation under

extreme temperatures and pressures. This was to aid in determining if carbides are the primary catalytic species in CVD-based nanotube growth (as argued by some [99, 100]), and if not, whether the ability to form a carbide (as a necessary intermediate species, for example) is required for nanotube growth. Rhodium was also selected as a Group VIIIB analog comparison with iron which has been previously demonstrated to catalyze nanotube growth. Tungsten was selected as an example of a "carbophilic" metal, that is, a metal which exhibits a rich phase diagram with carbon similar to iron, but which possesses significantly different chemical behavior from iron otherwise (due to its higher number of thermodynamically-accessible oxidation states). Niobium was selected as an example of Group VB element, since growth employing Group VB elements has not previously been demonstrated. Lastly, Tantalum was selected as an example of a metal which forms very stable refractory oxides that are not readily reduced to metallic tantalum for investigating whether metal oxides are catalytic towards nanotube growth or not. As Rh, W, and Au have been previously demonstrated to be catalytic towards nanotube growth, these metals were expected to successfully grow nanotubes and thus serve as verification controls.

4.2 Experimental

4.2.1 Materials and Methods

Preparation of Precursor Gels

A solution of potassium 2,4-dihydroxybenzoate was prepared by adding K_2CO_3 (1.29 g, 9.4 mmol) to a solution of 2,4-dihydroxybenzoic acid (2.9 g, 18.8 mmol) in deionized water (100 mL). Formaldehyde (2.98 g 37% w/v in water, 37 mmol) was then added along with an additional amount of K_2CO_3 (26 mg, 0.188 mmol) to serve as a polymerization catalyst. The solution was then stirred for 24 h, after which the solution was transferred into plastic or glass vials, sealed, and thermoset in an oven at 80°C for 72 h. The resulting K^+-loaded gels were obtained as dark red, transparent monoliths. The gels were then removed from their plastic vials and sliced into 5-10 mm discs with a razor blade.

Doping of Precursor Gels

Gel slices were doped with Au, Nb, Re, Rh, Ta, or W by diffusive ion exchange in a 0.1 M solution of a chloride of the target dopant metal for 3 d with fresh solution exchanged in every 24 h. Doping with Nb, Re, Ta, and W was accomplished with 0.1 M solutions of anhydrous rhenium(V) chloride, tantalum(V) chloride, niobium(V) chloride, and tungsten(VI) chloride in N,N'-dimethylformamide (DMF), respectively. Doping with Rh was accomplished with 0.1 M aqueous rhodium chloride. Doping with Au was accomplished with 0.1 M aqueous auric acid. Following ion exchange, the gels were transferred into pure solvent (either DMF or deionized water, depending on the dopant solution used) and soaked for 3 d, again exchanging in fresh solvent every 24 h to remove excess unbound ions from the pores of the gels. A third solvent exchange into acetone was then performed in a similar manner over the course of 3 d to make the gel liquor compatible for exchange and subsequent supercritical extraction with carbon dioxide.

Supercritical Drying

Gels were placed in a supercritical extractor and soaked under liquid carbon dioxide (5.2 MPa and 15°C) for 2 d, with the extractor flushed through with fresh liquid carbon dioxide every 6 h. Once the gels were sufficiently diffused through with liquid carbon dioxide, the vessel was heated past the critical point of carbon dioxide (31.1°C and 7.38 MPa) at a rate of 1°C per min to a temperature of 50°C and pressure of 9.65 MPa. The vessel was allowed to remain at these conditions for 1-2 h followed by isothermal depressurization below the critical point of carbon dioxide over the course of ~1 h. At this point the vessel was allowed to cool and depressurize to ambient conditions over the course of ~1 h. The newly formed metal-doped phenolic aerogels were then removed from the vessel.

Pyrolysis

Metal-doped phenolic aerogels were carbonized by pyrolyzing at 800°C or 1050°C under a flow of 200 sccm Ar for 10.5 hrs. Pyrolyzed samples are denoted by

a part number with the format "Mxxxx", where "M" is the dopant metal and "xxxx" is the pyrolysis temperature in degrees Celsius.

Chemical Vapor Deposition

Metal-doped carbon aerogels pyrolyzed at 800°C were processed by chemical vapor deposition (CVD) to evaluate their propensity for catalyzing carbon nanotubes growth. In a typical process, an aerogel was placed in a 2.5-cm long segment of quartz tubing inserted into the middle of a 2.5-cm diameter by 30.0 cm quartz process tube. Ar was then flowed through the tube at a rate of 200 sccm for 20-40 minutes to remove as much air from the mesoporosity of the aerogel as possible. The tube was then placed into a clamshell furnace preheated to a temperature ranging from 800-950°C. Upon opening, the furnace temperature would drop 50-100°C. A target temperature of 600°C, 700°C, or 800°C was then set on the furnace temperature controller and attained within 2-3 m. H_2, CH_4 and/or C_2H_4 were flowed over the aerogel for 10-20 minutes at this temperature. The tube was then taken out of the furnace and placed under a flow of 500 sccm Ar until the tube cooled to ambient temperature. Samples having undergone CVD are denoted with a part number with the format "Mxxxx-yyyy", where "xxxx" is the temperature at which the aerogel was pyrolyzed, "yyyy" is the temperature at which CVD was performed, and occasionally appended with the denotation "/tt", where "tt" is the length of the CVD process in min.

4.2.2 Characterization

Metal-doped carbon aerogels were characterized by powder XRD (X-ray diffraction), XPS (X-ray photoelectron spectroscopy), TEM (transmission electron microscopy), and Raman spectroscopy prior to attempting CVD growth of carbon nanotubes. Following CVD, the aerogels were characterized by Raman spectroscopy and scanning electron microscopy (SEM) to determine if nanotube growth was successful. The exterior surface of the aerogels was then scraped off under dichloroethane, deposited on a TEM grid, and analyzed.

Density was calculated by dimensional analysis of monolithic aerogel discs.

High-resolution scanning electron microscopy was performed with a JEOL 6320 operating at 5 kV. High-resolution transmission electron microscopy of metal-doped carbon aerogels and derived nanotube composites was performed on a JEOL JEM-200CX operating at 200 keV.

XRD spectra were obtained using a Rigaku 300 X-ray diffractometer operating with the following measurement parameters: high voltage = 60 kV; current = 300 mA; divergence slit = 1°; scatter slit = 2°; receiving slit = 0.6°; scan mode = continuous; scan type = standard; axis = $2\theta/\theta$; scan = 10° to 80°; scan speed = 0.25° min^{-1}; sampling interval = 0.03°. Phase identification was made using MDI Jade 7 equipped with the ICSD and NIST databases of XRD spectra.

XPS spectra were obtained on an AXIS HIS 165 and ULTRA Spectrometer (Kratos Analytical Limited, England) using Al K radiation (energy = 1486.6 eV) in a vacuum of 5 x 10^{-9} torr. Samples were prepared by grinding into a fine powder, adhering to adhesive copper tape, and mounting the copper tape on a sample holder using double-sided adhesive carbon tape. X-ray slots of 750 by 350 μm, an X-ray power of 150 W (15 kV and 10 mA), and a pass energy of 20-80 eV (dependent on the metal being analyzed) were used. Spectral deconvolution and elemental percent composition[4] was performed with CasaXPS version 2.2.99. Charge correction was not performed., as spectra collected matched reference spectra and each other well.

Raman spectra were obtained using a custom-built micro-Raman spectrometer at excitation wavelengths of 785 nm and 676 nm.

4.3 Results and Discussion

4.3.1 The Rhodium System

Description of Monoliths

Rh-doped phenolic aerogels were afforded as dark reddish-brown monoliths with the consistency of cork. A darker colored ring around the edge of the

[4] Briefly, elemental percent composition is calculated by taking the ratio of the integrated area of signals for two or more elements, normalized to the relative sensitivity factor (R.S.F.) for each element. As XPS is more sensitive to some elements than others, the relative sensitivity factor of an element is used to scale the signal intensity of that element accordingly for quantitative analysis, where the R.S.F. for carbon is defined as 1.

monolithic discs was also observed. The density of the unpyrolyzed monoliths was measured to be 0.20 g cm^{-3}. The pyrolyzed Rh-doped carbon aerogels were black in color with a slight graphite-colored film on the outer edges. The density of the Rh-doped carbon aerogels was measured to be slightly higher than the unpyrolyzed monoliths at 0.29 g cm^{-3}.

X-Ray Diffraction Analysis

XRD spectra for Rh-doped carbon aerogels pyrolyzed at 800°C and 1050°C are shown in Figure 4-1. A broad amorphous peak attributed to the carbon aerogel framework is observed at ~22° two-theta, just as observed in the iron system. The average crystallite size does not change with pyrolysis temperature, suggesting that no appreciable ordering of the carbon structure occurs within 10.5 h at either temperature. Phase identification reveals the presence of metallic Rh at both pyrolysis temperatures [101]. Unlike the iron system, phase identification of the spectra attributes all observed peaks to Rh metal, with no carbide present. Also notable is that unlike its chemical analog cobalt, the rhodium system exhibits no graphite peaks. Table 4-1 lists measured peak positions, full-width at half-maximum (FWHM) values, relative intensities, and calculated crystallite sizes for Rh800 and Rh1050 samples. As expected, an increase in average crystallite size of Rh crystallites is observed with higher pyrolysis temperature, consistent with a one-component particle coarsening mechanism. Both samples possess a mean crystallite size that is smaller than in the iron system. Figure 4-2 shows Rh800 as seen by TEM. As expected, a sponge-like mesoporous nanocrystalline carbon framework dotted with dark Rh crystallites is observed, verifying the absence of the types of graphitic nanostructures characteristic of Co- and Ni-doped carbon aerogels [11].

X-Ray Photoelectron Spectroscopy Analysis

Figure 4-3 shows the C 1s, O 1s, and Rh 3p regions of the XPS spectra for Rh800 and Rh1050 samples. Spectral deconvolution (Table 4-2) was accomplished using Shirley background fitting with placement of Guassian-Lorentzian peaks (70% Guassian, 30% Lorentzian). Both Rh800 and Rh1050 exhibit virtually identical XPS

spectra, indicating no pyrolysis temperature-induced changes in surface chemistry occur between 800°C and 1050°C. Three carbon peaks are observed in the C 1s region. The broad peak at high binding energy is attributed to π-π^* shake-up transitions, possibly from nano-sized graphite domains distributed throughout the aerogel framework or from unvolatilized carboxylate moieties leftover from the phenolic precursor. The remaining two peaks suggest two distinct carbon surface chemistries, likely graphitic carbon and amorphous (disordered, H-terminated) carbon. Only one oxygen chemistry is detected and is typical of a carbon aerogel material. Only one surface chemistry of rhodium is discernible, with the Rh $3p_{3/2}$ peak appearing at 496 eV and the Rh $3p_{1/2}$ peak at 521 eV, matching what is expected for Rh^0 [77]. No signals corresponding to Rh_2O_3 (which would appear at a higher binding energy) are observed, correlating with the detection of only one distinct oxygen chemistry to suggest the surface Rh-containing nanoparticles in the aerogel is unoxidized, metallic rhodium.

Sample	Assigned Reflection	2-θ (°)	FWHM (°)	Rel. Peak Height	Crystallite Size (nm)
Rh800	Rh (111)	41.2	1.28	1.00	6.6
	Rh (200)	47.8	1.32	0.41	6.6
	Rh (220)	69.9	1.50	0.29	6.5
	C (Amorph)	22.0	6.78	-	1.2
Rh1050	Rh (111)	41.1	0.524	1.00	16.5
	Rh (200)	47.8	0.609	0.45	14.5
	Rh (220)	70.0	0.605	0.23	16.3
	C (Amorph)	22.4	6.921	-	1.2

Table 4-1 Analysis of XRD spectra for Rh-doped carbon aerogels with estimated average crystallite sizes.

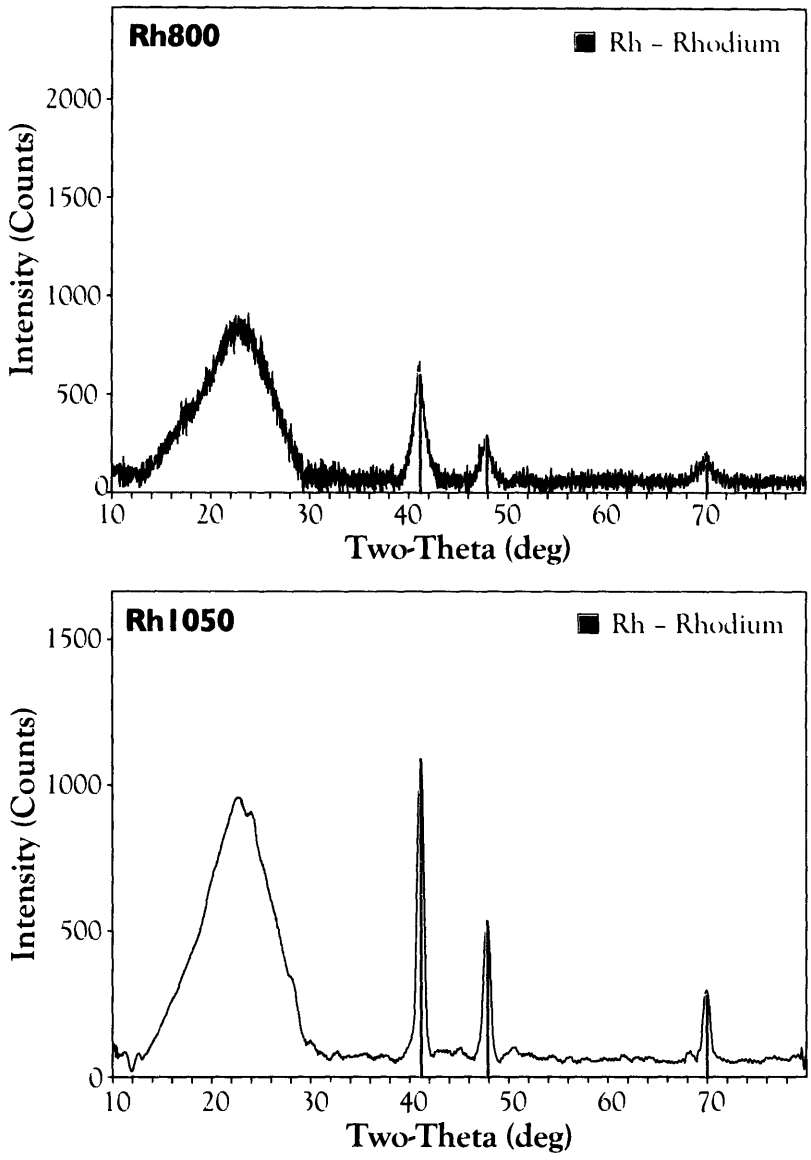

Figure 4-1 Powder XRD spectra and phase identification for Rh-doped carbon aerogels pyrolyzed at 800°C and 1050°C (see Table 4-1).

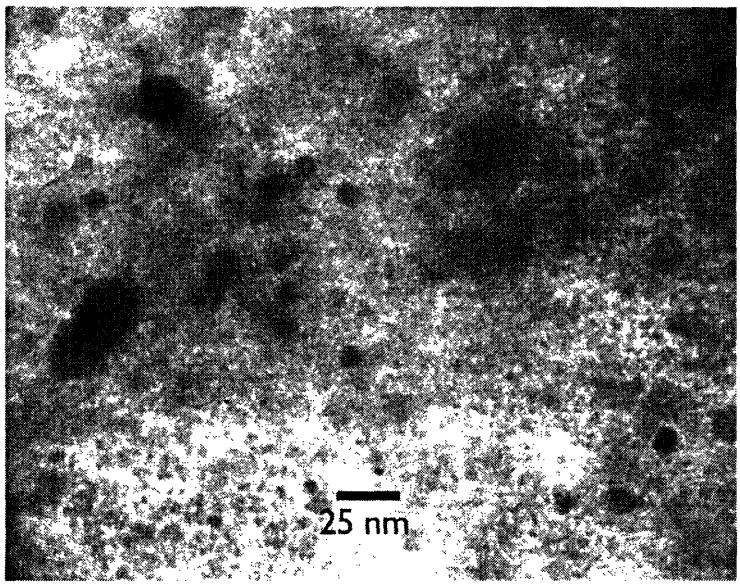

Figure 4-2 TEM micrograph of Rh800 sample.

Table 4-3 shows calculated elemental compositions for Rh800 and Rh1050 based on analysis of XPS spectral deconvolution (as described in Section 4.2.2). Overall, the ion-exchange technique appears to result in an effective loading of approximately 0.7% Rh by mass.

Effects of Chemical Vapor Deposition

As a starting point for finding a set of process parameters that would allow for carbon nanotube growth (if possible), the optimal process parameters for the Fe system were attempted first, that is, using monoliths pyrolyzed at 800°C and performing CVD at 700°C under a flow 20 sccm ethylene, 30 sccm of methane, and 500 sccm of hydrogen. Surprisingly, this set of conditions was successful in growing carbon nanotubes. Figure 4-4 shows SEM images after attempting CVD growth of carbon nanotubes on Rh800 monoliths under such conditions. After a 10-minute CVD process, large populations of what appear to be multiwall carbon nanotubes are observed. The large majority of nanotubes appear to be of similar diameter; however, clusters of carbon fibers 50-100 nm in diameter appear occasionally across the surface of the sample. These larger diameter fibers are assumed to result from the presence of occasional, more heavily coarsened nanoparticles distributed throughout the sample. Figure 4-5 shows TEM micrographs of scrapings from the

surface of the monolith. Multiwall carbon nanotubes, verified to be nanotubes by diffraction of the walls, are observed. On average, the observed nanotubes are approximately 15 nm in diameter and appear to be less defective than those produced by the iron system.

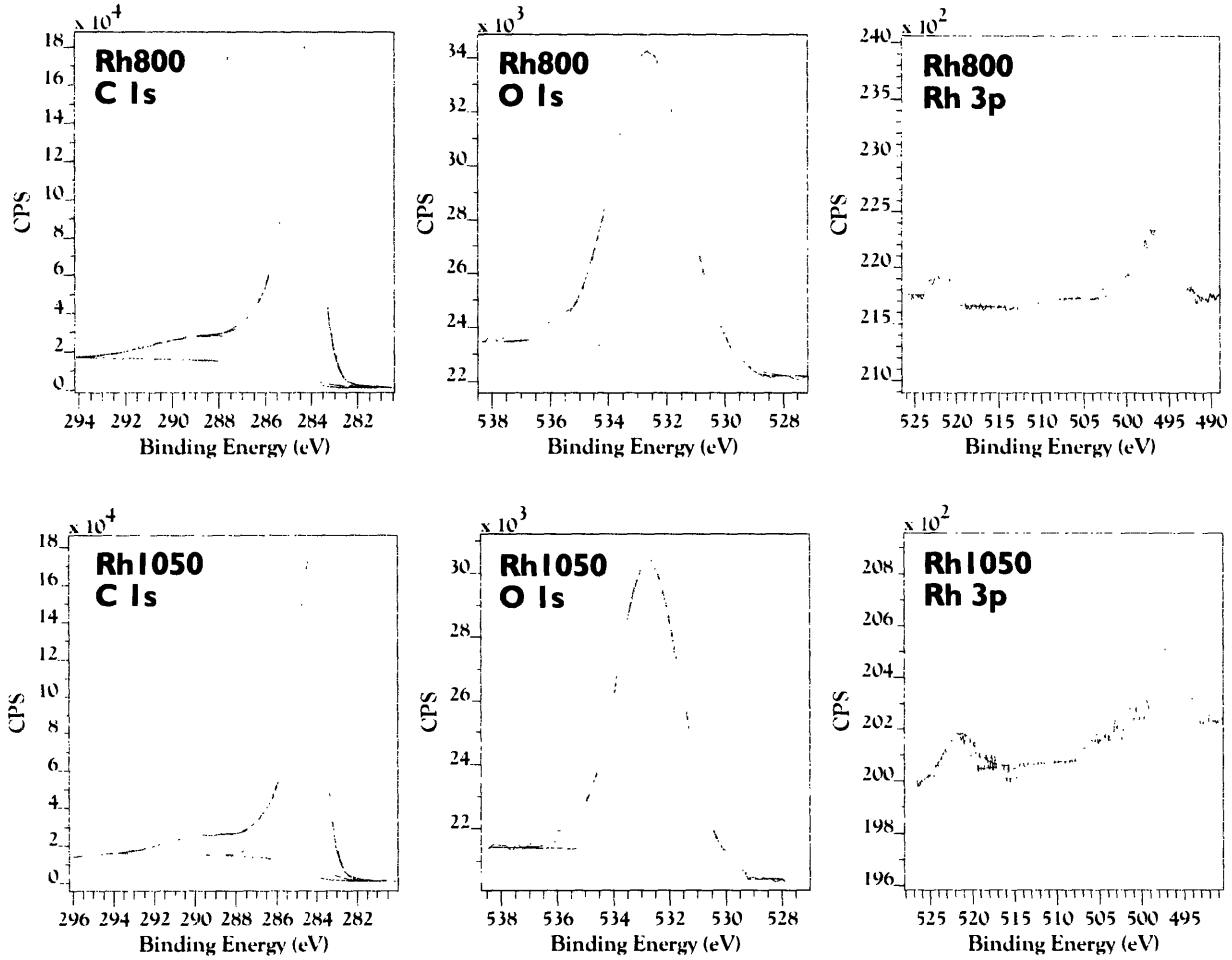

Figure 4-3 *(Top, left to right)* C 1s, O 1s, and Rh 3p regions of the XPS spectrum for Rh800; *(bottom, left to right)* C 1s, O 1s, and Rh 3p regions of the XPS spectrum for Rh1050.

Sample	Energy Region	Assignment	Position (eV)	FWHM (eV)	Area (eV counts)	R.S.F.*
Rh800	C 1s	Amorphous	284.34	1.41	33550.6	1
	C 1s	sp^2 Carbon	285.38	2.22	13479.3	1
	C 1s	π-π^* Shake-Up	288.34	5.28	11096.2	1
	O 1s	Carboxylate	532.61	2.87	4629.2	2.93
	Rh 3p	Rh $3p_{3/2}$	496.68	5.23	471.1	10.9
	Rh 3p	Rh $3p_{1/2}$	521.40	2.79	94.9	10.9
Rh1050	C 1s	Amorphous	284.33	1.37	31391	1
	C 1s	sp^2 Carbon	285.39	2.25	14122.3	1
	C 1s	π-π^* Shake-Up	288.80	5.05	9217.7	1
	O 1s	Carboxylate	532.72	2.68	3583.1	2.93
	Rh 3p	Rh $3p_{3/2}$	497.02	4.45	207.7	10.9
	Rh 3p	Rh $3p_{1/2}$	521.82	4.37	98.4	10.9

* Relative sensitivity factor (see Section 4.2.2)

Table 4-2 Deconvolution results for XPS spectra of Rh-doped carbon aerogels.

Sample	Element	% Mass Concentration	% Atomic Concentration
Rh800	C	95.74	97.22
	O	3.53	2.69
	Rh	0.73	0.09
Rh1050	C	96.32	97.69
	O	2.92	2.22
	Rh	0.77	0.09

Table 4-3 Elemental compositions of Rh-doped carbon aerogels as determined by XPS.

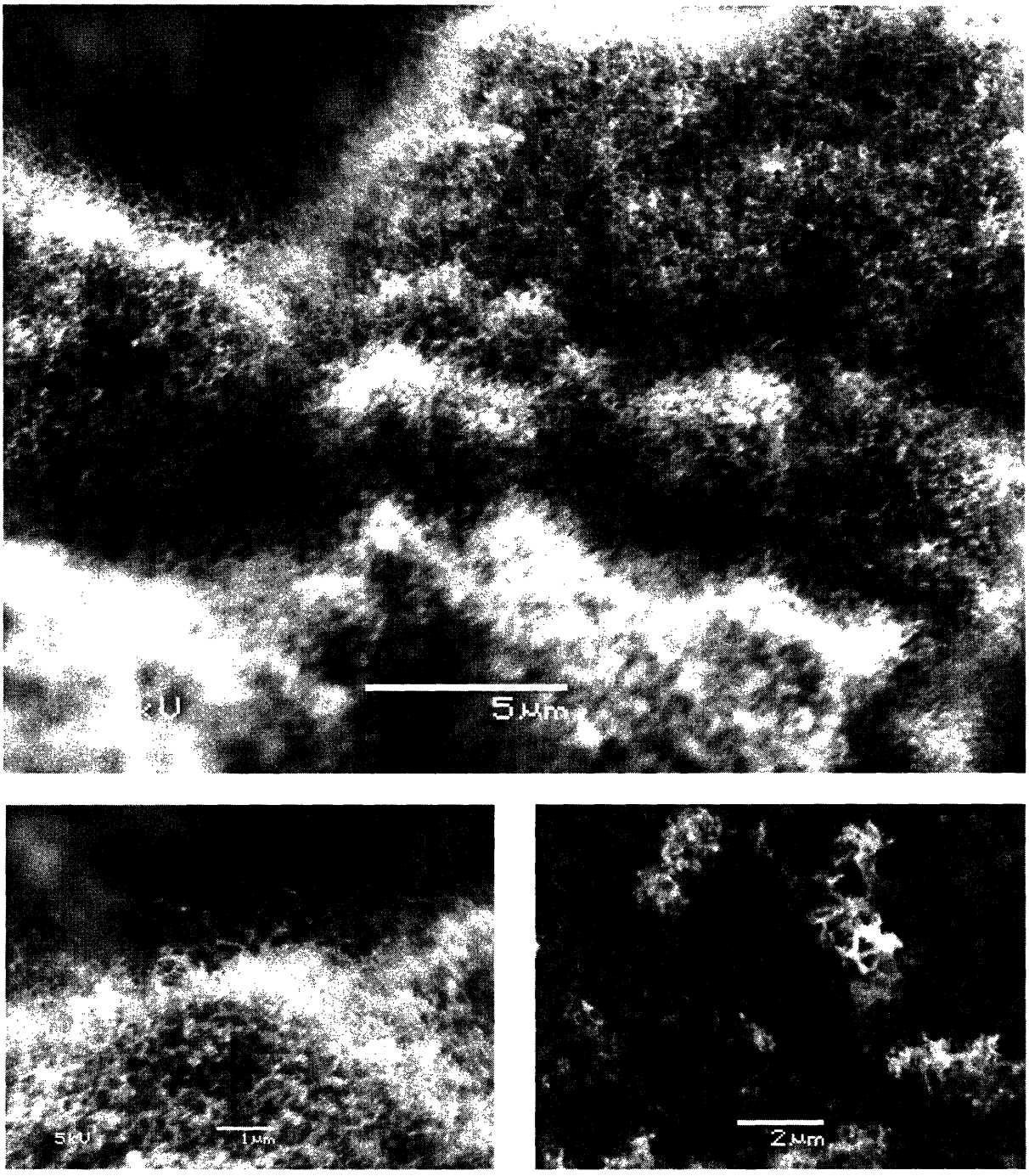

Figure 4-4 SEM micrographs of Rh800-700 monolith surfaces showing high yields of carbon nanotubes *(top, bottom left)*; micrograph showing a region resulting in carbon fiber growth *(bottom right)*.

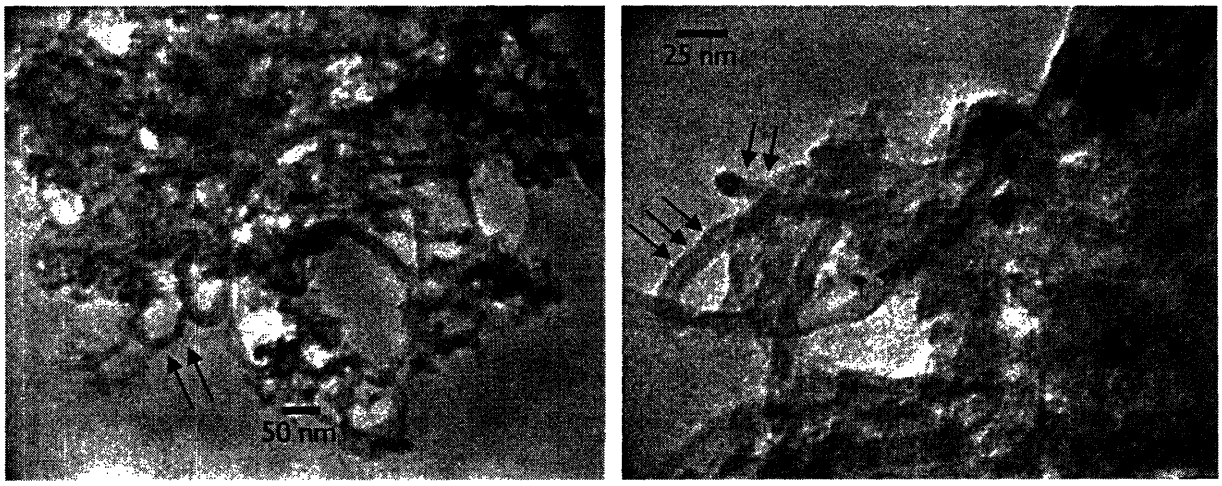

Figure 4-5 Multiwall carbon nanotubes attached to Rh-doped carbon aerogel *(left)*; detail aerogel surface showing relatively defect-free multiwall nanotubes with a diameter of approximately 15 nm *(right)*.

Raman Spectroscopy

To determine if Raman spectroscopy could be used as a simplified method for evaluating successful nanotube growth, Raman spectra (taken at 676 nm) were collected before and after CVD (Figure 4-6). Unfortunately, virtually no difference in the Raman spectrum is observed after growth, and no radial breathing mode (RBM) is observed despite the presence of nanotubes as verified by SEM and TEM. This lack of RBM and other spectral features arising from nanotubes is likely due to the extensive entangling of nanotubes on the monolith, compounded by the nanotubes being multiwalled and defective. Like the Fe-doped system, a broad disorder-induced D band and pronounced G band are observed both before and after CVD. No appreciable G′ signal is detected in either case. Both the D band and G band are shouldered and appear to consist of multiple components. Deconvolution of the spectra was accomplished using a four-peak Gaussian-Lorentzian peaks (Table 4-4) and reveals an increase in intensity in portions of these bands after growth of nanotubes—the increase in the G band corresponding to an increase in graphitic carbon from the presence of nanotubes, and the increase in the D band likely arising from defects in the nanotubes and from non-graphitic carbon deposited during CVD. Raman spectra for every metal-doped carbon aerogel system investigated are virtually identical exhibiting the same general increase in D-

band and G-band intensity after CVD whether or not nanotubes are present (since other graphitic nanostructures can form over nanoparticles if nanotubes do not grow), and so it is concluded that Raman spectroscopy is not a useful technique for evaluating success of nanotube growth. Using Knight's formula [102],

$$L_a = C_\lambda (I_D / I_G)^{-1} \tag{4-1}$$

where L_a is the average crystallite size, I_D/I_G is the ratio of the integrated area of the D-band to that of the G-band, and C_λ is a fitting parameter which adjusts for the laser wavelength used to generate the spectrum, the average carbon crystallite size before and after growth was calculated. Implementing the equation $C_\lambda \approx C_0 + \lambda C_1$ where C_0 is estimated to be -12.6 nm and C_1 is estimated to be 0.033 [81], C_λ was estimated to be 9.708. Using peak area ratios for the primary band components, a pre-growth carbon crystallite size of 1.96 nm was calculated (compared with 1.2 nm calculated from XRD), with this value increasing to 2.28 nm after growth. Assuming this increase in average crystallite size is solely due to contributions to the Raman spectrum by carbon nanotubes added by CVD, the fraction of the aerogel surface with nanotubes attached κ can be estimated through the approximation

$$\kappa = \frac{L_{a,f} - L_{a,i}}{d_{av}} \tag{4-2}$$

where $L_{a,i}$ is the pre-growth carbon crystallite size, $L_{a,f}$ is the post-growth carbon crystallite size, and d_{av} is the estimated mean nanotube diameter. Assuming this value to 6.6 nm (based on the mean Rh crystallite size from XRD), a value of 4.8% is obtained for κ. This value seems low based on SEM images taken. It is possible that the high yield of nanotubes produced obstructs laser light from hitting the carbon aerogel surface and the value of 2.28 nm $L_{a,f}$ actually corresponds to the mean nanotube diameter.

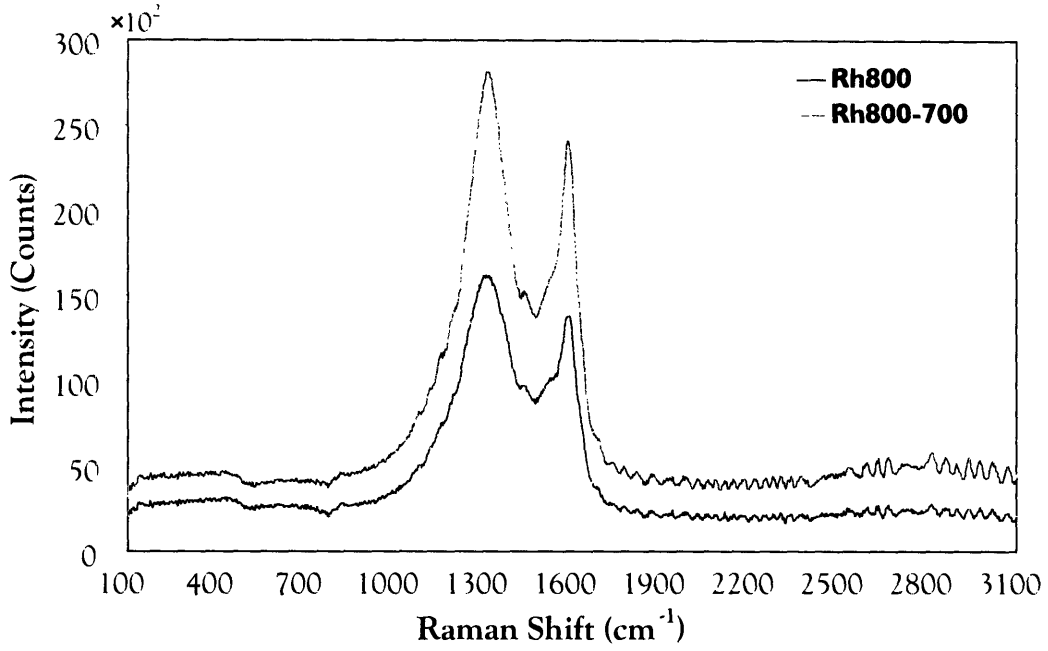

Figure 4-6 Raman spectra for Rh800 monolith (before CVD) and nanotube-laden Rh800-700 monolith (after CVD) at 676 nm excitation wavelength.

Sample	Band	Peak Center (cm^{-1})	FWHM (cm^{-1})	Amplitude (counts)	Area (cm^{-1} counts)
Rh800 (Before CVD)	D	1309.0	231.0	13540.0	4451000
	Band	1452.9	34.2	1015.9	49460
	G	1519.5	75.2	3888.0	415800
	Band	1588.8	66.2	9566.6	900500
Rh800-700 (After CVD)	D	1311.4	189.8	23200.0	6776000
	Band	1454.3	39.7	1807.6	110400
	G	1521.2	72.5	5419.5	604300
	Band	1587.6	61.6	16790.0	1590000

Table 4-4 Rough deconvolution for Raman spectra at 676 nm of Rh-doped carbon aerogels before and after CVD.

Conclusions

In summary, Rh is effective at catalyzing carbon nanotube growth through thermal CVD. The successful growth of carbon nanotubes in the absence of any metal carbide or oxide, either in crystallite form or as surface coatings, demonstrates that metals are catalytic towards nanotube growth and that oxidized and carburized

species are, at the very least, not necessary for catalytic growth of carbon nanotubes by thermal CVD. Despite being surrounded by an overwhelming amount of carbon and oxygen at elevated temperatures (pyrolysis of the carbon aerogel), the lack of species other than metallic rhodium in Rh-doped carbon aerogels demonstrates the resistance of the metal against oxidation or carburization. This suggests that rhodium may be an ideal nanotube catalyst, as it is resistant against the two most probable chemical poisoning mechanisms present in heterogeneous nanotube catalysis. Investigations into the maximum lifetime and thus maximum nanotube length attainable with rhodium catalysts are underway.

4.3.2 The Rhenium System

As mentioned, rhenium was selected as an example of a metal which exhibits only a simple eutectic with carbon and thus does not form stable carbides except for at high temperatures under elevated pressure [103-105] - another example of a so-called "carbophobe". Rhenium, which exhibits chemical behavior significantly different from the Group VIII metals and possesses a melting point nearly twice as high, has not previously been demonstrated to catalyze nanotube growth. Successful growth with rhenium as a catalyst would provide a further understanding of the properties prerequisite (or not prerequisite) for a nanoparticle to catalyze (or not catalyze) nanotube growth, as well as extend the metals available for experimentation in nanotube catalyst engineering. Doing so would also provide further evidence that carbides are not necessary for, nor are they the primary catalytic species in, heterogeneous catalysis of nanotube growth by thermal CVD.

Description of Re-Doped Carbon Aerogel Monoliths

Re-doped phenolic aerogels were afforded as black monoliths with a density of 0.22 g cm^{-3}. Pyrolysis of Re-doped phenolic aerogels resulted in typical black monoliths. Pyrolysis of Re-doped phenolic aerogels at 1050°C, however, resulted in an unusual formation of a rhenium metal layer on the top surface of the monolith. Figure 4-8 shows images of this sample. It appears that the same underlying thermodynamics which limits the interaction between rhenium and carbon in

forming carbides also favor phase separation of the two in carbon aerogels. The top of the sample likely experienced a slightly higher temperature than the rest of the monolith during pyrolysis due to convection in the quartz process tube and provides just enough temperature to overcome the activation energy barrier for this phenomenon to occur. In fact, increasing the Ar flow rate during pyrolysis from 200 to 500 sccm provide enough added cooling to prevent this film from forming. The density of Re-doped carbon aerogels post-pyrolysis was measured to be slightly higher than the pre-pyrolysis monoliths at 0.28 g cm^{-3}.

X-Ray Diffraction Analysis

Figure 4-7 shows XRD spectra for Re-doped carbon aerogels pyrolyzed at 800°C and 1050°C. Like the rhodium system, only crystallites of rhenium metal are detected and crystalline rhenium oxide is not observed [106]. A nanocrystalline carbon band centered around 24° two-theta is present. The mean carbon crystallite size changes slightly with increasing pyrolysis temperature. Again, no peaks corresponding to graphite are detected, suggesting rhenium also does not catalyze the nanocrystalline carbon framework into graphitic nanostructures during pyrolysis.

Sample	Assigned Reflection	2-θ (°)	FWHM (°)	Relative Peak Height	Crystallite Size (nm)
Re800	Re (100)	37.9	0.69	0.33	12.3
	Re (002)	40.5	0.59	0.30	14.6
	Re (101)	42.9	0.53	1.00	16.5
	Re (102)	57.0	0.71	0.28	12.9
	Re (110)	67.6	0.69	0.25	14.0
	Re (103)	75.2	0.63	0.20	16.2
	C (Amorph)	24.4	8.90	-	0.9
Re1050	Re (100)	37.8	0.73	0.36	11.6
	Re (002)	40.5	0.52	0.40	16.6
	Re (101)	42.9	0.53	1.00	16.3
	Re (102)	56.5	0.63	0.21	14.6
	Re (110)	68.0	0.49	0.19	20.0
	Re (103)	75.4	0.45	0.21	22.7
	C (Amorph)	22.9	6.53	-	1.2

Table 4-5 Analysis of XRD spectra for Re-doped carbon aerogels.

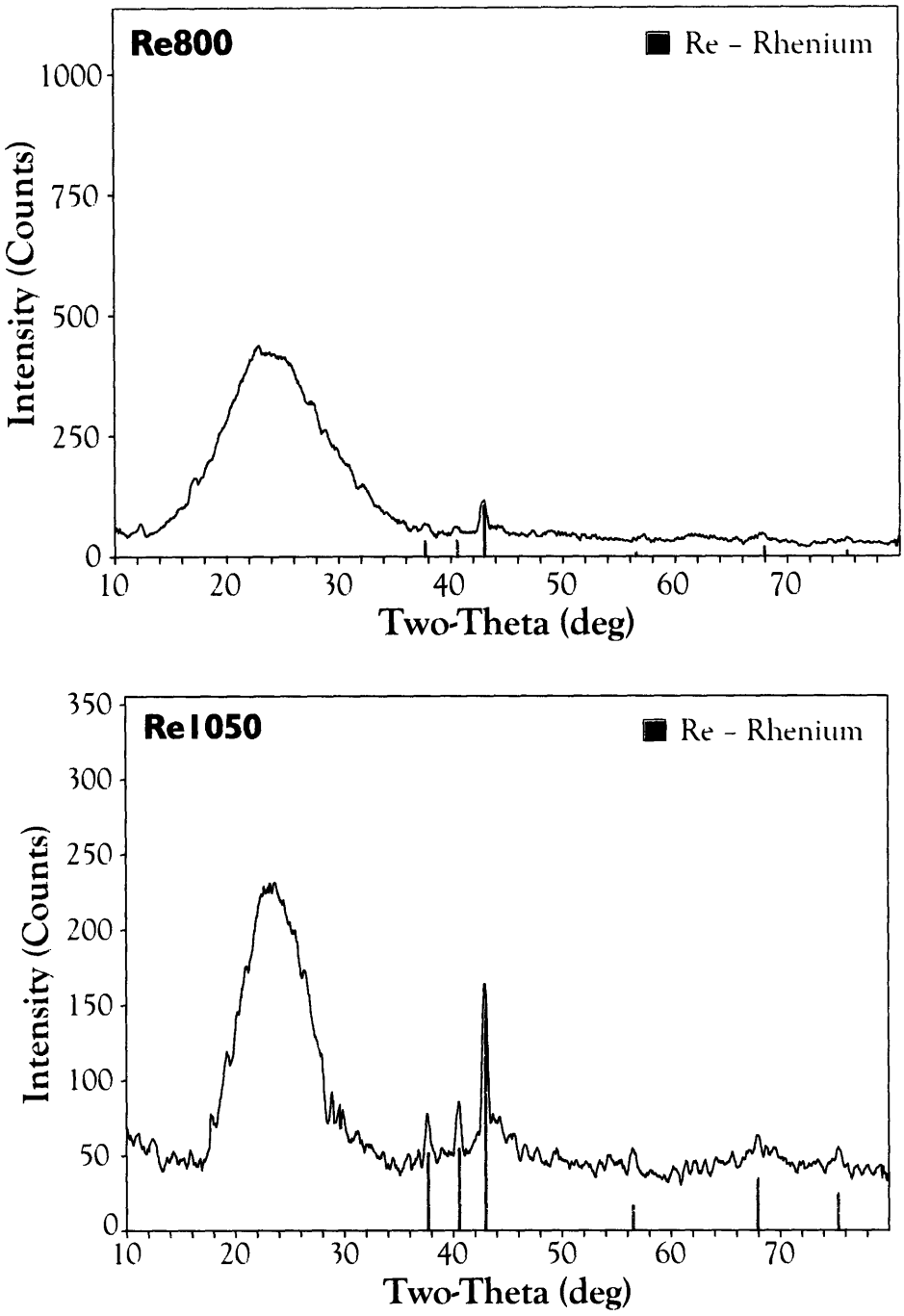

Figure 4-7 Powder XRD spectra and phase identification for Re-doped carbon aerogels.

Table 4-5 lists measured peak positions, full-width at half-maximum (FWHM) values, relative intensities, and calculated crystallite sizes for Re800 and Re1050 samples. Averaging the calculated crystallite sizes for each reflection, it is seen that the mean Re crystallite size increases from 14.4 nm for a pyrolysis temperature of

800°C to 17.0 nm at 1050°C, consistent with a particle coarsening mechanism as expected.

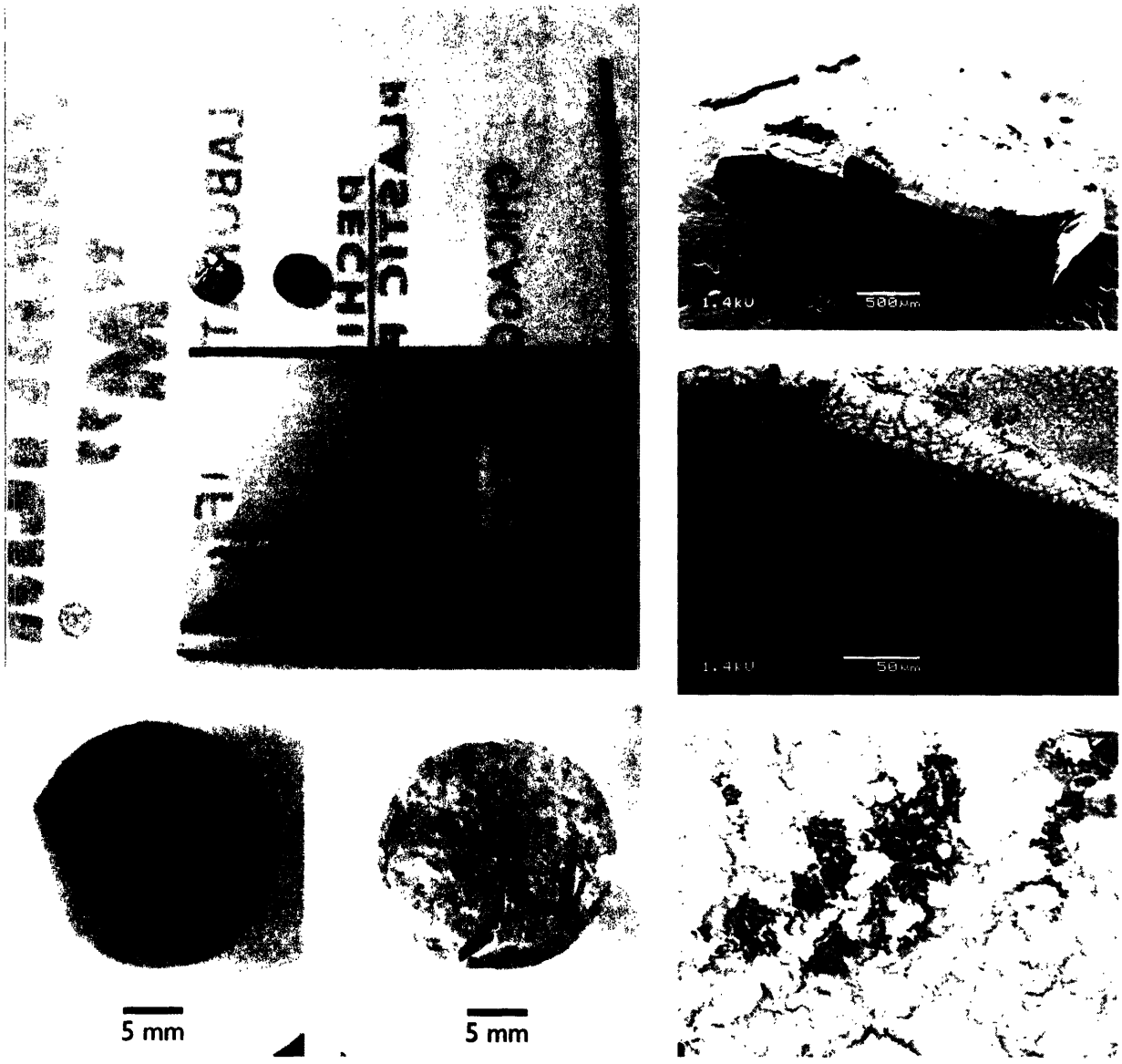

Figure 4-8 Photograph of Re1050 carbon aerogel monoliths showing Re-metallized surface and unmetallized bottom *(top, left)*; optical microscope images of Re1050 monoliths showing metallized and unmetallized surfaces *(bottom, left and center)*; cross-section of Re1050 under SEM showing no Re metallization on the interior of the monolith *(top, right)*; detail of interface between the metallized surface and unmetallized interior under SEM *(middle, right)*; metallized layer at 10 microns, showing Re layer hugging the contours of the aerogel surface *(bottom, right)*.

Figure 4-9 shows Re800 samples as seen under TEM. Similar to the Fe and Rh systems, sponge-like nanocrystalline carbon aerogel containing dark regions of Re metal is seen. However, instead of a few dark metal crystallite spots dispersed among large regions of aerogel, clusters of leaf-like structures hugging the carbon aerogel structure are seen. This is the first metal-doped carbon aerogel system to display this type of morphology.

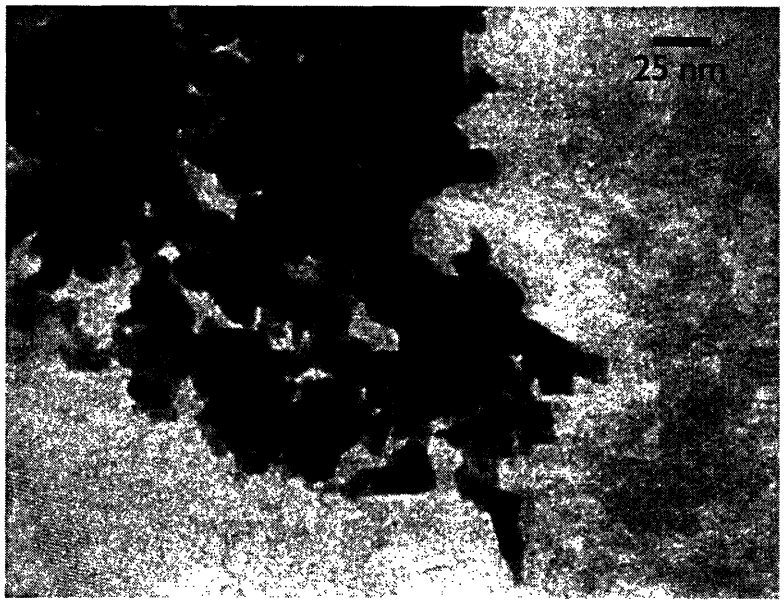

Figure 4-9 TEM micrograph of Re800 showing unusual dark, leaf-like clusters of Re (left) hugging sponge-like carbon aerogel structure.

X-Ray Photoelectron Spectroscopy Analysis

XPS spectra for rhenium-doped carbon aerogels pyrolyzed at 800°C and 1050°C are shown in Figure 4-10. As mentioned earlier, XPS analysis was performed on powderized samples and not only on monolith surfaces, as to give the most representative view of the material's surface chemistry.

It should be noted that the Re $5p_{1/2}$ peak falls within the energy window of the Re 4f region, however the relative sensitivity factor (RSF) for these photoelectrons is only 0.387, compared with an RSF of 11.1 for Re 4f photoelectrons and thus the signal contribution from this peak is negligible. Like the Rh system, deconvolution of the carbon region for both Re800 and Re1050 shows the presence of two carbon

chemistries and a broad, high-binding-energy π-π^* shake-up satellite. Both the π-π^* shake-up peak and peak centered near 285 eV become slightly more pronounced from the 800°C to 1050°C pyrolysis temperature, suggestive of an enhanced signal contribution from graphitic surface domains. Unlike the Rh system, the O 1s region shows the presence of two oxygen chemistries. Deconvolution of the Re 4f region reveals the presence of three rhenium chemistries in Re800. The spin-orbit splitting peaks at 40.1 and 42.5 eV are attributable to metallic Re. The peaks at 40.1 and 43.2 eV are likely attributable to rhenium(IV) oxide [77]. The high-binding-energy peaks at 45.0 and 47.5 eV then match well with rhenium(VI) oxide. The rhenium(IV) chemistry seems to disappear at 1050°C in favor of metallic rhenium, which indicates the nanocrystalline carbon in the aerogel effectively reduces this species from the surface of rhenium-containing nanoparticles during pyrolysis. The presence of surface-accessible metallic rhenium in both samples suggests that if rhenium can catalyze carbon nanotube growth, either sample should do so effectively.

Elemental compositions as determined from peak fitting are listed in Table 4-7. Interestingly, the rhenium loading is 1.5-2.5% by mass, approximately twice as effective as Rh or Fe by atomic percent. It seems that aprotic DMF-based ion exchange may be more effective in displacing K^+ in the phenolic gel precursor than aqueous exchange.

Effects of Chemical Vapor Deposition

As a starting point for CVD growth, the optimal conditions determined for the Fe system and successful in the Rh system were again implemented—monoliths pyrolyzed at 800°C with CVD at 700°C for 10 min under a flow of 20 sccm ethylene, 30 sccm methane, and 500 sccm hydrogen. These conditions were in fact successful in growing carbon nanotubes on Re800 monoliths, however at much lower yield than for either Fe or Rh. SEM micrographs of Re800-700 samples are shown in Figure 4-11. The nanotubes again appear to be multiwalled, which is to be expected based on the average rhenium crystallite size detected by XRD. With the major observed difference between the Re and Rh system being the presence of oxidized

nanoparticle surfaces in the Re system, the reduction in yield is attributed to the inability of rhenium oxide-coated nanoparticles to catalyze growth, where the oxide-free nanoparticles are capable of catalyzing growth.

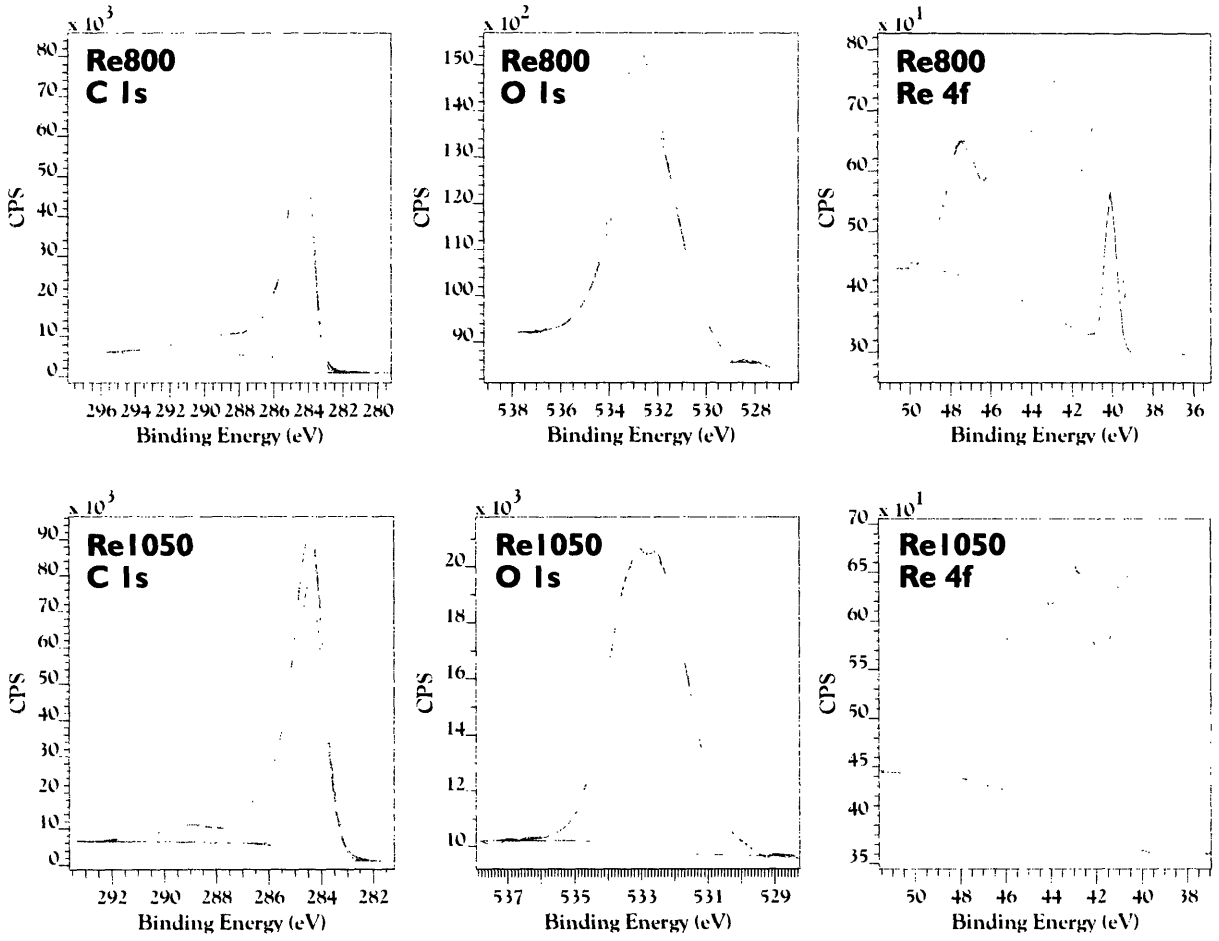

Figure 4-10 *(Top, left to right)* C 1s, O 1s, and Re 4f regions of the XPS spectrum for Re800; *(bottom, left to right)* C 1s, O 1s, and Re 4f regions of the XPS spectrum for Re1050.

Sample	Energy Region	Assignment	Position (eV)	FWHM (eV)	Area (eV counts)	R.S.F.*
	C 1s	Amorphous	284.31	1.11	25850.4	1
	C 1s	sp^2 Carbon	285.21	1.98	13323.2	1
	C 1s	π-π^* Shake-Up	288.23	6.00	11356.7	1
	O 1s	Carboxylate	532.45	2.94	4623.5	2.93
	O 1s	Re Oxides	533.03	1.35	640.8	2.93
Re800	Re 4f	Re^0 $4f_{7/2}$	40.08	0.66	72.2	11.1
	Re 4f	ReO_2 $4f_{7/2}$	40.84	1.87	279.3	11.1
	Re 4f	Re^0 $4f_{5/2}$	42.46	0.77	76.7	11.1
	Re 4f	ReO_2 $4f_{5/2}$	43.18	1.50	183.2	11.1
	Re 4f	ReO_3 $4f_{7/2}$	44.99	1.78	275.6	11.1
	Re 4f	ReO_3 $4f_{5/2}$	47.45	1.93	181.3	11.1
	C 1s	Amorphous	284.43	1.18	30848.7	1
	C 1s	sp^2 Carbon	285.43	2.40	18813.5	1
	C 1s	π-π^* Shake-Up	289.09	2.61	4275.4	1
	O 1s	Carboxylate	532.66	2.38	7678	2.93
Re1050	O 1s	Re Oxides	533.75	1.08	670	2.93
	Re 4f	Re^0 $4f_{7/2}$	40.63	1.59	189.8	11.1
	Re 4f	Re^0 $4f_{5/2}$	42.95	2.02	223.5	11.1
	Re 4f	ReO_3 $4f_{7/2}$	45.02	1.77	154.3	11.1
	Re 4f	ReO_3 $4f_{5/2}$	47.42	2.51	146.4	11.1

* Relative sensitivity factor

Table 4-6 Deconvolution results for XPS spectra of Re-doped carbon aerogels.

Sample	Element	% Mass Concentration	% Atomic Concentration
Re800	C	92.82	96.39
	O	4.40	3.43
	Re	2.79	0.19
Re1050	C	91.72	94.81
	O	6.53	5.07
	Re	1.75	0.12

Table 4-7 Elemental compositions of Re-doped carbon aerogels as determined by XPS.

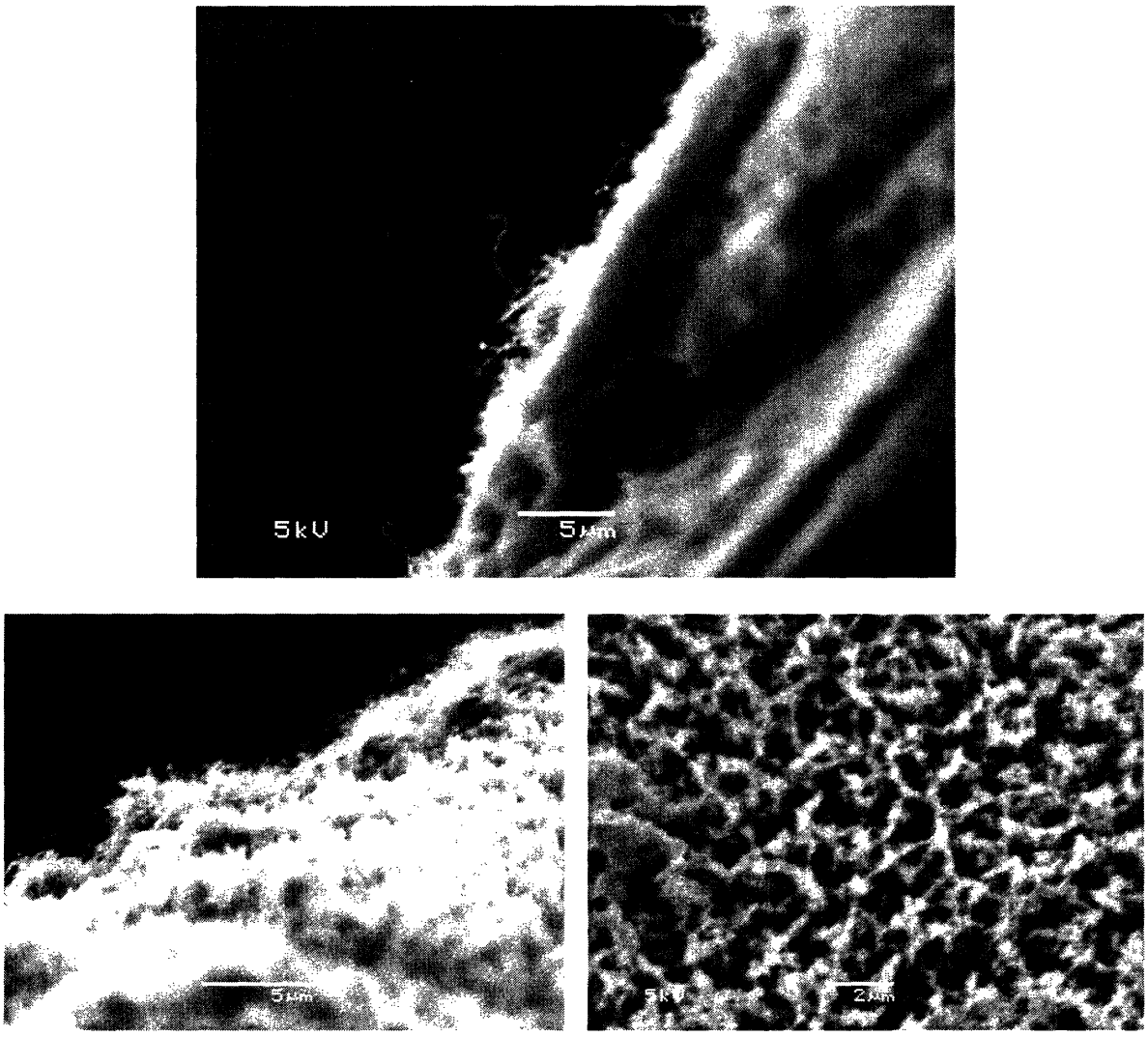

Figure 4-11 Successful growth of carbon nanotubes on rhenium-doped carbon aerogels *(top and bottom left)*. Nanotubes are present at every location on the monolith, however in a smaller population than observed for Re or Fe. Nanotubes can also be resolved overhead against the aerogel background *(bottom right)*.

To verify the fibers seen under SEM were indeed carbon nanotubes, scrapings from the exterior surfaces of Re800-700 monoliths were analyzed under TEM (Figure 4-12). Again, clusters of leaf-like Re crystallites are observed, however this time with what is clearly multiwalled carbon nanotubes emanating from them. Large, tangled masses of defective, multiwalled nanotubes are observed.

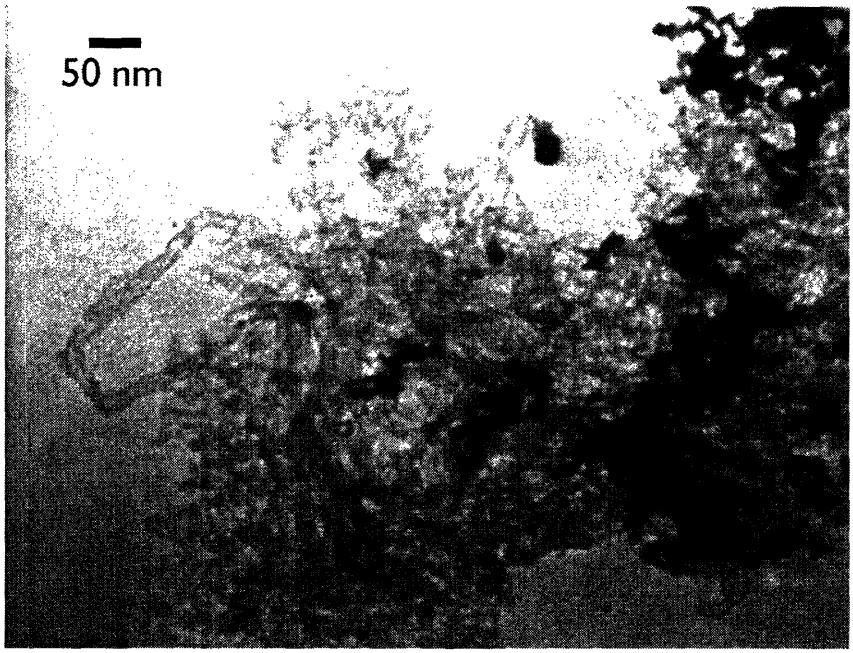

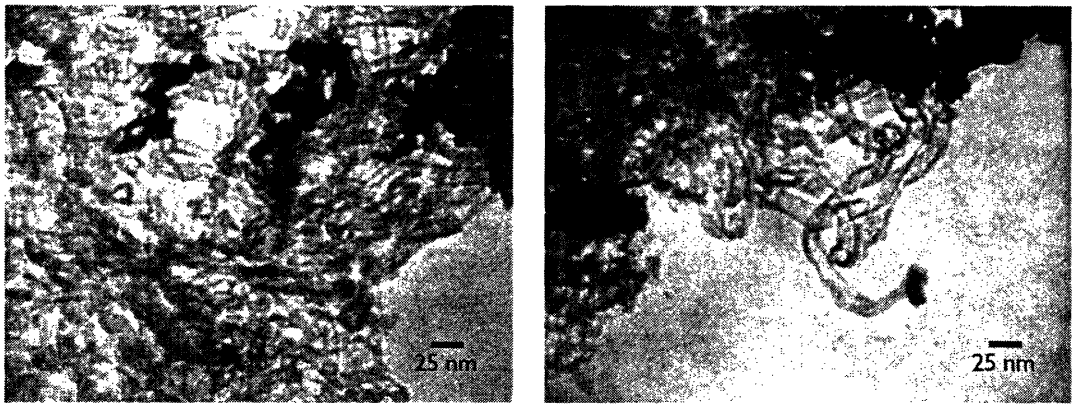

Figure 4-12 Defective, multiwalled nanotubes growing from Re nanoparticles embedded in a carbon aerogel matrix *(top)*; tangled mass of nanotubes extending from Re nanoparticle clusters *(bottom left)*; detail of nanotubes extending from Re-doped carbon aerogel surface *(bottom right)*.

Conclusions

Rhenium is capable of catalyzing carbon nanotube growth. As seen from XRD analysis of Re nanoparticles formed through pyrolysis of Re-doped carbon aerogels, Re seems to be immune to carburization. Unlike Rh, Re is victim to forming what is concluded to be uncatalytic oxide surfaces.

The fact that rhenium is capable of catalyzing nanotube growth provides evidence against the necessity for a vapor-liquid-solid (VLS) growth mechanism for

carbon nanotubes. Given that the mean crystallite diameter of rhenium nanoparticles in this system was measured to be between 14 and 17 nm, the nanoparticles are too large for any significant reduction in melting point due to size effects [107]. Thus, the melting point of rhenium nanoparticles in this system is expected to be approximately the same as the bulk melting point of bulk rhenium. As the bulk melting point of rhenium is 3186°C (compared with that of iron at 1538°C), at no time during pyrolysis or CVD do the nanoparticles approach their melting point. Furthermore, rhenium and carbon form a simple eutectic system at 16.9 atomic percent carbon at a temperature of 2480°C [105], again too high for the temperatures encountered in this study. Taking into account these considerations, it is concluded that at no time are the nanoparticles which catalyze nanotube growth in this system in a liquid state or close to being in a liquid state, precluding a VLS growth mechanism in this system.

The absence of carbides in the rhenium-carbon phase diagram provides further evidence that formation of a metal carbide is not required for nanotube growth, and would further suggest that observations of metal carbide nanoparticles embedded in the tips of nanotubes are likely poisoned or partially-poisoned species as opposed to the active catalyst from which the nanotube grew [32, 41, 42, 92, 99]. It is also possible that for some metals a carbide intermediate does occur during nanotube growth, but given the results obtained for Rh- and Re-doped carbon aerogels in this work, carbides are apparently not prerequisite. If carbide formation is in fact a poisoning mechanism, rhodium and rhenium may exhibit longer catalytic lifetimes in a thermal CVD process than iron, cobalt, or nickel, which would lend them to be better suited for growth of indefinitely long carbon nanotubes. Investigations into the lifetime of rhodium and rhenium catalysts are underway.

The unusual precipitation of and wetting of the carbon aerogel by rhenium metal suggests Re-doped carbon aerogels could be useful precursors in forming nanoporous metal substrates or producing high-surface-area metal-coated electrodes. Further investigations of this phenomenon are also underway.

4.3.3 The Gold System

Gold, like rhenium, is a so-called carbophobe. Gold and carbon in the solid state are essentially insoluble in one another, and no carbide is observed in the phase diagram at ambient pressures [104, 108]. The equilibrium phase of liquid Au-C consists of approximately 4.7 atomic percent carbon, with the face-centered cubic terminal solid solution (Au-like) having approximately 0.08 atomic percent solid solubility of carbon in gold, and the graphite-type terminal solid solution (C-like) exhibiting no solubility of gold [108]. It generally does not oxidize, however under conditions involving oxygen-containing radicals (such as those found in thermal CVD), Au_2O_3 can form [109-114]. Au has been demonstrated to catalyze nanotube growth previously [95] and so it is expected to catalyze nanotube growth in a carbon aerogel as well.

Description of Monoliths

Au-doped phenolic aerogels were afforded as opaque orange/clay-colored monoliths. This coloration was verified to be uniform throughout the interior of the monoliths as well. The density of the monoliths was surprisingly high at 0.55 g cm^{-3}, although the volume of the discs was comparable to the other metal-doped carbon aerogels investigated in this chapter. The mass of the monoliths, however, were about twice as high as the other metal-doped carbon aerogels, indicating the high density is not due to a densified aerogel structure but likely due to a high metal loading into the aerogel.

Interestingly, pyrolysis of Au-doped phenolic aerogels results in the formation of a leopard print-like plating of a metallic gold thin film on the top and side edges of the resulting carbon aerogel monoliths (Figure 4-13). This phenomenon occurs at both 800°C and 1050°C pyrolysis temperatures. Like rhenium, the carbophobic nature of gold may be a governing factor in this behavior (see Section 4.3.2). Like the unpyrolyzed aerogels, the density of the pyrolyzed monoliths was also surprisingly high at 1.21 g cm^{-3}. This was verified by XPS and TEM not to be due to densification of the aerogel structure, but instead to a tremendously high loading of gold into the aerogel.

Figure 4-13 Gold plating of exterior monolith surfaces observed on Au-doped carbon aerogels.

X-Ray Diffraction Analysis

Figure 4-14 shows the powder XRD spectra for Au-doped carbon aerogels pyrolyzed at 800°C and 1050°C. Again a broad nanocrystalline carbon peak is observed at approximately 24° two-theta. Most notable is the intense signal strength of the gold reflections [115] in comparison to the nanocrystalline carbon peak. Based on this observation, it would be expected that there is a much larger amount of crystalline metal in the aerogels than observed for Fe, Rh, or Re systems. Table 4-8 lists measured peak positions, full-width at half-maximum (FWHM) values, relative intensities, and calculated crystallite sizes for Au800 and Au1050 samples. A small increase in the mean diameter of carbon crystallites (from 0.7 to 1.0 nm) and gold crystallites (from 25.4 to 28.0 nm) is observed with an increase in pyrolysis temperature. The increase in carbon crystallite size indicates a slight ordering effect by the gold on the nanocrystalline carbon framework of the aerogel. The increase in gold crystallite size is expected and consistent with a single-component particle coarsening mechanism. No peaks attributable to gold oxide are present, and all peaks are well accounted for, indicating the presence of only carbon and metallic gold crystallites throughout the aerogel. The mean gold crystallite diameter is larger than this value in the Rh and Re systems, and if nanotube growth is successful, larger diameter nanotubes would be expected.

X-Ray Photoelectron Spectroscopy Analysis

XPS spectra for Au-doped carbon aerogels pyrolyzed at 800°C and 1050°C are shown in Figure 4-15. Four carbon chemistries are required to properly account for the C 1s region peak shape, unlike in the cases of the Rh and Re systems. An extra peak close in binding energy to the primary aerogel carbon peak appears. As Au is an active heterogeneous catalyst for many different types of hydrocarbon transformations, it is assumed this extra carbon chemistry is due to aliphatic carbon from hydrocarbons catalyzed by the gold during pyrolysis. It has been observed that pyrolysis of gold-doped carbon aerogels results in a deposition of waxy, pale yellow solids with an asphalt-like smell outside of the hot zone of the quartz process tube, which further supports this claim.

Two chemistries of Au are required to properly deconvolute the Au 4f region of the XPS spectra. The major chemistry (with a spin-orbit split pair at binding energies of 84.0 and 87.7 eV) matches that of metallic Au [77]. At slightly higher binding energy is another chemistry with diminished intensity. This is not believed to be attributable to Au_2O_3, which appear at a higher binding energy, and is instead assumed to be a sulfide tarnish on the surface of metallic Au nanoparticles.

Sample	Assigned Reflection	2-θ (°)	FWHM (°)	Relative Peak Height	Crystallite Size (nm)
Au800	Au (111)	38.3	0.32	1.00	27.9
	Au (100)	44.5	0.36	0.47	24.7
	Au (220)	64.7	0.39	0.30	24.8
	Au (311)	77.7	0.44	0.31	24.1
	C (Amorph)	24.0	11.04	-	0.7
Au1050	Au (111)	28.3	0.29	1.00	31.0
	Au (200)	44.5	0.33	0.49	27.5
	Au (220)	64.7	0.35	0.35	27.8
	Au (311)	77.7	0.41	0.39	25.8
	C (Amorph)	24.1	7.91	-	1.0

Table 4-8 Analysis of XRD spectra for Au-doped carbon aerogels.

Table 4-10 lists calculated elemental compositions for Au800 and Au1050. As expected from the intense signal intensity from Au reflections in the XRD spectra, a significantly higher loading of gold (21-22% by mass) is detected than in the Fe, Rh,

and Re systems. The high acidity of auric acid ($AuCl_4H$) used to dope the aerogel may promote the ion exchange process in the precursor gel, resulting in a higher loading of gold than other metals. Figure 4-16 shows a TEM micrograph of Au800, verifying a large abundance of gold throughout the aerogel.

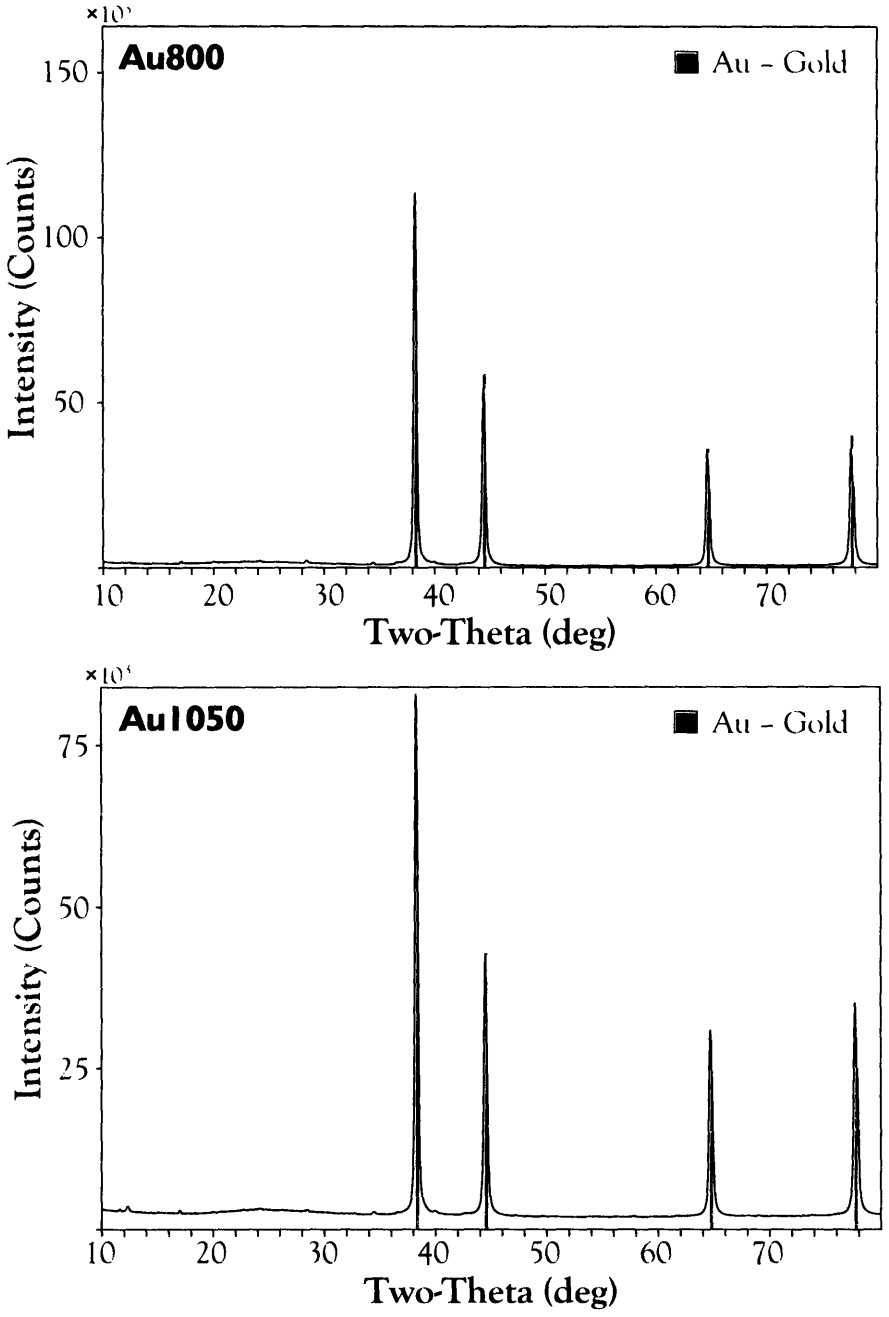

Figure 4-14 Powder XRD spectra and phase identification for Au-doped carbon aerogels. The nanocrystalline carbon peak at 24° two-theta is dwarfed by intense reflections from Au.

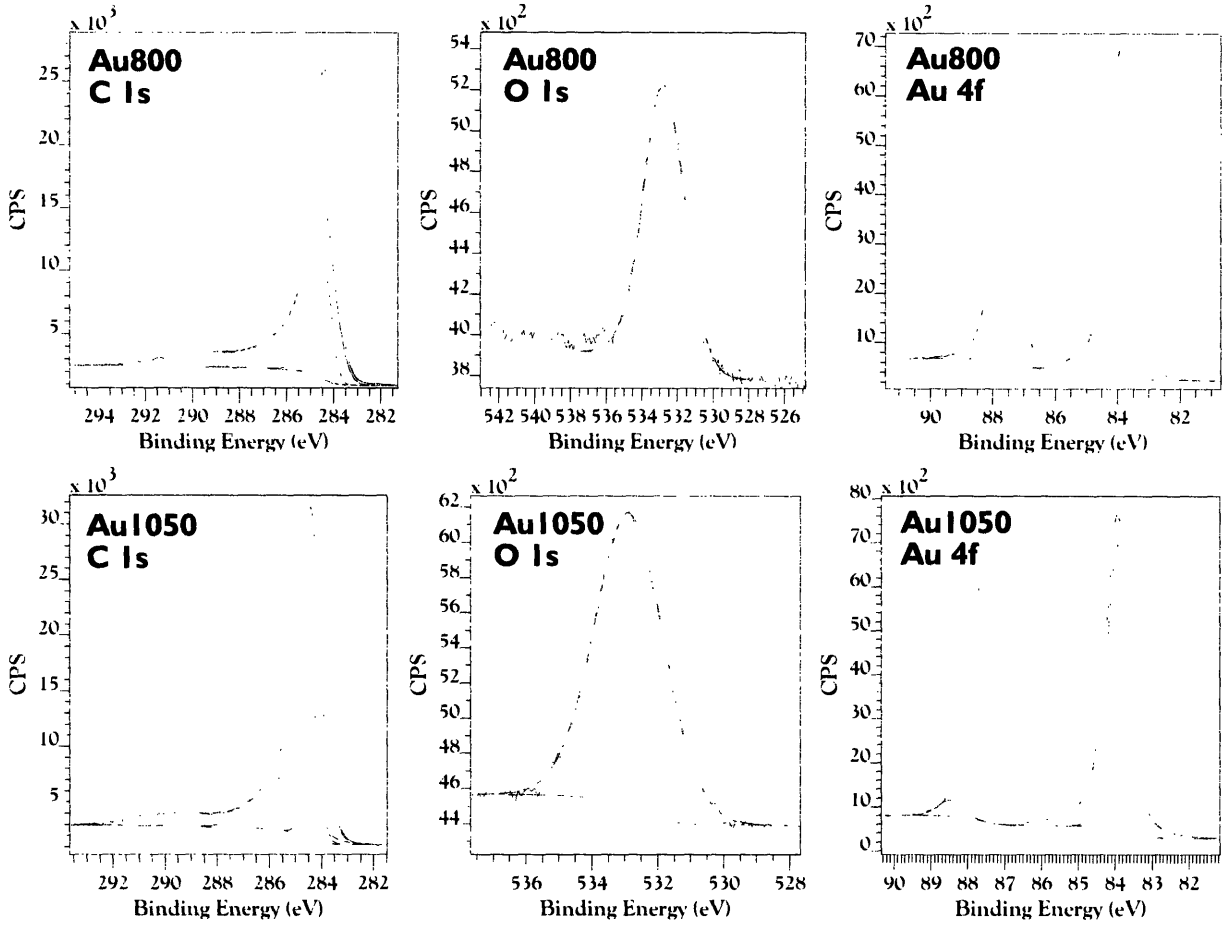

Figure 4-15 *(Top, left to right)* C 1s, O 1s, and Au 4f regions of the XPS spectrum for Au800; *(bottom, left to right)* C 1s, O 1s, and Au 4f regions of the XPS spectrum for Au1050.

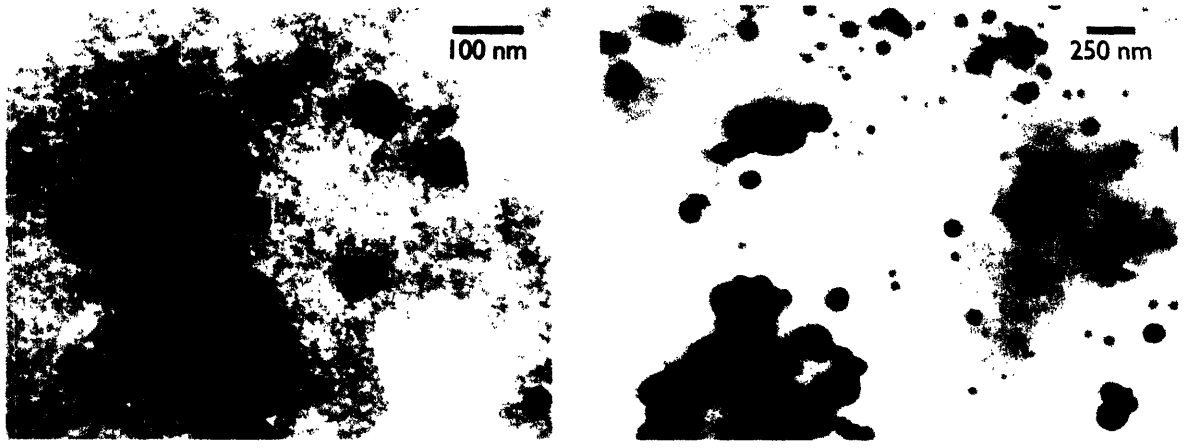

Figure 4-16 TEM micrographs of Au-doped carbon aerogel pyrolyzed at 800°C with a high loading of gold, resulting in a large population of gold crystallites (dark regions).

Sample	Energy Region	Assignment	Position (eV)	FWHM (eV)	Area (eV counts)	R.S.F.*
	C 1s	Aliphatic	284.4	0.67	4793.0	1
	C 1s	Amorphous	284.55	1.20	14779.4	1
	C 1s	sp^2 Carbon	285.53	2.43	7513.0	1
	C 1s	π-π^* Shake-Up	288.94	4.71	4756.6	1
Au800	O 1s	Carboxylate	532.78	2.70	2904.7	2.93
	Au 4f	Au $4f_{7/2}$	83.97	0.67	3567.0	17.1
	Au 4f	Tarnish? Au $4_{f7/2}$	84.13	1.65	1871.2	17.1
	Au 4f	Au $4f_{5/2}$	87.66	0.65	2513.4	17.1
	Au 4f	Tarnish? $4f_{5/2}$	87.71	1.57	1735.7	17.1
	C 1s	Aliphatic	284.39	0.63	6914.2	1
	C 1s	Amorphous	284.55	1.21	15486.4	1
	C 1s	sp^2 Carbon	285.53	2.23	8785.7	1
	C 1s	π-π^* Shake-Up	289.19	4.25	4543.1	1
Au1050	O 1s	Carboxylate	532.88	2.43	3215.6	2.93
	Au 4f	Au $4f_{7/2}$	83.96	0.70	4441.5	17.1
	Au 4f	Tarnish? $4f_{7/2}$	84.21	2.26	1577.7	17.1
	Au 4f	Au $4f_{5/2}$	87.63	0.76	4030.0	17.1
	Au 4f	Tarnish? $4f_{5/2}$	88.51	0.77	259.6	17.1

* Relative sensitivity factor

Table 4-9 Deconvolution results for XPS spectra of Au-doped carbon aerogels.

Sample	Element	% Mass Concentration	% Atomic Concentration
	C	74.80	95.22
Au800	O	3.22	3.08
	Au	21.98	1.71
	C	75.74	95.48
Au1050	O	3.06	2.90
	Au	21.20	1.63

Table 4-10 Elemental compositions of Au-doped carbon aerogels as determined by XPS

Effects of Chemical Vapor Deposition

The optimal CVD conditions employed successfully in the Fe, Rh, and Re system were again used as a starting point for attempting nanotube growth—monoliths pyrolyzed at 800°C, with CVD performed at 700°C for 10 min under a flow of 20 sccm ethylene, 30 sccm methane, and 500 sccm hydrogen. Figure 4-17 shows SEM images of Au800-700/10 (10-minute growth) and Au800-700/25 (25-minute growth) samples. At high magnification, fibers not present in untreated Au800 samples are visible on Au800-700/10. To the experienced eye, it is evident that short-length

multiwall nanotubes and/or carbon fibers are present on the aerogel background and are not imaging artifacts.

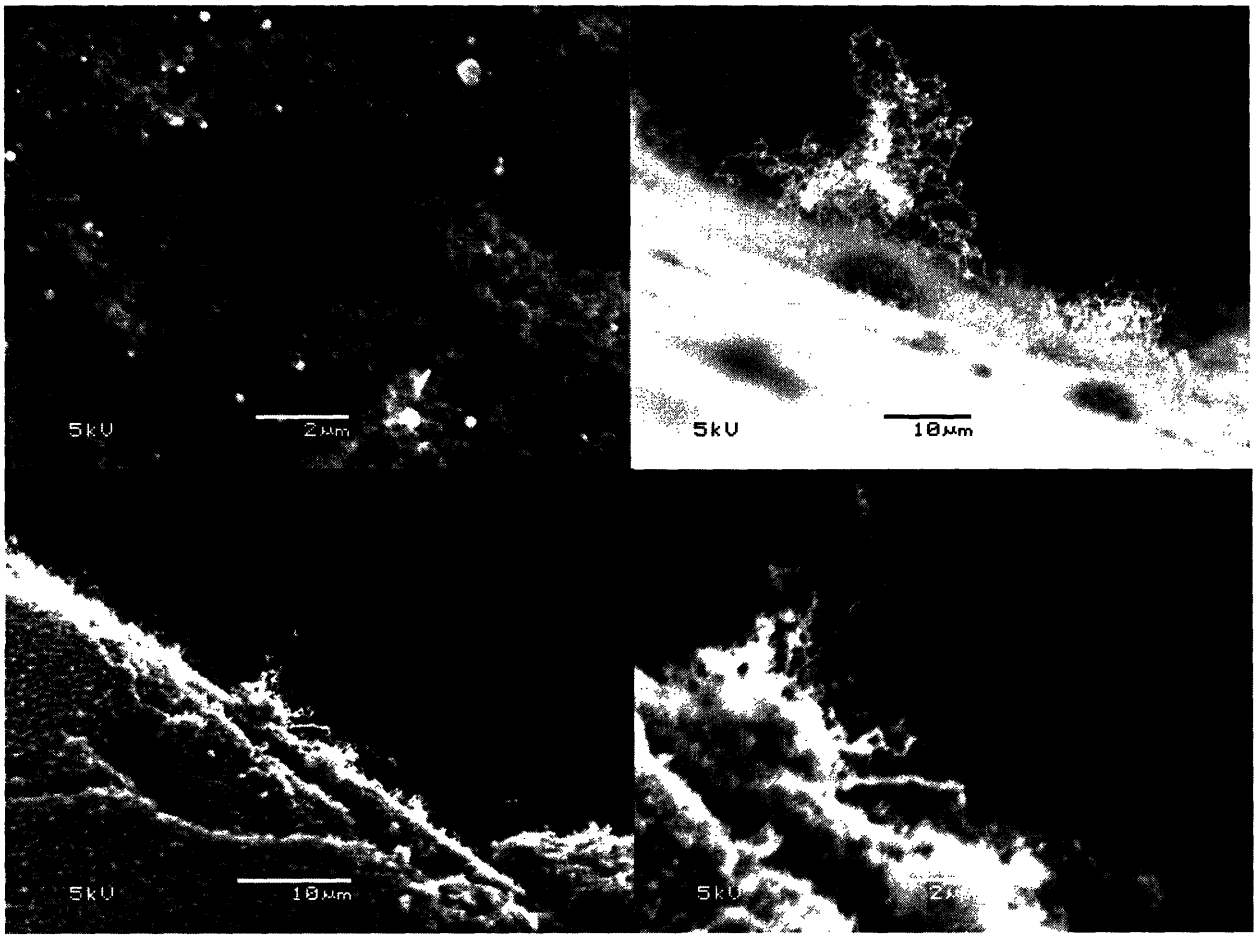

Figure 4-17 Growth of large diameter defective multiwall nanotubes and carbon fibers on Au800 monolith after 10-minute CVD process *(top left)*; long, small diameter nanotubes on Au800 monolith after 25-minute CVD process *(top right)*; edge shot of Au800-700/25 showing assortment of small-diameter nanotubes, multiwall nanotubes, and carbon fibers *(bottom left)*; detail of Au800-700/25 edge shot *(bottom right)*.

To verify this was indeed the case, samples of Au800-700/25 were prepared. Edge shots of these samples clearly reveal successful growth of small-diameter carbon nanotubes, multiwall nanotubes, and larger diameter carbon fibers. The absence of obvious small-diameter and multiwall nanotubes on the edge of Au800-700/10 may be due to the following scenario. As seen under TEM, Au800 samples contain Au nanoparticles with a wide distribution of sizes. The larger of these

particles have untarnished or thinly tarnished surfaces and are either capable of growing nanotubes or fibers immediately or are sufficiently reduced by hydrogen in the CVD stream within 10 minutes to become catalytically active. The smaller of these particles are more likely to have more heavily tarnished surfaces due to surface energy considerations, effectively coated with an uncatalytic shell, and are not sufficiently reduced within 10 minutes to initiate nanotube growth. This shell is effectively reduced by hydrogen within the time span of a 25-minute growth, however, during which they become catalytically active (metallic) and can grow the smaller-diameter nanotubes that are observed. This notion of *in situ* reduction of catalyst particles is not unique to Au-doped carbon aerogels, nor to Au itself [75], and plays an important role in implementation of Fe catalysts in determining effective CVD process parameters.

Conclusions

Au successfully catalyzes growth of carbon nanotubes, providing further evidence that nanotubes growth does not require carbide intermediates. Growth of carbon nanotubes and carbon fibers can be achieved on Au-doped carbon aerogel monoliths. A reductive treatment may be necessary to activate Au nanoparticles which possess a native oxide shell before growth of nanotubes can begin.

Despite differences in melting points, chemical behavior, and affinity for carbon, Fe-, Rh-, Re-, and Au-doped carbon aerogels have all successfully grown carbon nanotubes in some form under the same CVD conditions. This suggests that the primary activation energy required for nanotube growth is likely independent of the metal used and more a consideration of thermal cracking of the CVD gases and hidden "built-in" reduction processes required to activate certain catalysts.

Additionally, like the rhenium system, gold-doped carbon aerogels may be useful precursors for producing metal-plated nanoporous materials for use as electrodes, in hydrogen storage, and high-surface-area catalysts.

4.3.4 The Niobium System

Unlike the carbophobic metals rhodium, rhenium, and gold, niobium (a Group VB metal) readily forms stable carbides and oxides [116]. Like both rhenium and molybdenum (which is used frequently in conjunction with cobalt and iron), niobium exhibits multiple thermodynamically-accessible oxidation states at room temperature and above, and possesses a high (2468°C) melting point. No examples of Nb-catalyzed growth of carbon nanotubes (or examples of growth with any of the Group VB metals) were found in the literature as of the date this thesis was completed. Demonstration of nanotube growth using Nb catalysts would extend the metals available for use in engineering new catalyst alloys for research on how to control the metal-to-semiconducting ratio of single-walled carbon nanotubes grown through thermal CVD processes [91].

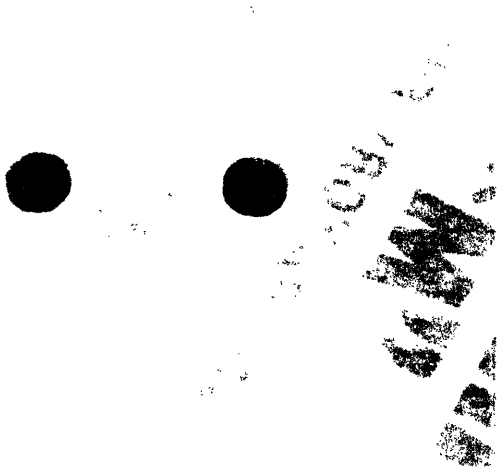

Figure 4-18 Photograph of Nb800 monoliths coated with slate-blue film.

Description of Monoliths

Figure 4-18 shows a photograph of Nb-doped carbon aerogels pyrolyzed at 800°C. The outer surfaces of the monoliths are coated with a slate-blue film, assumed to be Nb_2O_5. This film on the exterior of the monoliths was also observed for samples pyrolyzed at 1050°C. The density of the Nb-loaded phenolic aerogel precursors was measured to be 0.25 g cm^{-3}, increasing to 0.31 g cm^{-3} after pyrolysis.

X-Ray Diffraction Analysis

XRD spectra for Nb-doped carbon aerogels pyrolyzed at 800°C and 1050°C are shown in Figure 4-19. Curiously, Nb800 exhibits virtually no structure other than an nanocrystalline carbon peak centered at 24° two-theta. Nb1050 exhibits definite structure in its spectrum, with broad peaks matching the expected peak positions for niobium carbide [117] (see Figure 4-19) but a mean crystallite size of only approximately 2.0 nm (see Table 4-11). It appears that in both samples, most of the niobium is dispersed in sub-nanometer domains too small for powder XRD to detect.

X-Ray Photoelectron Spectroscopy Analysis

Given the lack of information present in the XRD spectra and the likelihood that any niobium present in the aerogels is localized in sub-nanometer domains, XPS plays an important role in characterizing these materials. Figure 4-20 shows XPS spectra for Nb800 and Nb1050 samples. Table 4-13 lists calculated ratios of Nb, C, and O in these samples. Indeed Nb is present in both samples and apparently in an appreciable quantity—approximately 12 percent by mass (1.7-1.9 atomic percent). Only a single niobium chemistry is seen at high binding energy in the Nb 3d region of Nb800, attributed to Nb_2O_5 [77]. A second chemistry emerges in this region in Nb1050 which could potentially be NbO, however is more likely NbC, as this species is observed in the XRD spectrum of Nb1050 samples. The O 1s region clearly exhibits at least two different oxygen chemistries, further suggestive of the presence of Nb_2O_5 in both samples. Like the Au system, a carbon chemistry attributed to aliphatic hydrocarbons is also assigned.

Figure 4-21 shows TEM micrographs of Nb800. Very small dark crystallites < 5 nm in diameter are found embedded throughout the carbon aerogel framework along with occasional larger (approximately 35 nm) crystallites.

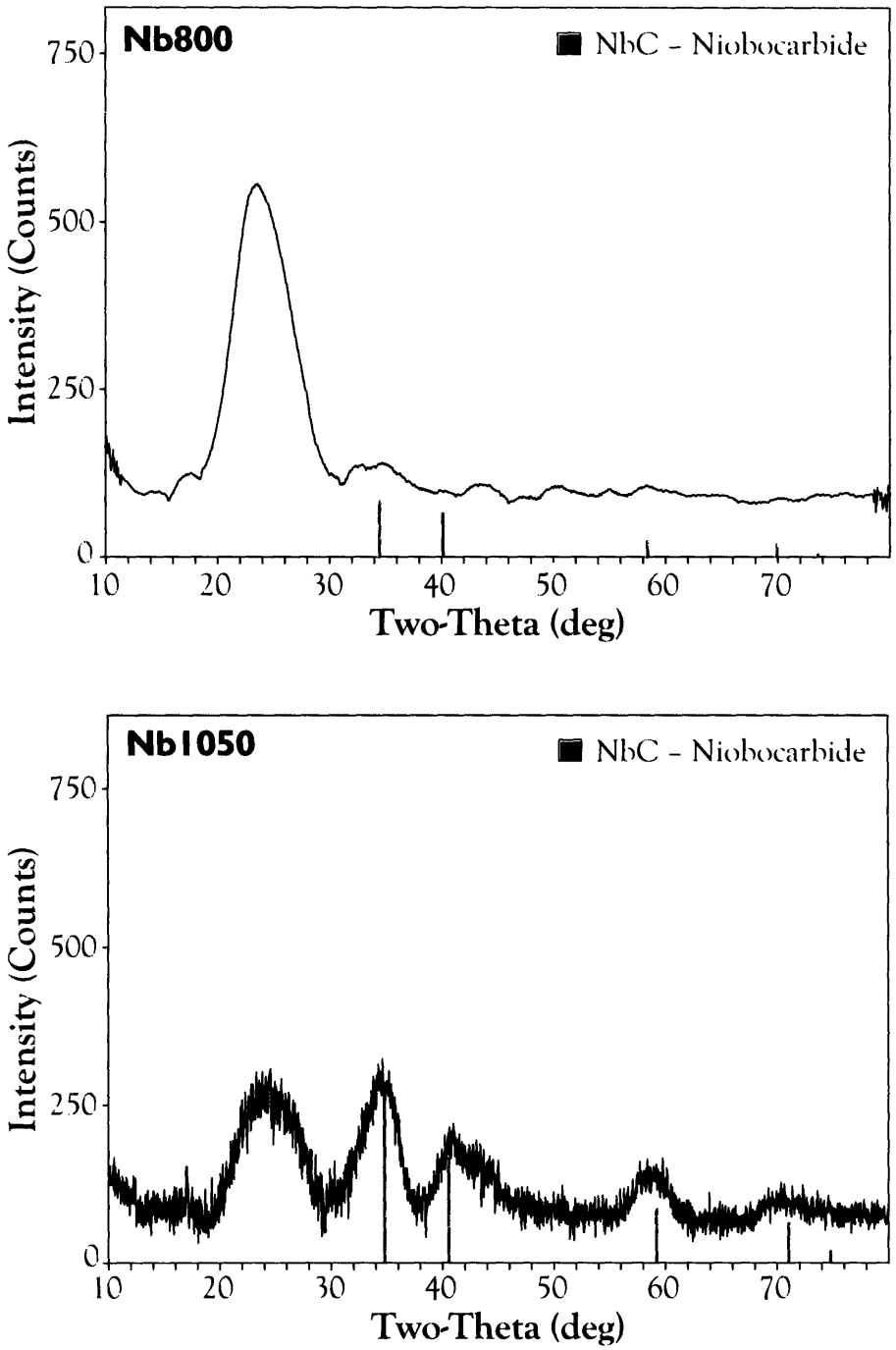

Figure 4-19 Powder XRD spectra and phase identification for Nb-doped carbon aerogels. No phase assignment can be made for Nb800 due to lack of X-ray reflections.

Sample	Assigned Reflection	2-θ (°)	FWHM (°)	Rel. Peak Height	Crystallite Size (nm)
Nb800	C (Amorph)	24.0	4.91	-	1.7
Nb1050	NbC (111)	34.7	3.46	1.00	2.4
	NbC (200)	40.5	5.37	0.51	1.6
	NbC (220)	59.0	3.32	0.34	2.8
	NbC (311)	69.8	7.19	0.14	1.3
	C (Amorph)	24.1	5.39	-	1.5

Table 4-11 Analysis of XRD spectra for Nb-doped carbon aerogels.

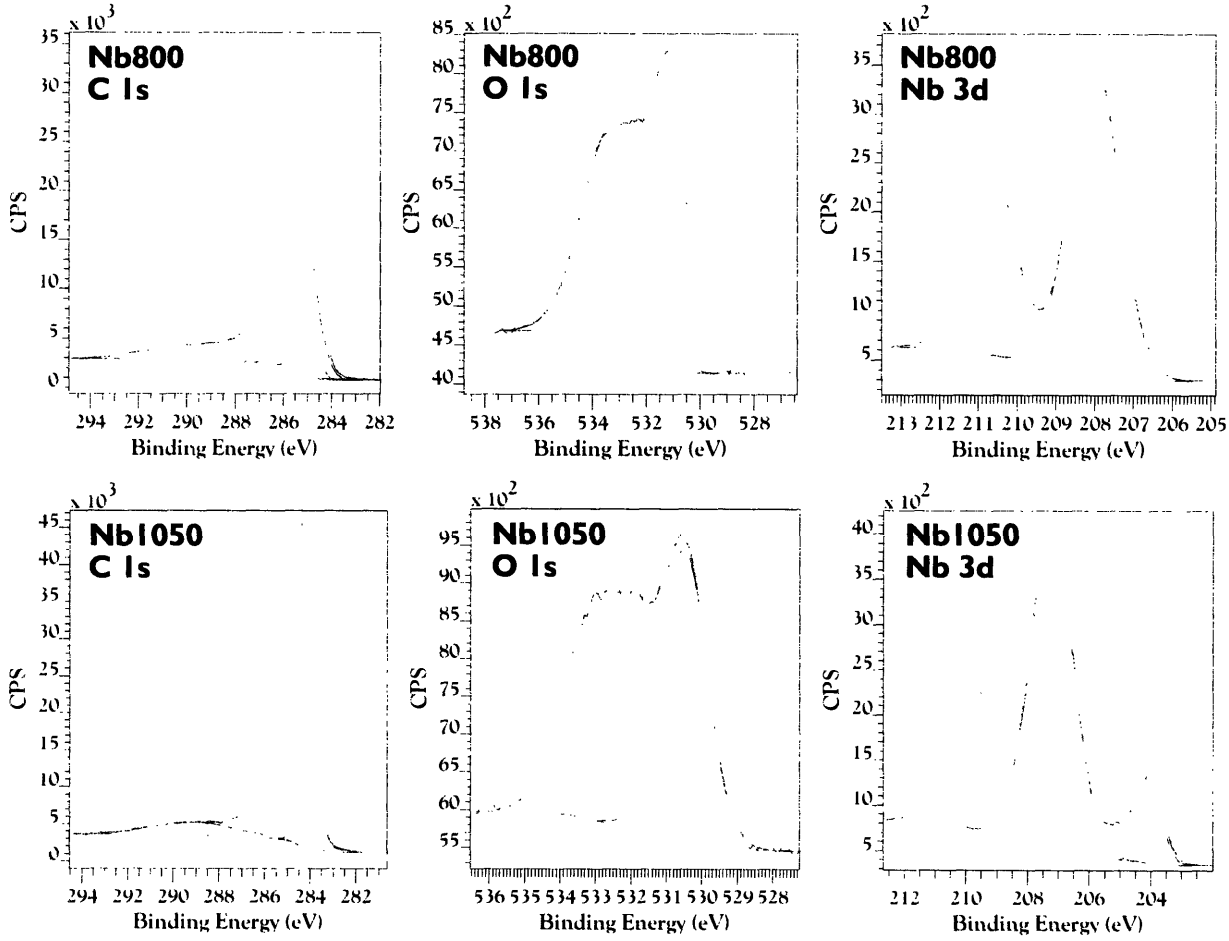

Figure 4-20 *(Top, left to right)* C 1s, O 1s, and Nb 3d regions of the XPS spectrum for Nb800; *(bottom, left to right)* C 1s, O 1s, and Nb 3d regions of the XPS spectrum for Nb1050.

Sample	Energy Region	Assignment	Position (eV)	FWHM (eV)	Area (eV counts)	R.S.F.*
	C 1s	Aliphatic	285.1	0.75	8905.2	1
	C 1s	Amorphous	285.3	1.26	17999.0	1
	C 1s	sp^2 Carbon	286.2	2.25	10194.0	1
	C 1s	π-π^* Shake-Up	289.3	4.91	7040.5	1
Nb800	O 1s	Carboxylate	531.2	1.51	4310.3	2.93
	O 1s	NbO_x ?	532.5	0.95	416.2	2.93
	O 1s	Nb_2O_5	533.4	2.43	5123.7	2.93
	Nb 3d	Nb_2O_5 $3d_{5/2}$	208.0	1.44	4160.2	8.21
	Nb 3d	Nb_2O_5 $3d_{3/2}$	210.8	1.43	2744.3	8.21
	C 1s	Aliphatic	284.4	0.67	10108.7	1
	C 1s	Amorphous	284.5	1.19	22897.0	1
	C 1s	sp^2 Carbon	285.4	2.51	14176.9	1
	C 1s	π-π^* Shake-Up	289.2	4.07	5993.6	1
	O 1s	Carboxylate	530.5	1.51	4596.1	2.93
Nb1050	O 1s	NbO_x ?	531.9	1.29	1663.0	2.93
	O 1s	Nb_2O_5	533.1	1.91	4135.1	2.93
	Nb 3d	NbC $3d_{5/2}$	204.0	0.78	546.7	8.21
	Nb 3d	NbC $3d_{3/2}$	204.7	1.57	634.3	8.21
	Nb 3d	Nb_2O_5 $3d_{5/2}$	207.2	1.62	5100.9	8.21
	Nb 3d	Nb_2O_5 $3d_{3/2}$	210.0	1.48	2738.1	8.21

* Relative sensitivity factor

Table 4-12 Deconvolution results for XPS spectra of Nb-doped carbon aerogels.

Sample	Element	% Mass Concentration	% Atomic Concentration
	C	80.02	91.27
Nb800	O	8.15	6.98
	Nb	11.83	1.74
	C	80.06	91.93
Nb1050	O	7.15	6.17
	Nb	12.79	1.90

Table 4-13 Elemental compositions of Nb-doped carbon aerogels as determined by XPS.

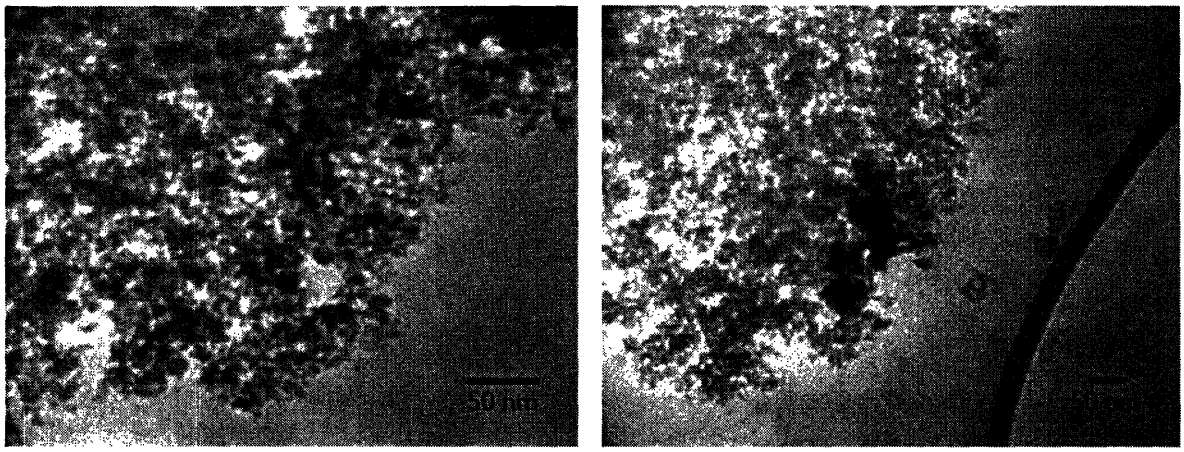

Figure 4-21 TEM micrographs of Nb800 sample showing small Nb-containing crystallites (dark spots) embedded throughout the amorphous carbon aerogel framework. These crystallites were too small to be detected by powder XRD.

Effects of Chemical Vapor Deposition

Given the lack of metallic niobium in the XPS and XRD spectra for both Nb800 and Nb1050, it was particularly uncertain whether nanotube growth would be successful or not. Again CVD was performed with the same conditions employed for the previous systems—monoliths pyrolyzed at 800°C were processed by CVD at 700°C for 10 min under a flow of 20 sccm ethylene, 30 sccm methane, and 500 sccm hydrogen. Figures 4-22 and 4-23 show SEM images of Nb800-700 samples. Carbon nanotubes are seen on the surface of the sample, however attached to unusual pillar-like structures protruding from the surface of the monolith. Close inspection of these structures shows they are covered in carbon nanotubes. Figure 4-24 shows TEM images of scrapings from the surface of a Nb800-700 sample. Several strange nanostructures are observed, including flat, circular and semi-circular "nanotortillas" littered among nanorods of some sort, possibly rolled-up versions of the nanotortillas ("nanoburritos"). The nanotortillas produce a hexagonal diffraction pattern and appear to be composed of graphite (Figure 4-24c, inset). Nanotubes are also seen, along with graphitic sheets and what appear to be hybrid structures of nanotubes shooting off from some sort of large-diameter carbon fibers.

It is uncertain whether or not the nanotortillas and nanorods are comprised of the same material. Interestingly, both types of structures are also observed in TEM images of Fe800/6-700/10 samples. The nanorods are presumed to be related to the nanotube-coated pillar-like structures seen under SEM. Inspection of the nanorods under high magnification reveals nanoparticles of some sort dotting their surface. One possibility is that the nanorods are composed of niobium oxide that, when exposed to hydrogen during CVD, form catalytically-active niobium nanoparticles on their surfaces. Further investigation would be required to verify this, however.

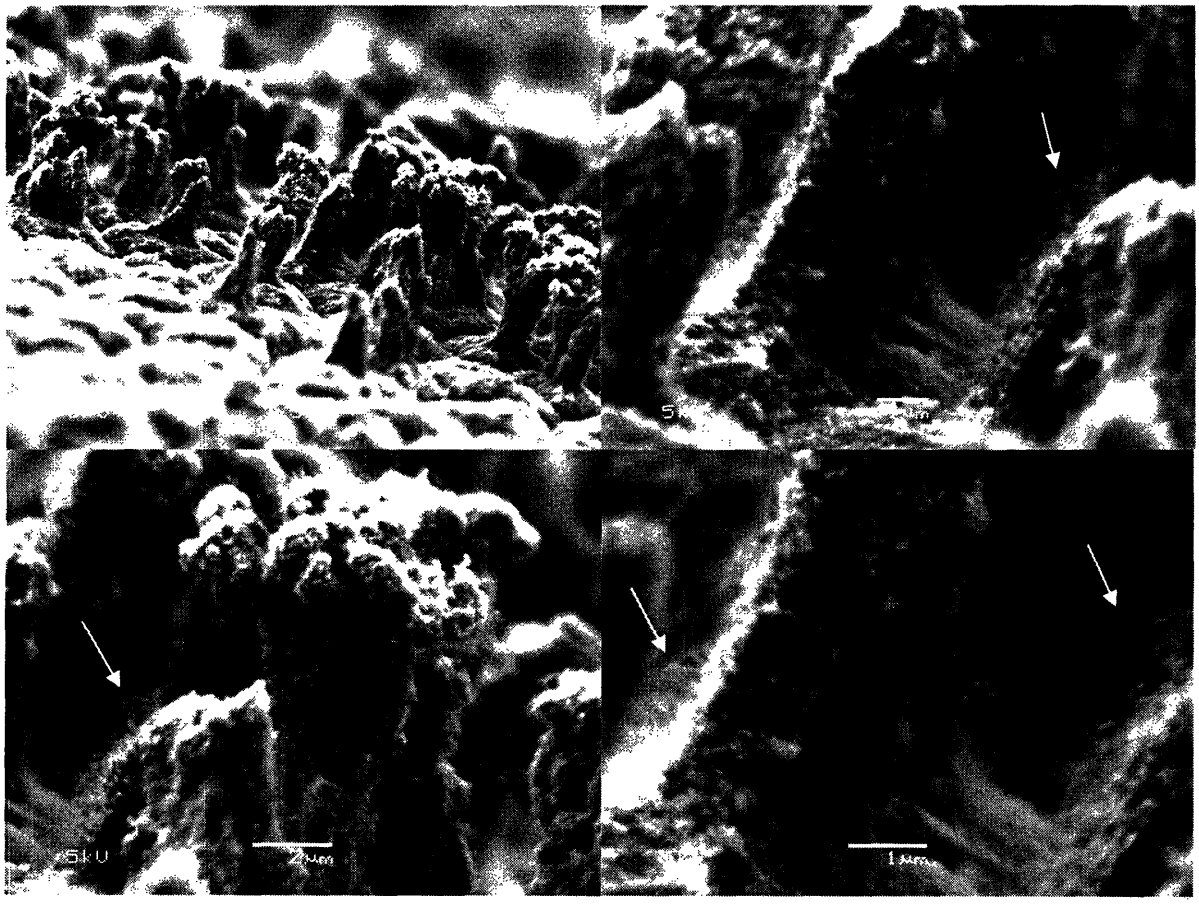

Figure 4-22 Pillar-like structures found covering Nb800-700 monoliths. Magnification of these structures reveals carbon nanotubes and carbon nanotube bundles pluming off their edges. Bundles of nanotubes are highlighted with white arrows.

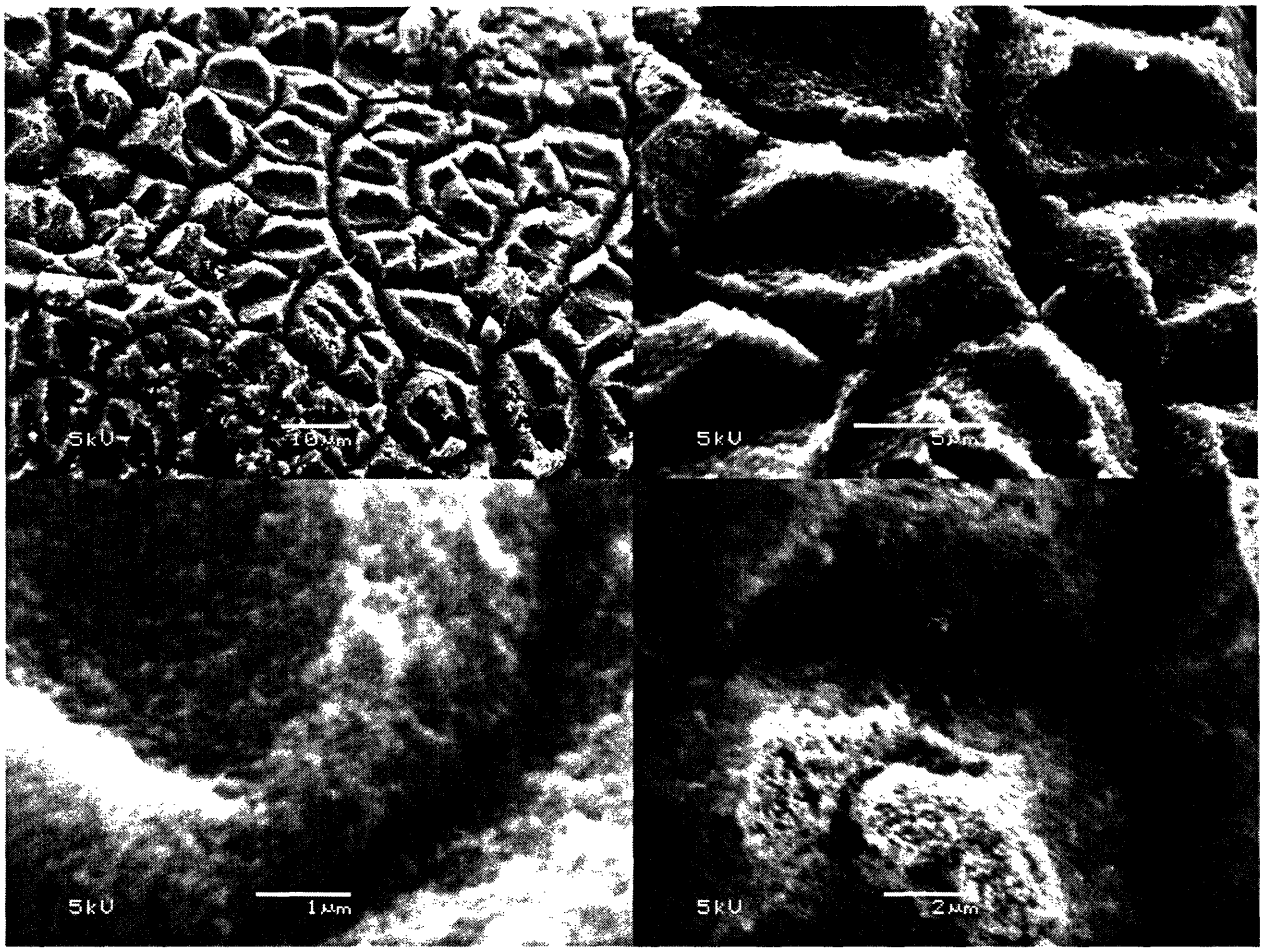

Figure 4-23 Top view of other pillar-like structures observed on Nb800-700 monoliths. At high magnification it becomes evident that the structures are covered in carbon nanotubes and carbon nanotube bundles.

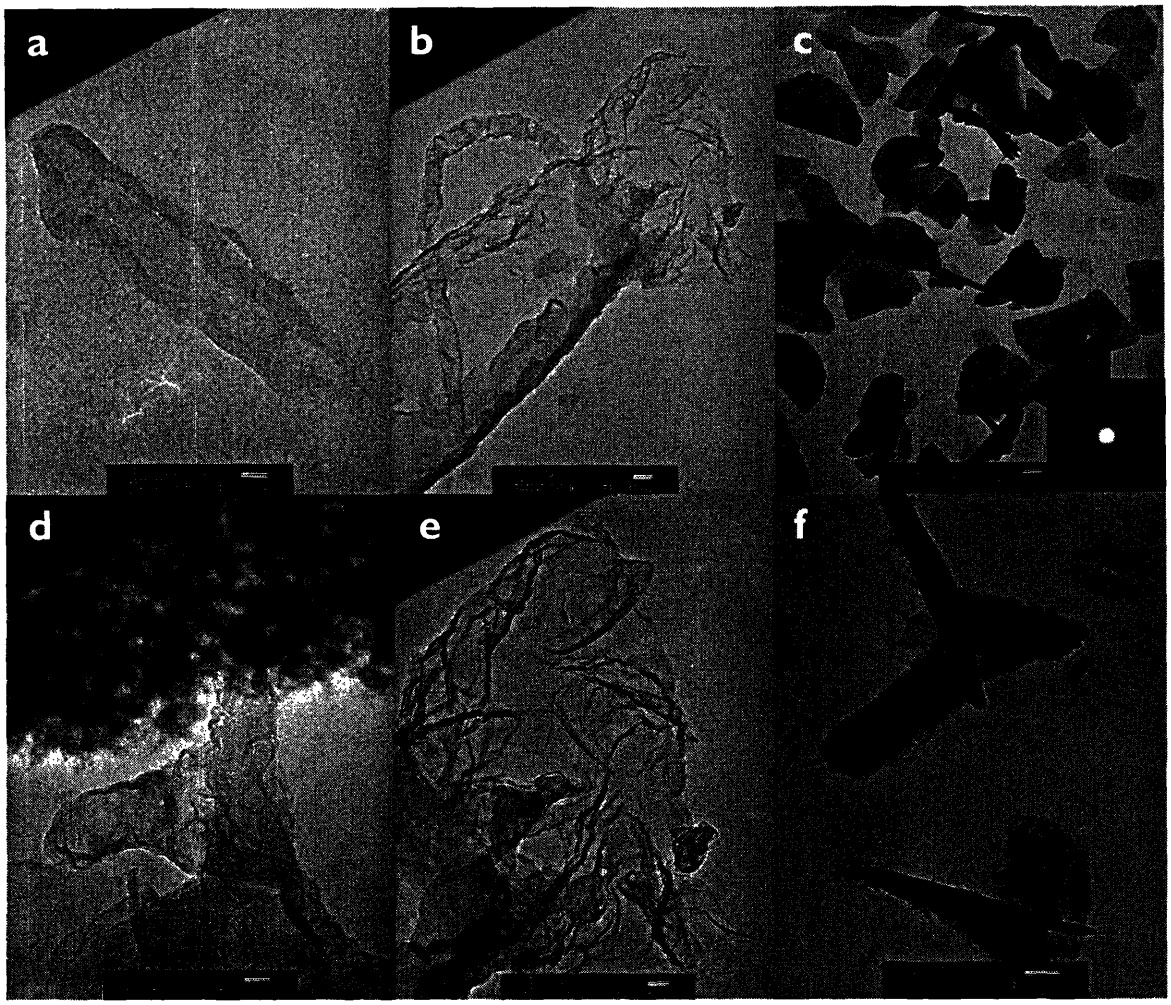

Figure 4-24 High-resolution TEM images of surface scrapings from Nb800-700; *(a)* wayward defective multiwall carbon nanotube (scale is 20 nm); *(b)* hybrid carbon fiber-carbon nanotube structure (scale is 100 nm); *(c)* nanorods and possibly graphitic "nanotortillas" which diffract to give a hexagonal pattern, inset (scale is 200 nm); *(d)* tubular graphitic sheets extending from aerogel mass (scale is 50 nm); *(e)* detail of graphitic sheets (scale is 50 nm); *(f)* detail of nanorods (scale is 100 nm).

Conclusions

Niobium successfully catalyzes carbon nanotube growth in addition to a multitude of other graphitic nanostructures. This said, as seen in the Fe system, changing pyrolysis conditions can steer a metal-doped carbon aerogel's catalytic behavior to favor carbon nanotube growth or give a broader spectrum of carbon nanostructures, and so it is very likely that the niobium system can be tailored in a similar way. Despite the apparent lack of niobium visible in the XRD spectrum,

nano-sized niobium crystallites are indeed present in Nb800 samples as seen directly under TEM and indirectly through successful nanotube growth. Employing the same set of CVD conditions employed for the other metal-doped carbon aerogel systems, Nb800 generates a remarkable spectrum of graphitic structures, including nanotubes, rolled-up graphitic fibers, graphitic sheets, and hybrid structures of these. The unusual nanotube-covered pillar-like structures observed under SEM are believed to be examples of hybrid structures of classic carbon fibers and carbon nanotubes.

Based upon XRD and TEM results, the mean nanoparticle diameter is apparently extremely small in Nb800. XPS detects a single niobium chemistry for this sample which is most likely Nb_2O_5 (as described above). Additionally, no niobium-containing crystallites are detectable by XRD in this sample, implying the presence of niobium is in the form of crystallites < 2 nm in diameter. Furthermore, metallic niobium is known to oxidize rapidly, even at ambient conditions [118]. Thus it can be concluded Nb800 contains nanometer-sized Nb_2O_5 crystallites or surface-oxidized Nb crystallites less than 2 nanometers in diameter. Due to the high surface area to volume ratio of these particles, these particles are most likely reduced by hydrogen in the CVD stream during growth to produce metallic niobium before nanotube growth is initiated. Further investigation is needed to verify if this is the case.

4.3.5 The Tantalum System

Given the interesting results from the niobium system, its heavier Group VB analog tantalum was also expected to be interesting. Tantalum metal readily forms a stable refractory oxide [119] and is typically produced through carbothermic reduction of this oxide. As mentioned, no reports of nanotube growth employing Ta were found in the literature.

Description of Ta-Doped Carbon Aerogel Monoliths

Similar to Nb-doped carbon aerogels, Ta-doped carbon aerogels exhibited a slate blue coating on the tops of the monoliths, however slightly lighter in color than in

the Nb case. This is assumed to be Ta_2O_5. The precursory Ta-doped phenolic aerogels were notably different from the other metal-doped phenolic aerogels investigated in this study in that they were chocolate-brown in color as (opposed to black) and lost approximately 25% less volume after doping than typical. A density of 0.22 g cm^{-3} was measured for the pre-pyrolysis Ta-doped phenolic aerogels, increasing to 0.37 g cm^{-3} for the pyrolyzed Ta-doped carbon aerogels.

X-Ray Diffraction Analysis

XRD spectra for Ta800 and Ta1050 are shown in Figure 4-25. Phase assignment for Ta800 is relatively straightforward, matching the expected peak positions and height ratios for tantalum pentoxide well [120, 121]. Phase assignment for Ta1050 is more difficult. Ta_2O_5 is detected again, this time in the form of larger crystallites (sharper peaks), however a blend of other reflections not belonging to Ta_2O_5 emerge as well. Most notably, high-intensity, broad peaks centered at 34.9°, 40.7°, 58.9°, and 69.8° two-theta, absent in the Ta800 spectrum, appear. These peaks all match closely with reference spectra for TaO, TaC, $Ta_2O_{2.2}$, $TaC_{0.95}$, and Ta_4C_5 (all of which crystallize into the same crystal structure) making definitive phase assignment difficult [122-127]. Figure 4-26 shows an alternative interpretation showing TaC instead of TaO for these peaks. Based on inspection of the Ta-C-O system phase diagram [116], it is unlikely that these peaks could be due to the presence of Ta_4C_5. In addition, a non-fractional stoichiometry is also more probable to form than a fractional stoichiometry, leaving TaO and TaC as the two most likely possibilities. As Ta800 exhibits reflections from Ta_2O_5 exclusively, it makes sense that the peaks which emerge in the Ta1050 spectrum are reflections from some thermally-induced product of Ta_2O_5. Since tantalum pentoxide would have to be reduced to metallic tantalum before TaC would form and no tantalum signals are detected, it is thus concluded that these peaks are most likely attributable to TaO formed through the partial reduction of Ta_2O_5 by carbon in the aerogel during pyrolysis.

Subtraction of the sample holder background from the XRD spectra collected for Ta800 and Ta1050 results in removal of virtually all of the signal in the nanocrystalline carbon region. As a result, no analysis of carbon crystallites in these

samples is made. No peaks corresponding to graphite or any other form of carbon are observed in the spectrum for Ta800 or Ta1050 and so it is assumed that the only form of carbon present is nanocrystalline carbon similar in structure to the niobium system.

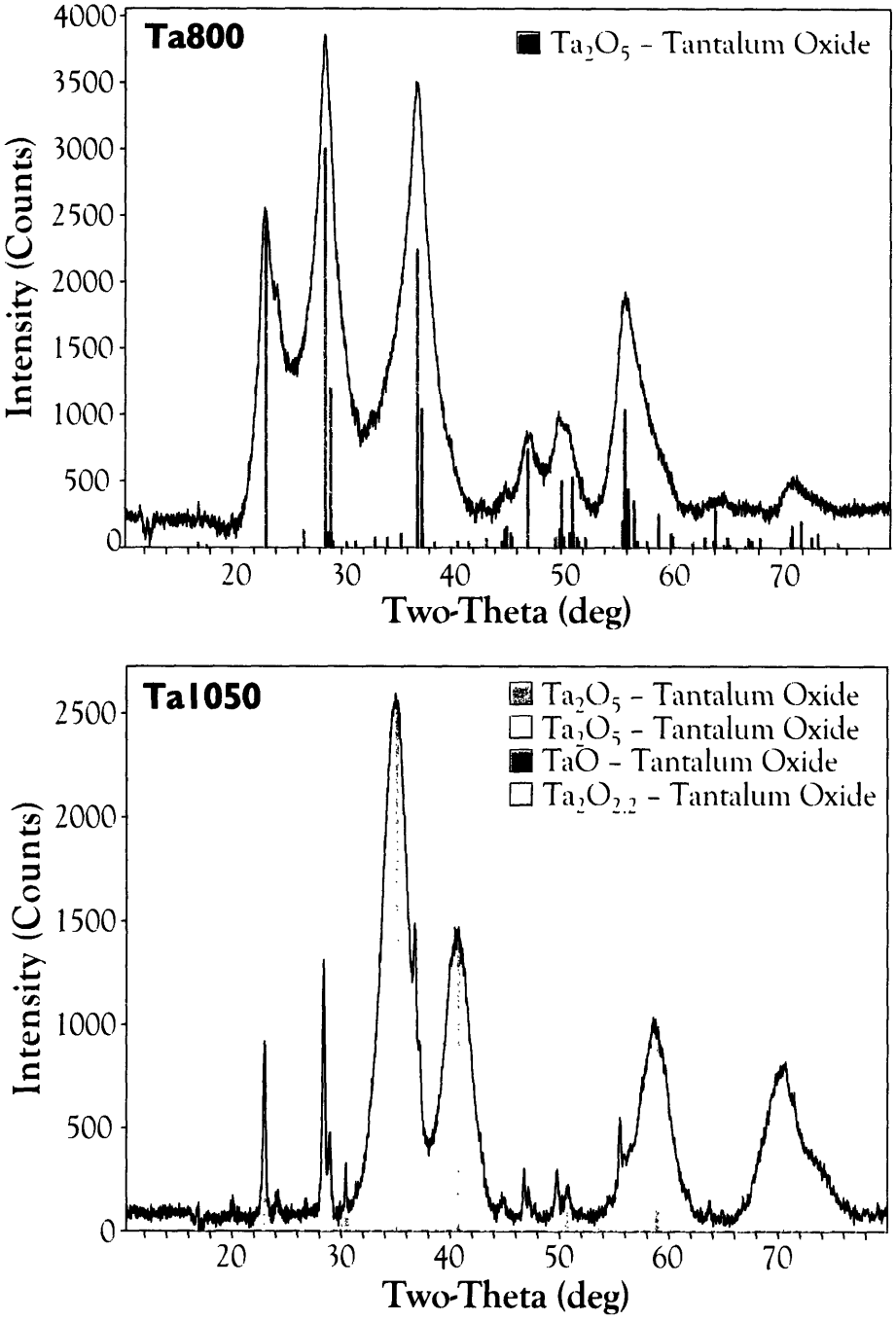

Figure 4-25 XRD spectrum and phase assignment for Ta800 *(top)*; XRD spectrum and best-guess phase-assignment for Ta1050 *(bottom)*.

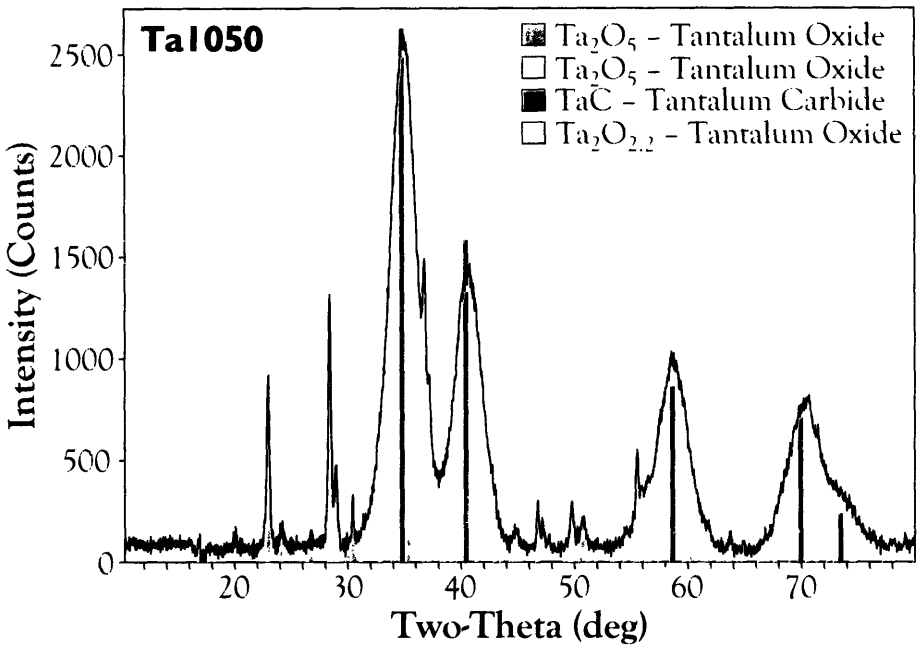

Figure 4-26 Possible alternative phase assignment for Ta1050 XRD spectrum.

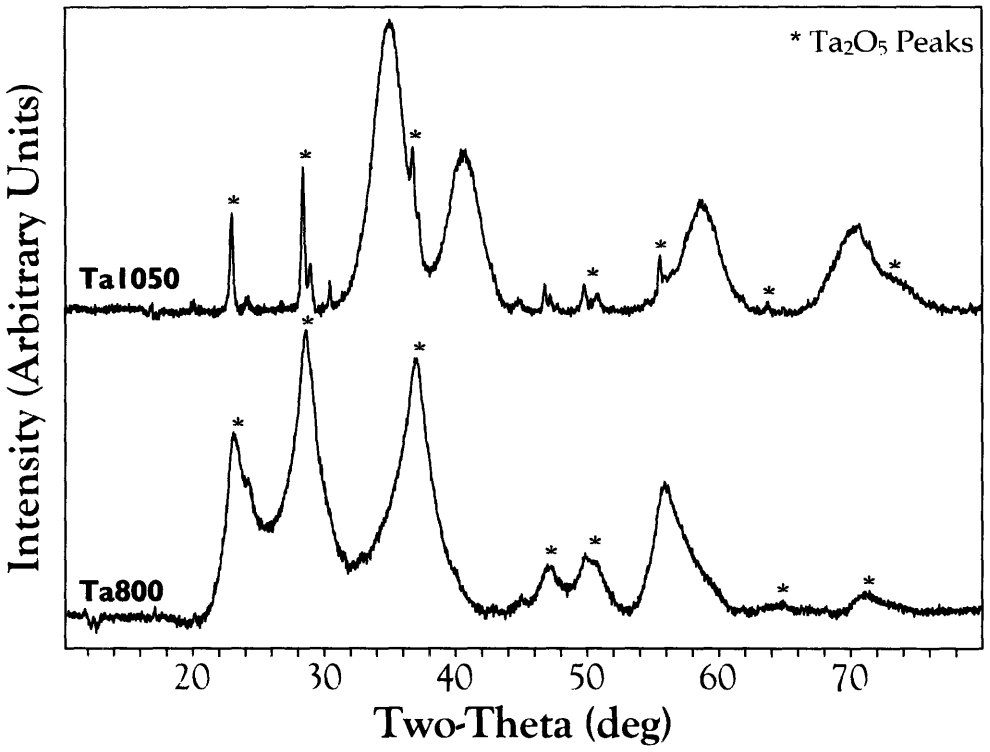

Figure 4-27 Phase change from Ta_2O_5 to a blend of Ta_2O_5 and what is believed to be TaO as a result of increased pyrolysis temperature.

Sample	Assigned Reflection	2-θ (°)	FWHM (°)	Rel. Peak Height	Crystallite Size (nm)
Ta800	Ta_2O_5 (1 11 0)	28.3	3.90	1.00	2.1
	Ta_2O_5 (0 0 1)	23.0	2.60	0.99	3.1
	Ta_2O_5 (0 0 2)	47.0	2.37	0.37	3.7
Ta1050	Ta_2O_5 (0 0 1)	22.9	0.30	0.67	28.8
	Ta_2O_5 (1 11 0)	28.4	0.29	1.00	29.7
	Ta_2O_5 (0 0 2)	46.7	0.41	0.19	22.1
	Ta_2O_5 (0 22 0)	49.8	0.34	0.17	27.2
	Ta_2O_5 (2 15 1)	50.8	0.42	0.11	21.3
	TaO *or* TaC (1 1 1)	34.9	2.61	1.00	3.2
	TaO *or* TaC (2 0 0)	40.7	2.34	0.55	3.6
	TaO *or* TaC (2 2 0)	58.9	3.51	0.38	2.6
	TaO *or* TaC (3 1 1)	69.8	5.07	0.30	1.9

Table 4-14 Analysis of XRD spectra for Ta-doped carbon aerogels.

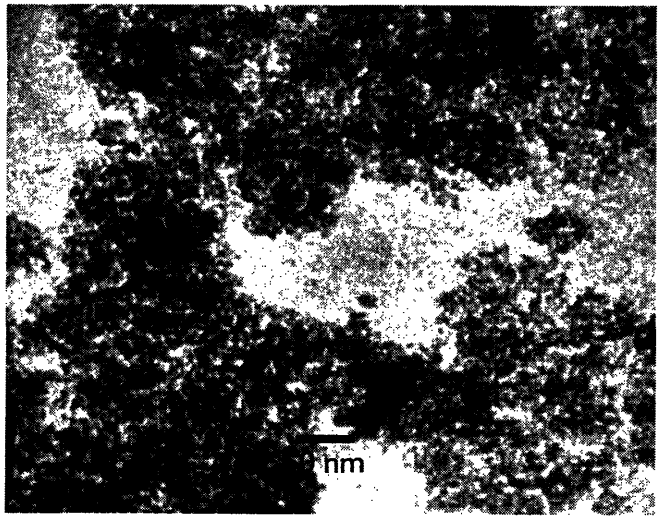

Figure 4-28 TEM micrograph of Ta800 showing Ta-containing crystallites (dark regions) dispersed throughout amorphous carbon aerogel.

Figure 4-28 shows Ta800 as seen under TEM, verifying a typical, low-crystallinity carbon aerogel structure dotted with occasional Ta-containing crystallites (seen as dark spots among the aerogel).

X-Ray Photoelectron Spectroscopy Analysis

Figure 4-29 shows the XPS spectra for Ta800 and Ta1050. Correlating with the results from XRD, only one pair of spin-orbit split peaks corresponding to one chemistry of Ta is observed in the Ta 4f region of the Ta800 spectrum. This matches

well with reference spectra for Ta_2O_5 (see Table 4-15) [77]. A second chemistry appears in Ta1050 which falls within the energy region expected for TaO (Table 4-15) [77]. Two chemistries of surface oxygen are present in both Ta800 and Ta1050, with the low-binding-energy peak assigned to aerogel carboxylate groups (based on the previous systems) and the high-binding-energy peak assigned to tantalum oxides. The magnitude of surface oxygen attributable to tantalum oxides increases with respect to the carboxylate signal from 800°C to 1050°C, which indicates that the aerogel's carboxylate oxygen is being consumed by tantalum in the aerogel.

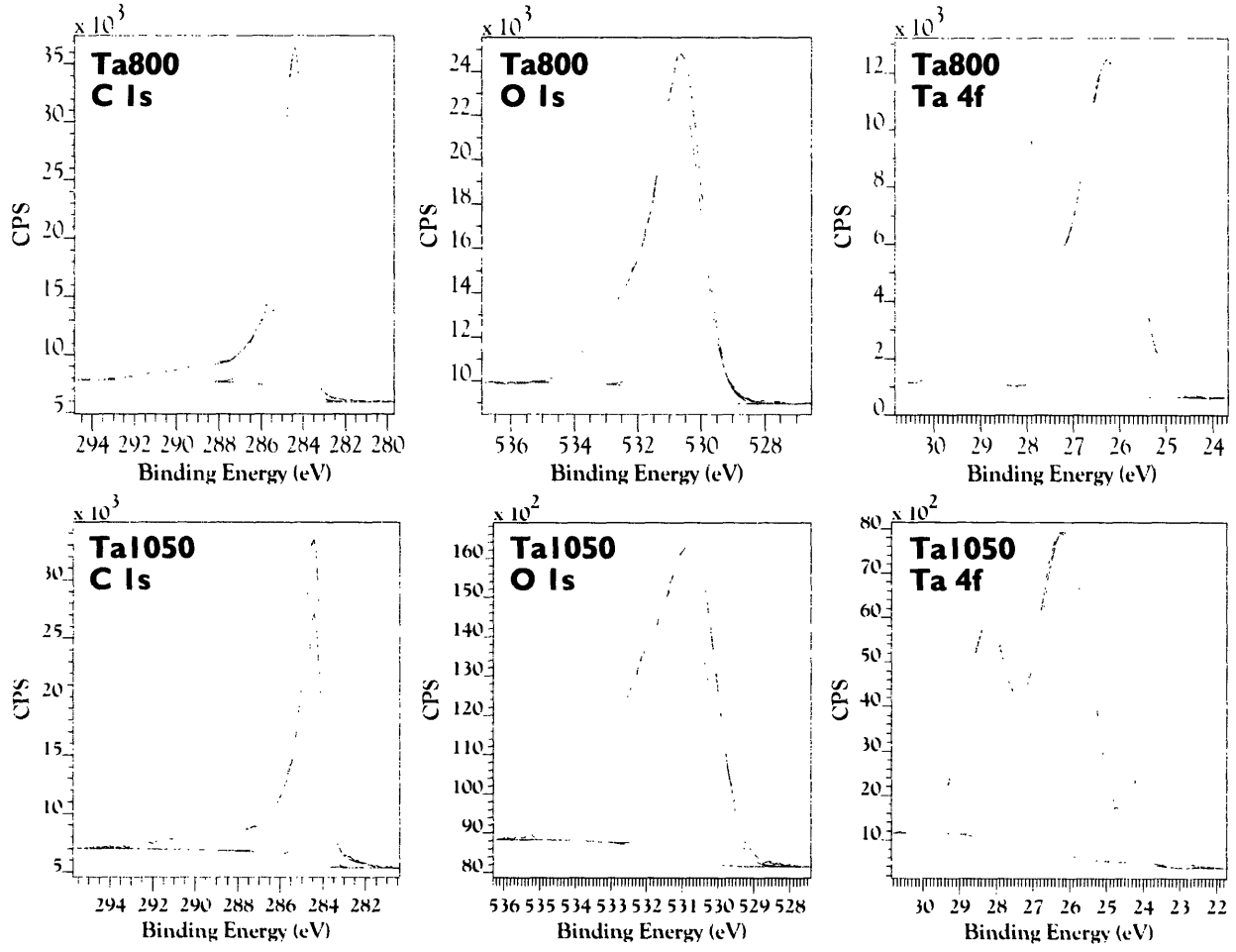

Figure 4-29 *(Top, left to right)* C 1s, O 1s, and Ta 4f regions of the XPS spectrum for Ta800; *(bottom, left to right)* C 1s, O 1s, and Ta 4f regions of the XPS spectrum for Ta1050.

Interestingly, the loading of tantalum in the aerogel (Table 4-16) was calculated to be between 46.8-47.8% by mass (5.7-6.0 atomic percent). This is by far the highest level of doping achieved in any metal-doped carbon aerogel investigated in this research. It is also noteworthy to mention that it is the only metal-doped carbon aerogel system which resulted in the formation of crystalline metal oxides as opposed to metallic metal or metal carbides, and furthermore results *only* in the formation of crystalline oxides.

Effects of Chemical Vapor Deposition

Given the lack of unoxidized species in Ta800 aerogels (neither as crystallites nor nanoparticle surfaces), it was predicted that Ta800 would not catalyze nanotube growth. The standard set of conditions was implemented for growth—use of monoliths pyrolyzed at 800°C processed by CVD at 700°C under a flow 20 sccm ethylene, 30 sccm of methane, and 500 sccm of hydrogen for 10 minutes. Figure 4-30 shows SEM images from Ta800-700 samples. Thorough survey of these samples by SEM and TEM failed to reveal the presence of any kind of additional carbon nanostructures.

It was then hypothesized that a reduction under hydrogen for 5 minutes at 900°C may generate Ta^0 from Ta_2O_5 crystallites in Ta800 and enable growth. This process was then attempted using 500 sccm of hydrogen and followed by CVD under the same conditions as the first attempt. Figure 4-31 shows SEM images surveying this sample after growth. Again, no nanotubes are seen.

The next attempt was to use the same growth conditions but on Ta1050 instead to ascertain whether or not the compositional differences detected in this sample by XRD and XPS would make a difference. Figure 4-32 shows the results of this growth. With the exception of one area along the monolith edge, no nanotubes were identified anywhere on the monolith. On one region of the edge of the top side of the monolith, however, a high yield of small-diameter, short-length carbon nanotubes was found. This was rather surprising, but was verified to not be a process anomaly. One possible explanation for this circumstantial growth is the following scenario. As seen by XRD and XPS, TaO nanoparticles are present in

Ta1050 due to the reduction of Ta_2O_5 nanoparticles by carbon in the aerogel at 1050°C. These particles are not present in Ta800. The Ta^{5+} state is more difficult to reduce than the Ta^{2+} in TaO and so it is unlikely that metallic tantalum would evolve from Ta_2O_5 crystallites within the time span of a typical CVD process. As has been observed through the deposition of Au and Re films on the top of aerogel monoliths after pyrolysis of the gold and rhenium systems, respectively, the top edges are apparently hotter than the rest of the monolith during pyrolysis which, in the case of Ta1050, provided just enough activation energy to carbon from the aerogel locally reduce TaO to Ta^0. Alternatively, this region of the monolith containing a high population of TaO nanoparticles may have been hot enough during the 10-minute CVD growth for the hydrogen in the CVD stream to reduce them to Ta^0 as well. Once rendered into the metallic state, these particles were then capable of catalyzing nanotube growth. The majority of the sample, although also containing TaO nanoparticles, was apparently not reduced adequately during pyrolysis or within the time span of a 10-minute growth. Verification of this hypothesis by attempting CVD growth of carbon nanotubes on Ta-doped aerogels pyrolyzed for longer times (> 10.5 h) and at higher temperatures (> 1050°C) is underway. Due to the tight localization of nanotube growth, however, TEM samples containing nanotubes were not successfully prepared for Ta1050-700.

Conclusions

Prepared in the proper way, tantalum appears to be able to catalyze nanotube growth. Evidence from this study indicates that tantalum oxides are overwhelmingly uncatalytic. Tantalum's ability to form these very stable, uncatalytic refractory oxides makes implementation of tantalum for nanotube growth difficult, i.e., its oxide-death poisoning mechanism leads to a very stable potential energy minimum. For this reason, tantalum is not an ideal nanotube catalyst as defined in this work.

The conditional catalytic activity observed in this system bears many resemblances to the conditional success of surface-based iron nanoparticles used for typical nanotube synthesis in our research group, which has recently been

determined to be heavily influenced by the oxidation state of the iron catalyst achieved before growth. This is discussed in more detail in Section 4.4.

Lastly, Ta-doped carbon aerogels were the only system evaluated in this study which resulted in crystalline oxide nanoparticles instead of metallic metal or metal carbide nanoparticles. They also showed the highest level of doping of any metal evaluated. This may be the case because of tantalum's affinity for oxygen enabling it to make strong bonds to carboxylate moieties in the K^+-doped phenolic gel precursor.

Sample	Energy Region	Assignment	Position (eV)	FWHM (eV)	Area (eV counts)	R.S.F.*
Ta800	C 1s	Amorphous	284.5	0.862	15520.3	1
	C 1s	sp^2 Carbon	285.1	1.897	11417.9	1
	C 1s	π-π^* Shake-Up	287.5	6.67	10538.1	1
	O 1s	Carboxylate	530.6	1.42	14600.3	2.93
	O 1s	Ta_2O_5	532.0	2.62	10008.2	2.93
	Ta 4f	Ta_2O_5 $4f_{7/2}$	26.3	1.22	14419.3	8.62
	Ta 4f	Ta_2O_5 $4f_{5/2}$	28.2	1.37	12788.4	8.62
Ta1050	C 1s	Amorphous	284.5	0.86	15520.3	1
	C 1s	sp^2 Carbon	285.1	1.90	11417.9	1
	C 1s	π-π^* Shake-Up	287.5	6.67	10538.1	1
	O 1s	Carboxylate	530.6	1.36	5852.1	2.93
	O 1s	Ta_2O_5	531.9	2.58	9498.1	2.93
	Ta 4f	TaO $4f_{7/2}$	23.6	0.68	2576.6	8.62
	Ta 4f	TaO $4f_{5/2}$	24.2	0.61	775.6	8.62
	Ta 4f	Ta_2O_5 $4f_{7/2}$	26.2	1.69	12318.2	8.62
	Ta 4f	Ta_2O_5 $4f_{5/2}$	28.3	1.37	6475.2	8.62

* Relative sensitivity factor

Table 4-15 Deconvolution results for XPS spectra of Ta-doped carbon aerogels.

Sample	Element	% Mass Concentration	% Atomic Concentration
Ta800	C	40.93	77.91
	O	11.23	16.04
	Ta	47.84	6.04
Ta1050	C	44.85	82.66
	O	8.40	11.62
	Ta	46.75	5.72

Table 4-16 Elemental compositions of Ta-doped carbon aerogels as determined by XPS.

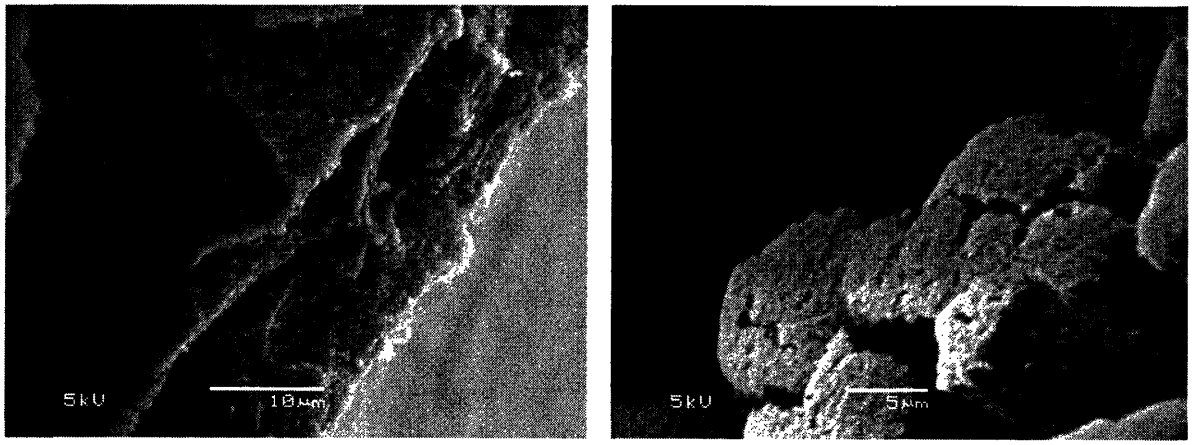

Figure 4-30 SEM images of Ta800-700 showing no growth of nanotubes.

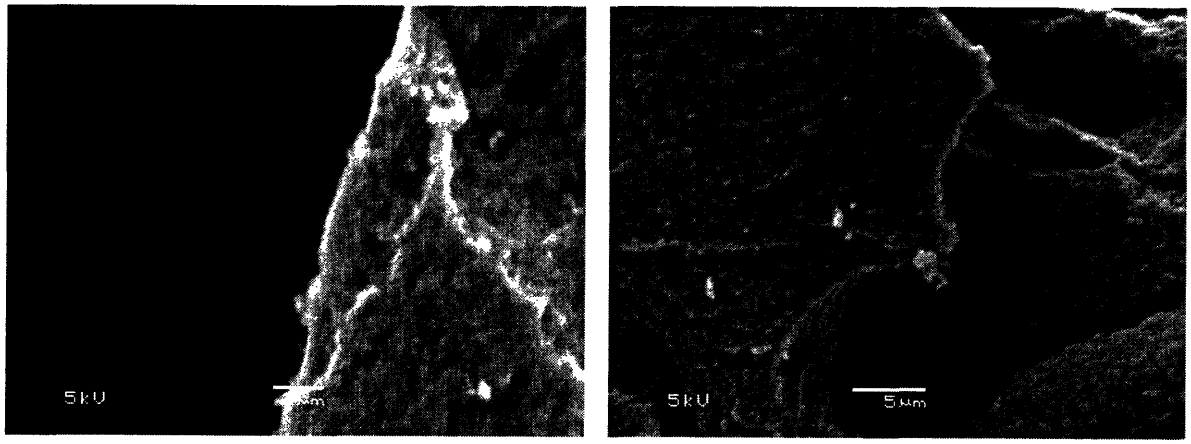

Figure 4-31 SEM images of Ta800-700 treated with a flow of 500 sccm H_2 at 900°C for 5 minutes prior to growth, also showing no growth of nanotubes.

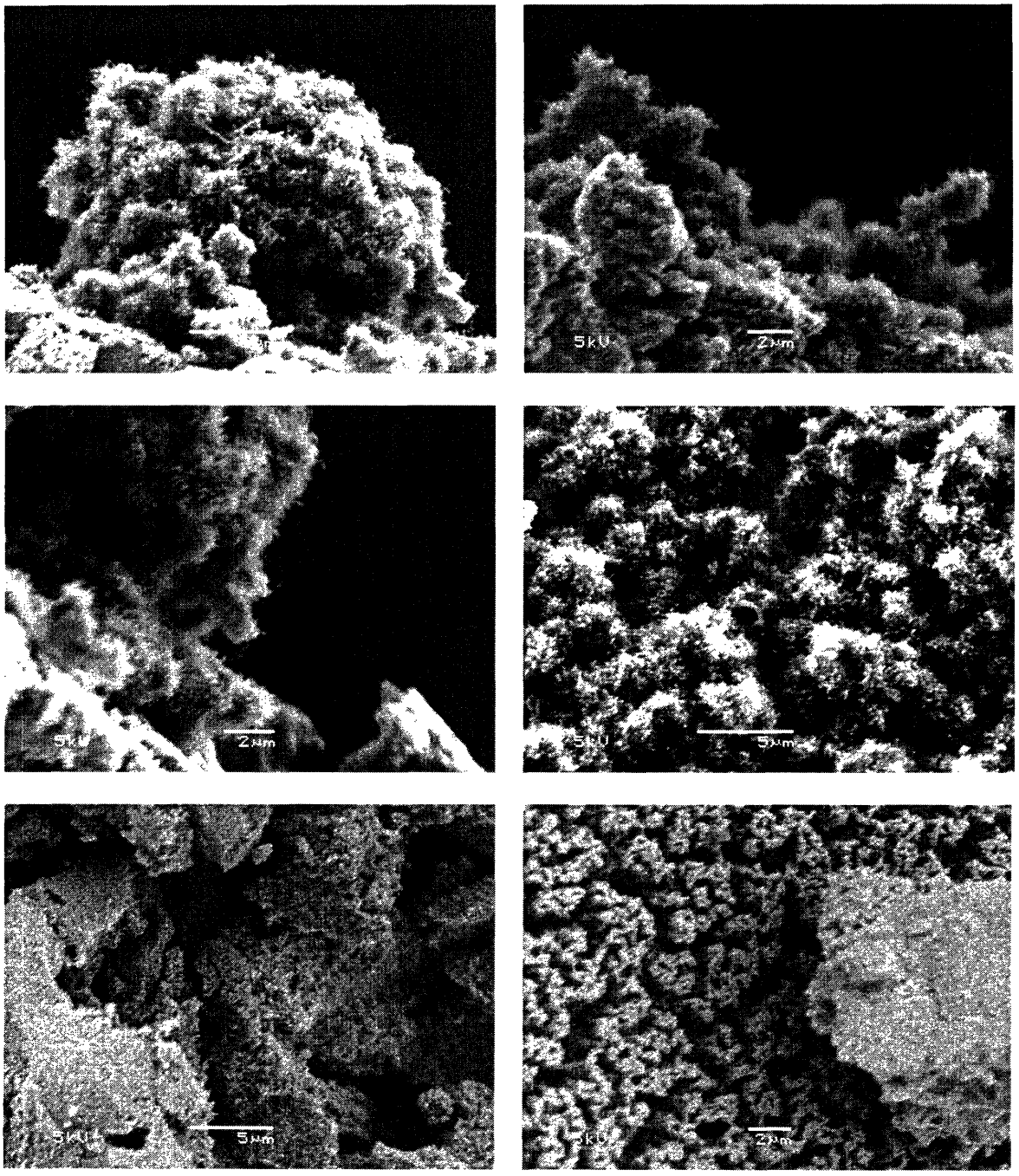

Figure 4-32 *(Top and middle)* SEM images of regions on Ta1050-700 where nanotube growth was successful; *(bottom)* SEM images representative of the majority of Ta1050-700, exhibiting no nanotube growth.

4.3.6 The Tungsten System

The last system evaluated was the tungsten system. Tungsten has been previously demonstrated to catalyze nanotube growth when implemented as a floating catalyst through decomposition of tungsten hexacarbonyl [67]. W-doped carbon aerogel-like materials have been previously prepared through addition of ammonium tungstate to aqueous solutions of resorcinol with formaldehyde [47]. However, it is known that the morphology of carbon aerogels prepared through phenolic polymerization reactions is strongly pH-sensitive [7, 44, 45], and thus the strong alkalinity of this preparation technique results in macroporous materials as opposed to true, mesoporous aerogels.

Tungsten is similar to iron in many regards in that it forms several stable carbides and oxides. The catalytic behavior of tungsten was thus expected to be fairly similar to iron.

Sample	Assigned Reflection	2-θ (°)	FWHM (°)	Rel. Peak Height	Crystallite Size (nm)
W800	W_{fcc} (110)	40.3	0.21	1.00	44.6
	W_{fcc} (200)	58.3	0.22	0.18	46.7
	W_{fcc} (211)	73.3	0.24	0.28	44.4
	W_{bcc} (111)	37.6	1.29	1.00	6.5
	W_{bcc} (200)	44.0	1.36	0.79	6.3
	W_{bcc} (220)	63.8	1.47	0.40	6.4
	W_{bcc} (311)	76.8	1.60	0.28	6.3
	$W_{18}O_{49}$ (010)	23.5	0.19	-	48.7
	C (Amorph)	24.3	2.89	-	2.8
W1050	W_{fcc} (110)	40.3	0.24	1.00	39.5
	W_{fcc} (100)	58.3	0.29	0.11	33.6
	W_{fcc} (211)	73.2	0.35	0.18	29.6
	W_2C (100)	34.3	0.59	0.31	14.2
	W_2C (002)	37.8	2.01	0.63	4.2
	W_2C (101)	39.5	0.88	1.00	9.7
	W_2C (103)	69.7	1.57	0.11	6.2
	W_2C (110)	61.7	1.14	0.39	8.2
	WC_{1-x} (200)	42.6	1.14	1.00	7.5
	WC_{1-x} (311)	74.6	1.92	1.57	5.2
	C (Amorph)	23.8	6.80	-	1.2

Table 4-17 Analysis of XRD spectra for W-doped carbon aerogels. *(Note - Due to spectral complexity, not all phase-assigned peaks are listed.)*

Description of W-doped Carbon Aerogel Monoliths

W-doped carbon aerogels exhibited a bluish coating on the top and side edges of the monoliths, similar to the Nb and Ta systems believed to be tungsten oxides. The density of the pre-pyrolysis W-doped phenolic aerogels was measured to be 0.25 g cm^{-3}, and post-pyrolysis to be 0.30 g cm^{-3}.

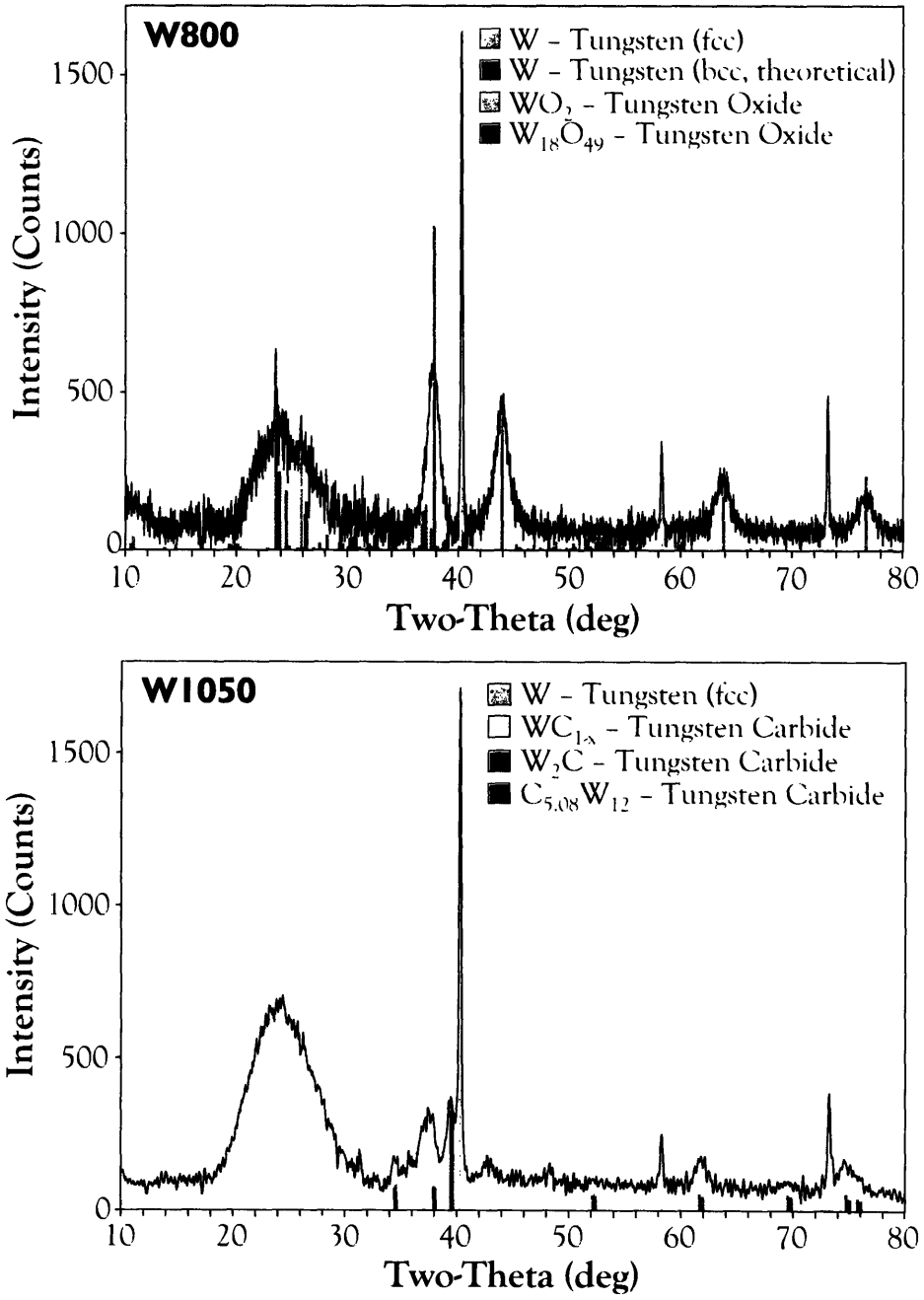

Figure 4-33 XRD spectra for W800 and W1050 samples, showing two different blends of multiple tungsten-containing phases.

X-Ray Diffraction Analysis

Figure 4-33 shows XRD spectra for W800 and W1050. Phase identification of these spectra reveals the presence of four different W-containing species, and a shift in crystallite composition is apparent between 800°C and 1050°C [128-134]. W800 contains tungsten both in a face-centered-cubic configuration and body-centered-cubic configuration, in addition to tungsten(IV) oxide and a tungsten oxide with a complex stoichiometry. W1050, however, shows no sign of oxides but rather tungsten carbides. As expected, a broad nanocrystalline carbon peak is found around 24° two-theta.

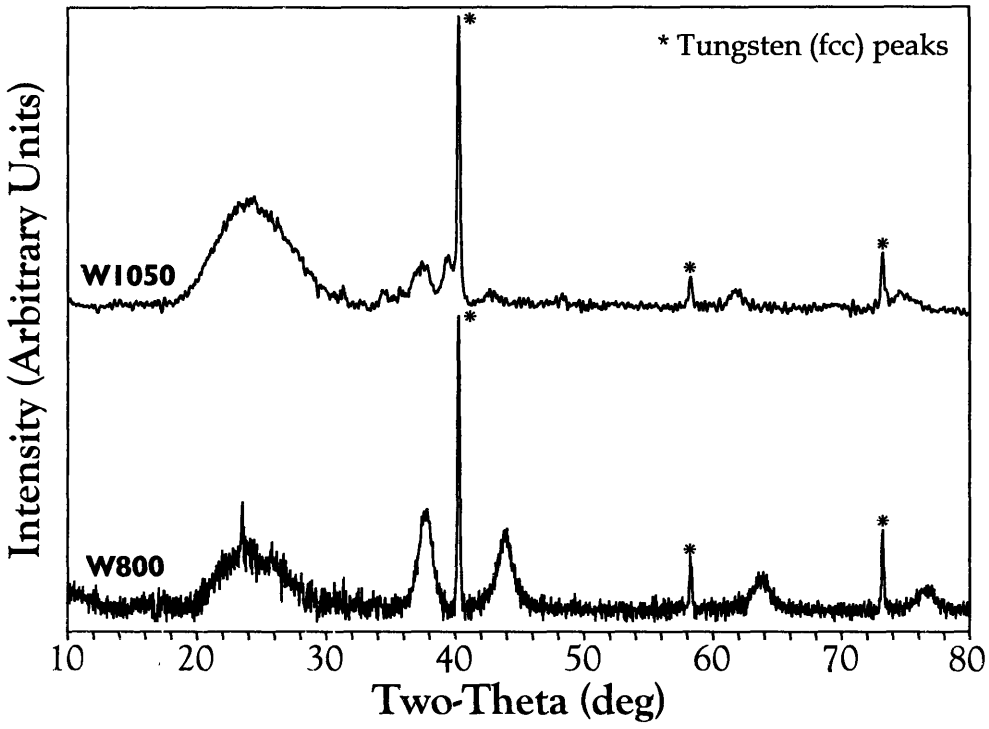

Figure 4-34 Changes in crystallite composition with pyrolysis temperature for W-doped carbon aerogels.

Figure 4-35 shows W800 under TEM. The sample is virtually identical to the other six metal-doped carbon aerogel system investigated in this study, with tungsten-containing crystallites (dark spots) dispersed among a carbon aerogel framework.

X-Ray Photoelectron Spectroscopy Analysis

Figure 4-36 shows the XPS spectra for W800 and W1050. Four chemistries of carbon are seen, in which case one becomes more pronounced at the higher pyrolysis temperature. This peak is attributed to carbon from the tungsten carbides seen in this sample and implies the tungsten nanoparticles in W800 possess carburized surfaces [77]. As seen in the iron system, carburized surfaces were associated with particles that did not catalyze carbon nanotube growth (poisoned particles). Two oxygen chemistries are found as well, one of which is attributed to the carboxylate moieties in the carbon aerogel framework (as usual) and the other to tungsten oxides. Interestingly, this second oxygen chemistry is still present in W1050 despite the lack of oxides seen by XRD. Most likely this is from tungsten oxide crystallites which are too small to be seen by XRD which shrink with increasing pyrolysis temperature at the expense of particle coarsening of tungsten or tungsten carbide (Ostwald ripening). Two chemistries of tungsten are seen in the W 4f region, a high-binding energy chemistry which is distinctly attributable to tungsten oxides, and a lower-binding energy chemistry which is could either be W^0 or tungsten carbides. Unfortunately since the carbide stoichiometries in this material are apparently complex and the tungsten carbides fall in the same energy window as W^0, it is difficult to ascertain the true surface chemistry. It is assumed based on clues from the carbon and oxygen regions of the spectra that the low-binding energy spin-orbit-split pair of peaks is due to carburized tungsten surfaces and not W^0.

Based on these conclusions, it seems unlikely that these W-doped carbon aerogels will be capable of growing carbon nanotubes.

Effects of Chemical Vapor Deposition

The standard growth conditions of using monoliths pyrolyzed at 800°C and CVD performed at 700°C under 20 sccm ethylene, 30 sccm methane, and 500 sccm hydrogen were used for the first attempts at growing carbon nanotubes on W-doped carbon aerogels. Figure 4-37 shows SEM images of W800-700 samples. At first glance, it appeared that CVD successfully resulted in carbon nanotube growth on

the sample, producing what appears to be straight, multiwall nanotubes. Further investigation, revealed virtually every one of these structures to be suspiciously straighter and very different from any of the nanotubes observed in other metal-doped carbon aerogel-carbon nanotube composite systems. In fact, in their preparation of W-containing carbon aerogel-like monoliths, Moreno-Castilla *et al.* describe similar spear-like structures which they identify as WO_3 nanorods [47]. To verify if these were indeed what is observed in this system, SEM images of W800 samples were taken showing these structures also exist before CVD. Based on XRD, the nanorods observed in this system are likely to be of the stoichiometry $W_{18}O_{49}$. Some structures on W800-700 samples appear to be curlier than others and could be carbon nanotubes; however they are a minority product.

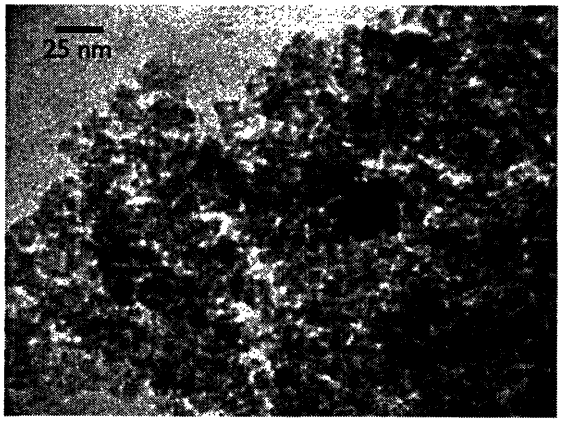

Figure 4-35 TEM image of W800 sample, showing tungsten-containing crystallites (dark regions) among a nanocrystalline carbon aerogel framework.

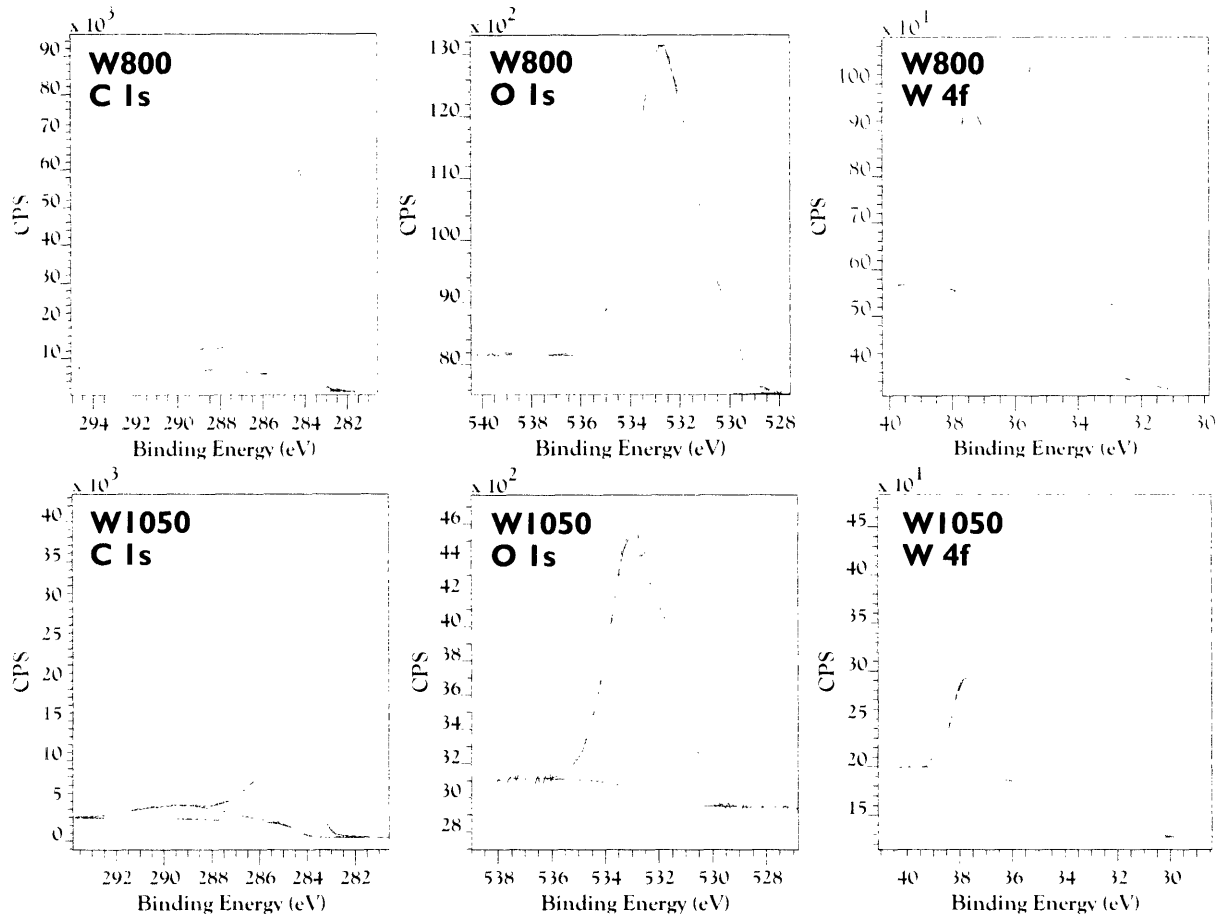

Figure 4-36 *(Top, left to right)* C 1s, O 1s, and W 4f regions of the XPS spectrum for W800; (*bottom, left to right*) C 1s, O 1s, and W 4f regions of the XPS spectrum for W1050.

Sample	Energy Region	Assignment	Position (eV)	FWHM (eV)	Area (eV counts)	R.S.F.*
W800	C 1s	Amorphous C	284.3	1.05	20669.3	1
	C 1s	W Carbides	284.8	1.42	14378.3	1
	C 1s	sp^2 Carbon	285.5	2.47	12635.5	1
	C 1s	π-π^* Shake-Up	288.9	5.39	10049.4	1
	O 1s	W Oxides	530.6	1.84	545.4	2.93
	O 1s	Carboxylate	532.7	2.64	4194.7	2.93
	W 4f	W/WC_x $4f_{7/2}$	32.0	1.41	126.3	9.8
	W 4f	W/WC_x $4f_{5/2}$	34.0	1.76	167.8	9.8
	W 4f	W Oxides $4f_{7/2}$	35.3	1.45	411.3	9.8
	W 4f	W Oxides $4f_{5/2}$	37.4	1.58	262.5	9.8
W1050	C 1s	Amorphous C	284.4	0.67	10393.6	1
	C 1s	W Carbides	284.5	1.22	20004.7	1
	C 1s	sp^2 Carbon	285.5	2.51	12509.9	1
	C 1s	π-π^* Shake-Up	289.3	4.14	6095.1	1
	O 1s	W Oxides	531.4	1.58	714.5	2.93
	O 1s	Carboxylate	533.0	2.05	2367.8	2.93
	W 4f	W/WC_x $4f_{7/2}$	31.6	0.94	315.0	9.8
	W 4f	W/WC_x $4f_{5/2}$	33.7	0.98	255.9	9.8
	W 4f	W Oxides $4f_{7/2}$	35.6	2.00	242.9	9.8
	W 4f	W Oxides $4f_{5/2}$	37.8	1.10	107.6	9.8

* Relative sensitivity factor

Table 4-18 Deconvolution results for XPS spectra of W-doped carbon aerogels.

Sample	Element	% Mass Concentration	% Atomic Concentration
W800	C	93.94	97.01
	O	3.64	2.82
	W	2.42	0.16
W1050	C	94.56	97.76
	O	2.64	2.05
	W	2.80	0.19

Table 4-19 Elemental compositions of W-doped carbon aerogels as determined by XPS.

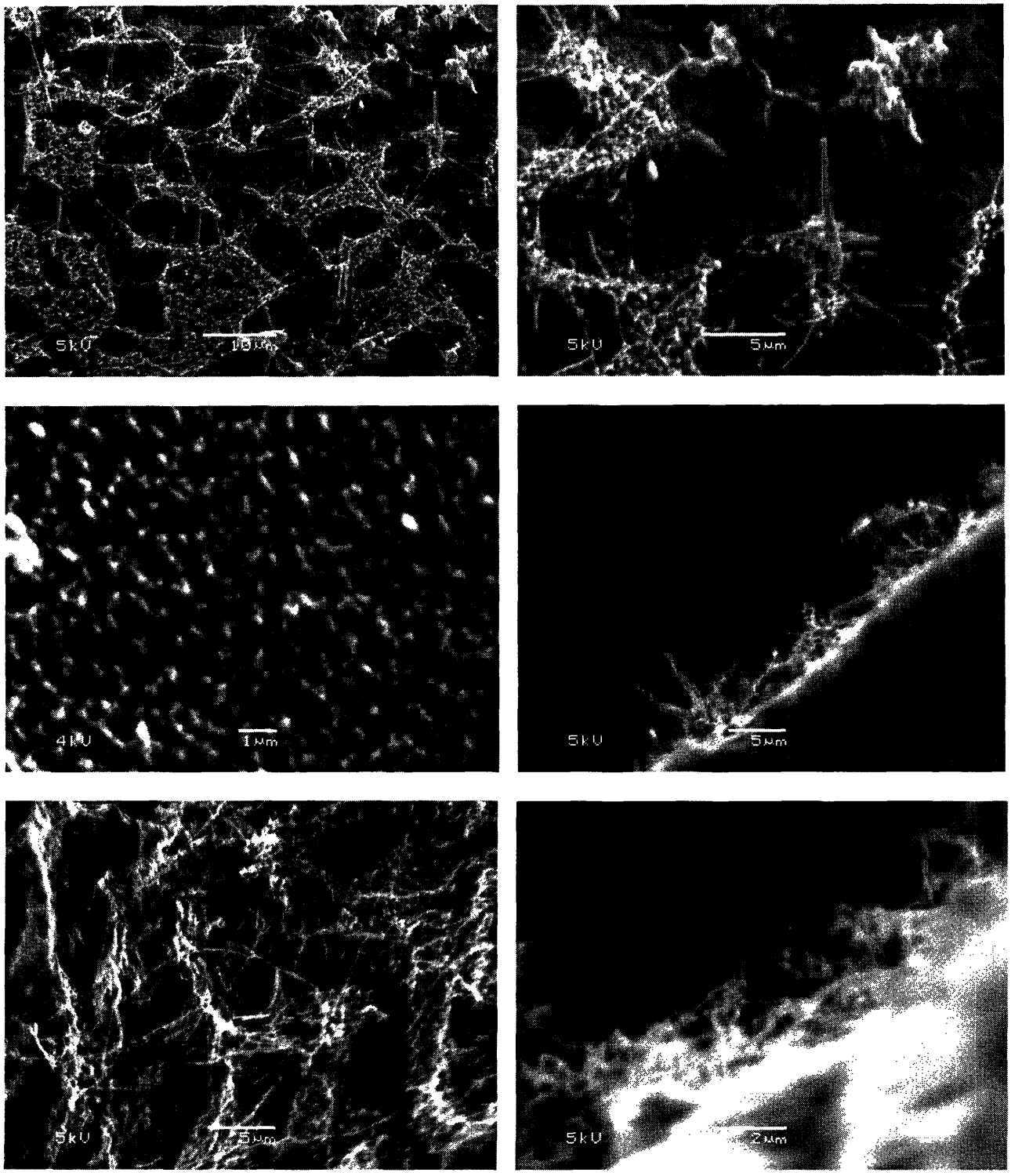

Figure 4-37 SEM images of W800-700 showing tungsten oxide nanorods and possibly carbon nanotubes; *(top)* overhead view of nanorods spanning cracks in the aerogel monolith; *(middle)* close-up shots of tungsten oxide nanorods; *(bottom)* regions containing nanostructures too curly to be nanorods which are likely carbon nanotubes.

Raman Spectroscopy

Raman spectra for W800 and W800-700 were taken in an attempt to differentiate nanotubes from nanorods (Figure 4-38). Again, no RBM is observed. In an attempt to determine if a change in carbon crystallite size possibly attributable to the addition of carbon nanotubes occurred from CVD, a similar analysis of carbon crystallite sizes as was performed for the rhodium system was implemented. A crystallite size of 2.07 nm before was calculated for W800 (compared with a value of 2.8 nm from XRD) and 2.32 for W800-700. Using an estimated mean nanotube diameter of 6.35 nm (based on the mean diameter of the smaller tungsten crystallite species present), a value of 3.9% is obtained for the approximate percentage of aerogel surface with nanotubes attached (Equation 4-2). Although this value is close to the value calculated for the rhodium system (4.8%), the population density of structures seen under SEM which could potentially be carbon nanotubes was no where close to what was observed for the rhodium system, and so it is concluded that the increase in carbon crystallite size is due to miscellaneous carbon deposits on the sample resulting from CVD.

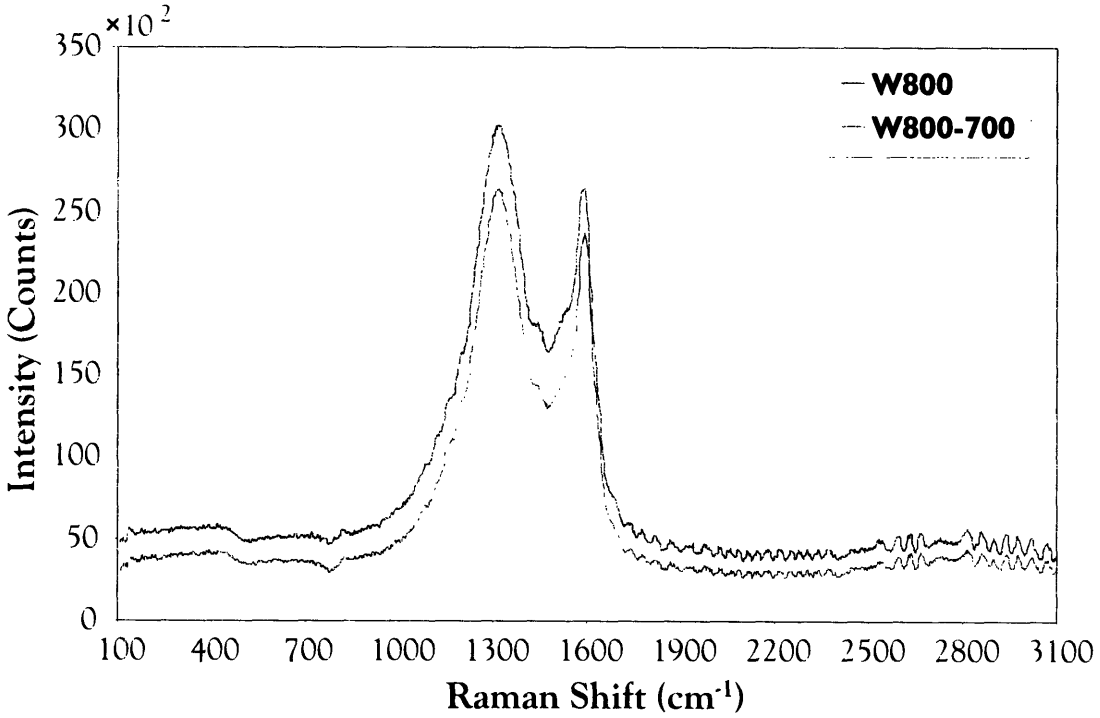

Figure 4-38 Raman spectra for W800 and W800-700 samples taken at 676 nm.

Sample	Band	Peak Center (cm^{-1})	FWHM (cm^{-1})	Amplitude (counts)	Area (cm^{-1} counts)
W800 (Before CVD)	D Band	1313.7	220.7	24850.0	8000000
		1453.4	31.4	1739.3	79760
	G Band	1520.0	74.5	6786.5	737700
		1589.4	64.7	18060.0	1706000
W800-700 (After CVD)	D Band	1311.5	194.8	22760.0	6911000
		1456.1	39.1	1609.8	91470
	G Band	1518.2	82.0	4795.9	572000
		1591.0	64.5	17620.0	1651000

Table 4-20 Deconvolution results for Raman spectra at 676 nm of W-doped carbon aerogels before and after CVD.

Sample	I_D/I_G[a]	L_a (nm)[b]	κ[c]
W800	4.69	2.07	3.9%
W800-700	4.19	2.32	

[a]Ratio of D-band to G-band areas; [b]Calculated carbon crystallite size using Equation 4-1; [c]Estimated fraction of aerogel surface with nanotubes potentially attached using Equation 4-2 assuming (D_{av} = 6.4 nm.)

Table 4-21 Carbon crystallite size estimates from analysis of Raman spectrum for W800 and W800--700

Conclusions

Although tungsten is already known to catalyze carbon nanotube growth, in this particular W-doped carbon aerogel system it is not certain whether or not it does. Additional TEM imaging and more exhaustive exploration of CVD parameter space are needed to answer this question more fully. What can be concluded from this study is that the multitude of oxide and carbide phases tungsten can assume under CVD-like conditions render its implementation for nanotube catalysis complicated.

Novel W-doped carbon aerogel-nanorod composites were, however, produced. This type of nanoarchitecture may lend itself to some type of high-surface-area electrode, catalysis, or sensor application. It may also serve as a useful scaffold on which to deposit other materials (such as metals by CVD or ALD).

4.3.7 Summary of the Six Systems

Table 4-22 summarizes results obtained from characterization and experimentation with the six metal-doped carbon aerogel systems presented in this work.

Sample	Oxide Present?	Carbide Present?	Successful Nanotube Growth?	Previously Known to Catalyze Growth?	Notes
Rh	No	No	Yes	Yes [ref]	Very high yields of nanotubes
Re	Yes (Surface)	No	Yes	No	Interesting leaf-like Re plating on aerogel
Au	Yes (Surface)	No	Yes (Conditional)	Yes [ref]	Successful growth only after 25 min
Nb	Yes (Surface)	No	Yes	No	Pillars, nanotortillas, and nanorods seen in addition to NT
Ta	Yes	No	Yes (Conditional, Limited)	No	Growth only on small region of monolith
W	Yes	Yes	Inconclusive	Yes [ref]	Tungsten oxide nanorods observed, possible low NT yield
Fe	Yes (Surface)	Yes (Crystallite and Surface)	Yes	Yes	Higher populations of carbide nanoparticles decreased yield

Table 4-22 Summary of results of CVD on metal-doped carbon aerogels.

4.4 Conclusions

Carbon aerogels doped with rhodium, rhenium, gold, niobium, tantalum, and tungsten were prepared. With the exception of the gold system (which has been produced by Lawrence Livermore National Laboratory for internal use), the materials produced in this study are the first examples of true, mesoporous carbon aerogels doped with these metals. Production of these materials was facilitated by

the development a new, aprotic ion exchange technique which enables doping of K^+-loaded phenolic gels with water-reactive metal chlorides (such as $ReCl_5$) and eliminates detrimental solution dynamics arising from interference from water. These catalytic metal-doped carbon aerogels may be useful for catalysis applications or as electrodes for fuel cells.

Nb and W exhibited growth of unusual nanostructures which merit further investigation. Under certain conditions, carbon aerogels doped with the heavy carbophobic metals Re and Au formed metal films hugging the contour of the carbon structure. Presumably, other carbophobic metals such as Rh, Pd, Pt, Au, and Ir would do the same at certain temperatures. This offers an interesting possibility for producing high-surface-area metal substrates for applications such as electrodes, catalytic converters, and hydrogen storage by non-stoichiometric metal hydride formation.

Rh, Re, Au, Nb, and Ta were all shown to catalyze carbon nanotube growth on carbon aerogel monoliths. This information will provide a useful starting point in developing new catalyst compositions and extends the number possible bimetallic and trimetallic alloys which can be expected to successfully catalyze nanotube growth.

Overall, metal-doped carbon aerogel systems proved to be a useful testing ground for evaluating a metal's ability to catalyze nanotube growth. One important feature of metal-doped carbon aerogels which facilitates this is the ability to create a quantity of nanoparticles large enough to perform phase analysis by XRD. The presence of nanocrystalline carbon from the aerogel framework was shown to act as a carbothermic reducing agent which brings oxidized nanoparticles in the aerogel down to their metallic state during pyrolysis.

Carbides are not required for nanotube catalysis, nor is the ability for a metal to form carbides. Overall, metal carbides and metal oxides appear to be generally uncatalytic. This does not preclude their application as catalyst precursors which can be reduced or oxidized *in situ* prior to or during CVD. Clever selection of metal nanoparticle precursors, such as a high oxide which must proceed through a lower oxide before reducing to metal, could be a valuable feature for an application where

a delayed or controlled growth is desirable. Similarly, the ideal nanotube catalyst for robust growth not requiring preprocessing and not in danger of carbide poisoning would be a metal which does not form native oxides readily and forms only a simple eutectic with carbon. Such metals include Rh, Pd, Pt, Au, and Ir.

With the exception of iridium, these metals are already known to be catalytic [35, 61, 94, 95, 135], however the implication here is that these metals are expected to offer several advantages over more commonly employed catalysts such as Fe, Co, Ni, and W. They are expected to be easy to prepare and robust in that being noble metals, they do not form substantial native oxide surfaces nor do they oxidize easily and thus retain their metallic state well. This eliminates the threat of oxidative poisoning, if this in fact exists as a potential poisoning mechanism for nanotube catalysis. Furthermore, they all form simple eutectics with carbon and exhibit no compound formation with carbon, eliminating the possibility for carbide death poisoning (again, if this exists for nanotube catalysis). Based on these facts, Rh, Pd, Pt, Au, and Ir are expected to have intrinsically long catalyst lifetimes. Long catalyst lifetime translates into the ability to grow long carbon nanotubes, an important consideration for applications of carbon nanotubes for electronic interconnects and for high strength-to-weight ratio composites based on nanotube fibers. Although long catalyst lifetimes with Fe have been demonstrated [60, 65, 70], they are only achieved through a carefully balanced CVD process (which may be plasma-assisted as well) in which introduction of an oxidizing agent counteracts reduction of Fe nanoparticles into iron carbide. Furthermore, such CVD processes are often equipment-specific and difficult to reproduce or scale. Although these metals are expensive, their long intrinsic expected lifetimes can be exploited for recycling of the catalyst. If implemented on a surface which favors a base-growth mechanism (as opposed to a tip-growth mechanism), nanotubes could potentially be removed from the particles and growth reinitiated, with multiple uses of the catalyst. If complete removal of carbon from the catalyst substrate is required, these catalysts would also withstand an oxidation treatment without being rendered uncatalytic. Furthermore, these metals are all known to be very active catalysts for hydrogenation and

dehydrogenation of alkanes, which implies these catalysts would facilitate cracking of CVD gases well.

In any case, since it has been demonstrated here that a carbide intermediate is not necessary for catalyzing nanotube growth, the mechanisms proposed for nanotube formation which include this may merit reconsideration [41, 99, 100]. It is, however, very likely that catalysis of nanotube growth with metals which form carbides does involve some type of carbide intermediate, or at least that the presence of carbides affects the thermodynamic and kinetic landscapes of those systems.

In conclusion, because of their freedom from oxidative and reductive poisoning mechanisms, metal compositions which do not readily oxidize or carburize are predicted to be the ideal catalysts for nanotube growth.

4.5 Future Work

This work could easily be extended to survey the catalytic propensity of the rest of the transition and lanthanide metals. Investigation of Pd-, Pt-, and Ir-doped carbon aerogels is planned. Development of techniques for reliably producing monodisperse, small-diameter nanoparticles of Rh, Pd, Pt, Au, and Ir and investigation into their effectiveness as nanotube growth catalysts for the production of long nanotubes is also planned.

Chapter 5

Growth of Single-Wall Carbon Nanotubes With Gold, Rhenium, and Gold-Rhenium Bimetallic Catalyst Nanoparticles

5.1 Introduction

The ability to synthesize single-wall carbon nanotubes with macroscopic lengths is advantageous for applications such as high strength-to-weight ratio composites and electrical interconnects for integrated circuits. As discussed in Chapters 2 and 3, the catalytic activity of iron-based catalysts appears to be contingent on the chemical composition of the nanoparticles. Additionally, carburization of the catalyst appears to result in the loss of catalytic activity (discussed in greater detail in Chapters 2 and 3). The fate of an iron-based catalyst undergoing thermal CVD is likely carburization due to gradual diffusion of carbon from the carbon chemical vapor deposition stream unless a very carefully balanced, equipment-specific chemical vapor deposition process is implemented. For these reasons, successful growth of ultralong carbon nanotubes over iron-based catalysts can be difficult to perfect. For purely deterministically-controlled growth of carbon nanotubes, an "ideal catalyst"

of the characteristics described in Section 3.3.3 (such as the elements Rh, Pd, Pt, Ir, and possibly Au as described in Section 4.4) is desirable.

As demonstrated in Chapter 4, a number of metals whose phase diagrams form only simple eutectics with carbon (exhibiting no compound formation) are capable of growing carbon nanotubes. The potential advantage in using such catalysts is the elimination of potential carbide poisoning mechanisms. This, of course, does not preclude other deactivation mechanisms (see Chapter 1.3.6) such as surface obstruction, mechanical jamming of nanotube extrusion (due to tangling or attraction to the substrate, for example), or kinetic particle coarsening; however, these issues can be independently addressed in a relatively straightforward fashion as described in Chapter 1.

With these considerations in mind, work was begun to develop a technique for preparing a surface-based nanoparticle catalyst which would potentially be free of chemical poisoning during CVD. It should be noted that this work was performed concurrently with the work performed in Chapters 3 and 4. Based on available data at the time, two elements were selected for evaluation—gold, which appeared to be an "ideal" nanotube catalyst as defined in Chapters 3 and 4, and rhenium, which was believed to be an ideal catalyst at the time since it does not carburize although it does oxidize. Rhenium is known for its resistance to catalyst poisoning [103] and, as demonstrated in Chapter 4, rhenium can catalyze nanotube growth. Gold is similar in this regard, and has previously been demonstrated to catalyze nanotube growth as surface-based nanoparticles [95].

It this work, growth of single-wall carbon nanotubes on gold, rhenium, and gold-rhenium bimetallic catalyst nanoparticles is demonstrated. Characterization of the catalyst in terms of the peculiar chemistry of this system is discussed. This work is intended to serve as a first step towards development of surface-based nanoparticle catalysts comprised of metals free from oxidation and carburization poisoning mechanisms, with the goal of developing catalysts for the growth of single-wall carbon nanotubes of indefinite length. Although an "ideal" catalyst was not produced in these investigations, the gold-rhenium system exhibited a unique, rich chemistry which did enable growth of single-wall carbon nanotubes and provided

further insight into the chemical compositions suitable for catalyzing nanotube growth by thermal CVD.

5.2 Experimental

5.2.1 Deposition of Nanoparticles

Preparation of Substrate

Silicon wafers (SQI Wafer, (100), 5 Ω, 100.0 nm wet oxide) were cleaved into ~1.0 cm^2 chips. A hydroxyl-terminated substrate was found to be necessary for the proper adhesion of nanoparticles. Each chip was then sonicated under acetone for 5 min, rinsed with acetone, and then rinsed with isopropanol.

Preparation of Metal Chloride and Nucleating Solutions

Successive quantitative dilutions of stock solutions were used for preparation of all solutions. *For reproducible results, all reagents must be kept free of moisture.* Metal chloride solutions were prepared as follows. Anhydrous rhenium(V) chloride (2.194×10^{-3} g, 4.485×10^{-5} mol) was added to 10.0 mL of dry *N,N'*-dimethylformamide (DMF). Anhydrous gold(III) chloride was then added to the solution in the amount necessary to obtain a desired molar ratio of Au to Re (0.964 mg for 5% loading, 2.023 mg for 10% loading, 4.577 mg for 20% loading, and 18.31 mg for 50% loading). Solutions with a loading of 100% were prepared by omitting addition of any gold(III) chloride. Solutions with a loading of 100% gold were prepared by adding 18.31 mg (4.485×10^{-5} mol) of anhydrous gold(III) chloride to 10.0 mL of DMF.

Nucleating solution was prepared as follows. $NH_2OH{\cdot}HCl$ (3.876×10^{-2} g) was dissolved in 10.0 mL of deionized water. A 100-μL aliquot of this solution and a 30-μL aliquot of metal chloride solution were then added to 10.0 mL of dry DMF.

Deposition

Clean wafer chips were placed in nucleating solution for 5 min and blow-dried. The chips were then placed in metal chloride solution for 3 min and blow-dried again. Surveys of the chips were performed with atomic force microscopy (AFM) to

verify successful deposition of nanoparticles. Samples are denoted in terms of the molar ratio of Au to Re ("m/n") in the solution used to prepare the nanoparticles.

5.2.2 Nanoparticle Pretreatments

A reductive pretreatment under H_2 is normally used to anneal and reduce freshly deposited nanoparticles into a metallic state. If, however, this reductive pretreatment is followed by an oxidative pretreatment prior to CVD growth (which would ordinarily be considered as a way to render the catalyst nanoparticles uncatalytic), an unusual chemistry intrinsic to the gold-rhenium system is observed which conditionally still enables carbon nanotube growth, as discussed below.

5.2.2.1 Reductive Pretreatment

Following nanoparticle deposition, chips were placed inside a short segment of 1.0-cm diameter quartz tubing and placed in the center of a 2.5-cm diameter quartz process tube. After flushing with a flow of 200 scmm Ar for 2 min, the tube was placed in an electric clamshell furnace preheated to 900°C. Upon opening, the furnace temperature would drop by ~100-150°C. After ~1-2 min the furnace reached 900°C again at which point the Ar was shut off and a flow of 440 sccm H_2 was activated for 10 min. During this time, any residual chloride is removed and the metals are brought to their metallic state. After 10 min, the tube was removed from the furnace, a flow of 200 sccm Ar was activated, and the flow of H_2 was deactivated.

5.2.2.2 Oxidative Pretreatment

Following thermal reduction under hydrogen, the quartz process tube was optionally opened to atmosphere and placed in the furnace at 900°C for another 4 min. During this time the sample is reoxidized by oxygen.

5.2.3 Chemical Vapor Deposition

With the samples still in the quartz process tube, the tube was again flushed with a flow of 200 sccm Ar for 2 min after which it was placed in the furnace preheated to 1100°C. Upon opening, the furnace temperature would drop ~200°C. The temperature set point of the furnace was then set to 900°C. After 1-2 min, the furnace reached 900°C at which point the samples were placed under a flow of CVD gases for 10 min. For alcohol-based growth, the flow consisted of 88 sccm H_2 and 600 sccm ethanol-saturated Ar. For hydrocarbon-based growth, the flow consisted of 30 sccm C_2H_4, 20 sccm CH_4, and 500 sccm H_2. After 10 min, a flow of 200 sccm Ar was activated, the tube was removed from the furnace, and the CVD gases were shut off. The tube then remained under a flow of Ar until cool.

5.2.4 Characterization

X-ray photoelectron spectroscopy (XPS) and atomic force microscopy (AFM) were used to characterize the nanoparticles after deposition, reduction, oxidation, and CVD growth. Samples containing carbon nanotubes were further characterized by scanning electron microscopy (SEM) and Raman spectroscopy.

AFM images were acquired using a Veeco Instruments atomic force microscope. High-resolution scanning electron microscopy was performed with a JEOL 6320 instrument operating at 5 kV. XPS spectra were obtained on an AXIS HIS 165 and ULTRA Spectrometer (Kratos Analytical Limited, England) using Al K radiation (energy = 1486.6 eV) in a vacuum of 5×10^{-9} torr. Samples were analyzed as prepared by on a sample holder with double-sided adhesive carbon tape. X-ray slots of 750 by 350 μm, an X-ray power of 150 W (15 kV and 10 mA), and a pass energy of 80 eV (dependent on the metal being analyzed) were used. Raman spectra were obtained using a custom-built micro-Raman spectrometer at excitation wavelength 676 nm.

5.3 Results

5.3.1 Development of Nanoparticle Deposition Technique

Very little is known about the gold-rhenium system, partly because rhenium is extremely rare, relatively expensive, and was only discovered relatively recently in 1925 [136]. No phase diagram exists for the system and little has been done with it [137]. A study done on reactions of alkanes over rhenium and gold-rhenium films found a maximum solubility of Au in Re of 42 atomic percent at 500°C, but that Re was practically insoluble in Au [138]. It has also been reported that Au and Re form sharp phase boundaries only one monolayer thick [139]. Neither element is known to form a stable carbide [104]. Although rhenium metal is relatively oxidation-resistant, above 540°C it will oxidize to form Re_2O_7, a volatile oxide which readily sublimes until the entire metal has vaporized [103]. Rhenium exhibits valence states from +7 to -1 and can also form non-volatile oxides, such as ReO_2, ReO_3, and Re_2O_3.

The goal of this work was to evaluate gold, rhenium, and gold-rhenium bimetallic catalyst nanoparticles. For bimetallic compositions, a target composition of 20% Au and 80% rhenium was selected as a reasonable starting point since it is approximately half of the reported maximum solubility of gold in rhenium at elevated temperatures.

The technique developed for preparing gold-rhenium nanoparticles was adapted from a similar technique used to prepare iron nanoparticles through trial and error. $ReCl_5$ and $AuCl_3$ were selected as the starting reagents, however as both of these compounds decompose in water, an organic solvent was needed. *N,N'*-dimethylformamide was chosen since both $ReCl_5$ and $AuCl_3$ were found to be readily solubilized by it and to complex with it very slowly.

Figure 5-1 shows AFM images of successfully deposited rhenium-only nanoparticles and rhenium nanoparticles intended to have a gold content of 5%, 10%, and 20%. Multiple particle size regimes are observed in the samples regardless of the intended Au-Re ratio, with most particles tens of nm in diameter, many ~75 nm and ~250 nm in diameter, and a sporadic large clumps several microns in diameter. Figure 5-2 shows AFM images of nanoparticles with an intended 50/50

ratio of Au-Re before and after reductive pretreatment, verifying the survival of the nanoparticles through this processing step.

Figure 5-3 shows the C 1s, O 1*s*, Re 4f, and Au 4f energy regions of the XPS spectrum for Au-Re nanoparticles with an intended composition of 20/80. Only one pair of spin-orbit-split peaks is present in the Au 4f region, indicating only one chemistry of gold is present. The binding energy of these peaks matches reference spectra for metallic gold [77]. The Re 4f region contains three peaks, one of which is the inconveniently placed Re $5p_{1/2}$ peak which happens to overlap in this region. The remaining peaks are the Re $4f_{7/2}$ and Re $4f_{5/2}$ peaks; thus it is concluded only one chemistry of rhenium is present. If rhenium were in the form of ReO_2, the Re $4f_{7/2}$ peak would fall at a higher binding energy of ~43 eV, and if it were in the form ReO_3 this peak would fall even higher (~46.5 eV). So, based on the low binding energy (41.2 eV) of the $4f_{7/2}$ peak, it is concluded that rhenium is in the metallic state as well. Table 5-1 summarizes the gold-rhenium ratio as determined by XPS compared with the molar ratio of gold to rhenium in the metal chloride deposition solution used to prepare the nanoparticles. Solution dynamics apparently favors nucleation of rhenium over gold. XPS sampling at various locations on each sample indicates the overall surface chemistry to be homogenous. Deconvolution results of the XPS spectrum for 20/80 nanoparticles are listed in Table 5-2.

Figure 5-4 contrasts the Re 4f region of the XPS spectrum for a 20/80 sample processed by reductive and oxidative pretreatments which successfully grew carbon nanotubes (discussed in more depth in Section 5.3.2) with that of a 20/80 sample which under the same processing conditions did not. In the sample which resulted in successful growth, the Re $4f_{7/2}$ peak falls at a low binding energy corresponding to Re metal. The unsuccessful sample shows this peak at a higher binding energy of 43.5 eV, which suggests this sample contains Re^{3+} or Re^{4+} in the form of an oxide [77, 140]. It was later discovered that samples which exhibited the higher binding energy Re $4f_{7/2}$ peaks had been prepared using moisture-exposed $ReCl_5$, which slowly hydrolyzes to form $Re_2O_3 \cdot xH_2O$ upon exposure to atmosphere [103]. Thus it was concluded that for successful nanotube growth, fresh, anhydrous $ReCl_5$ was necessary.

Au-Re Ratio in Metal Chloride Solution	Mass % Re from XPS	Mass % Au from XPS	Atomic % Re from XPS	Atomic % Au from XPS	Ratio of Difference
5% Au 95% Re	98.32	1.68	98.41	1.59	0.32
10% Au 90% Re	98.09	1.91	98.19	1.81	0.18
20% Au 80% Re	93.65	6.35	93.97	6.03	0.30

Table 5-1 Calculated Au-Re ratios as determined by XPS compared with the molar ratio of Au-Re present in metal chloride nanoparticle deposition solutions.

5.3.2 Effects of Chemical Vapor Deposition

5.3.2.1 CVD Following Reductive Pretreatment Only

Figure 5-5 shows AFM images of Au, Re, and bimetallic Au-Re nanoparticles processed with reductive pretreatment followed by hydrocarbon-based CVD at 900°C. All samples were found to grow single-wall carbon nanotubes in good yield. Re-only samples showed slightly less yield than the Au-Re alloys or Au by itself. This is attributed to a reduction in yield due to intractable surface oxidation. CVD at 700°C was also attempted for Au, Re, and bimetallic Au-Re nanoparticles. Only Au, 20/80 Au-Re and 50/50 Au-Re nanoparticles were found to successfully catalyze nanotube growth at 700°C, however. Re-only nanoparticles only catalyzed growth of carbon nanotubes at 900°C.

5.3.2.2 CVD Following Reductive and Oxidative Pretreatments

Table 5-3 lists the results of experiments leading up to the determination of the global optimum CVD nanotube growth process parameters for Au-Re 20/80 nanoparticles processed by reductive and oxidative pretreatments. A number of experiments involving variations in annealing time, oxidation time, CVD growth temperature, and H_2 flow rate were executed and varied around conditions which resulted in successful growth of carbon nanotubes. Figure 5-6 shows AFM images of the first Au-Re samples processed by an oxidative pretreatment which exhibited carbon nanotube growth. These samples were had 20/80 Au-Re ratios and were grown using the CVD conditions listed for Trial 14 in Table 5-3 conducted for 10

min. This growth was repeated several times successfully, although again only when using nanoparticles which had been prepared with anhydrous $ReCl_5$.

Further experimentation to optimize the CVD process used to grow nanotubes with the 20/80 Au-Re catalyst failed to produce any significant changes in yield. It seemed strange that the yield from this catalyst was as low as it was, given the high populations of suitably-sized nanoparticles seen under AFM and verified presence of rhenium and gold on the sample. As a result, experimentation with changing the Au-Re ratio was conducted to ascertain if changing the composition of the catalyst would be beneficial.

Numerous attempts of 5/95 and 10/90 Au-Re nanoparticles processed by reductive and oxidative pretreatments resulted in no successful growth of carbon nanotubes. Interestingly, 50/50 nanoparticle samples did, and with dramatically improved yield over 20/80 nanoparticles. Figure 5-7 shows AFM images from CVD growth on 50/50 nanoparticles. A large population of single-wall nanotubes (mean diameter ~1.8 nm from AFM) and multiwall nanotubes are found at various locations on the chip. Figure 5-8 shows two batches of post-CVD 50/50 catalyst samples as seen under SEM, which revealed a large coverage of nanotubes across the entire sample. To further verify that among the structures observed under AFM and SEM were single-wall carbon nanotubes, Raman spectra taken at a laser excitation wavelength of 676 nm were collected (Figure 5-9). Radial breathing modes (denoted by ω) are found at 183.4, 244.2, and 304.3 cm^{-1} are observed. A sharp G-band (1586.4 cm^{-1}) and diminished disorder-induced D-band (1323.3 cm^{-1}) are seen in addition to the double-resonance process-enabled G' band at 2614 cm^{-1}. The diameter of the nanotube in resonance with the laser at that energy for individual single-wall carbon nanotubes on a Si/SiO_2 substrate can be approximated by the relation [141]:

$$\omega = \frac{248\ \mathrm{cm}^{-1}}{d_t} \qquad (5\text{-}1)$$

giving nanotube diameters of 1.35, 1.02, and 0.81 nm, respectively. In conjunction with the nanotube diameters measured by AFM, it is concluded that single-wall carbon nanotubes were successfully grown on this sample. Additionally, the ratio of the D-band to G-band integrated areas (Table 5-4) gives a general measure of how defective the nanotubes on the sample are. For these samples, a value of $I_D/I_G = 0.76$ was calculated, indicating a high presence of disordered carbon and/or defective carbon nanotubes.

XPS depth profiling (Figure 5-10) of post-CVD 50/50 samples gave puzzling results. Reasonable were the surveys of the Au 4f region, which turned up two chemistries of gold (attributed to gold and gold oxide) on the surface after growth, giving way to a decreasing Au^0 signal with increasing penetration. The Re 4f region, however, showed no signal of any kind and remained unchanged with depth. In fact, XPS analysis of the 50/50 sample post-oxidation but pre-CVD (Figure 5-11) revealed the same situation. At first glance it would then appear that no rhenium was ever present during CVD, however this is not believed to be the case as is discussed below.

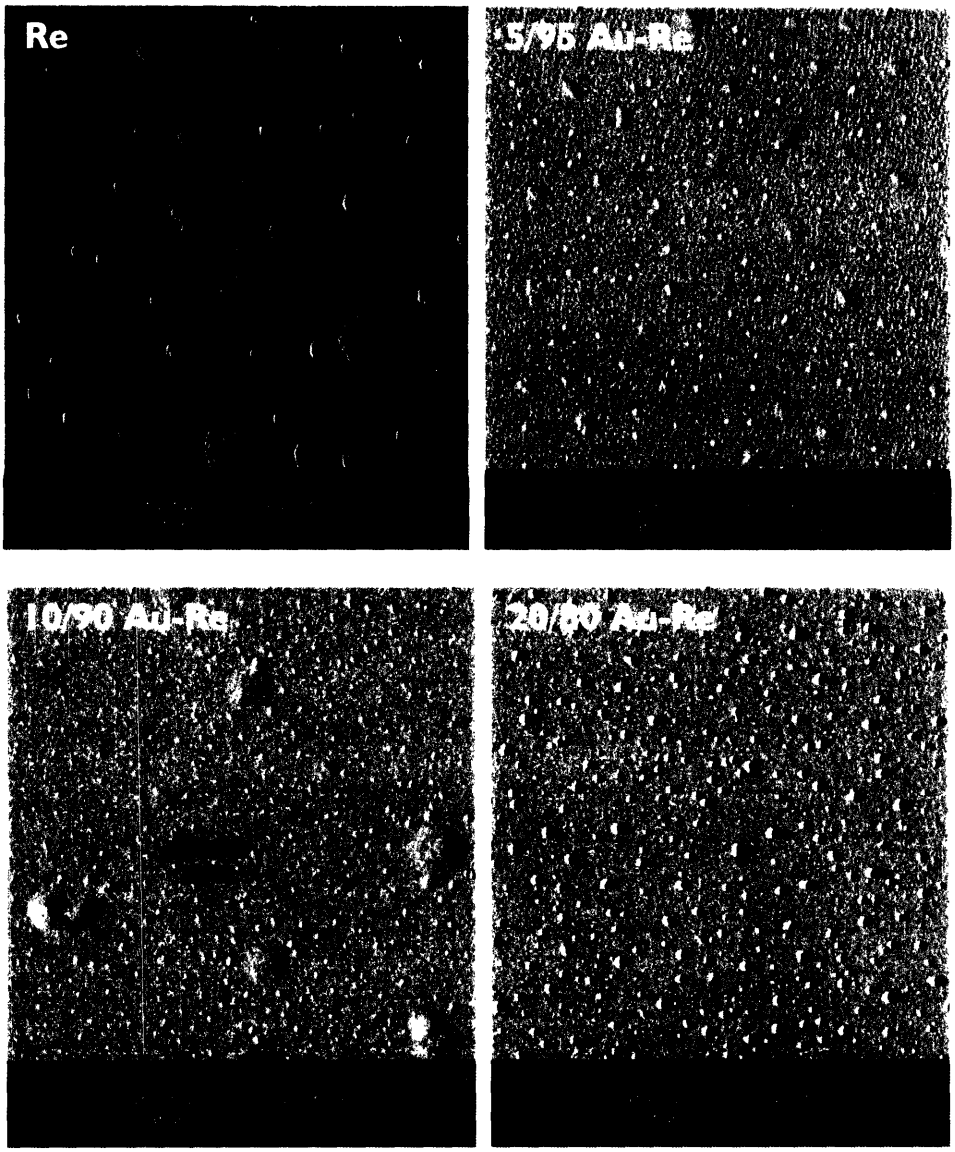

Figure 5-1 AFM images of Re-only and Au-Re nanoparticles with varying concentrations of gold. The nanoparticle size distribution is essentially independent of the Au-Re ratio (image width represents 5 μm).

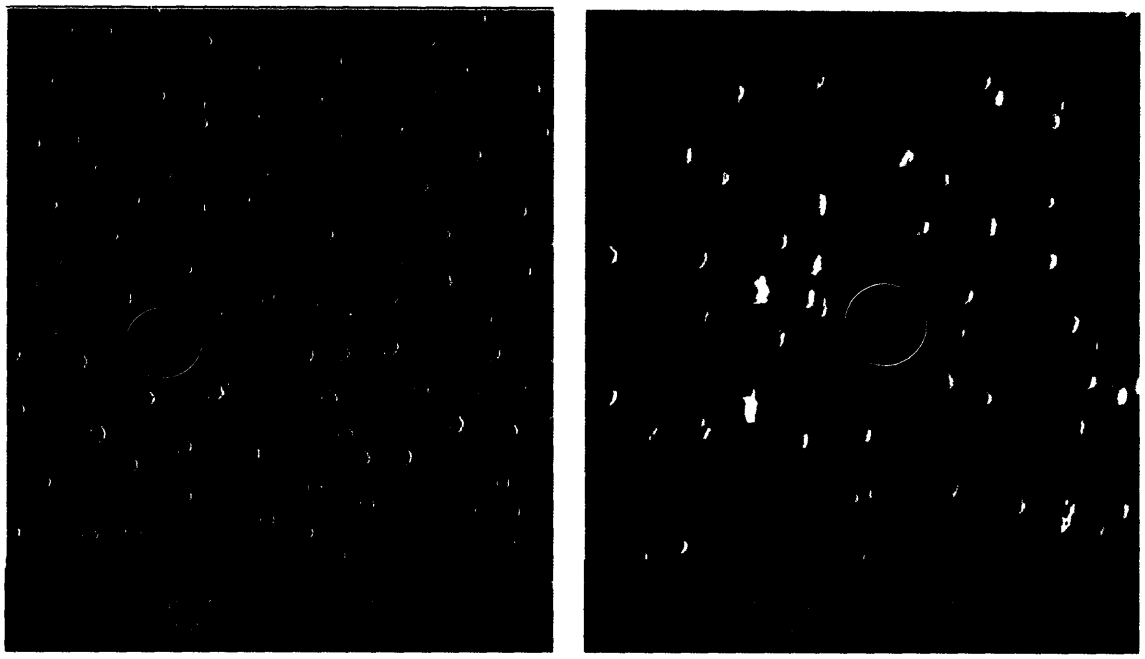

Figure 5-2 Au-Re nanoparticles produced from metal chloride solution with a molar ratio of 50/50 Au-Re after being freshly deposited *(left)* and after reductive annealing under hydrogen *(right)*. Particle coarsening in two nanoparticle size regimes is observed (small-diameter nanoparticles can be seen in the circles). The width of each image represents 5 μm.

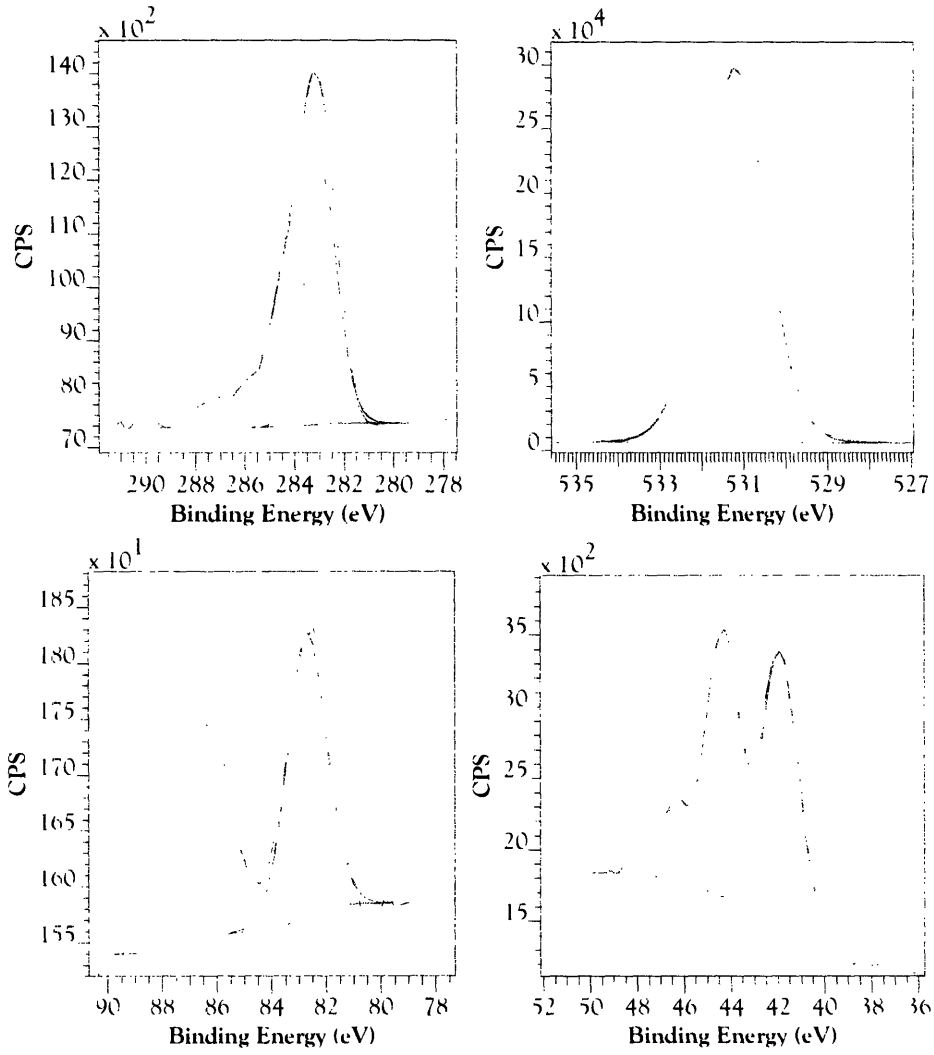

Figure 5-3 C 1s *(top left)*, O 1s *(top right)*, Au 4f *(bottom left)*, and Re 4f *(bottom right)* energy regions of XPS spectrum for 20/80 sample, showing both Au and Re to be in their metallic states in freshly prepared nanoparticles (note the Re $3p_{3/2}$ peak overlaps the Re 4f region and there is in fact only one chemistry of Re present).

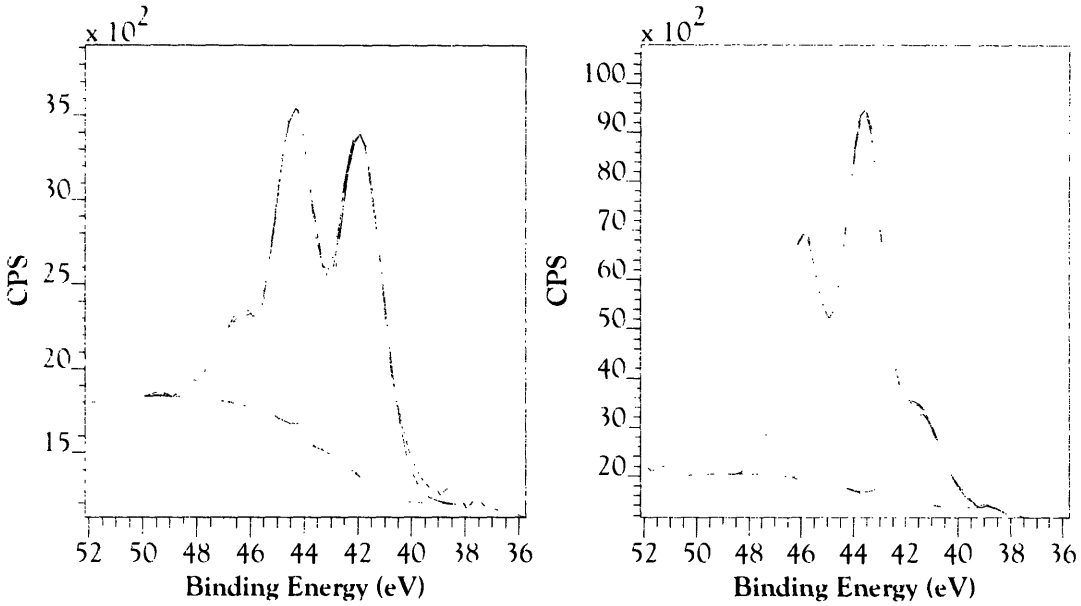

Figure 5-4 Difference in chemistry observed in the Re 4f region of the XPS spectra between samples prepared with anhydrous $ReCl_5$ (left) and samples prepared with moisture-exposed $ReCl_5$ (right).

Energy Region	Peak Assignment	Peak Center (eV)	FWHM (eV)	Area (eV counts)	R.S.F.*	Percent Contribution
C 1s	Organics	282.96	1.532	693.2	1	4.27
C 1s	Organics	283.96	2.036	623.9	1	3.85
C 1s	C=O π-π*	286.62	3.198	184.1	1	1.14
O 1s	Organics	531.23	1.725	42912.8	2.93	90.30
Re 4f	Re $4f_{7/2}$	41.93	1.968	382.1	11.1	0.21
Re 4f	Re $4f_{5/2}$	44.35	1.543	272	11.1	0.15
Re 4f	Re $5p_{1/2}$	46.41	2.234	105.5	11.1	0.06
Au 4f	Au $4f_{7/2}$	82.74	1.677	40.8	17.1	0.02
Au 4f	Au $4f_{5/2}$	86.28	1.895	35.7	17.1	0.01

*Relative sensitivity factor.

Table 5-2 Deconvolution results for XPS spectrum of 20/80 Au-Re nanoparticles (see Figure 5-3). The peak positions for this sample are representative of nanoparticles of any Au-Re ratio.

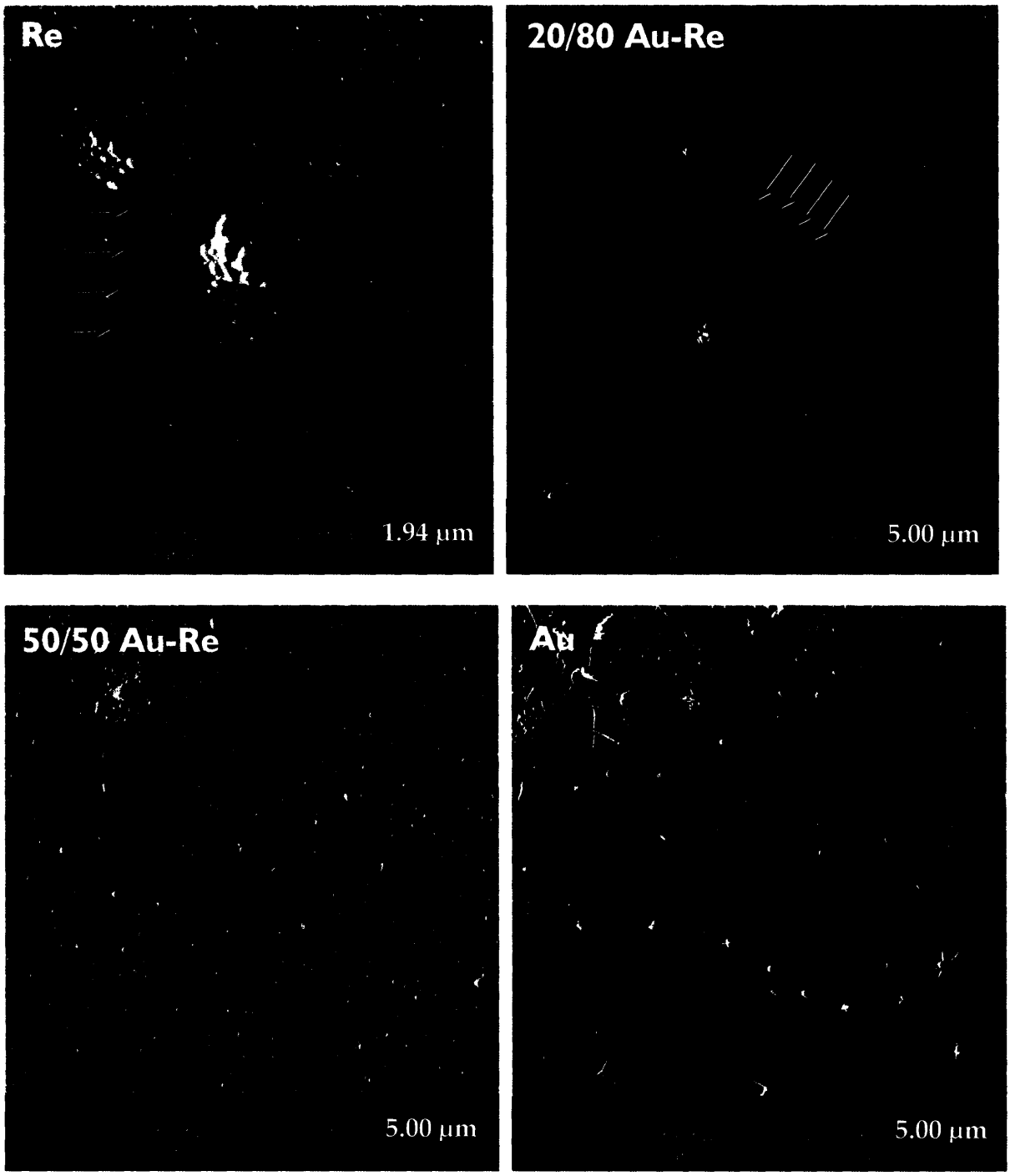

Figure 5-5 AFM images of nanotubes grown through hydrocarbon-based CVD on nanoparticles of Re *(top left)*, 20/80 Au-Re *(top right)*, 50/50 Au-Re *(bottom left)* and Au *(bottom right)* processed with reductive pretreatment only.

Trial	Reductively Annealed?	Oxidized?	CVD Growth Temperature	Flow Rate of H_2 (sccm)	Results
1	No	No	900°C	440	No Growth
2	No	Yes (10 min)	900°C	440	Volatilization of Nanoparticles
3	No	Yes (4 min)	900°C	440	No Growth, Retained Particles
4	Yes	No	900°C	440	No Growth
5	Yes	Yes	900°C	440	Nanotubes Found, Extremely Low Yield
6	Yes	Yes	1100°C	88	Amorphous Carbon Deposits
7	Yes	No	900°C	88	No Growth
8	Yes	Yes	900°C	440	No Growth
9	Yes	Yes	1100°C	440	No Growth, No Amorphous Carbon
11	Yes	Yes	1100°C	220	No Growth, Some Amorphous Carbon
12	Yes	Yes	900°C	44	No Growth
13	Yes	Yes	900°C	176	Nanotubes Found, Low Yield
14	Yes	Yes	900°C	88	Nanotubes Found, Moderate Yield

Table 5-3 Exploration of CVD process parameter space in determining the best conditions (Trial 14) for growth after reductive and oxidative pretreatment of 20/80 Au-Re nanoparticles.

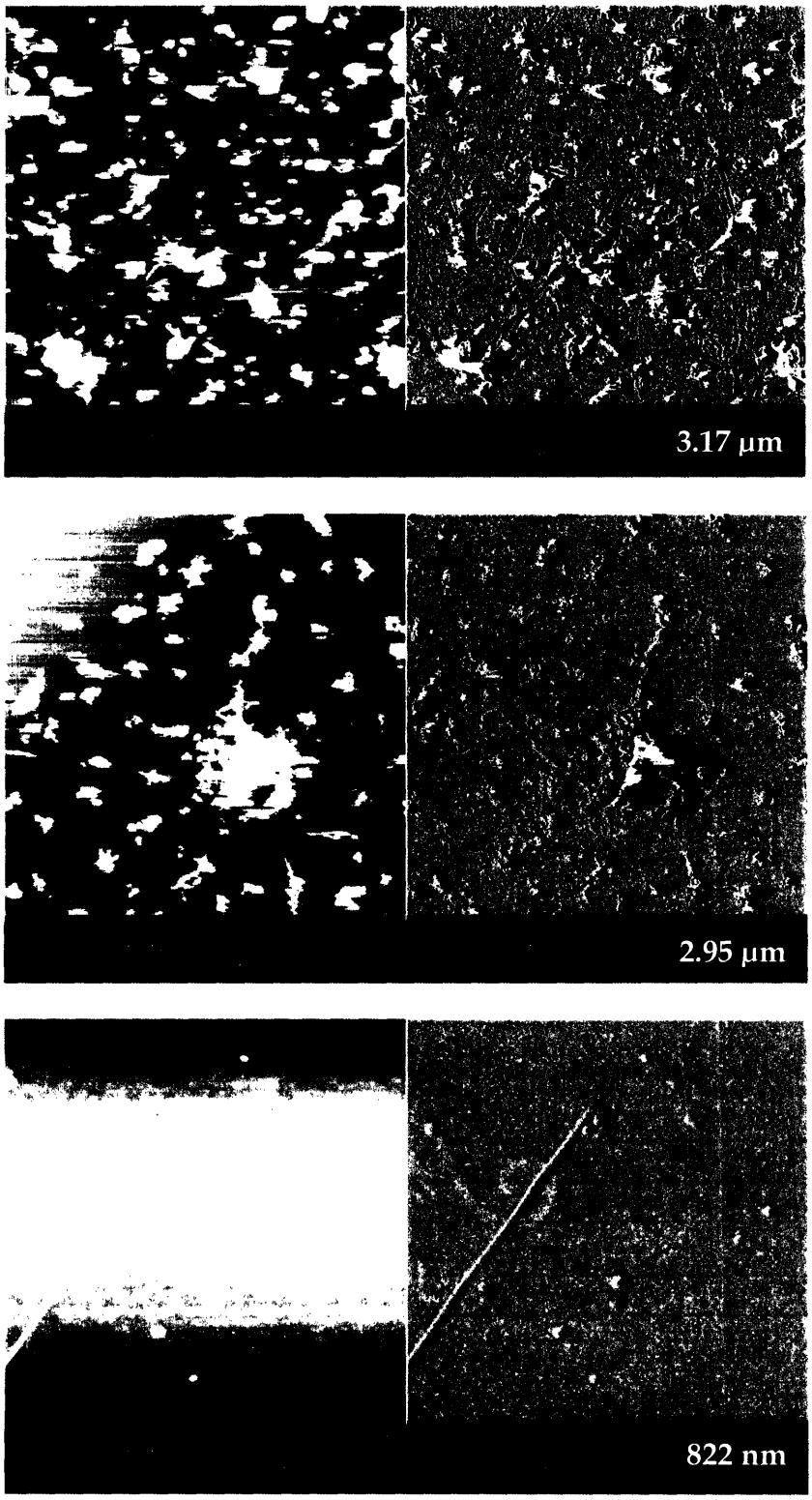

Figure 5-6 Results of CVD on 20/80 Au-Re samples as seen by AFM. Single-wall and multiwall carbon nanotubes are observed at various locations throughout the sample. The majority of nanoparticles on these samples, however, exhibit no catalytic activity.

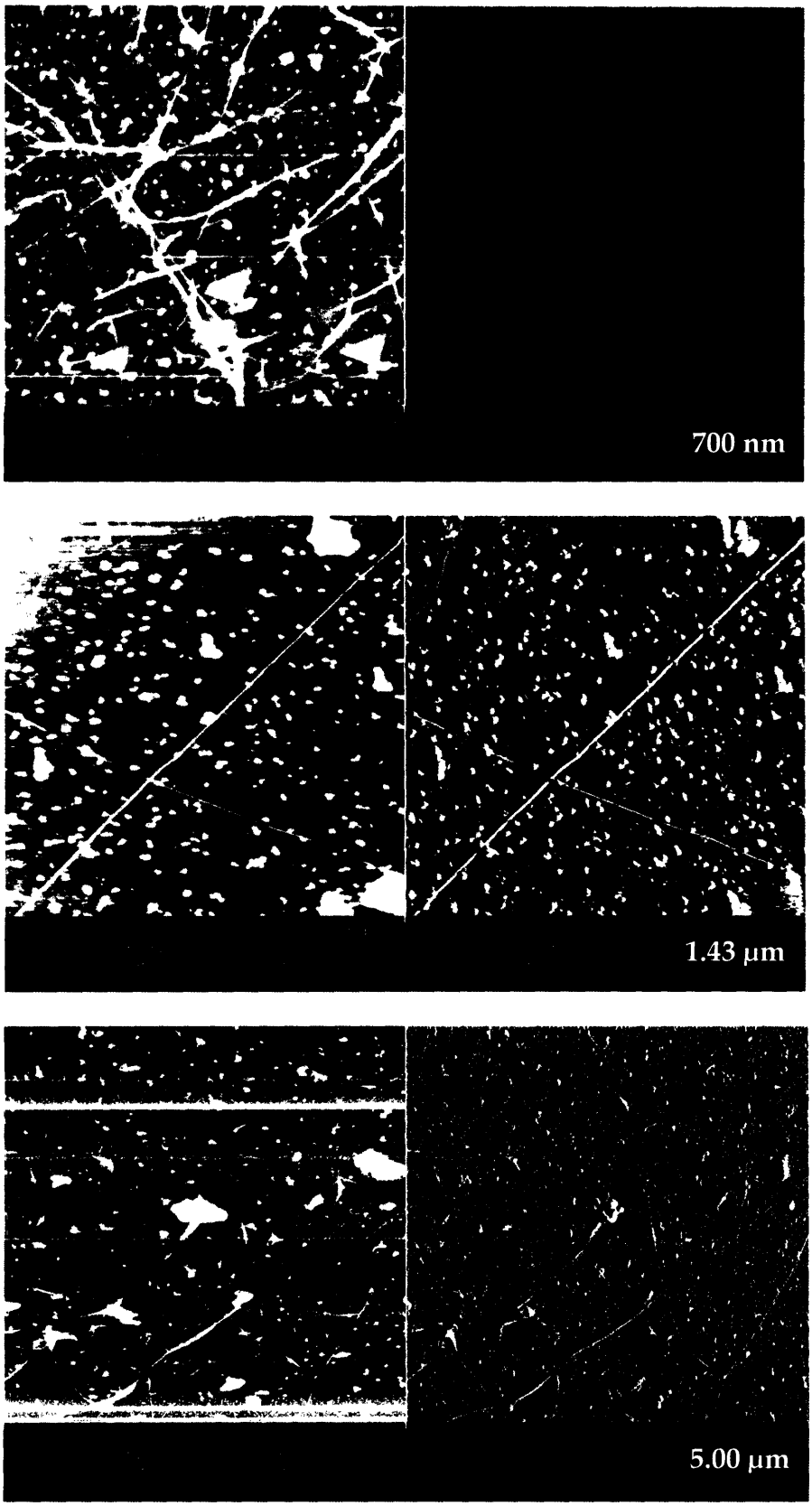

Figure 5-7 Single-wall and multiwall carbon nanotubes grown by 50/50 Au-Re as seen under AFM.

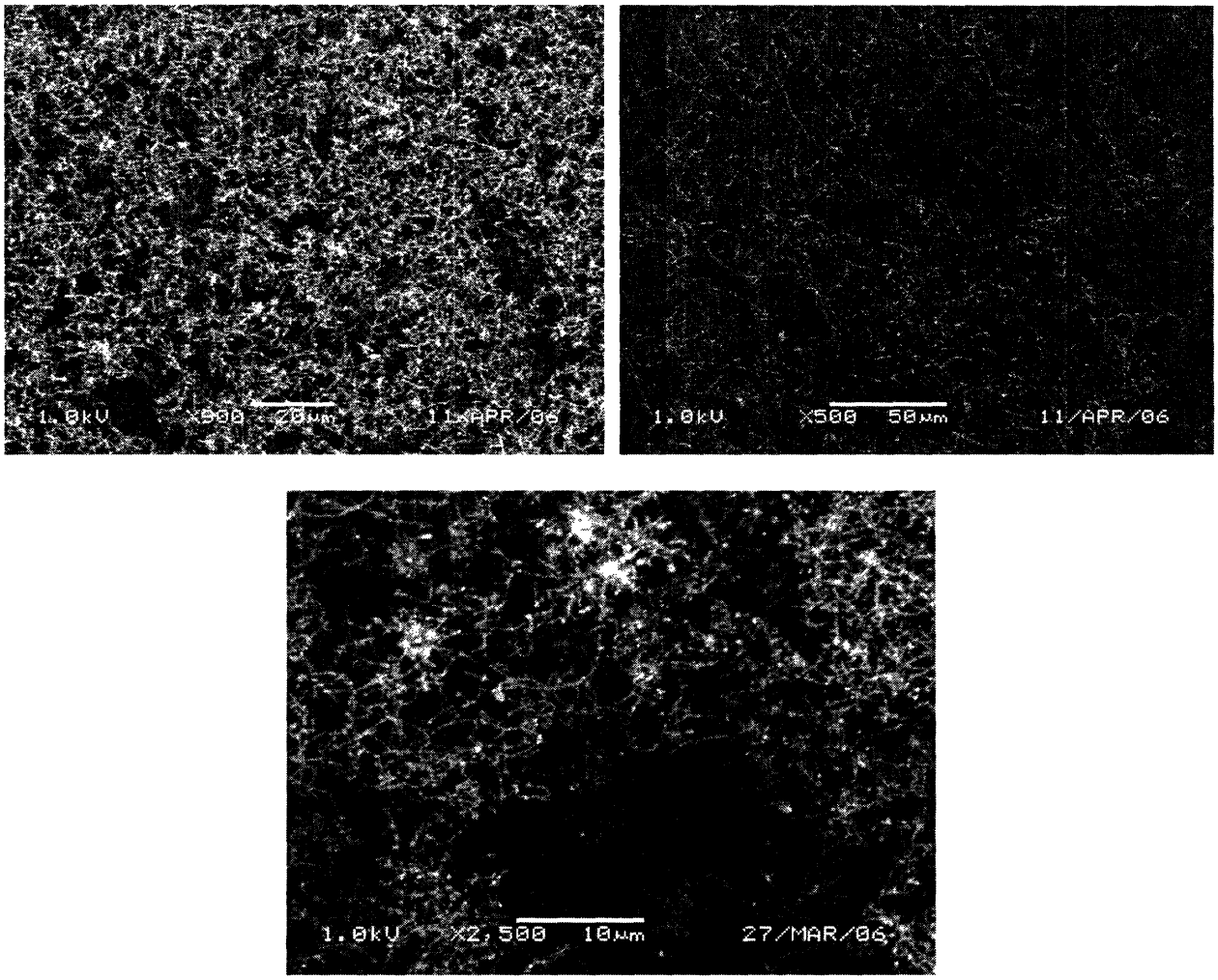

Figure 5-8 SEM micrograph of carbon nanotubes grown on two different 50/50 Au-Re nanoparticle catalyst batches.

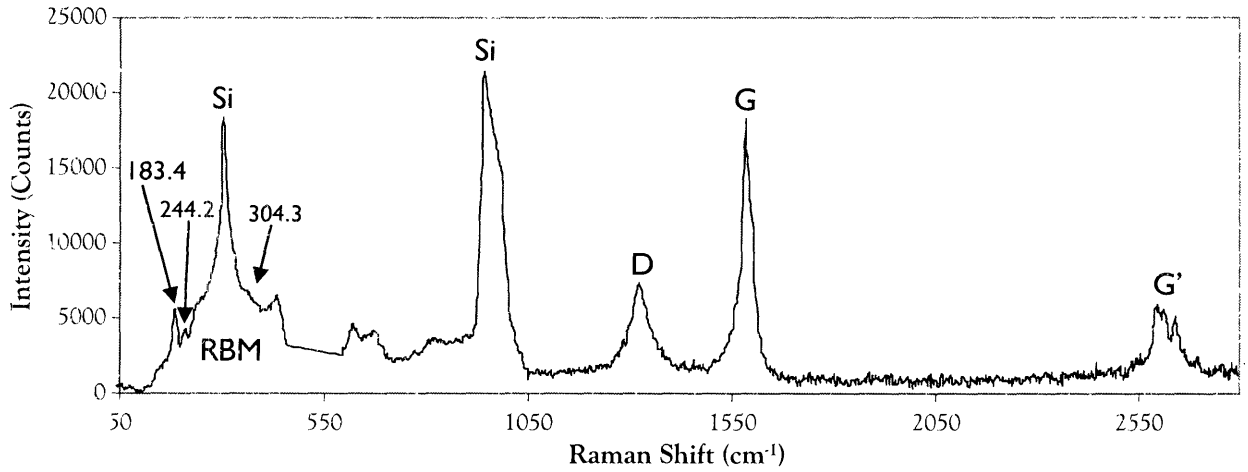

Figure 5-9 Raman spectrum of 50/50 Au-Re nanoparticle catalyst samples after CVD.

Peak Position (cm^{-1})	Assignment	FWHM (cm^{-1})	Amplitude	Area (cm^{-1} counts)
183.4	RBM	24.1	4035	1.53×10^{5}
244.2	RBM	60.2	3925	2.52×10^{5}
304.3	RBM	38.0	13900	8.31×10^{5}
396.1	Si	155.2	4947	8.17×10^{5}
618.5	Unknown	52.0	2830	2.31×10^{5}
670.7	Unknown	51.0	2305	1.85×10^{5}
849.7	Silicon	191.0	2772	7.72×10^{5}
1323.3	D-Band	64.6	5784	5.87×10^{5}
1586.4	G-Band	32.2	15600	7.77×10^{5}
2595.0	G'	22.7	3977	1.42×10^{5}
2614.3	G'	16.7	2554	5.46×10^{4}
2641.0	G'	17.1	3221	8.64×10^{4}

Table 5-4 Raman spectral features of carbon nanotubes grown by 50/50 Au-Re catalyst nanoparticles.

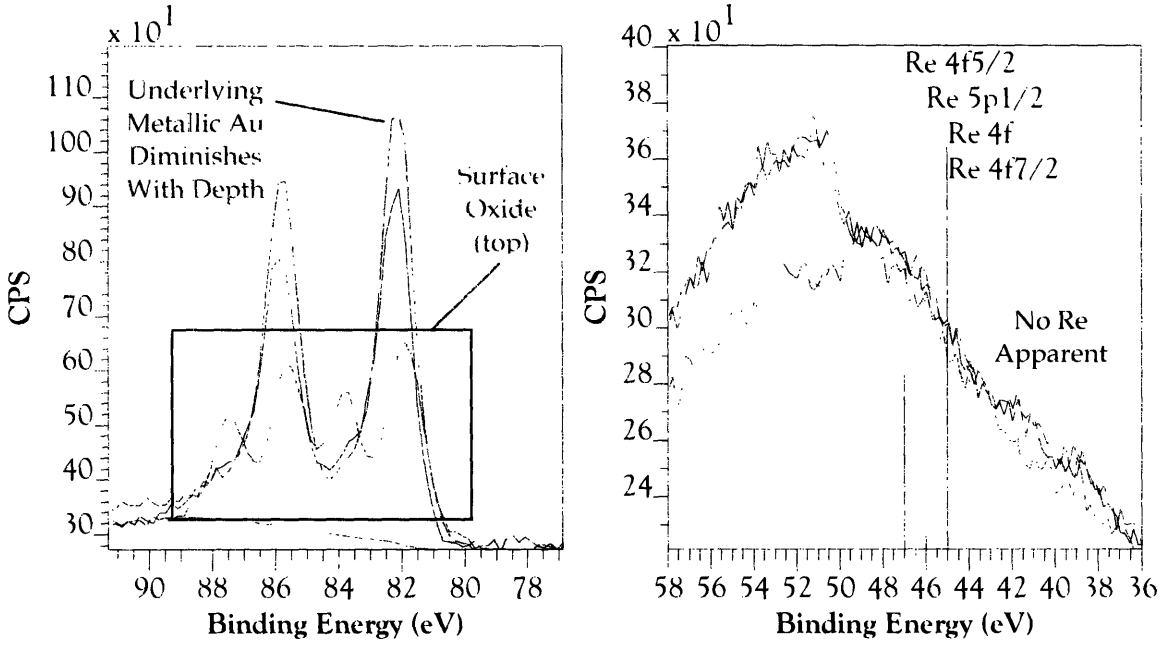

Figure 5-10 XPS depth profiling by Ar^{+} ion sputtering showing post-CVD gold and rhenium chemistry as a function of surface depth. Re is apparently absent from the surface at each depth.

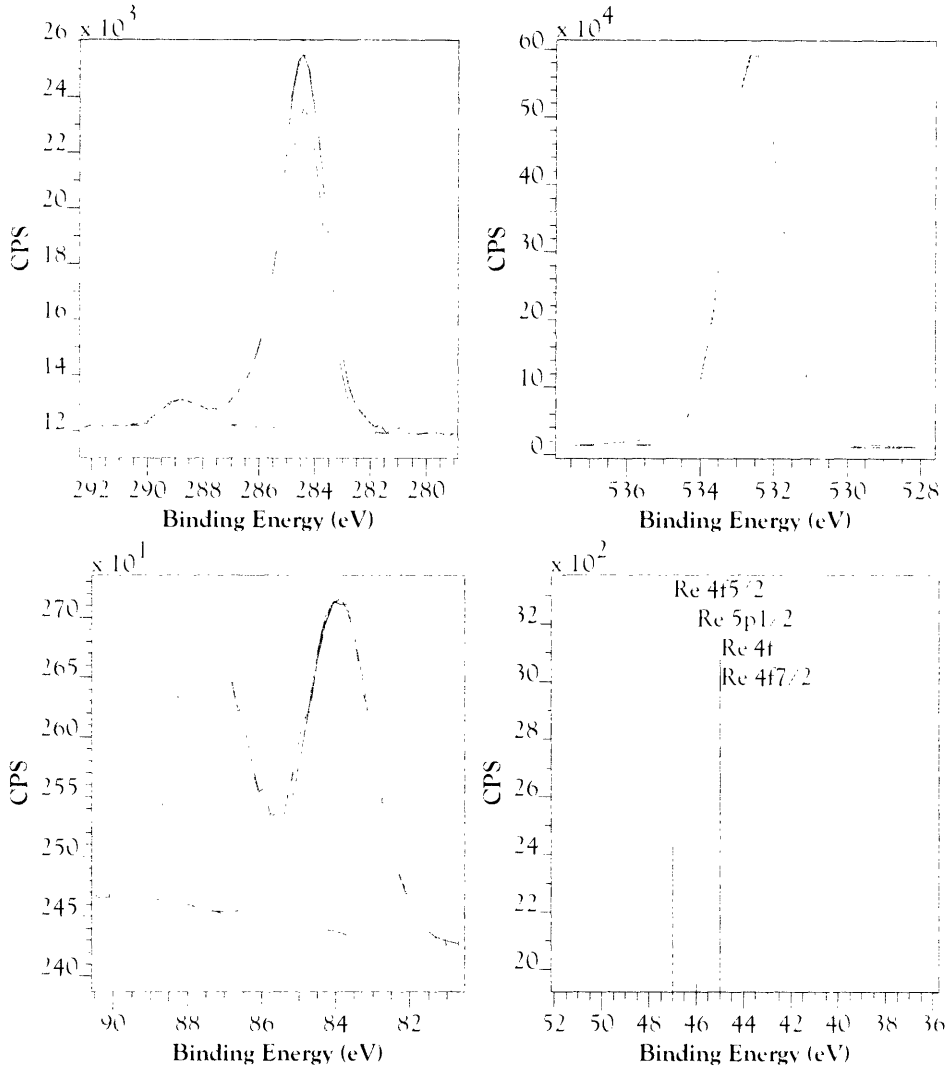

Figure 5-11 C 1s *(top left)*, O 1s *(top right)*, Au 4f *(bottom left)*, and Re 4f *(bottom right)* energy regions of XPS spectrum for 50/50 Au-Re nanoparticles after oxidation but before CVD, implying Re is absent form the sample surface before growth.

5.4 Discussion

Re, Au, and bimetallic Au-Re nanoparticles processed by reductive pretreatment all successfully grew single-wall carbon nanotubes (as determined by AFM) when hydrocarbon CVD feedstock was used. Re-only nanoparticles exhibited a slightly lower yield than the Au-Re and Au nanoparticles. Au-only, 20/80 Au-Re, and 50/50 Au-Re nanoparticles were all found to be capable of catalyzing nanotube

growth at both 700°C and 900°C, where Re-only nanoparticles only catalyzed growth at 900°C. These two facts combined suggest that a chemical change may be necessary to activate Re nanoparticles (such as reduction of non-volatile oxide from the surface of the Re nanoparticles), which requires elevated temperatures to occur, and that even after reductive pretreatment and CVD growth at 900°C for 10 min not all of the Re nanoparticles will be activated. This could be verified by punctuated XPS process analysis and by extending growth times to see if yield improves.

Addition of an oxidative pretreatment and use of alcohol as a carbon feedstock for CVD growth was found to result in successful growth of single-wall carbon nanotubes only for Au nanoparticles and Au-Re bimetallic nanoparticles with a composition of 20/80 or 50/50. Of these three compositions, 50/50 Au-Re nanoparticles resulted in the highest yields of nanotubes. Based on the measurements made on the Au-Re ratio for freshly deposited nanoparticles, it is estimated that the actual Au-Re ratio in the "50/50" sample is something closer to 18% Au, 82% Re (the actual ratio has yet to be measured). This said, it is reasonable to assume the nanoparticles in this sample are comprised primarily of rhenium, into which the gold dissolves to form a solid solution [137, 138].

It is interesting that after the oxidative pretreatment, only Au metal is detected on the surface of nanoparticles, but after growth, a surface oxide is detected. Gold oxides do not form under ambient conditions and typically require oxygen-containing radicals to form [109-114]. This implies that oxygen-containing radicals generated by thermolysis of ethanol during CVD actually oxidize the gold, and certainly do the same to Re. Although the XPS analysis of oxidized pre-CVD nanoparticles and the post-CVD XPS depth profiling experiment suggest Re is absent from the so-called 50/50 samples both before and after growth, it is uncertain whether or not Re is truly removed from the substrate or just no longer detectable by XPS (coated over with gold, atomically dispersed, etc.)

So why do only the higher gold content Au-Re nanoparticles result in nanotube growth when oxidatively pretreated prior to CVD? As mentioned in the introduction to this chapter, rhenium is known to form a volatile oxide at elevated temperatures (Re_2O_7) which will continue to form and sublime away the metal until

oxidation is ceased. As rhenium easily oxidizes at the temperatures required for nanotube growth, high rhenium-content nanoparticles are quickly oxidized and thus deactivated during the oxidative pretreatment. In turn, much of the rhenium volatilizes relatively quickly (explaining the disappearance of nanoparticles after Trial 2 in Table 5-3). It is postulated that past a certain gold-to-rhenium ratio, however, the added gold dissolved in the rhenium forms an oxidation-resistant alloy or intermetallic (just as alloying common metals with gold can increase their corrosion resistance), affording catalytic metallic nanoparticles. These alloy particles survive into CVD, catalyze nanotube growth, and become encased inside nanotubes or graphitic shells. The remainder of the rhenium on the substrate is volatilized away by OH· from ethanol in the CVD stream. As a result, Re is no longer easily detected by XPS. Au-Re nanoparticles with higher gold content are thus necessary in order to facilitate the hypothesized gold-rhenium alloy/intermetallic which can withstand oxidation and thus enable carbon nanotube growth. The oxidative pretreatment then, in essence, adjusts the Au-Re ratio by volatilizing rhenium away until the proper composition of Au in Re is achieved. Further investigation is required to understand the role of rhenium in this system.

Another plausible explanation is that the oxidative pretreatment volatilizes away all of the rhenium from Au-Re nanoparticles, and that the remaining gold nanoparticles are the species which catalyze nanotube growth. The justification for why Au-Re nanoparticles containing less than 20% gold do not successfully catalyze nanotube growth is simply because there is not enough gold present to catalyze nanotube growth by itself once all the rhenium has been volatilized away, or that the increased rhenium content results in not all of the rhenium volatilizing away in these samples, resulting in a layer of rhenium oxide coating over otherwise catalytic gold nanoparticles. This scenario, however, does not explain why 50/50 Au-Re nanoparticles result in a higher yield of nanotubes than Au-only nanoparticles.

Of the samples investigated by XPS in this study, the only samples which exhibited rhenium signals in their XPS spectra post-CVD are those which also did not grow carbon nanotubes (such as the sample which produced the XPS spectrum on the right-hand side of Figure 5-4). Incidentally, these samples were also

ascertained to contain Re_2O_3 before growth (most probably, but possibly another low-oxidation-state rhenium oxide) as a result of nanoparticle preparation with hydrolyzed $ReCl_5$. This oxide, which is almost certainly catalytically inactive, does not volatilize as easily as Re_2O_7 [103], and therefore survives into XPS even after CVD.

For most catalysts, it is advantageous for nanotube growth if the nanoparticles are oxidized (to burn off leftover organics) and then reduced (to their catalytic metallic state). However, given the added complexity of this system due to the facile volatilization of rhenium in oxygen, reversal of the pretreatments happened to be advantageous for this system.

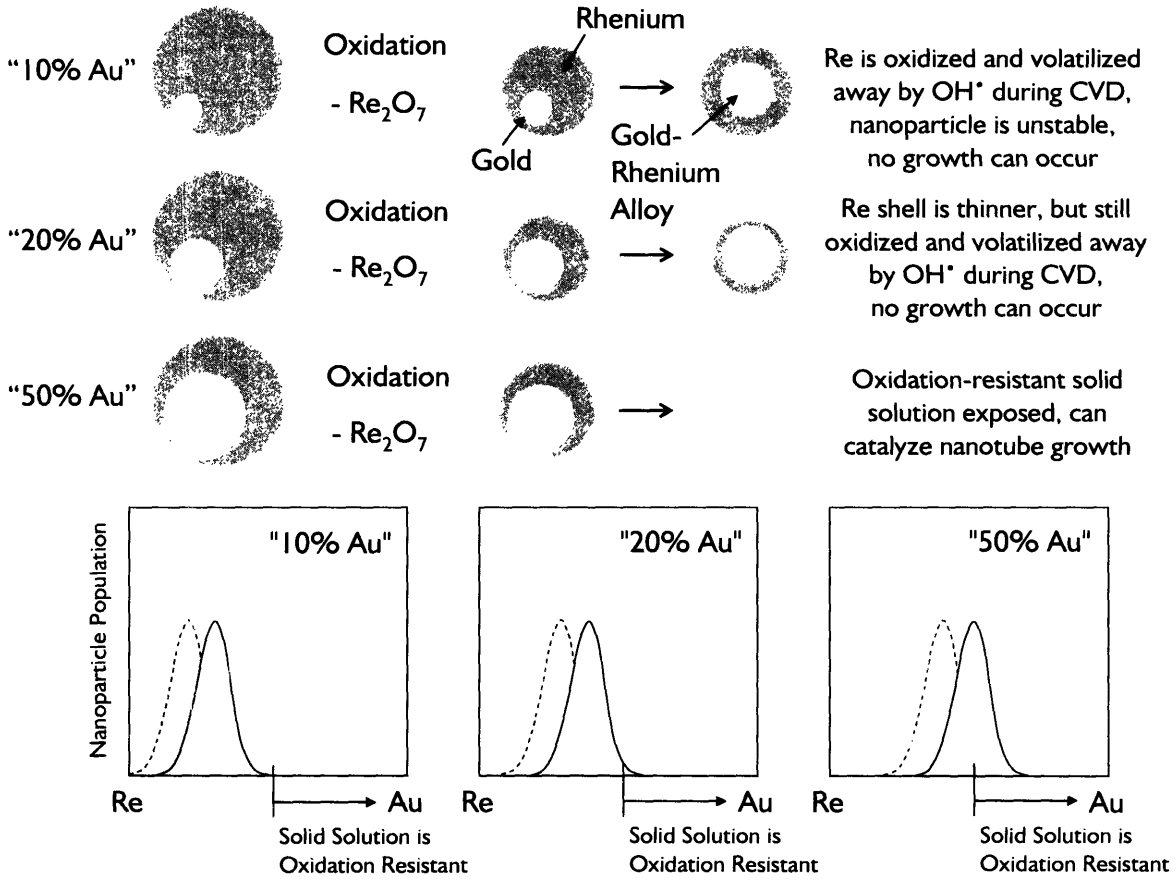

Figure 5-12 Schematic representation of the hypothesis proposed to explain the conditional catalytic activity of Au-Re nanoparticles following oxidative pretreatment.

Verification of the proposed mechanism by which 50/50 Au-Re nanoparticles result in high yield of nanotube growth could be conducted by elemental analysis or Auger spectroscopy of nanoparticles in the tips of nanotubes grown with Au-Re catalysts or by intentionally depositing more gold to intentionally form an oxide-resistant alloy without having to etch excess rhenium away.

The facile volatilization of oxidized rhenium at elevated temperatures may also enable a novel method for nanotemplating nanoporous metals through dealloying. In this technique, a bimetallic alloy of rhenium and another metal (gold for example, or a noble metal such as platinum or palladium which is likely to be reasonably insoluble in rhenium the way gold is) such that grains of rhenium extend throughout the alloy beyond the percolation limit. Subsequent heating of such an alloy under oxygen would then volatilize the rhenium out from the alloy structure, leaving behind a nanoporous metal complement. This technique could also be used to fabricate nanoparticles or other nanostructured materials by "burning off" rhenium templates.

5.5 Conclusions

A technique for preparing bimetallic nanoparticles composed of gold and rhenium was developed and characterized. This technique should be easily extensible to other metals as well. Solution dynamics were found to play an important role in determining the composition of nanoparticles prepared with this technique.

Subsequently, growth of single-wall carbon nanotubes with gold, rhenium, and gold-rhenium nanoparticles catalysts was demonstrated. Rhenium was found to easily catalyze carbon nanotube growth provided oxidation-free processing, but was difficult to work with as a surface-based nanoparticle catalyst due to its propensity for being oxidized and for its oxides to volatilize. For these reasons, rhenium is a non-ideal nanotube catalyst. Metals such as those presented in the conclusions of Chapter 4 which remain resistant to oxidation at elevated temperatures as well as not forming stable carbides should be considered more appealing targets for research in developing chemically-resistant nanoparticle catalysts for nanotube

growth. Gold was found to catalyze nanotube growth successfully both when processed without oxidative pretreatment followed by hydrocarbon-based CVD and when processed with oxidative pretreatment followed by alcohol-based CVD. Given its efficacy under oxidative and non-oxidative conditions and the fact that it does not form stable carbides, gold appears to be an ideal nanotube catalyst as defined in Chapter 3.

Lastly, Au-Re nanoparticles deposited from solutions containing a 1:1 molar ratio of Au to Re were found to produce high yields of carbon nanotubes when processed without oxidative pretreatment followed by hydrocarbon-based CVD and when with oxidative pretreatment followed by alcohol-based CVD, where Re nanoparticles and Au-Re nanoparticles deposited from solutions containing less than a 1:4 molar ratio of Au to Re resulted in no growth of carbon nanotubes. This is tentatively attributed to the formation of an oxidation-resistant Au-Re alloy or intermetallic facilitated by partial volatilization of Re from the nanoparticles during oxidative pretreatment and CVD growth.

In summary, the Au-Re system exhibits a unique and rich chemistry with the capable of catalyzing growth of single-wall carbon nanotubes. Further investigations into this system are required to fully understand its behavior and its potential.

Chapter 6

Development of a Multifunctional Apparatus for Optimized Nanotube Growth

6.1 Introduction

The growth of carbon nanotubes by heterogeneous catalyst-based thermal CVD is frequently performed using technologies adapted from the semiconductor industry, such as clamshell process tube furnaces and mass flow controllers. However, in many respects, the equipment and processing techniques optimized for CVD of thin films are not optimal for nanotube growth, particularly with respect to the incorporation of nanotubes into integrated circuits. Although the fundamental reactions which enable CVD growth of carbon nanotubes occur within the surface-reaction-limited regime of CVD, bulk gas-phase mass transport also plays an important role. Aerodynamic turbulence in the CVD stream, for example, can cause nanotubes to tangle or unexpectedly hit the substrate surface as their lengths exceed a few microns, resulting in defects and/or termination of growth. Thermal gradients and convection currents over macroscopic length scales in the quartz process tube can cause inhomogeneities in the activity of catalyst nanoparticles over a substrate as well. But most significantly, the high temperatures typically required for feedstock gas cracking using standard CVD equipment for nanotube growth

preclude implementation of critical materials on nanotube-containing integrated circuits such as aluminum and gold [142-144]. Additionally, elevated temperatures promote diffusion, particle coarsening, and Ostwald ripening, which can result in a loss of control over nanotube placement, diameter, and yield, respectively.

The reasons why nanotube growth is typically most successful at temperatures of 800-900°C are likely threefold. The first reason may be a need for reducing metal oxide in the nanoparticles to a catalytic metallic state (as argued in this thesis). If this is the case, it is almost always a "transparent process" to which the experimenter is ignorant. In the case of the metal-doped carbon aerogels explored in Chapters 2-4, for examples, growth temperatures of only 700°C were sufficient, facilitated the high degree of *in situ* carbothermic reduction of nanoparticles in the aerogel. The second reason is the need for thermolytic feedstock gas cracking, which decreases with temperature, to supplement catalytic cracking by the nanoparticles. It appears that the temperature required for adequate thermolytic feedstock cracking is several hundred degrees higher than the minimum temperature required for nanotube nucleation and growth processes [66, 142-145]. As a result, standard CVD equipment forces a compromise between the minimum temperature required for adequate thermolytic cracking of the feedstock gas and the temperatures which the catalyst nanoparticles must tolerate. The third reason arises from the fact that the incoming CVD gas stream is at room temperature when it first enters the hot zone and needs to be heated before feedstock cracking and nanotube growth can occur.

In response to the above problems, a new CVD system optimized for CVD growth of carbon nanotubes was designed. Dubbed the Advanced Multifunctional Apparatus for Nanotube Optimization or "AMANO", this system aims to eliminate problems arising from aerodynamics, thermal inhomogeneities, and high process temperatures.

6.2 System Overview

The AMANO system combines attributes of several systems reported in the literature which innovate on the equipment typically employed in CVD growth of

carbon nanotubes in order to improve some aspect of nanotube growth. These attributes are as follows:

- *Low-pressure CVD processing,* to provide a quiescent, quasi-static environment for nanotube growth. This aids in eliminating problems arising from aerodynamics inherent to typical CVD growth procedures and facilitates vertically-aligned nanotube growth [143].
- *Separation of substrate heating and thermolytic gas cracking* to independently optimize the temperature required for each process. This is a lesson learned by the nanodiamond community over a decade ago and could likely benefit nanotube growth as well [143].
- *Use of a hot filament* placed in the path of incoming feedstock gas and operating at 2000°C for efficient thermolytic cracking before it reaches the substrate [66, 145].
- *Use of a ceramic hot plate* for homogenous heating of the catalyst substrate. An embedded type-K thermocouple allows for unambiguous substrate temperature characterization during growth.
- *Narrow-range mass flow controllers and liquid reservoirs,* enabling experimentation with a wide variety of gaseous and liquid feedstocks, etching agents, and dopants with a high level of precision [60, 64, 65, 144].

Additional attributes implemented in the design of the AMANO system unique to this system include:

- *Near-complete process automation and software-based equipment controls* to reduce factors arising from user error and procedural inconsistencies.
- *User-friendly software interface* to reduce errors which arise from variations in equipment use from user to user and which vary with experience.
- *Process visualization from multiple angles* enabling *in situ* observation of growth and the possibility for *in situ* Raman characterization.
- *Versatile, modular architecture* enabling for easy integration of new process technologies into the system, such as electric field- and plasma-assisted growth [52, 60].

6.2.1 Primary Apparatus

Figure 6-1 shows a schematic overview of the apparatus. The vessel is composed exclusively of off-the-shelf, modular vacuum quick-flange (QF/KF/NW), con-flat (CF), and tube fittings. The core of the reactor is a 2 ¾" CF six-way cross. Wrapped around the core is a copper pipe brazed to the surface which can serve as a heat exchanger for thermal management. To this cross are attached components for flow control, the sample plate module, the cracking filament module, and two quartz sight glasses. With the exception of the core, all components are QF-25 form factor. Figure 6-2 shows a photograph of the actual system.

Two electrically-actuated valves control the flow of gases to the vacuum pump—a gate valve for rapid pump-down, and a solenoid valve in series with a multi-turn throttling valve. The throttling valve must be adjusted manually, but once set, flow through this valve can be opened or closed by the solenoid valve. Attached to the back side of the six-way cross (not shown) is a 2 ¾" CF to QF-40 reducer. A QF-40 blank flange is then clamped onto this reducer to provide quick access to the interior of the apparatus. Samples are inserted and removed through this fitting.

6.2.2 Electrical Interface and Power Electronics

Figure 6-3 shows a block-level schematic of the system's electrical interface. With the exception of sample loading and unloading, every aspect of the CVD process is controlled by computer and can be executed automatically (see Section 6.2.3). System pressure is monitored by a MEMS-based Micropirani 925C vacuum gauge with a range of atmosphere to 10^{-6} torr which communicates with the computer through an RS-232 interface. The temperature of the sample plate is measured by an embedded Type-K thermocouple (Figure 6-4), read by an Omega CNi-3252 temperature controller. The temperature controller then regulates power to a tungsten filament embedded in the sample plate (Figure 6-4) via a Eurotherm silicon controlled rectifier (SCR) phase-angle-fired power controller, which delivers power in a way which helps to preserve filament life. The temperature controller can be adjusted manually on the front panel of the interface box or by computer through an RS-485 interface.

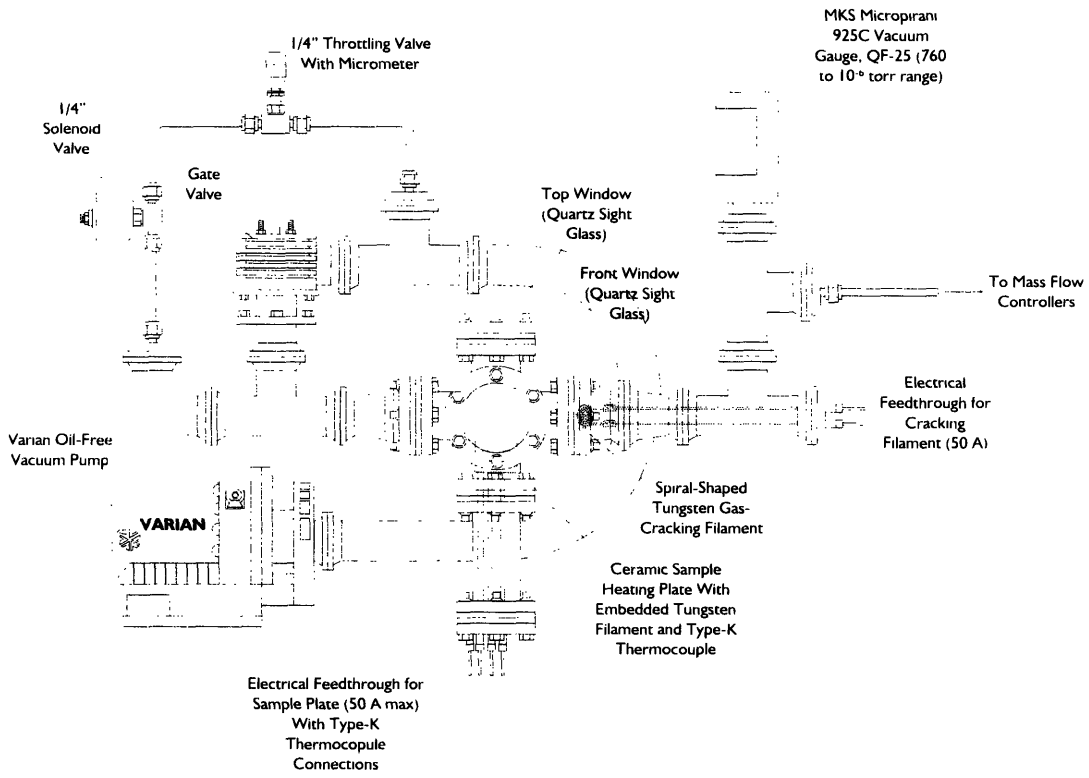

Figure 6-1 Schematic of AMANO apparatus.

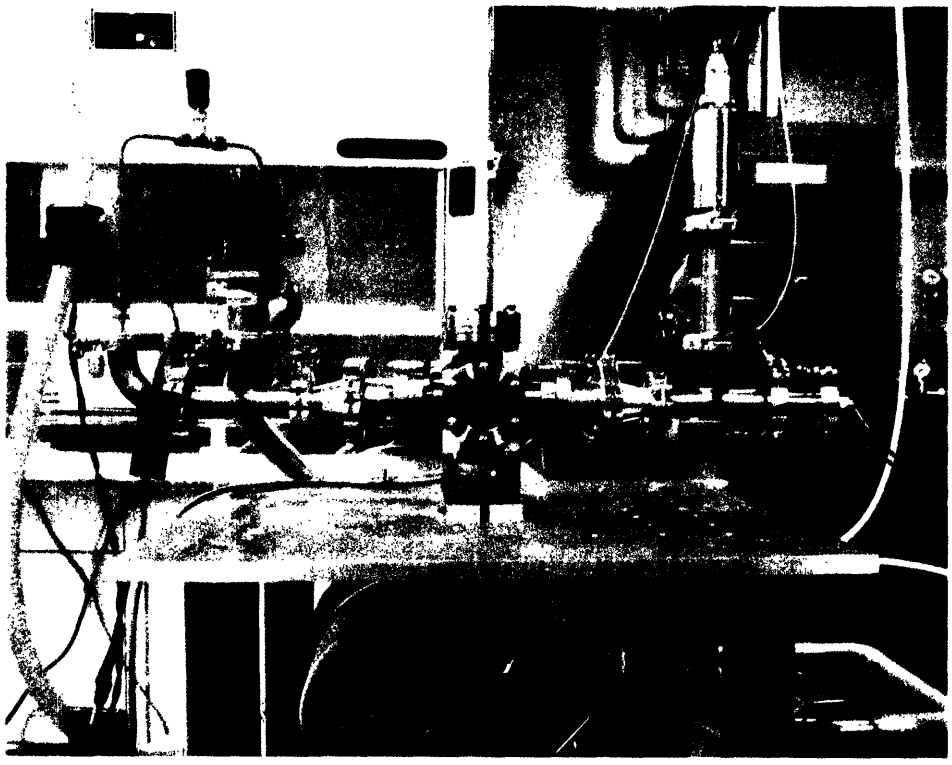

Figure 6-2 Photograph of AMANO apparatus.

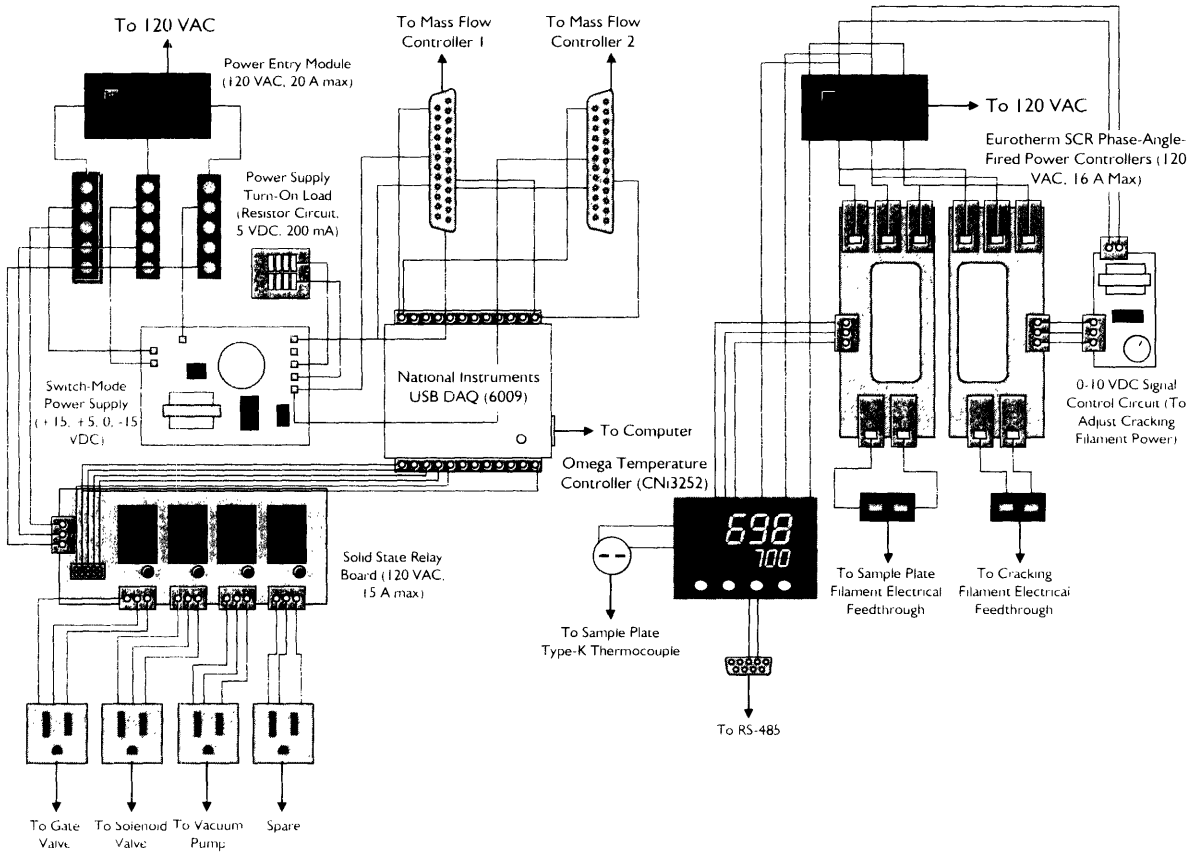

Figure 6-3 Electrical block diagram for the AMANO system control interface.

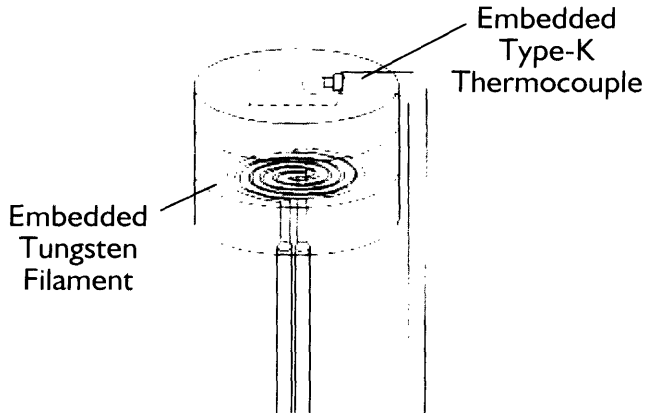

Figure 6-4 Detail of the ceramic heating plate with embedded spiral-shaped tungsten filament and Type-K thermocouple. The dotted lines indicate where a sample would be optimally placed.

6.2.3 Software Interface

Figure 6-5 shows a screen-shot from the software interface written for manual control of the apparatus. Both manual and automated process controls are available for use. Controllable devices, which include the valves, mass flow controllers, vacuum pump, cracking filament, and sample plate, are activated simply by clicking on a picture of the device. The picture illuminates or grays-out depending on whether it is active or inactive. Each device control is equipped with an optional timer function which will change the state of the device after a specified period of time has elapsed. Mass flow controllers have an additional control allowing for specification of flow rate. Temperature devices have a control allowing for the specification of temperature.

Automated control is accomplished using the FLAPL™ fuzzy logic/natural language parsing process automation engine[5]. Commands for controlling process components are written using a subset of plain English in script form. The FLAPL engine then interprets each line of the script and sequentially executes each command. Any command which can be executed using the manual control interface can be executed via the automated controls. Complex growth experiments are best planned out ahead of time and implemented in script form with automated processing. Below is a sample process script written in FLAPL.

```
> close throttle valve
> open gate valve
> turn vacuum pump on
> start loop
> if the pressure stagnates and the pressure is greater than 1 torr then
  email ssteiner@mit.edu with a messaging saying "A possible leak or
  substrate off-gassing has been detected.  Please attend to the AMANO
  system."
> if the pressure stagnates and the pressure is less than 1 torr then
  exit loop
> repeat loop
> close gate valve
> open throttle valve
> email ssteiner@mit.edu with a message saying "Greetings.  System
  pressure has equilibrated.  Keep writing--no intervention is required.
  Thanks, The AMANO System."
> set sample plate temperature to 700 deg C
```

[5] FLAPL™ is a trademark of Aerogel Technologies, LLC. FLAPL process automation technology used under license from Aerogel Technologies.

```
> wait until the sample plate reaches 700 deg C
> activate cracking filament 'which is the same as saying "turn  on
  cracking filament"
> set mfc1 to 20 sccm 'hydrogen
> open mfc1
> open liquid reservoir 'methanol/benzylamine
> wait for 10 min
> close liquid reservoir
> close mfc1
> turn cracking filament off
> turn sample plate off
> wait until sample plate is cool enough for the likes of me
> email ssteiner@mit.edu and tell him "Growth complete.  Please attend
  to the AMANO system."
```

This example highlights the versatility of the AMANO system's process automation capabilities and the FLAPL engine's tolerance for syntax.

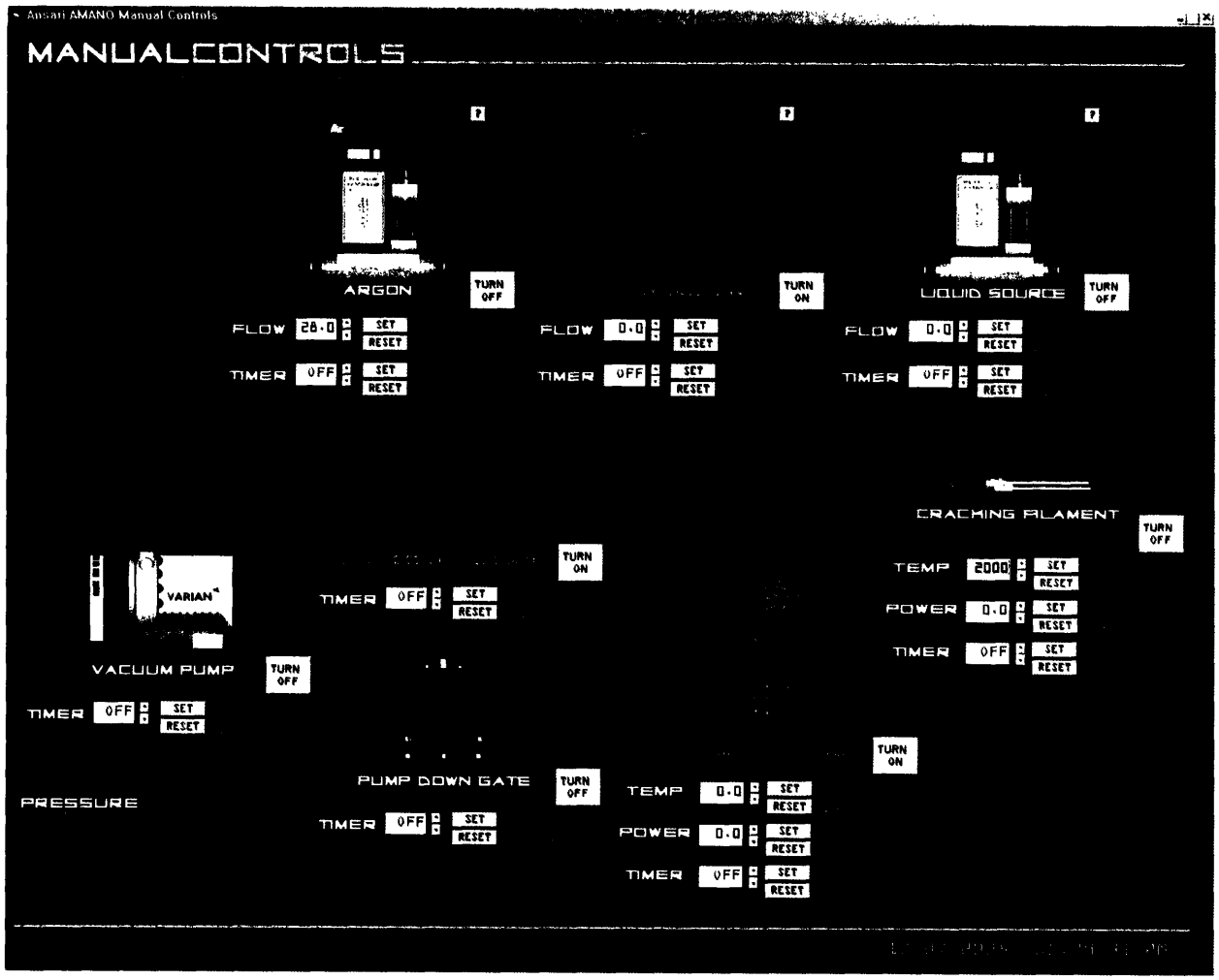

Figure 6-5 Screen-shot of the AMANO control software.

6.3 Current Status and Planned Experiments

The AMANO system central apparatus and control software have been completed. The electronics interface is nearly complete, with the exception of the power control electronics for automation of the hot filaments. The filaments have been successfully tested using manually-controlled DC power supplies (Figure 6-6). However, the SCR phase-angle-fired power controllers have so far not successfully been able to heat the filaments and require further investigation. The system has been shown to hold vacuum, with the lowest vacuum achieved so far approximately 10^{-3} torr.

The first experiments planned for the system will be proof-of-concept growths employing ethanol over iron-doped carbon aerogels. Since iron-doped carbon aerogels do not require any reductive or oxidative pretreatment for growth, they are ideal for a "quick and dirty" evaluation of CVD with this system. Following successful growth on iron-doped carbon aerogels, growth with ethanol using surface-based iron nanoparticles will be attempted, eventually transitioning to methanol. The system's medium-term goal is to produce single-wall carbon nanotubes from various metal catalysts using ^{13}C-enriched methanol, for ^{13}C NMR experiments aimed at determining the ratio of metallic-to-semiconducting nanotubes produced by different catalysts. Methanol is preferred over ethanol for these experiments since ^{13}C-enriched ethanol is twice as expensive as ^{13}C-enriched methanol per gram.

6.4 Conclusions and Future Considerations

The AMANO system offers great potential for developing new, optimized CVD techniques for producing carbon nanotubes and for streamlining experimentation with nanotube growth. The greatest challenges encountered in the system so far have been in dealing with efficient heating and automated control of the hot filaments. So far, the cracking filament has worked as expected. The sample plate, however, has been found to be fairly sluggish in reaching its target temperature (requiring over 30 minutes to go from ambient temperature to 700°C) and a redesign

may be required if faster heating is necessary. Additionally, automated control of power to the filaments has so far been unsuccessful and will require further refinement if not a complete redesign.

Figure 6-6 AMANO system with sample plate and cracking filaments in operation.

Chapter 7

Conclusions

This work has demonstrated and characterized techniques for producing new carbon aerogel-based materials as well as explored fundamentals underlying the chemistry of carbon nanotube catalysis. The following is a discussion of lessons learned from these experiments and ideas for new nanostructured materials based on unexpected results encountered in their execution.

It was found that Fe-doped carbon aerogels respond quite differently to pyrolytic treatment than Co or Ni, in that a spectrum of nanoparticles comprised of both metal and metal carbides emerges in response to increased pyrolysis temperature instead of a solid-state transformation of the aerogel framework into graphitic nanoribbons. In fact, no significant graphitization of the aerogel was observed in these materials for pyrolysis temperatures up to 1050°C. It has since been reported that pyrolysis of Fe-doped carbon aerogel-like materials can result in graphitization of the aerogel, however only for pyrolysis temperatures above 1400°C [80]. In exploit of the lack of graphitization below 1400°C in this system (which would otherwise encapsulate metal-containing nanoparticles in the aerogel with graphitic shells and other carbon nanostructures), it was found that nanoparticles in Fe-doped carbon aerogels can be catalytic towards the growth of carbon nanotubes by thermal chemical vapor deposition enabling direct growth of carbon nanotubes on the aerogel monolith. Fe-doped carbon aerogel samples containing high populations of iron carbide nanoparticles (more specifically, high populations of nanoparticles with predominantly carburized surfaces) were found not to result in nanotube growth as

well as samples with oxidized surfaces. It is believed that oxidized surfaces are reduced to metallic iron during CVD at which point they can facilitate nanotube growth, where carburized surfaces are characteristic of catalytically inactive nanoparticles. In fact, it has been demonstrated in other heterogeneous catalysis systems similar to thermal CVD growth of carbon nanotubes that carbides are associated with poisoned catalysts [41, 42, 88]. As discussed in Chapter 3, carbides are also not known to be particularly catalytic towards dehydrogenation reactions [87, 88]. It can be further argued that diffusion of carbon through the ceramic metal carbide lattice is just too slow at CVD growth temperatures to facilitate the mechanisms required for diffusion, nucleation, and precipitation of carbon for nanotubes [88]. It is possible, however, that under the right conditions, metal carbide nanoparticles can decompose into a mixture of metal carbide and carbon-saturated metal which could then allow for precipitation of a crystalline carbon nanotube [41, 89]. Additionally, carbides can potentially be oxidized back to metallic iron by oxidizing agents in the CVD stream and then enable growth of nanotubes. Depending on the stability of the carbide, the temperature at which CVD is carried out, and the mixture of gases employed for CVD, carbides may either be undesirable or perfectly capable of contributing positively towards nanotube growth. In either case, however, carbides are likely not the active catalytic species.

Nanotubes were found to grow no deeper than ~1 μm from the exterior edge of the aerogel into confined porosity due to the short mean free path of diffusion (6-7 nm pore diameter) inherent to the mesoporous aerogel. These novel carbon aerogel-carbon nanotube composites exhibited an improvement in electrical conductivity over the already enhanced conductivity metal-doped carbon aerogels exhibit over undoped carbon aerogels. The specific surface area of the aerogel was found to decrease with the addition of carbon nanotubes due almost exclusively to a loss of accessible microporosity (which is not surprising). However, grinding the aerogel monolith into a powder before performing CVD resulted in partial recovery of the lost surface area thanks to a higher percentage of accessible nanoparticles and thus a higher nanotube-to-aerogel mass ratio. It is hypothesized that by growing

nanotubes long enough and with small enough diameters, all of the surface area lost due to CVD-induced obstruction of microporosity could be recovered and possibly exceeded to actually produce aerogels with greater specific surface area and electrical conductivity—circumventing the inversely proportional relationship of surface area and electrical conductivity otherwise intrinsic to carbon aerogels. Carbon aerogel-carbon nanotube composites could be of great utility for use as high-surface-area electrodes for supercapacitors, desalination systems, fuel cells, and rechargeable batteries. In addition, carbon aerogel-carbon nanotube composites, provided demonstration of adequate thermal transport, could also be of great use in physisorption-based storage of hydrogen.

Several techniques towards optimizing carbon aerogel-carbon nanotube composites were explored. Templating of a macroporous gas-diffusion network into otherwise mesoporous Fe-doped carbon aerogels resulted in a material with a bimodal pore structure which enabled carbon nanotubes coverage throughout the interior porosity of the aerogel monolith. Unfortunately, this came at the expense of reduced material strength. Refinement of this technique, perhaps by reducing the mean macropore diameter or by implementing an ordered array of macropores could help mitigate this trade-off. A new class of carbon aerogel-nanoparticle composites was explored in which prefabricated, monodisperse nanoparticles of Fe_3O_4 were introduced into a carbon aerogel with the intention of facilitating growth of single-wall carbon nanotubes. These materials were found to be primarily macroporous due to pH-induced morphology changes encountered in the incorporation of surfactant-stabilized nanoparticles into the phenolic sol precursor. This could be conceivably overcome by adjusting the chemistry of this precursor. The Fe_3O_4 nanoparticles were found to require some carbothermic reduction in the form of pyrolysis of the aerogel in order to be capable of inducing nanotube growth. Longer pyrolysis and thus longer carbothermic reduction of these composites was found to result in higher populations of nanotubes but a shorter mean nanotube length. Shorter pyrolysis (and thus less carbothermic reduction) was found to result in lower populations of nanotubes but with a much longer average length. Based on XRD, XPS, and SEM data from this system and Fe-doped carbon aerogels prepared

through ion exchange, a model proposing a chemistry-sensitive catalytic activity of iron nanoparticles was developed, suggesting that oxides and carbides are not the catalytic species directly and that controlling the composition of iron nanoparticles such that they maintain high metallic iron content is beneficial to reproducible and long-lived nanotube growth. It should be noted that metal oxides could serve in the role of dehydrogenation catalysts [90], but like carbides, the diffusion of carbon through metal oxides is just too slow for a nanotube growth mechanism which involves diffusion of carbon into a nanoparticle and precipitation as crystalline carbon [88]. Novel nanorope structures composed of two perfectly intertwined multiwall nanotubes extending for several microns were observed. It is hypothesized that pairs of contacting nanoparticles result in the extrusion of such structures, which may be promising to investigate for mechanical applications.

Fe-doped carbon aerogels prepared with reduced Fe doping levels were also evaluated as candidates for growth of single-wall carbon nanotubes on a carbon aerogel monolith. Although some bundles of very small-diameter nanotubes (probably single-walled) were observed after CVD was performed on these samples, the majority of graphitic structures formed were large diameter tubules which appear too large to be nanotubes and were concluded to be carbon fibers. XRD of these aerogels revealed that they exhibit low nanoparticle crystallinity, implying that the catalyst nanoparticles may be too small for nanotube growth and when present in high concentration work together to catalyze graphitic fibers.

Although the iron-carbon system enables a great deal of versatility in the catalysis in the CVD growth of carbon nanotubes, it is also very complex and, in many ways, not ideal for deterministic control over carbon nanotube growth. In a deterministic heterogeneous nanotube catalysis system, however, transparent processes such as nanoparticle-enhanced feedstock cracking (dehydrogenation) and *in situ* reduction of nanoparticles to a catalytic state would be well characterized, intelligently controlled, and non-statistical in nature. The rich chemistry of iron, cobalt, and nickel facilitates the tendency for a range of chemical states to emerge among catalyst nanoparticles, each of which may contribute to the overall CVD growth of nanotubes in a different way (such as by facilitating feedstock cracking,

diffusion of carbon into the nanoparticle, nucleation of graphite, combating catalyst poisoning, etc.). The emergence of these various compositions and the nature of their respective contributions are likely statistical in nature and are certainly not well characterized. Thus, it is proposed that the "ideal" nanotube catalyst would be a material whose sole function is the diffusion, nucleation, and precipitation of crystalline carbon and which would not be susceptible to chemical changes during growth or require a pretreatment for activation that could result in a statistical spread of chemical states among catalyst nanoparticles. Based on the findings of Chapter 4, it is proposed that Rh, Pd, Ir, Pt, and possibly Au may be such catalysts.

Metal-doped carbon aerogels were found to be useful testing grounds for evaluating the chemical response of metal-containing nanoparticles to the presence of excess carbon and oxygen at elevated temperatures—a system analogous in many ways to CVD growth of carbon nanotubes over metal nanoparticles. Based on this observation, a series of six new metal-doped carbon aerogel systems were evaluated in the context of identifying and charactering catalytic propensity in these six metals. The three carbophobic metals selected—Re, Au, and Rh—exhibited no carbide compound formation as a result of pyrolysis at 800°C or 1050°C, suggesting these three metals are resistant to potential carbide poisoning mechanisms. Of the three, Rh-doped carbon aerogels gave the highest yields and highest quality of nanotubes. The successful growths on Re-doped carbon aerogels are the first reported examples of the ability of rhenium to catalyze nanotube growth. Re-doped carbon aerogels pyrolyzed at 1050°C also exhibited an unusual metallization of the exterior surface of the monolith, offering an interest starting point for investigating the possibility of producing nanoporous metals based on Re-plated carbon aerogels. The three carbophilic metals—W, Ta, and Nb—exhibited carbide compound formation as a result of pyrolysis, as expected. Ta and W both formed significant crystalline oxides as well. Nb-doped carbon aerogels were found to catalyze growth of carbon nanotubes, also resulting in the formation of nanorods and unusual graphitic "nanotortillas" over the surface of the sample. This is believed to be the first report of Nb catalyzing nanotube growth. Only Ta-doped carbon aerogels pyrolyzed at 1050°C were found to catalyze nanotube growth,

implying that the nanoparticles composed of the oxides of tantalum require thorough carbothermic reduction before they can be rendered catalytic. This is believed to be the first report of Ta-based catalysis of nanotube growth as well. Lastly, CVD on W-doped carbon aerogels was found to be inconclusive, however crystalline W nanorods believed to be composed of $W_{18}O_{49}$ were observed, which as it turns out agrees with investigations made on W-doped carbon aerogel-like materials previously [47].

A technique for preparing surface-based nanoparticles composed of Au, Re, and combinations of Au and Re was developed. Nanoparticles prepared through this technique were then investigated for use in the CVD growth of carbon nanotubes. It was found that Au, Re, and bimetallic Au-Re nanoparticles were all capable of growing single-wall carbon nanotubes when reduced prior to CVD but not oxidized, and when hydrocarbons were used as the carbon feedstock for CVD instead of alcohol. It was also found that only Au and some compositions of Au and Re nanoparticles were capable of growing nanotubes when both reduced and subsequently oxidized prior to CVD, or when alcohol was used as the carbon feedstock for CVD. It is known that Re oxidizes above 540°C to afford a volatile oxide of the stoichiometry Re_2O_7 [103], and based on XPS and AFM characterizations made at various stages of nanoparticle implementation, it is believed that this oxidation pathway is why rhenium nanoparticles did not result in nanotube growth when oxidized and why such nanoparticles frequently disappeared from the substrate altogether. The oxidative volatilization of rhenium at elevated temperatures may, however, be a route to a novel nanotemplating technique which could be employed to produce nanoporous metals through dealloying of bimetallic rhenium alloys. Based on the observed oxidative rhenium volatilization, it is hypothesized that successful growth with oxidized Au-Re nanoparticles may be due to the emergence of a particular gold-enriched oxidation-resistant Au-Re alloy or intermetallic which results from an increased in the Au:Re ratio of nanoparticles resulting from rhenium volatilization. It is also possible that all of the Re is volatilized off and that the successful growth is due solely to catalysis by gold remaining on the surface. The surfaces of gold nanoparticles were found to

oxidize as a result of ethanol-based CVD where they were found not to oxidize in air at 900°C. This provides evidence of highly oxidative $OH^{\cdot}$ radicals present in CVD when ethanol is employed [109-114]. Non-volatile rhenium oxide-coated nanoparticles resulting from a wet $ReCl_5$ precursor were not observed to volatilize after oxidative pretreatment or CVD, but also did not catalyze nanotube growth. This provides evidence that rhenium oxide itself is not catalytic and requires reduction to rhenium metal before nanotubes growth can be catalyzed. This necessity for reductive pretreatment imposes a higher activation energy barrier for initiating growth if done *in situ* during CVD, which may explain why nanotube growth was observed with Au at both 700°C and 900°C but only at 900°C with Re.

Lastly, a new chemical vapor deposition system design for optimizing nanotube growth is presented. The system is centered on the concept of eliminating problems arising from aerodynamics and thermal gradients during CVD. Further development and experimentation with this system is underway.

This thesis began with the characterization of what seemed to be an uninteresting system of Fe-doped carbon aerogels which later proved to be useful in the generation of a class of novel new materials—carbon aerogel-carbon nanotube composites. Correlating compositional characterization of these materials with their ability to catalyze nanotube growth by thermal CVD proved to provide valuable insights into the fundamentals of the preparation of another material—carbon nanotubes. As we progress in developing nanoscale technologies for the future, it is important to remember that value lies not only in steering intentional investigations to a desired outcome, but also in identifying novelty in unexpected responses encountered along the way.

Bibliography

[1] Physorg.com. *Nanosys, Sharp to Develop Nanotechnology-Enabled Fuel Cells.* 21 Jan 2005 [cited 30 May 2006]; Available from: http://www.physorg.com/news2782.html.

[2] Physorg.com. *Toshiba's 'Nanobattery' Recharges in Only One Minute.* 29 Mar 2005 [cited 30 May 2006]; Available from: http://www.physorg.com/news3539.html.

[3] Wikipedia contributors. *Supercapacitor.* [cited 30 May 2006]; Available from: http://en.wikipedia.org/w/index.php?title=Supercapacitor&oldid=54679243.

[4] Simmons, G. *Nanotech's Tiny Focus Has Far Reaches.* 08 May 2006 [cited 30 May 2006]; Available from: http://www.foxnews.com/story/0,2933,194733,00.html.

[5] Bordjiba, T. and Dao, L. H. *Development of Advanced Supercapacitors Based on Carbon Nanotubes/Carbonized Aerogels Composite Materials.* in *207th ECS Meeting.* 2005. Quebec City, Canada.

[6] Wang, J.; Zhang, S. Q.; Guo, Y. Z.; Shen, J.; Attia, S. M.; Zhou, B.; Zheng, G. Z.; Gui, Y. S., *Morphological Effects on the Electrical and Electrochemical Properties of Carbon Aerogels.* Journal of The Electrochemical Society, 2001. **148**(6): p. D75-D77.

[7] Brandt, R.; Petricevic, R.; Pröbstle, H.; Fricke, J., *Acetic Acid Catalyzed Carbon Aerogels.* Journal of Porous Materials, 2003. **10**: p. 171-178.

[8] Fu, R.; Lin, Y.-M.; Rabin, O.; Dresselhaus, G.; Dresselhaus, M. S.; Satcher, J. H.; Baumann, T. F., *Transport Properties of Copper-Doped Carbon Aerogels.* Journal of Non-Crystalline Solids, 2003. **317**(3): p. 247-253.

[9] Endo, M.; Hayashi, T.; Yoong, A. K.; Terrones, M.; Dresselhaus, M. S., *Applications of Carbon Nanotubes in the Twenty-First Century.* Philosophical

transactions. Series A, Mathematical, physical, and engineering sciences, 2004. **362**(1823): p. 2223-2238.

[10] Baumann, T. F.; Fox, G. A.; Satcher, J. H., Jr.; Yoshizawa, N.; Fu, R.; Dresselhaus, M. S., *Synthesis and Characterization of Copper-Doped Carbon Aerogels.* Langmuir, 2002. **18**(18): p. 7073-7076.

[11] Baumann, T. F.; Fu, R.; Cronin, S.; Dresselhaus, G.; Dresselhaus, M. S.; Satcher, J. H., *Formation of Graphitic Structures in Cobalt- and Nickel-Doped Carbon Aerogels.* Langmuir, 2005. **21**: p. 2647-2651.

[12] Baumann, T. F. and Satcher, J. H., Jr., *Homogeneous Incorporation of Metal Nanoparticles into Ordered Macroporous Carbons.* Chemistry of Materials, 2003. **15**(20): p. 3745-3747.

[13] Fu, R.; Dresselhaus, M. S.; Dresselhaus, G.; Zheng, B.; Liu, J.; Jr., J. S.; Baumann, T. F., *The Growth of Carbon Nanostructures on Cobalt-Doped Carbon Aerogels.* Journal of Non-Crystalline Solids, 2003. **318**: p. 223-232.

[14] Fu, R.; Yoshizawa, N.; Dresselhaus, M. S.; Dresselhaus, G.; Satcher, J. H., Jr.; Baumann, T. F., *XPS Study of Copper-Doped Carbon Aerogels.* Langmuir, 2002. **18**(26): p. 10100-10104.

[15] Yoshizawa, N.; Fu, R.; Dresselhaus, M. S.; Dresselhaus, G.; Satcher, J.; Baumann, T., *The Structures of Copper-Doped Carbon Aerogels Prepared by an Ion Exchange Method.* Materials Research Society Symposium Proceedings, 2002. **697**(Surface Engineering 2001): p. 383-388.

[16] Cao, W.; Song, X. Y.; Hunt, A. J., *Preparation and Characterization of Aerogel-Based Carbon Nanocomposites.* Materials Research Society Symposium Proceedings, 1994. **349**(Novel Forms of Carbon II): p. 87-92.

[17] Song, X. Y.; Cao, W.; Hunt, A. J., *AEM and HREM Evaluation of Carbon Nanostructures in Silica Aerogels.* Materials Research Society Symposium Proceedings, 1994. **349**(Novel Forms of Carbon II): p. 269-74.

[18] Song, X.-Y.; Cao, W.; Ayers, M. R.; Hunt, A. J., *Carbon Nanostructures in Silica Aerogel Composites.* Journal of Materials Research, 1995. **10**(2): p. 251-4.

[19] Li, X.; Yuan, G.; Brown, A.; Westwood, A.; Brydson, R.; Rand, B., *The Removal of Encapsulated Catalyst Particles from Carbon Nanotubes Using Molten Salts.* Carbon, 2006. **44**(9): p. 1699-1705.

[20] Li, X.; Zuo, X.; Liu, J., *Preparation of Co/MgO Aerogel Catalyst for Carbon Nanotube Production.* 2006, (Wuhan University of Science and Technology, Peop. Rep. China). Application: CN. p. 7.

[21] Ji, D.; Li, X.; Zhao, H.; Wang, H., *Effect of Preparing Parameters on Morphology of Multi-Walled Carbon Nanotube.* Huagong Xinxing Cailiao, 2005. **33**(11): p. 29-31.

[22] Zhang, D.; Shi, L.; Fang, J.; Li, X.; Dai, K., *Preparation and Modification of Carbon Nanotubes.* Materials Letters, 2005. **59**(29-30): p. 4044-4047.

[23] Zhang, D.-S.; Dai, K.; Fang, J.-H.; Shi, L.-Y.; Li, X.-K.; Lei, Z.-X., *Preparation and Modification of Multi-Walled Carbon Nanotubes.* Huaxue Yanjiu, 2004. **15**(3): p. 12-15.

[24] Piao, L.; Chen, J.; Li, Y., *Carbon Nanotubes Via Methane Decomposition on an Alumina Supported Cobalt Aerogel Catalyst.* China Particuology, 2003. **1**(6): p. 266-270.

[25] Lei, Z.-X.; Liu, J.; Wang, J.-B.; Li, X.-K.; Wang, H.-Z., *Effects of Catalyst Structure and Morphology on the Growth of Carbon Nanotubes.* Xinxing Tan Cailiao, 2003. **18**(4): p. 271-276.

[26] Yang, Y., *Method for Making an Improved Aerogel Catalyst for Manufacturing Single-Wall Carbon Nanotubes by Chemical Vapor Deposition.* 2003, (USA). Application: US. p. 3.

[27] Li, Y.; Pu, L.; Chen, J.; Chen, X., *Alumina Aerogel Supported Catalyst and Its Application in Preparation of Carbon Nanotube by Methane Cracking.* 2002, (Tianjin Univ., Peop. Rep. China). Application: CN. p. 8.

[28] Piao, L.-Y. and Li, Y.-D., *Structure of Carbon Nanotubes from Decomposition of Methane on an Aerogel Catalyst.* Wuli Huaxue Xuebao, 2003. **19**(4): p. 347-351.

[29] Ji, D.-J.; Li, X.-K.; Wang, H.-Z.; Hong, X.-Q.; Chen, J.-W., *Effect of Deposition Time on Yield and Morphology of Multi-Walled Carbon Nanotubes Prepared by CVD Method.* Tansu Jishu, 2002(5): p. 10-13.

[30] Tang, S.; Lin, J.; Tan, K. L.; Wu, X., *Large-Scale Synthesis of Single-Walled Carbon Nanotubes by Catalytic Decomposition of a Hydrocarbon.* 2003, (National University of Singapore, Singapore). Application: WO. p. 32.

[31] Wu, M.-Z.; Yao, L.-Z.; Jiang, G.-W.; Liu, W.-F.; Cai, W.-L.; Li, X.-G.; Yao, Z., *Fabrication, Characterization and Growth Mechanism of Helical Carbon Nanotubes.* Wuji Cailiao Xuebao, 2003. **18**(1): p. 115-120.

[32] Lei, Z.-X.; Li, X.-K.; Wang, H.-Z.; Hong, X.-Q.; Chen, J.-W., *Magnetic Properties of Carbon Nanotubes Encapsulating Nanosized Nickel Particles.* Xinxing Tan Cailiao, 2002. **17**(4): p. 67-70.

[33] Pu, L.-Y.; Zhou, X.-Z.; Chen, J.-L.; Li, Y.-D., *Production of Carbon Nanotubes from Methane Decomposition over a Al_2O_3 Supported Cobalt Aerogel Catalyst.* Sichuan Daxue Xuebao, Gongcheng Kexueban, 2002. **34**(5): p. 42-46.

[34] Piao, L.; Li, Y.; Chen, J.; Chang, L.; Lin, J. Y. S., *Methane Decomposition to Carbon Nanotubes and Hydrogen on an Alumina Supported Nickel Aerogel Catalyst.* Catalysis Today, 2002. **74**(1-2): p. 145-155.

[35] Liu, J., *High Yield Vapor Phase Deposition Method for Large Scale Single Walled Carbon Nanotube Preparation.* 2001, (Duke University, USA). Application: WO. p. 22.

[36] Li, X.; Zuo, X.; Liu, J., *Preparation of Fe_2O_3/Al_2O_3 Aerogel Catalyst for Single Wall Carbon Nanotube Production.* 2006, (Wuhan University of Science and Technology, Peop. Rep. China). Application: CN. p. 6.

[37] Li, X.; Zuo, X.; Yuan, G.; Brown, A.; Westwood, A.; Brydson, R.; Rand, B., *The Synthesis of Single-Walled Carbon Nanotubes over an Al_2O_3/Fe_2O_3 Binary Aerogel Catalyst.* Journal of Physics: Conference Series, 2005. **26**: p. 308-311.

[38] Zuo, X.; Li, X.; Yuan, G.; Su, Y.; Liao, Q.; Lei, Z., *Study of the Synthesis of Single-Walled Carbon Nanotubes on Coo/MgO Aerogel Catalyst.* Huagong Xinxing Cailiao, 2005. **33**(3): p. 32-35.

[39] Ermakova, M. A.; Ermakov, D. Y.; Chuvilin, A. L.; Kuvshinov, G. G., *Decomposition of Methane over Iron Catalysts at the Range of Moderate Temperatures: The Influence of Structure of the Catalytic Systems and the Reaction Conditions on the Yield of Carbon and Morphology of Carbon Filaments.* Journal of Catalysis, 2001. **201**: p. 183–197.

[40] Reina Cecco, A., *Growth of Aligned Single-Wall Carbon Nanotubes Using Iron-Based Catalysts (Unpublished Work).* 2006, Massachusetts Institute of Technology.

[41] Bonnet, F.; Ropital, F.; Berthier, Y.; Marcus, P., *Filamentous Carbon Formation Caused by Catalytic Metal Particles from Iron Oxide.* Materials and Corrosion, 2003. **54**(11): p. 870-880.

[42] Consortium for Fossil Fuel Science, *C1 Chemistry for the Production of Ultra-Clean Liquid Transportation Fuels and Hydrogen*, G.P. Huffman, Editor. 2004, University of Kentucky.

[43] Kocabas, C.; Shim, M.; Rogers, J. A., *Spatially Selective Guided Growth of High-Coverage Arrays and Random Networks of Single-Walled Carbon Nanotubes and Their Integration into Electronic Devices.* Journal of the American Chemical Society, 2006. **128**: p. 4540-4541.

[44] Pekala, R. W. and Kong, F.-M., *A Synthetic Route to Organic Aerogels - Mechanism, Structure, and Properties.* 1988, Lawrence Livermore National Laboratory.

[45] Pekala, R. W.; Alviso, C. T.; LeMay, J. D., *Organic Aerogels: Microstructural Dependence of Mechanical Properties in Compression.* Journal of Non-Crystalline Solids, 1990. **125**(1-2): p. 67-75.

[46] Lu, X.; Nilsson, O.; Fricke, J.; Pekala, R. W., *Thermal and Electrical Conductivity of Monolithic Carbon Aerogels.* Journal of Applied Physics, 1993. **73**(2): p. 581-4.

[47] Maldonado-Hodar, F. J.; Moreno-Castilla, C.; Rivera-Utrilla, J.; Ferro-Garcia, M. A., *Metal-Carbon Aerogels as Catalysts and Catalyst Supports.* Studies in Surface

Science and Catalysis, 2000. **130B (International Congress on Catalysis, 2000, Part B)**: p. 1007-1012.

[48] Iijima, S., *Helical Microtubules of Graphitic Carbon.* Nature (London, United Kingdom), 1991. **354**(6348): p. 56-8.

[49] Iijima, S. and Ichihashi, T., *Single-Shell Carbon Nanotubes of 1-Nm Diameter.* Nature (London, United Kingdom), 1993. **363**(6430): p. 603-5.

[50] Qin, L. C.; Zhao, X.; Hirahara, K.; Miyamoto, Y.; Ando, Y.; Iijima, S., *The Smallest Carbon Nanotube.* Nature, 2000. **408**(6808): p. 50.

[51] Oberlin, A.; Endo, M.; Koyama, T., *Filamentous Growth of Carbon through Benzene Decomposition.* Journal of Crystal Growth, 1976. **32**(3): p. 335-49.

[52] Joselevich, E. and Lieber, C. M., *Vectorial Growth of Metallic and Semiconducting Single-Wall Carbon Nanotubes.* Nano Letters, 2002. **2**(10): p. 1137-1141.

[53] Hafner, J. H.; Bronikowski, M. J.; Azamian, B. R.; Nikolaev, P.; Rinzler, A. G.; Colbert, D. T.; Smith, K. A.; Smalley, R. E., *Catalytic Growth of Single-Wall Carbon Nanotubes from Metal Particles.* Chemical Physics Letters, 1998. **296**(1,2): p. 195-202.

[54] Kong, J.; Cassell, A. M.; Dai, H., *Chemical Vapor Deposition of Methane for Single-Walled Carbon Nanotubes.* Chemical Physics Letters, 1998. **292**(4,5,6): p. 567-574.

[55] Cassell, A. M.; Franklin, N. R.; Tombler, T. W.; Chan, E. M.; Han, J.; Dai, H., *Directed Growth of Free-Standing Single-Walled Carbon Nanotubes.* Journal of the American Chemical Society, 1999. **121**(34): p. 7975-7976.

[56] Li, Y.; Kim, W.; Zhang, Y.; Rolandi, M.; Wang, D.; Dai, H., *Growth of Single-Walled Carbon Nanotubes from Discrete Catalytic Nanoparticles of Various Sizes.* Journal of Physical Chemistry B, 2001. **105**(46): p. 11424-11431.

[57] Cassell, A. M.; Raymakers, J. A.; Kong, J.; Dai, H., *Large Scale CVD Synthesis of Single-Walled Carbon Nanotubes.* Journal of Physical Chemistry B, 1999. **103**(31): p. 6484-6492.

[58] Fan, S.; Chapline, M. G.; Franklin, N. R.; Tombler, T. W.; Cassell, A. M.; Dai, H., *Self-Oriented Regular Arrays of Carbon Nanotubes and Their Field Emission Properties.* Science, 1999. **283**: p. 512-514.

[59] Kong, J.; Soh, H. T.; Cassell, A. M.; Quate, C. F.; Dai, H., *Synthesis of Individual Single-Walled Carbon Nanotubes on Patterned Silicon Wafers.* Nature (London), 1998. **395**(6705): p. 878-881.

[60] Zhang, G.; Mann, D.; Zhang, L.; Javey, A.; Li, Y.; Yenilmez, E.; Wang, Q.; McVittie, J.; Nishi, Y.; Gibbons, J.; Dai, H., *Ultra-High Yield Growth of Vertical Single-Walled Carbon Nanotubes: Hidden Roles of Hydrogen and Oxygen.* Los Alamos National Laboratory, Preprint Archive, Condensed Matter, 2005: p. 1-25, arXiv:cond-mat/0511035.

[61] Wang, X.; Yue, W.; He, M.; Liu, M.; Zhang, J.; Liu, Z., *Bimetallic Catalysts for the Efficient Growth of Swnts on Surfaces.* Chemistry of Materials, 2004. **16**(5): p. 799-805.

[62] Zheng, B.; Li, Y.; Liu, J., *CVD Synthesis and Purification of Single-Walled Carbon Nanotubes on Aerogel-Supported Catalyst.* Applied Physics A: Materials Science & Processing, 2002. **74**(3): p. 345-348.

[63] Su, M.; Zheng, B.; Liu, J., *A Scalable CVD Method for the Synthesis of Single-Walled Carbon Nanotubes with High Catalyst Productivity.* Chemical Physics Letters, 2000. **322**(5): p. 321-326.

[64] Futaba Don, N.; Hata, K.; Yamada, T.; Mizuno, K.; Yumura, M.; Iijima, S., *Kinetics of Water-Assisted Single-Walled Carbon Nanotube Synthesis Revealed by a Time-Evolution Analysis.* Physical review letters, 2005. **95**(5): p. 056104.

[65] Hata, K.; Futaba, D. N.; Mizuno, K.; Namai, T.; Yumura, M.; Iijima, S., *Water-Assisted Highly Efficient Synthesis of Impurity-Free Single-Walled Carbon Nanotubes.* Science, 2004. **306**: p. 1362-1364.

[66] Dillon, A. C.; Mahan, A. H.; Parilla, P. A.; Alleman, J. L.; Heben, M. J.; Jones, K. M.; Gilbert, K. E. H., *Continuous Hot Wire Chemical Vapor Deposition of High-Density Carbon Multiwall Nanotubes.* Nano Letters, 2003. **3**(10): p. 1425-1429.

[67] Lee, C. J.; Lyu, S. C.; Kim, H.-W.; Park, J. W.; Jung, H. M.; Park, J., *Carbon Nanotubes Produced by Tungsten-Based Catalyst Using Vapor Phase Deposition Method.* Chemical Physics Letters, 2002. **361**(5,6): p. 469-472.

[68] Wang, Y. Y.; Gupta, S.; Nemanich, R. J.; Liu, Z. J.; Qin, L. C., *Hollow to Bamboolike Internal Structure Transition Observed in Carbon Nanotube Films.* Journal of Applied Physics, 2005. **98**(1): p. 014312/1-014312/6.

[69] Li, Y.-L.; Kinloch, I. A.; Windle, A. H., *Direct Spinning of Carbon Nanotube Fibers from Chemical Vapor Deposition Synthesis.* Science, 2004. **304**: p. 276-278.

[70] Hong, B. H.; Lee, J. Y.; Beetz, T.; Zhu, Y.; Kim, P.; Kim, K. S., *Quasi-Continuous Growth of Ultralong Carbon Nanotube Arrays.* Journal of the American Chemical Society, 2005. **127**(44): p. 15336-15337.

[71] Louchev, O. A.; Sato, Y.; Kanda, H., *Growth Mechanism of Carbon Nanotube Forests by Chemical Vapor Deposition.* Applied Physics Letters, 2002. **80**(15): p. 2752-2754.

[72] Li, W.; Xie, S.; Liu, W.; Zhao, R.; Zhang, Y.; Zhou, W.; Wang, G.; Qian, L., *A Structure Model and Growth Mechanism for Novel Carbon Nanotubes.* Journal of Materials Science, 1999. **34**(11): p. 2745-2749.

[73] Mo, Y. H.; Kibria, A. K. M. F.; Nahm, K. S., *The Growth Mechanism of Carbon Nanotubes from Thermal Cracking of Acetylene over Nickel Catalyst Supported on Alumina.* Synthetic Metals, 2001. **122**(2): p. 443-447.

[74] Jeong, H. J.; Shin, Y. M.; Kim, K. S.; Jeong, S. Y.; Park, Y. S.; Choi, Y. C.; Lee, Y. H., *Temperature and Time Dependence of the Growth of Carbon Nanotubes by Thermal Chemical Vapor Deposition.* AIP Conference Proceedings, 2001. **590**(Nanonetwork Materials): p. 35-38.

[75] Dupuis, A.-C., *The Catalyst in the CCVD of Carbon Nanotubes - a Review.* Progress in Materials Science, 2005. **50**(8): p. 929.

[76] Shunk, F. A., *Constitution of Binary Alloys, Second Supplement.* 1969, McGraw-Hill: New York.

[77] Moulder, J. F.; Stickle, W. F.; Sobol, P. E.; Bomben, K. D., *Handbook of X-Ray Photoelectron Spectroscopy*, ed. J. Chastain and J. Rojer C. King: Physical Electronics, Inc.

[78] Welsh, I. D. and Sherwood, P. M. A., *Photoemission and Electronic Structure of FeOOH: Distinguishing between Oxide and Oxyhydroxide.* Physical Review B, 1989. **40**(9): p. 6386-6392.

[79] Gaskell, D. R., *Metal Production: Ellingham Diagrams*, in *Encyclopedia of Materials: Science and Technology*. 2001, Elsevier. p. 5481-5486.

[80] Maldonado-Hodar, F. J.; Moreno-Castilla, C.; Rivera-Utrilla, J.; Hanzawa, Y.; Yamada, M., *Catalytic Graphitization of Carbon Aerogels by Transition Metals.* Langmuir, 2000. **16**: p. 4367.

[81] Matthews, M. J.; Pimenta, M. A.; Dresselhaus, G.; Dresselhaus, M. S.; Endo, M., *Origin of Dispersive Effects of the Raman D Band in Carbon Materials.* Physical Review B, 1999. **59**(10): p. R6585-R6588.

[82] Brunauer, S.; Emmett, P. H.; Teller, E., *Adsorption of Gases in Multimolecular Layers.* Journal of the American Chemical Society, 1938. **60**: p. 309.

[83] Barrett, E. P.; Joyner, L. G.; Halenda, P. P., *The Determination of Pore Volume and Area Distributions in Porous Substances. I. Computations from Nitrogen Isotherms.* Journal of the American Chemical Society, 1951. **73**: p. 373-380.

[84] Liu, X.; Fu, L.; Hong, S.; Dravid, V. P.; Mirkin, C. A., *Arrays of Magnetic Nanoparticles Patterned Via "Dip-Pen" Nanolithography.* Advanced Materials, 2002. **14**(3): p. 231-234.

[85] Yamamuro, S.; Ando, T.; Sumiyama, K.; Uchida, T.; Kojima, I., *Monodisperse Metallic Iron Nanoparticles Synthesized from Noncarbonyl Complex.* Japanese Journal of Applied Physics, Part 1: Regular Papers, Short Notes & Review Papers, 2004. **43**(7A): p. 4458-4459.

[86] Hyeon, T.-H., *Synthesis of Mono-Disperse and Highly-Crystalline Nanoparticles of Metals, Alloys, Metal Oxides, and Multi-Metallic Oxides without a Size Selection*

Process. 2003, (Korea Nano Technology Co., Ltd., S. Korea). Application: WO. p. 43.

[87] Bianchini, E. C. and Lund, C. R. F., Journal of Catalysis, 1989. **177**: p. 455.

[88] Shah, N.; Pattanaik, S.; Huggins, F. E.; Panjala, D.; Huffman, G. P., *XAFS and Mössbauer Spectroscopy Characterization of Supported Binary Catalysts for Nonoxidative Dehydrogenation of Methane.* Fuel Processing Technology, 2003. **83**: p. 163-173.

[89] Diaz-Barriga-Arceo, L.; Rendon-Vazquez, L.; Orozco, E.; Lopez-Hirata, V. M.; Garibay-Febles, V., *Nanoparticles Obtained from Mechanically Alloyed and Heat Treated Cobalt Carbide.* Journal of Metastable and Nanocrystalline Materials, 2004. **20-21**: p. 287-290.

[90] Hauffe, K., *The Importance of Electron-Defect Structure for Nonmetallic Heterogeneous Catalysts.* DECHEMA Monographien, 1956. **26**: p. 301-32.

[91] Tang, X.-P.; Kleinhammes, A.; Shimoda, H.; Fleming, L.; Bennoune, K. Y.; Sinha, S.; Bower, C.; Zhou, O.; Wu, Y., *Electronic Structures of Single-Walled Carbon Nanotubes Determined by NMR.* Science, 2000. **288**: p. 492-494.

[92] Ajayan, P. M.; Lambert, J. M.; Bernier, P.; Barbedette, L.; Colliex, C.; Planeix, J. M., *Growth Morphologies During Cobalt-Catalyzed Single-Shell Carbon Nanotube Synthesis.* Chemical Physics Letters, 1993. **215**(5): p. 509-17.

[93] Jeong, H. J.; Jeong, S. Y.; Shin, Y. M.; Han, J. H.; Lim, S. C.; Eum, S. J.; Yang, C. W.; Kim, N.-g.; Park, C.-Y.; Lee, Y. H., *Dual-Catalyst Growth of Vertically Aligned Carbon Nanotubes at Low Temperature in Thermal Chemical Vapor Deposition.* Chemical Physics Letters, 2002. **361**(3,4): p. 189-195.

[94] Wang, Y. G.; Shah, N.; Huffman, G. P., *Simultaneous Production of Hydrogen and Carbon Nanostructures by Decomposition of Propane and Cyclohexane over Alumina Supported Binary Catalysts.* Catalysis Today, 2005. **99**(3,4): p. 359-364.

[95] Lee, S. Y.; Yamada, M.; Miyake, M., *Synthesis of Carbon Nanotubes over Gold Nanoparticle Supported Catalysts.* Carbon, 2005. **43**(13): p. 2654-2663.

[96] Kamide, K.; Araki, H.; Yoshino, K., *Controlled Growth of Carbon Nanotubes on Micropatterned Au/Cr Composite Film and Field Emission from Their Arrays.* Japanese Journal of Applied Physics, Part 2: Letters, 2003. **42**(12B): p. L1539-L1542.

[97] Wal, R. L. V.; Ticich, T. M.; Curtis, V. E., *Substrate-Support Interactions in Metal-Catalyzed Carbon Nanofiber Growth.* Carbon, 2001. **39**(15): p. 2277-2289.

[98] Lambert, J. M.; Ajayan, P. M.; Bernier, P., *Synthesis of Single and Multi-Shell Carbon Nanotubes.* Synthetic Metals, 1995. **70**(1-3): p. 1475-6.

[99] Iijima, S. and Ichihashi, T., *Manufacture of Nanotubular Carbon Fibers (Carbon Nanotubes) with Single-Layer Spiral Cylindrical Structure in the Presence of Gaseous Catalysts.* 1994, (Nippon Electric Co, Japan). Application: JP. p. 6.

[100] Zaikovskii, V. I.; Chesnokov, V. V.; Buyanov, R. A., *The Relationship between the State of Active Species in a Ni/Al_2O_3 Catalyst and the Mechanism of Growth of Filamentous Carbon.* Kinetics and Catalysis (Translation of Kinetika i Kataliz), 2001. **42**(6): p. 813-820.

[101] *PDF00-005-0685 (Rhodium - Rh) in ICDD Powder Diffraction File 4+ (PDF-4+).* 2005, International Centre for Diffraction Data.

[102] Knight, D. S. and White, W. B., *Characterization of Diamond Films by Raman Spectroscopy.* Journal of Materials Research, 1989. **4**(2): p. 385-393.

[103] Leddicotte, G. W., *The Radiochemistry of Rhenium*, in *Nuclear Science Series*, National Academy of Sciences Subcommittee on Radiochemistry, Editor. 1961, Oak Ridge National Laboratory: Oak Ridge, Tennessee.

[104] Shatynski, S. R., *The Thermochemistry of Transition Metal Carbides.* Oxidation of Metals, 1979. **13**(2): p. 105-118.

[105] Shunk, F. A., *Constitution of Binary Alloys, Second Supplement.* 1969, McGraw-Hill: New York. p. 155.

[106] *PDF00-005-0702 (Rhenium - Re) in ICDD Powder Diffraction File 4+ (PDF-4+).* 2005, International Centre for Diffraction Data.

[107] Buffat, P. and Borel, J.-P., *Size Effect on the Melting Temperature of Gold Particles.* Physical Review A, 1976. **13**(6): p. 2287-2296.

[108] Okamoto, H. and Massalaski, T. B., *The Au-C (Gold-Carbon) System.* Bulletin of Alloy Phase Diagrams, 1984. **5**(4): p. 378-379.

[109] B. Koslowki *et al.*, Surface Science, 2001. **475**: p. 1.

[110] Boyen, H.-G.; Kästle, G.; Weigl, F.; Koslowski, B.; Dietrich, C.; Ziemann, P.; Spatz, J. P.; Riethmüller, S.; Hartmann, C.; Möller, M.; Schmid, G.; Garnier, M. G.; Oelhafen, P., *Oxidation-Resistant Gold-55 Clusters.* Science, 2002. **297**: p. 1533-1536.

[111] Eley, D. D. and Moore, P. B., Surface Science, 1978. **76**: p. L599.

[112] Parker, D. H. and Koel, B. E., Journal of Vacuum Science and Technology A, 1990. **8**: p. 2585.

[113] Pireau, J. J.; Liehr, M.; Thiry, P. A.; Delrue, J. P.; Caudano, R., Surface Science, 1984. **141**: p. 221.

[114] Ron, H. and Rubinstein, I., Langmuir, 1994. **10**: p. 4566.

[115] *PDF00-004-0784 (Gold - Au) in ICDD Powder Diffraction File 4+ (PDF-4+).* 2005, International Centre for Diffraction Data.

[116] Worrell, W. L. and Chipman, J., *A Thermodynamic Analysis of the Ta-C-O, Cb-C-O, and V-C-O Systems.* Transactions of the Metallurgical Society of AIME, 1964. **230**: p. 1682-1686.

[117] *PDF00-038-1364 (Niobocarbide - NbC) in ICDD Powder Diffraction File 4+ (PDF-4+).* 2005, International Centre for Diffraction Data.

[118] Pierson, H. O., *Carbides of Group V: Vanadium, Niobium, and Tantalum Carbides*, in *Handbook of Refractory Carbides and Nitrides.* 1996, William Andrew Publishing/Noyes. p. 81-99.

[119] Hammond, C. R., *The Elements*, in *CRC Handbook of Chemistry and Physics, 86th Edition*, D.R. Lide, Editor. 2005-2006, Chemical Rubber Company. p. 35-36.

[120] *PDF00-025-0922 (Ta_2O_5 - Tantalum Oxide) in ICDD Powder Diffraction File 4+ (PDF-4+).* 2005, International Centre for Diffraction Data.

[121] *PDF00-021-1199 (Ta_2O_5 - Tantalum Oxide) in ICDD Powder Diffraction File 4+ (PDF-4+).* 2005, International Centre for Diffraction Data.

[122] *PDF03-065-4090 (TaO - Tantalum Oxide) in ICDD Powder Diffraction File 4+ (PDF-4+)*. 2005, International Centre for Diffraction Data.

[123] *PDF03-065-8145 ($TaC_{0.95}$ - Tantalum Carbide) in ICDD Powder Diffraction File 4+ (PDF-4+)*. 2005, International Centre for Diffraction Data.

[124] *PDF03-065-3191 (Ta_4C_3 - Tantalum Carbide) in ICDD Powder Diffraction File 4+ (PDF-4+)*. 2005, International Centre for Diffraction Data.

[125] *PDF01-089-2121 ($Ta_4C_{3.04}$ - Tantalum Carbide) in ICDD Powder Diffraction File 4+ (PDF-4+)*. 2005, International Centre for Diffraction Data.

[126] *PDF01-089-2721 ($TaC_{0.957}$ - Tantalum Carbide) in ICDD Powder Diffraction File 4+ (PDF-4+)*. 2005, International Centre for Diffraction Data.

[127] *PDF03-065-0282 (TaC - Tantalum Carbide) in ICDD Powder Diffraction File 4+ (PDF-4+)*. 2005, International Centre for Diffraction Data.

[128] *PDF00-004-0806 (W - Wolfram) in ICDD Powder Diffraction File 4+ (PDF-4+)*. 2005, International Centre for Diffraction Data.

[129] *PDF01-088-2339 (W - Tungsten) in ICDD Powder Diffraction File 4+ (PDF-4+)*. 2005, International Centre for Diffraction Data.

[130] *PDF00-032-1393 (WO_2 - Tungsten Oxide) in ICDD Powder Diffraction File 4+ (PDF-4+)*. 2005, International Centre for Diffraction Data.

[131] *PDF01-084-1516 ($W_{18}O_{49}$ - Tungsten Oxide) in ICDD Powder Diffraction File 4+ (PDF-4+)*. 2005, International Centre for Diffraction Data.

[132] *PDF00-020-1316 (WC_{1-X} - Tungsten Carbide) in ICDD Powder Diffraction File 4+ (PDF-4+)*. 2005, International Centre for Diffraction Data.

[133] *PDF00-035-0776 (W_2C - Tungsten Carbide) in ICDD Powder Diffraction File 4+ (PDF-4+)*. 2005, International Centre for Diffraction Data.

[134] *PDF00-031-1408 ($W_{12}C_{5.08}$ - Tungsten Carbide) in ICDD Powder Diffraction File 4+ (PDF-4+)*. 2005, International Centre for Diffraction Data.

[135] Vajtai, R.; Kordas, K.; Wei, B. Q.; Bekesi, J.; Leppavuori, S.; George, T. F.; Ajayan, P. M., *Carbon Nanotube Network Growth on Palladium Seeds*. Materials Science &

Engineering C - Biomimetic and Supramolecular Systems, 2002. **19**(1,2): p. 271-274.

[136] Wikipedia contributors. *Rhenium.* [cited 6 May 2006]; Available from: http://en.wikipedia.org/w/index.php?title=Supercapacitor&oldid=54679243.

[137] Okamoto, H. and Massalaski, T. B., *The Au-Re (Gold-Rhenium) System.* Bulletin of Alloy Phase Diagrams, 1984. **5**(4): p. 383.

[138] Clarke, J. K. A. and Taylor, J. F., *Reactions of Alkanes on Rhenium and Rhenium-Gold Films.* Journal of the Chemical Society, Faraday Transactions 1, 1974. **71**(10): p. 2063-2071.

[139] Bastl, Z. and Pick, Š., *Angle Resolved X-Ray Photoelectron Spectroscopy Study of Au Deposited on Pt and Re Surfaces.* Surface Science, 2004. **566-568**: p. 832-836.

[140] Babu, K. M. and Mucalo, M. R., *Xps Studies of Freshly Prepared Rhenium Nanoparticle Dispersions from Hydrazinium Hydrate and Borohydride Reduction of Hexachlororhenate Solutions.* Journal of Materials Science Letters, 2003. **22**: p. 1755-1757.

[141] Jorio, A.; Fantini, C.; Pimenta, M. A.; Capaz, R. B.; Samsonidze, G. G.; Dresselhaus, G.; Dresselhaus, M. S.; Jiang, J.; Kobayashi, N.; Grüneis, A.; Saito, R., *Resonance Raman Spectroscopy (N,M)-Dependent Effects in Small-Diameter Single-Wall Carbon Nanotubes.* Physical Review B, 2005. **71**(075401).

[142] Lee, C. J.; Son, K. H.; Park, J.; Yoo, J. E.; Huh, Y.; Lee, J. Y., *Low Temperature Growth of Vertically Aligned Carbon Nanotubes by Thermal Chemical Vapor Deposition.* Chemical Physics Letters, 2001. **338**(2,3): p. 113-117.

[143] Liao, H. and Hafner, J. H., *Low-Temperature Single-Wall Carbon Nanotube Synthesis by Thermal Chemical Vapor Deposition.* Journal of Physical Chemistry B, 2004. **108**(22): p. 6941-6943.

[144] Maruyama, S.; Kojima, R.; Miyauchi, Y.; Chiashi, S.; Kohno, M., *Low-Temperature Synthesis of High-Purity Single-Walled Carbon Nanotubes from Alcohol.* Chemical Physics Letters, 2002. **360**: p. 229-234.

[145] Okazaki, T. and Shinohara, H., *Synthesis and Characterization of Single-Wall Carbon Nanotubes by Hot-Filament Assisted Chemical Vapor Deposition.* Chemical Physics Letters, 2003. **376**: p. 606-611.